Department of Materials
Imperial College London

PhD Thesis

Investigation of structure and conductivity of $LaNb_{0.9}Mo_{0.1}O_{4.05}$ based materials

Yidong Han

Supervisor: Prof. Stephen Skinner
Co-Supervisor: Dr Sivaprakash Sengodan

謹以此文紀念岳忠武王飛，宋提點刑獄公事慈，文信國公天祥，以及我敬愛的毛主席！

「人間萬苦人最苦，終不悔九死落塵埃」

Declaration

I, Yidong Han, declare that this thesis has been composed solely by myself and that it has not been submitted, in whole or in part, in any previous application for a degree. Except where state otherwise by reference or acknowledgment, the work presented is entirely my own.

The copyright of this thesis rests with the author. Unless otherwise indicated, its contents are licensed under a Creative Commons Attribution-Non Commercial 4.0 International Licence (CC BY-NC). Under this licence, you may copy and redistribute the material in any medium or format. You may also create and distribute modified versions of the work. This is on the condition that: you credit the author and do not use it, or any derivative works, for a commercial purpose. When reusing or sharing this work, ensure you make the licence terms clear to others by naming the licence and linking to the licence text. Where a work has been adapted, you should indicate that the work has been changed and describe those changes. Please seek permission from the copyright holder for uses of this work that are not included in this licence or permitted under UK Copyright Law.

Acknowledgements

First, I would like to express my appreciation to my supervisor, Prof. Stephen Skinner, whom I heard about when I was still in China. Since I joined the group, he has guided me through these four years with care, patience and encouragement. His enthusiasm and dedication to academic work continue to inspire me and help me improve.

I would also like to thank Dr Cati Ware, Dr Mahmoud Ardakani and Dr Gwilherm Kerherve for their help with SEM, TEM and XPS, respectively. Additionally, I am grateful to Dr Giannantonio Cibin, Dr Diego Gianolio, Dr Donato Decarolis and Dr Iuliia Mikulska for their assistance during the beamtime at Diamond Light Source. I would also like to acknowledge Dr Andrey Berenov, my favourite facility manager. Our discussions on XRD and crystallography, as well as our conversations raging from Chekhov's novels to Chinese calligraphy, have made my PhD life more colourful.

I would thank my past and present group members, especially Miss Siqi Li and Mr. Kehan Huang, for their help with the experiments in Chapter 5 (materials synthesis) and 6 (EPR measurements), respectively. I also appreciate Mr. Sivakkumaran Sukumaran, Miss Tayeba Safdar, Miss Chun Gan and Dr Arim Seong for their funny jokes in our daily life and their support during my job search. I wish them all the best in their careers.

Finally, I would like to express my deep gratitude to my beloved parents and my fiancée, Thea. Without your support and love, I could not reach this milestone.

Special thanks go to Harry Kane. The resilience I have learned from you continues to make me stronger.

Abstract

In the search for electrolyte materials for solid oxide fuel cells (SOFCs), $LaNbO_4$ based materials have attracted great attention due to their competitive ionic conductivity and good chemical stability. $LaNbO_4$ with acceptor substituents (Ca/Sr) on La sites exhibits pure proton conductivity, which can be maintained to high temperatures across a wide range of oxygen partial pressures under humidified conditions. However, the conductivity is hindered by the low solubility of the substituents on La sites and a transition from monoclinic phase to tetragonal phase is unavoidable at intermediate temperatures, leading to potential mechanical failures of the devices. Another system, $LaNbO_4$ with donor substituents (W/Mo) on Nb sites, possessing modulated structures, avoids those two drawbacks and exhibits pure oxygen ion conductivities. However, the effects of modulated structures on their electrochemical performances are still unclear.

This work shows that Mo substituted $LaNbO_4$ possesses a 2D incommensurately modulated structure and the modulated structures are eliminated by slightly substituting Gd or W on La or Nb sites, respectively. The modulated structures have negative effects on the electrochemical performance, as the activation energy of an unmodulated structure is about 0.9 eV lower than that of a modulated one. With increasing the content of substituents, either the increased porosity or the emergence of a secondary phase decreases the conductivities.

This work also investigates the stability of $LaNb_{0.9}Mo_{0.1}O_{4.05}$ under different atmospheres. The results show that the oxidation state of Mo is stable under oxygen, air and nitrogen; however, under vacuum or hydrogen, Mo is reduced and the structure of $LaNb_{0.9}Mo_{0.1}O_{4.05}$ changes. X-ray absorption spectroscopy results show that these changes are accompanied by changes in the coordination environments of Nb sites. The electrochemical impedance spectroscopy data show that $LaNb_{0.9}Mo_{0.1}O_{4.05}$ annealed under hydrogen exhibits proton and electronic conductivity, which could be utilised as the anode for SOFCs.

List of Publications

Chapter 4 contains information from:

Han, Y. and Skinner, S.J., 2023. Investigation of the crystal structure and electrochemical performance of Gd doped $LaNb_{0.9}Mo_{0.1}O_{4.05}$. *Materials Advances*, *4*(17), pp.3759-3766.

Chapter 5 contains information from:

Han, Y., Li, S. and Skinner, S., 2024. Effect of W and Mo co-substitution on conductivity and structure of $LaNbO_4$. *Journal of Solid State Chemistry*, *332*, p.124590.

Contents

Declaration II

Acknowledgements III

Abstract IV

List of Publications V

List of Figures IX

List of Tables XIX

List of Acronyms XXI

Chapter 1. Introduction 1

1.1 Background 1

1.2 Proton conducting solid oxide fuel cells 4

1.2.1 Anode 4

1.2.2 Cathode 5

1.2.3 Electrolyte 6

1.3 Oxygen ion conducting solid oxide fuel cells 6

1.3.1 Anode 7

1.3.2 Cathode 7

1.3.3 Electrolyte 8

Chapter 2. Literature review 12

2.1 The structure of $LaNbO_4$ 12

2.2 Proton conduction mechanism in $LaNbO_4$ 13

2.3 Oxygen ion conduction mechanism in $LaNbO_4$ 17

2.4 Substituent strategies on La site 20

2.4.1 Calcium 20

2.4.2 Other alkaline elements and divalent elements 24

2.4.3 Lanthanides 25
2.5 Substituent strategies on Nb site 27
2.5.1 Elements working as acceptor substituents 28
2.5.2 Elements related to phase transition temperature 29
2.5.3 W and Mo 32
Chapter 3. Experimental details 38
3.1 Sample preparation 38
3.2 X-Ray related techniques 39
3.2.1 X-Ray diffraction 40
3.2.2 XRD refinement 43
3.2.3 X-Ray photoelectron spectroscopy 45
3.2.4 X-Ray absorption spectroscopy 46
3.3 Other techniques 50
3.3.1 Thermogravimetric analysis 50
3.3.2 Scanning electron microscopy 51
3.3.3 Transmission electron microscopy 52
3.3.4 Electrochemical impedance spectroscopy 54
3.3.5 Ultraviolet–visible spectroscopy 56
3.3.6 Electron paramagnetic resonance spectroscopy 57
Chapter 4. Investigation of crystal structure and electrochemical performance of Gd substituted $LaNb_{0.9}Mo_{0.1}O_{4.05}$ 59
4.1 Introduction 59
4.2 Structural and chemical study 61
4.3 Electrochemical study 75
4.4 Conclusion 79
Chapter 5. Effect of W and Mo co substitution on conductivity and structure of $LaNbO_4$ 80

5.1 Introduction....80
5.2 Structural evolution of $LaNb_{0.8}W_xMo_{0.2-x}O_{4.1}$ series....81
5.3 Microstructure of $LaNb_{0.8}W_xMo_{0.2-x}O_{4.1}$ series....85
5.4 Electrochemical properties of $LaNb_{0.8}W_xMo_{0.2-x}O_{4.1}$ series....91
5.5 Detailed analysis of $LaNb_{0.8}W_{0.02}Mo_{0.18}O_{4.1}$ 93
5.6 Conclusion 95
Chapter 6. Investigation of stability and oxidation states of Mo in $LaNb_{0.9}Mo_{0.1}O_{4.05}$ under different atmospheres 97
6.1 Introduction....98
6.2 Oxidation states of Mo in as-sintered LNM10 99
6.3 Study of LNM10 annealed under different atmospheres....105
6.4 In-situ XAS study of LNM10 annealed under 5% H_2/N_2 113
6.5 Electrochemical study of LNM10 under different atmospheres 127
6.6 Conclusion 131
Chapter 7. Conclusions and future works....133
7.1 Conclusions....133
7.2 Future works 135
References 137
Appendix 149
A1 Related information of La site substituted $LaNbO_4$ 149
A2 Related information of Nb site substituted $LaNbO_4$ 152
A3 Refined structural parameters of $La_{1-x}Gd_xNb_{0.9}Mo_{0.1}O_{4.05}$ series at 25 °C....157
A4 Transition behaviour of $La_{1-x}Gd_xNb_{0.9}Mo_{0.1}O_{4.05}$ series from m-phase to t-phase....158
A5 Refined structural parameters of $LaNb_{0.8}W_xMo_{0.2-x}O_{4.1}$ series at 25 °C 166
A6 Refined structural parameters of $LaNb_{0.8}W_xMo_{0.2-x}O_{4.1}$ series at 850 °C 167
A7 Permission documents....168

List of Figures

Figure 1.1.1. The CO_2 emissions from energy use. The data are extracted from the energy outlook of BP [1]. 2

Figure 1.1.2. The fraction of fuels used in heavy industries. The data are extracted from the energy outlook of BP [1]. 2

Figure 1.2.1. Schematic representations of active sites of TIEC (left) and mixture of MIEC and proton conducting materials (right). ''PCO'' represents the proton conducting oxides. Reproduced with permission [2]. Copyright (2022), Elsevier. 5

Figure 1.3.1. Schematic representations of oxygen vacancy mechanism (upper) and oxygen interstitial mechanism (lower) for oxygen ion conduction. The open circles represent the lattice oxygen ions. The squares and solid circles represent the oxygen vacancy and interstitial sites, respectively. The arrows represent the direction of the movement of the oxygen ions. 8

Figure 1.3.2. Conductivity data of YSZ, CGO and LSGM. Reproduced with permission [3]. Copyright (2010), American Chemical Society. 10

Figure 2.1.1. The structures of a) m-phase and b) t-phase $ReNbO_4$. The pink, blue and red balls represent rare earth, niobium, and oxygen atoms, respectively. Reproduced with permission [4]. Copyright (2016), American Institute of Physics. 13

Figure 2.2.1. Structures of a) t-$LaNbO_4$ and b) m-$LaNbO_4$. The red and green balls represent O and La sites, respectively. The niobium sites are represented by the green balls in the tetrahedra. Reproduced with permission [5]. Copyright (2010), Royal Society of Chemistry.15

Figure 2.2.2. Stable proton sites in a) t-$LaNbO_4$ and b) m-$LaNbO_4$. Reproduced with permission [5]. Copyright (2010), Royal Society of Chemistry. 15

Figure 2.2.3. Potential proton migration paths in a) t-$LaNbO_4$ and b) m-$LaNbO_4$. Reproduced with permission [5]. Copyright (2010), Royal Society of Chemistry. 16

Figure 2.2.4. Temperature dependence of $\Delta H_{mob,H}$ (squares) and O(1)-O(1) separation distance of $LaNbO_4$. Reproduced with permission [6]. Copyright (2012), Elsevier. 16

Figure 2.2.5. Relationship between incorporation energy and substituents radii for acceptor substituents on La site. Reproduced with permission [7]. Copyright (2010), American Chemistry Society. 17

Figure 2.3.1. The connection of interstitial sites in t-$LaNbO_4$. The different migration paths are labelled by numbers and the different oxygen interstitial sites are labelled as O_{int}-1 and O_{int}-2, respectively. Reproduced with permission [8]. Copyright (2018), Royal Society of Chemistry. 18

Figure 2.3.2. Schematic representations of a) the initial status of interstitialcy mechanism, b) the process of interstitialcy mechanism and c) the final status of interstitialcy mechanism. The steps are labelled as numbers. The solid and dashed circles represent the oxygen atoms at regular sites and interstitial sites, respectively. 19

Figure 2.3.3. The migration pathways of oxygen ions conductivity via interstitials a) in the *ab* plane and b) along the *c* axis. Reproduced with permission [8]. Copyright (2018), Royal Society of Chemistry. 20

Figure 2.4.1. Total conductivities of 1 mol% Ca substituted $LaNbO_4$ under different atmospheres. Reproduced with permission [9]. Copyright (2006), Nature. 21

Figure 2.4.2. A schematic representation of grain boundary core-space charge layer model. The grey area represents the grain boundary core. 25

Figure 2.5.1. Ionic radius (r_{ion}), coordination number and electronegativity (χ) of Nb Nb^{5+} and substituents (Ta^{5+}, Sb^{5+}, As^{5+} and V^{5+}) on Nb sites. Reproduced with permission [10]. Copyright (2018), Royal Society of Chemistry. 32

Figure 2.5.2. a) XRD patterns of $LaNb_{0.92}W_{0.08}O_{4.04}$ with satellite peaks marked with asterisk (inset), and b) ED patterns of $LaNb_{0.92}W_{0.08}O_{4.04}$ from [010] zone axis, respectively. Reproduced with permission [11]. Copyright (2013), Elsevier. 33

Figure 2.5.3 Schematic representations of a) a normal crystal lattice, b) a commensurately modulated lattice, c) an incommensurately modulated lattice and d) the corresponding diffraction patterns, respectively. 34

Figure 2.5.4 Phase diagram of $LaNb_{1-x}Mo_xO_{4+0.5x}$. Reproduced with permission [12]. Copyright (2021), Royal Society of Chemistry. 37

Figure 3.1.1. Flowchart of the preparation of the samples in this work. 39

Figure 3.2.1. The interactions between X-rays and materials. ''*I*'' and ''λ'' represent the intensities and wavelengths of the X-rays. ''μ'' and ''*x*'' represent the attenuation coefficient and thickness of the materials, respectively. The subscript ''*0*'' represents incident X-rays, the others represent the corresponding X-rays. ''XRF'' represents X-ray fluorescence. 40

Figure 3.2.2. Schematic representation of the incident X-ray λ diffracted by the grating with the interval of a. 41

Figure 3.2.3. Schematic representation of a plane *PQR* where the direction of the diffracted waves appears to be the direction of the reflected waves. 41

Figure 3.2.4. Schematic representation of Bragg's law. 42

Figure 3.2.5. Schematic representations of the energy levels of the samples and the spectrometer in the XPS measurements. 46

Figure 3.2.6. a) transitions of core electrons and their corresponding edges and b) energy diagram showing the origin of different regions in an XAS spectrum. 47

Figure 3.2.7. XAS spectrum showing regions of X-ray absorption near edge structure (XANES) and extended X-ray absorption fine structure (EXAFS). The letter ''n'' represents the principal quantum number. 48

Figure 3.3.1. The signals generated from the interactions between the electrons and the materials. 51

Figure 3.3.2. Schematic representation of the super space by rotating the modulation waves at each point atom. The grid lines highlight the translational symmetry in the superlattice. 53

Figure 3.3.3. Schematic representation of a typical spectrum of an electroceramic material. The notation ''gb'' and ''elec'' represent the grain boundary and sample-electrode interface, respectively. The ''CPE'' represents the constant phase element. 55

Figure 4.1.1. XRD patterns of $LaNb_{1-x}Mo_xO_{4+0.5x}$ (LNMO). The numbers denoted after LNMO are 100 times of the value of x. The satellite reflections from the modulated structures are marked by asterisks. Reproduced with permission [12]. Copyright (2021), Royal Society of Chemistry. 60

Figure 4.2.1. Room temperature XRD patterns of $La_{1-x}Gd_xNb_{0.9}Mo_{0.1}O_{4.05}$ series from 20° to 60° in 2θ. The satellite reflections of modulated structures are marked by arrows. 62

Figure 4.2.2. Simulated XRD patterns of $LaNbO_4$ at a) 20 °C, b) 470 °C, c) 499 °C and d) 716 °C, respectively. The XRD patterns were simulated with a monochromatic X Ray with a wavelength of 1.54059 Å based on the *in situ* XRD data from Sarin *et al* [13]. 63

Figure 4.2.3. Le Bail refinement results for XRD data of La5Gd5 at 25 °C with R_{wp} = 3.05%, χ2 = 3.20..... 64

Figure 4.2.4. Lattice parameters *a*, *b*, *c*, and volume *V* of the $La_{1-x}Gd_xNb_{0.9}Mo_{0.1}O_{4.05}$ series. Error bars are smaller than symbols. 64

Figure 4.2.5. XRD patterns of LNM10 recorded at 25 °C, 500 °C and 900 °C, respectively. 2θ range is selected from 20° to 60°to highlight the structure change from a modulated m-phase to a modulated t-phase then to an unmodulated t-phase. The satellite reflections from the modulated structures are marked by arrows. Reproduced with permission [14]. Copyright (2023), Royal Society of Chemistry. 65

Figure 4.2.6. XRD patterns of LNM10 recorded at 700 °C, 750 °C and 800 °C, respectively. 2θ range is selected from 20° to 60°to highlight the structure change from a modulated structure to an unmodulated structure. The satellite reflections from the modulated structures are marked by arrows. Reproduced with permission [14]. Copyright (2023), Royal Society of Chemistry. 66

Figure 4.2.7 SAED patterns of $LaNb_{0.9}Mo_{0.1}O_{4.05}$ along [010] zone axis. Two modulated vectors denoted as $\boldsymbol{q_1}$ and $\boldsymbol{q_2}$ are used. Reproduced with permission [14]. Copyright (2023), Royal Society of Chemistry. 67

Figure 4.2.8. XRD patterns of GNM10 recorded at 25 °C, 500 °C and 900 °C, respectively. 2θ range is selected from 20° to 60°to highlight the coexistence of m-phase and t-phase during the transition. The satellite reflections from the m-phase are marked by arrows. 68

Figure 4.2.9. XRD patterns of GNM10 from 27.8° to 29.8° 2θ recorded at 400 °C, 450 °C, 500 °C and 550 °C, respectively, showing the coexistence of two m-phases. 68

Figure 4.2.10. Phase diagram of $La_{1-x}Gd_xNb_{0.9}Mo_{0.1}O_{4.05}$ series. 70

Figure 4.2.11. Microstructures of surfaces of a) LNM10, c) La8Gd2, e) La6Gd4, g) La5Gd5 and cross-sections of b) LNM10, d) La8Gd2, f) La6Gd4, h) La5Gd5. The scale bars of all figures are 10 µm. 71

Figure 4.2.12. Microstructures of surfaces of a) La4Gd6, c) La2Gd8, e) GNM10 and cross-sections of b) La4Gd6, d) La2Gd8, f) GNM10. The scale bars of all figures are 10 µm. 72

Figure 4.2.13. BSE images of the surfaces of a) LNM10 and b) GNM10. 72

Figure 4.2.14. Particle size distribution of LNM10 (upper) and GNM10 (lower), respectively. 73

Figure 4.2.15. The calculated mean particle sizes of $La_{1-x}Gd_xNb_{0.9}Mo_{0.1}O_{4.05}$ series. 74

Figure 4.3.1. The Nyquist plot of LNM10 measured at 550 °C under dry air. The hollow circles show the measured value, and the red line shows the fitting results using the model in the inset. Reproduced with permission [14]. Copyright (2023), Royal Society of Chemistry..... 75

Figure 4.3.2. Total conductivity of $La_{1-x}Gd_xNb_{0.9}Mo_{0.1}O_{4.05}$ series under dry air..... 78

Figure 4.3.3. Arrhenius plot of the total conductivity of LNM10 showing the change of E_a. The results are also compared with other similar materials. 78

Figure 5.1.1. Arrhenius plot of the total conductivity of $LaNbO_4$. Data were extracted from the work of Li *et al* [11]. 81

Figure 5.2.1. XRD patterns of the $LaNb_{0.8}W_xMo_{0.2-x}O_{4.1}$ series, displayed as a function of increasing fraction of W from top to bottom. Peaks corresponding to the modulated structures are marked by asterisks. Impurities in LNW20 and LNW18Mo2 are marked by blue dots. Change of main peaks are exhibited in top right corner inset. Lattice planes in monoclinic Fergusonite phase of LNMo20 are labelled in blue, while lattice planes of the tetragonal Scheelite phase of LNW4Mo16 are labelled in orange. 82

Figure 5.2.2. a) Plot of XRD refinement result of LNW16Mo4 at room temperature, R_{wp}=6.07%, χ^2 = 3.99; lattice parameters of b) *c* and c) *a* in $LaNb_{0.8}W_xMo_{0.2-x}O_{4.1}$ series at room temperature. The symbols in orange represent the m-phase. Error bars are smaller than the symbols. 83

Figure 5.2.3. The phase diagram of $LaNb_{0.8}W_xMo_{0.2-x}O_{4.1}$ series from room temperature to 900 °C. Reproduced with permission [15]. Copyright (2024), Elsevier. 84

Figure 5.2.4. SAED patterns of LNW18Mo2 along zone axis [010] and $[1\bar{1}1]$ highlighting the modulated structures. Reproduced with permission [15]. Copyright (2024), Elsevier. 85

Figure 5.3.1. Microstructures of surfaces (left column) and cross-sections (right column) of a), b) LNMo20, c), d) LNW2Mo18, e), f) LNW4Mo16 and g), h) LNW10Mo10. The scale bars of all figures are 10 µm. 86

Figure 5.3.2. Microstructures of surfaces (left column) and cross-sections (right column) of a), b) LNW16Mo4, c), d) LNW18Mo2 and e), f) LNW20. The scale bars of all figures are 10 µm. 87

Figure 5.3.3. Particle size distribution of LNMo20 (left) and LNW20 (right), respectively. 88

Figure 5.3.4. The calculated mean particle sizes of $LaNb_{0.8}W_xMo_{0.2-x}O_{4.1}$ series. 89

Figure 5.3.5. Higher magnification surface image of LNW20. The red and blue ellipses highlight the raised stripes on the surface and grain boundaries, respectively..... 89

Figure 5.4.1. Total conductivities of the $LaNb_{0.8}W_xMo_{0.2-x}O_{4.1}$ series measured in the 500 °C – 900 °C temperature regime. 91

Figure 5.4.2. Impedance spectrum of LNW20 measured at 616 °C. The hollow circles represent the experimental data, and the red line represents the fitting results using the model in the inset..... 92

Figure 5.4.3. Unit cell volumes and total conductivities of $LaNb_{0.8}W_xMo_{0.2-x}O_{4.1}$ series at around 850 °C. Error bars are smaller than the symbols. 93

Figure 5.5.1. Lattice parameters *a*, *b*, *c*, *β* and volume of unit cell *V* of LNW2Mo18 within the temperature range from room temperature to 900 °C. 'm' and 't' symbolises m-phase and t-phase, respectively. Error bars are smaller than the symbols..... 94

Figure 5.5.2. Arrhenius plot of the total conductivity of LNW2Mo18 with calculated activation energy. Reproduced with permission [15]. Copyright (2024), Elsevier. 95

Figure 6.1.1. Room temperature XRD patterns of $LaNb_{0.8}Mo_{0.2}O_4$ after sintering, EIS measurement under 5% H_2/N_2 and reoxidisation under air at 900 °C for 5 hours. Reproduced with permission [16]. Copyright (2015), Elsevier. 99

Figure 6.2.1. TGA results of the as-sintered LNM10 from room temperature to 900 °C with an isothermal heating time of 20 minutes under air..... 100

Figure 6.2.2. Normalised XANES spectrum of the as-sintered LNM10 from Mo K-edge at room temperature under static air. Data were calibrated to a Mo reference foil with a K-edge position of 20,000 eV. The dashed lines represent the energy when normalised absorption equals to 1..... 101

Figure 6.2.3. The relationship between Mo K-edge positions from XANES spectra of different materials and their corresponding Mo oxidation states. Reproduced with permission [17]. Copyright (2021), Nature. 101

Figure 6.2.4. XPS spectra and the fitting results of Mo 3*d* orbitals of the as-sintered LNM10. The binding energy of C 1*s* peak (284.8 eV) was used for calibration. 104

Figure 6.2.5. Iteration scan of Mo in MoO_3. The solid and dashed lines represent the 1st and 30th scan of the iteration, respectively. The humps from lower Mo oxidation states are marked by arrows. The binding energy of C 1*s* peak (284.8 eV) was used for calibration.105

Figure 6.3.1. Room temperature XRD patterns of LNM10 after being annealed under different atmospheres at 800 °C for 2 hours. The satellite reflections of the modulated structures are marked by asterisks. The secondary phase observed after the sample being annealed under vacuum and 5% H_2/N_2 is marked by crosses. 106

Figure 6.3.2. Room temperature XRD patterns of LNM10 after being annealed under 5% H_2/N_2 at 800 °C for different dwell times. The satellite reflections of the modulated structures are

marked by asterisks. The secondary phase that emerged after the sample being annealed under 5% H_2/N_2 is marked by crosses..... 108

Figure 6.3.3. Room temperature XRD patterns of a) LNMo20 after being annealed under 5% H_2/N_2 at 800 °C for 2 hours, b) LNM10 after being annealed under 5% H_2/N_2 at 200 °C for 2 hours and c) LNM10 after being annealed under 5% H_2/N_2 at 800 °C for 8 hours with heating and cooling rates of 10 °C per minute. The satellite reflections of the modulated structures are marked by asterisks. The secondary phase is marked by crosses..... 110

Figure 6.3.4. Room temperature EPR results of LNM10 annealed under different atmospheres at 800 °C for 2 hours. 111

Figure 6.3.5. Tauc plots measured at room temperature of LNM10 annealed under different atmospheres at 800 °C for 2 hours. The dashed lines represent the linear fits..... 112

Figure 6.3.6. Microstructure of the cross-section of the as-sintered LNM10..... 113

Figure 6.3.7. Microstructures of the cross-sections of LNM10 annealed under O_2, N_2, vacuum and 5% H_2/N_2 at 800 °C for 2 hours, respectively..... 113

Figure 6.4.1. Room temperature XRD patterns of the as-sintered LNM10 annealed under 5% H_2/N_2 at 800 °C for 24 hours and it after being re-oxidised under static air at 800 °C for 4 hours. The satellite reflections of the modulated structures are marked by asterisks..... 114

Figure 6.4.2. XPS spectra and the fitting results of Mo 3*d* orbitals of LNM10 annealed under 5% H_2/N_2 at 800 °C for 24 hours. The binding energy of C 1*s* peak (284.8 eV) was used for calibration. 115

Figure 6.4.3. TGA results of LNM10 annealed under 5% H_2/N_2 at 800 °C for 24 hours measured from room temperature to 900 °C with an isothermal heating time of 20 minutes under compressed air. The dashed lines define the region where the mass changed. The red line and blue line represent the heating and cooling process, respectively. 116

Figure 6.4.4. *In-situ* synchrotron XRD patterns of LNM10 annealed under 5% H_2/N_2 at 800 °C for 24 hours measured from 100 °C to 400 °C. The modulated structures are marked by asterisks. The simulated XRD pattern of BN was based on the data from Li *et al* [18]..... 117

Figure 6.4.5. Synchrotron XRD patterns of the as-sintered LNM10 and LNM10 annealed under 5% H_2/N_2 at 800 °C for 24 hours measured at different temperatures. The modulated structures are marked by asterisks. The simulated XRD pattern of BN was based on the data from Li *et al* [18]. 118

Figure 6.4.6. Zoom-in synchrotron XRD patterns of LNM10 annealed under 5% H_2/N_2 at 800 °C for 24 hours measured at 250 °C. The peaks from the m-phase with higher symmetry are marked by crosses. 119

Figure 6.4.7. *In-situ* Mo K-edge XANES results of LNM10 annealed under 5%H_2/N_2 at 800 °C for 24 hours measured from 100 °C to 400 °C The inset shows the shift of E_0. Data were calibrated to a Mo reference foil with a K-edge position of 20,000 eV. 120

Figure 6.4.8. Values of D_1 and the calculated oxidation states of Mo in the annealed sample from room temperature to 800 °C. The blue line represents the linear fitting in the temperature range from 100 °C to 400 °C. Different stages are defined by dashed lines.120

Figure 6.4.9. *In-situ* Mo K-edge XANES results of LNM10 annealed under 5% H_2/N_2 at 800 °C for 24 hours measured from 100 °C to 400 °C The insets show the changes at different energy ranges. Data were calibrated to a Mo reference foil with a K-edge position of 20,000 eV.121

Figure 6.4.10. Mo K-edge XANES results of the as-sintered LNM10 measured at room temperature and 800 °C The insets show the changes at different energy ranges. Data were calibrated to a Mo reference foil with a K-edge position of 20,000 eV. 122

Figure 6.4.11. Nb K-edge XANES results of the as-sintered LNM10 measured at room temperature and 800 °C in the energy range from 19,000 eV to 19,050 eV. Data were calibrated to a Nb reference foil with a K-edge position of 18,986 eV. 123

Figure 6.4.12. The fitting results of (left) $k^3\chi(k)$ and (right) Fourier transform (FT) of the $k^3\chi(k)$ of the EXAFS results of annealed sample measured at room temperature. The blue and red lines represent the raw data and fitting results, respectively. 124

Figure 6.5.1. Total conductivities of the as-sintered LNM10 measured under compressed air and LNM10 annealed under 5% H_2/N_2 at 800 °C for 24 hours measured under 5% H_2/N_2 in the temperature range of 450 °C to 900 °C. 128

Figure 6.5.2. Energy-band scheme for (left) the as-sintered LNM10 and (right) LNM10 annealed under 5% H_2/N_2 at 800 °C for 24 hours. 129

Figure 6.5.3. XPS spectra of O 1*s* orbitals of as-sintered LNM10 and LNM10 annealed under 5% H_2/N_2 at 800 °C for 24 hours. The binding energy of C 1*s* peak (284.8 eV) was used for calibration. 131

Figure A1. XRD patterns of LNM10 recorded at 250 °C, 300 °C and 350 °C, respectively. The satellite reflections of the modulated structure are marked by arrows. Reproduced with permission [14]. Copyright (2023), Royal Society of Chemistry. 158

Figure A2. XRD patterns of La8Gd2 recorded at 250 °C, 300 °C and 350 °C, respectively. The satellite reflections of the modulated structure are marked by arrows. Reproduced with permission [14]. Copyright (2023), Royal Society of Chemistry. 159

Figure A3. XRD patterns of La6Gd4 recorded at 300 °C, 350 °C and 400 °C, respectively. Reproduced with permission [14]. Copyright (2023), Royal Society of Chemistry. 160

Figure A4. XRD patterns of La5Gd5 recorded at 350 °C, 400 °C and 450 °C, respectively. Reproduced with permission [14]. Copyright (2023), Royal Society of Chemistry. 161

Figure A5. XRD patterns of La4Gd6 recorded at 350 °C, 400 °C and 450 °C, respectively. Reproduced with permission [14]. Copyright (2023), Royal Society of Chemistry. 162

Figure A6. XRD patterns of La2Gd8 recorded at 450 °C, 500 °C and 550 °C, respectively. Reproduced with permission [14]. Copyright (2023), Royal Society of Chemistry. 163

Figure A7. XRD patterns of La6Gd4 and La5Gd5 recorded at 900 °C, respectively. 2θ range is selected from 20° to 60°to highlight the existence of m-phase. The peak from the new m-phase is marked by arrows. 164

Figure A8. XRD patterns of La4Gd6 and La2Gd8 recorded at 900 °C, respectively. 2θ range is selected from 20° to 60°to highlight the existence of m-phase. The peak from the new m-phase is marked by arrows. 165

List of Tables

Table 1.1. Characteristics of different types of fuel cells. The unit for operating temperature is °C. 3

Table 3.1. Characteristic capacitance values and their corresponding interpretations. 56

Table 4.1. Log-normal distribution parameters μ (expected value) and σ* (standard deviation) used for calculating the mean particle sizes of $La_{1-x}Gd_xNb_{0.9}Mo_{0.1}O_{4.05}$ series. 70

Table 4.2. Normalised atomic ratios of cations of $La_{1-x}Gd_xNb_{0.9}Mo_{0.1}O_{4.05}$ series. Reproduced with permission [14]. Copyright (2023), Royal Society of Chemistry. 74

Table 4.3 Activation energies, E_a, of $La_{1-x}Gd_xNb_{0.9}Mo_{0.1}O_{4.05}$ series calculated from the linear regressions from the Arrhenius plot. The subscripted U and M represent the unmodulated t-phase and modulated t-phase, respectively. 79

Table 5.1. Log-normal distribution parameters μ (expected value) and σ* (standard deviation) used for calculating the mean particle sizes of $LaNb_{0.8}W_xMo_{0.2-x}O_{4.1}$ series. 89

Table 5.2. Normalised atomic fractions of cations of $LaNb_{0.8}W_xMo_{0.2-x}O_{4.1}$ series. Reproduced with permission [15]. Copyright (2024), Elsevier. 90

Table 6.1. Values of K-edge positions, energies when normalised μ = 1 of the as-sintered LNM10 and the reference Mo foil and the differences (D_1 and D_2) among them. The values listed here are from the raw data without calibration. 103

Table 6.2. The derived structural parameters for the annealed sample at different temperature points (Temp). ''CN'' and ''d'' represent the average coordination number and bond length, respectively. 125

Table 6.3. The derived structural parameters for the as-sintered sample at different temperature points (Temp) and them for the undoped $LaNbO_4$ at room temperature. ''CN'' and ''d'' represent the average coordination number and bond length, respectively. 126

Table A1. Related information of La site substituted materials synthesised via different methods. Substitutes before and after the slash are both substituted on La sites. For activation energy, all values shown here are for t- phase. 149

Table A2. Related information of Nb site substituted materials synthesised via different methods. Substitutes which could stabilise m-phase or t-phase are marked in red or blue, respectively. Substitutes before and after the slash are substituted on La sites or Nb sites, respectively. For activation energy, values for m-phase are marked with (m)..... 152

Table A3. Refined structural parameters of $La_{1-x}Gd_xNb_{0.9}Mo_{0.1}O_{4.05}$ series from Le Bail refinements against XRD data collected at 25 °C. 157

Table A4. Refined structural parameters of $LaNb_{0.8}W_xMo_{0.2-x}O_{4.1}$ series from Le Bail refinements against XRD data collected at 25 °C. 166

Table A5. Refined structural parameters of $LaNb_{0.8}W_xMo_{0.2-x}O_{4.1}$ series from Le Bail refinements against XRD data collected at 850 °C. 167

List of Acronyms

AFC	Alkaline Fuel Cell
BSE	Backscattered electron
CB	Conduction Band
CCUS	Carbon Capture, Utilisation, and Storage
CGO	$Ce_{1-x}Gd_xO_{2-\delta}$
CPE	Constant Phase Element
DFT	Density Functional Theory
ED	Electron Diffraction
EDX	Energy Dispersive X-Ray Spectroscopy
EIS	Electrochemical Impedance Spectroscopy
EMF	Electromotive Force
EPR	Electron Paramagnetic Resonance Spectroscopy
EXAFS	Extended X-ray Absorption Fine Structure
FDP	Freeze-dried Precursors
IB	Intermediate Band
LSC	$La_{1-x}Sr_xCoO_{3-\delta}$
LSCF	$La_{1-x}Sr_xCo_{1-y}Fe_yO_{3-\delta}$
LSGM	$La_{1-x}Sr_xGa_{1-y}Mg_yO_{3-\delta}$
LSM	$La_{1-x}Sr_xMnO_{3-\delta}$
MCFC	Molten Carbonate Fuel Cell
MIEC	Mixed Ionic and Electronic Conductors
MS	Molten Salt

ND	Neutron Diffraction
ORR	Oxygen Reduction Reaction
PAFC	Phosphoric Acid Fuel Cell
PEMFC	Proton Exchange Membrane Fuel Cell
PLD	Pulsed Laser Deposition
SAED	Selected Area Electron Diffraction
SE	Secondary Electron
SEM	Scanning Electron Microscopy
SOFC	Solid Oxide Fuel Cell
SP	Spray Pyrolysis
SSR	Solid State Reaction
ScSZ	Sc_2O_3 Stabilised ZrO_2
TEC	Thermal Expansion Coefficient
TEM	Transmission Electron Microscopy
TGA	Thermogravimetric Analysis
TIEC	Triple Ionic and Electronic Conductors
VB	Valence Band
XANES	X-Ray Absorption Near Edge Structure
XAS	X-Ray Absorption Spectroscopy
XPS	X-Ray Photoelectron Spectroscopy
XRD	X-Ray Diffraction
XRF	X-Ray Fluorescence
YSZ	Y_2O_3 Stabilised ZrO_2

Chapter 1. Introduction

The aim of this chapter is to provide a general introduction to fuel cells, especially the basic knowledge of solid oxide fuel cells (SOFCs). The discussion of the components of SOFCs focuses on the requirements for the electrodes and electrolytes, highlighting the advantages and disadvantages of some widely used materials. It is worth noting that since the study of the electrodes for SOFCs is not the aim of this thesis, only brief information about them is provided. Additionally, since the aliovalent substituents always change the oxygen stoichiometry of the parent materials, it needs to be clarified that all oxygen stoichiometry values reported in this thesis have been kept the same as those reported in the corresponding references.

1.1 Background

In recent years, discussions and policies regarding global energy have emphasised the significance of decarbonising and transitioning to ‘‘Net Zero’’. The term ‘‘Net Zero’’ refers to the balance between the amount of the greenhouse gases produced and the amount removed from the atmosphere. Based on the consumption of fossil fuels, significant amounts of greenhouse gases, especially CO_2, are still emitted every year. **Figure 1.1.1** shows the emissions of CO_2 reproduced from the BP energy outlook [1]. It is clearly observed that in the past two decades, CO_2 emissions were still increasing; however, with the goal of ‘‘Net Zero’’, CO_2 emissions are required to be reduced almost to zero by 2050.

To achieve the goal of ‘‘Net Zero’’, the application of hydrogen and carbon capture, utilisation, and storage (CCUS) could help to decarbonise, especially in heavy industries. As shown in **Figure 1.1.2**, in 2019, the consumption of conventional energy (coal, natural gas, oil) still dominated heavy industries; however, with the goal of ‘‘Net Zero’’, hydrogen is expected to play an important role in the near future.

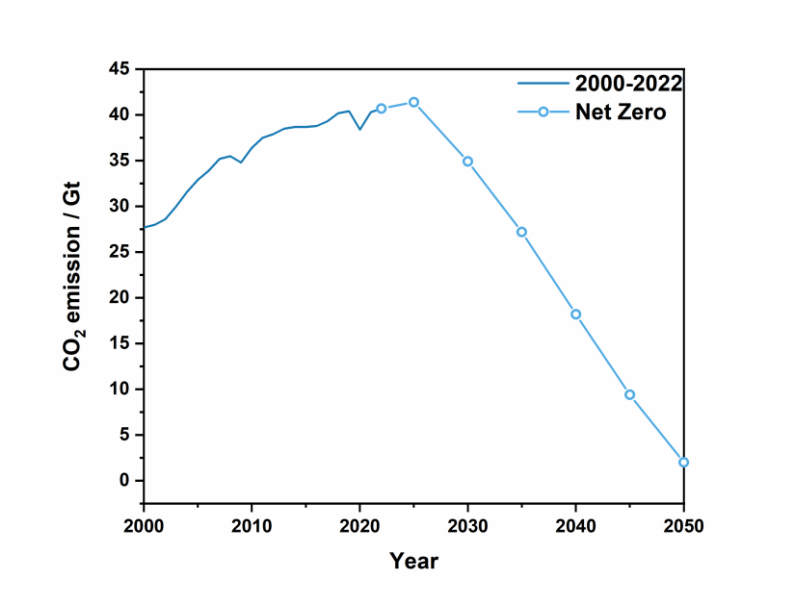


Figure 1.1.1. The CO_2 emissions from energy use. The data are extracted from the energy outlook of BP [1].

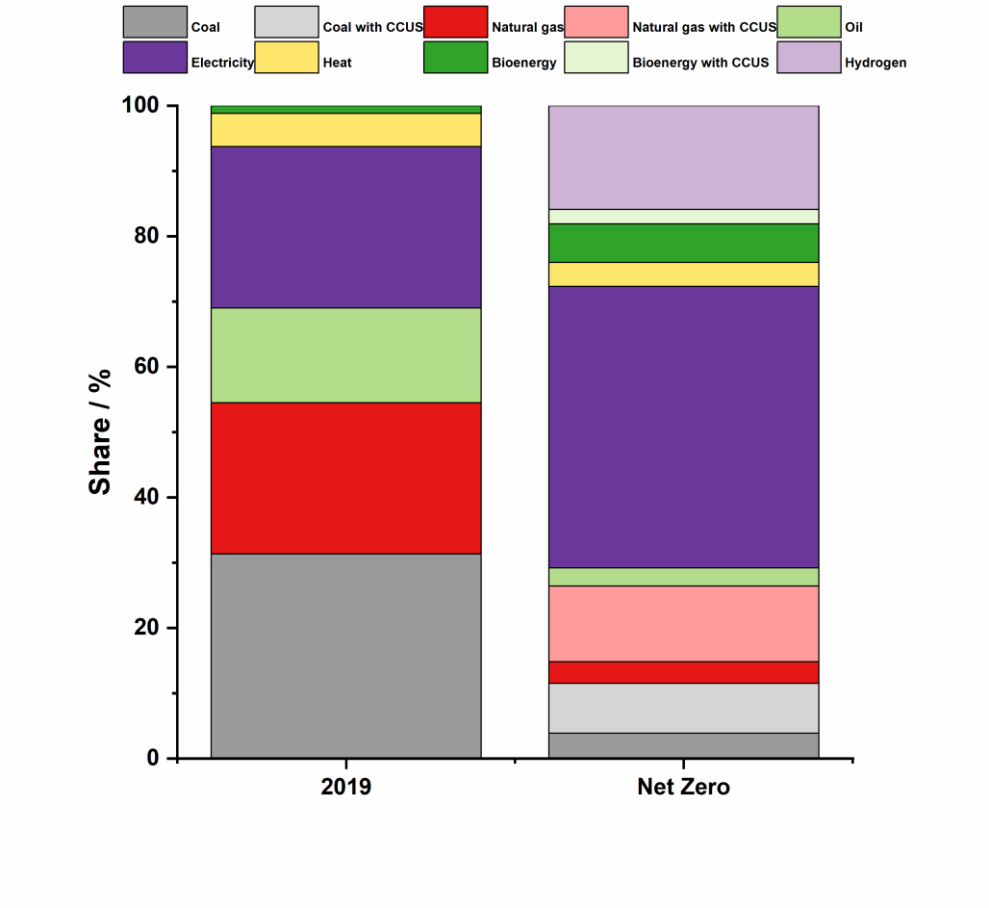


Figure 1.1.2. The fraction of fuels used in heavy industries. The data are extracted from the energy outlook of BP [1].

Fuel cells, which could use pure hydrogen as a fuel, will be one of the devices shifting the energy structure. In a fuel cell, the reaction of the hydrogen is expressed as:

$$\frac{1}{2}H_{2\,(g)} + O_{2\,(g)} \rightleftharpoons H_2O_{\,(g)} \qquad (1.1),$$

where water is the only product. Therefore, compared to conventional combustion engines using hydrocarbon fuels, fuel cells are more environmentally friendly. Fuel cells directly convert chemical energy to electric energy, which is also more efficient [19]. Based on the different electrolytes used, there are five types of fuel cells: alkaline fuel cell (AFC), phosphoric acid fuel cell (PAFC), proton exchange membrane/polymer electrolyte membrane fuel cell (PEMFC), molten carbonate fuel cell (MCFC) and SOFC. **Table 1** summarises some characteristics of these five types of fuel cells [20]. Each fuel cell has its own advantages and disadvantages. Since SOFCs consist of both solid electrodes and electrolyte and they are always operated at the higher temperature range (600 °C – 1000 °C) to achieve higher ionic conductivity, their advantages include fuel flexibility and the avoidance of noble metal catalysts [19]. However, due to the higher operating temperature, SOFCs always face sealing and mechanical issues of the different compartments within the cells due to the thermal expansions [19].

Table 1.1. Characteristics of different types of fuel cells [20]. The unit for operating temperature is °C.

	AFC	PAFC	PEMFC	MCFC	SOFC
Electrolyte	Liquid KOH	Liquid H_3PO_4	Polymer membrane	Molten carbonate	Dense ceramics
Charge carrier	OH^-	H^+	H^+	CO_3^{2-}	H^+/O^{2-}
Operating temperature	60-220	200	80	650	600-1000
Fuel	H_2	H_2	H_2/methanol	$H_2/CH_4/CO$	$H_2/CH_4/CO$

An SOFC consists of two porous electrodes (anode and cathode) and one dense electrolyte. The anode is the electrode where the fuel loses electrons and is oxidised, while the cathode is the electrode where the oxidants gain electrons and are reduced. The electrolyte separates two electrodes and transfer the charge carriers between electrodes. Based on the type of charge carriers the electrolyte could transfer, SOFCs are divided into two

groups: proton conducting SOFCs and oxygen ion conducting SOFCs. These two types of SOFCs are discussed in the following sections. It is worth noting that there are some electrolyte materials exhibiting a dual-ion (proton and oxygen ion) conductivity; therefore, a brief discussion of these types of materials are also provided in this chapter.

1.2 Proton conducting solid oxide fuel cells

For a proton conducting SOFC, the electrolyte transfers protons from the anode to the cathode. Therefore, water is generated at the cathode and the reactions at the electrodes are expressed as:

$$Anode: H_{2\,(g)} \rightleftharpoons 2H^+ + 2e' \quad (1.2),$$

$$Cathode: \frac{1}{2}O_{2\,(g)} + 2H^+ + 2e' \rightleftharpoons H_2O_{\,(g)} \quad (1.3).$$

1.2.1 Anode

For proton conducting SOFCs, the anode materials should possess sufficient electrocatalytic activity for the hydrogen oxidation reaction. Since electrons are transferred from the anode to the cathode through the external circuit, the anode materials should also possess good electronic conductivity [21]. Therefore, metals like Ni could be suitable candidates [21]. However, anode materials should also exhibit good thermal compatibility with electrolytes and good thermal stability under high temperatures; therefore, anodes are always fabricated by mixing NiO with the corresponding electrolyte used in the cell [3]. The electrolyte (proton conducting phase) used in the mixture, on one hand, could match the thermal expansion coefficient (TEC) with the electrolyte; on the other hand, it could expand the triple phase boundaries (gas/electronic conductor/ionic conductor) into the anode, increasing the active sites for hydrogen oxidation [22]. It is worth noting that NiO is used instead of Ni during the fabrication. This is because the reduction of NiO to Ni under the exposure to hydrogen atmospheres could create porosity, which is beneficial for the gas diffusion [22]. Essoumhi *et al* reported that with increasing the volume fraction of NiO in $BaCe_{0.9}Y_{0.1}O_{2.95}$ from 35% to 45%, the porosity increased from 22% to 48% and the conductivity at room temperature increased from 70 S cm^{-1} to 500 S cm^{-1} [23].

1.2.2 Cathode

Similar to the anodes, the cathode materials for proton conducting SOFCs should possess sufficient electrocatalytic activity for the oxygen reduction reaction (ORR) and high electronic conductivity. Mixed ionic and electronic conductors (MIECs) used for oxygen ion conducting SOFCs have been adopted as the cathode materials for proton conducting SOFCs [2]. These materials exhibit a combination of oxygen ion conductivity and electronic conductivity, which is discussed in detail in Section 1.3.2. However, due to the lack of proton conductivity in the cathode, the active sites are limited to the interface between the electrolyte and the cathode. Therefore, materials, that could conduct protons, oxygen ions and electrons, thus extending the active sites into the bulk of the cathode, should be considered [24]. Two strategies have been conducted to realise these triple ionic and electronic conductors (TIECs). One strategy involves substituting Co and Fe in mixed proton and oxygen ion conductors to achieve additional electronic conductivity, such as $BaCo_{0.4}Fe_{0.4}Zr_{0.1}Y_{0.1}O_{3-\delta}$ reported by Duan *et al* [25]. Another strategy is to mix the MIECs with proton conducting materials. For example, the mixture of $Sm_{0.5}Sr_{0.5}CoO_{3-\delta}$ and $BaZr_{0.8}Y_{0.2}O_{3-\delta}$ could be used as the cathode material for proton conducting SOFCs [26]. **Figure 1.2.1** shows schematic representations of the active sites for these two strategies.

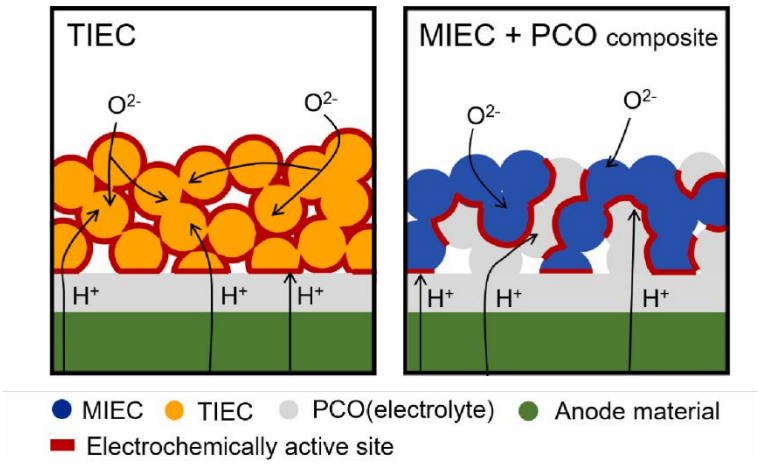


Figure 1.2.1. Schematic representations of active sites of TIEC (left) and mixture of MIEC and proton conducting materials (right). ‘‘PCO’’ represents the proton conducting oxides. Reproduced with permission [2]. Copyright (2022), Elsevier.

1.2.3 Electrolyte

The materials used for electrolytes in proton conducting SOFCs are mainly based on the substituted $BaCeO_3$ and $BaZrO_3$, which possess a perovskite structure [27][28][29]. For example, when Y is substituted on the Ce sites, because of the charge neutrality, oxygen vacancies are formed to compensate the Y'_{Ce}. In this thesis, Kröger-Vink notation is used to describe the type, location and effective charge of different species with a form of $Speices^{Charge}_{Site}$ [30]. Positive, negative and neutral charges are denoted as superscripted $\bullet$, $'$ and X, respectively. These oxygen vacancies could introduce the protonic defects $(OH)^{\bullet}_{O}$ into the system under humidified conditions; therefore, realising proton conduction. The mechanism of proton conductivity via oxygen vacancies under humidified conditions is discussed in Section 2.2 with $LaNbO_4$ as an example. For $BaCeO_3$ based materials, the conductivity of $BaCe_{0.9}Y_{0.1}O_{3-\delta}$ could reach at 0.02 S cm^{-1} at 600 °C under humidified air [31]; however, the main issue is the chemical stability of the phase under CO_2 containing atmospheres [32]. Since $BaCeO_3$ could react with CO_2 to form $BaCO_3$, which could decrease the ionic conductivity, the study of $BaCeO_3$ based materials has focused on how to improve the chemical stability [33]. $BaZrO_3$ based materials have exhibited good chemical stability under CO_2; however, their proton conductivities were one order of magnitude lower than those of the $BaCeO_3$ based materials [34]. Another issue with $BaZrO_3$ based materials is the poor sinterability, which could lead to porous samples and increase the amounts of poorly conductive grain boundaries [32]. Therefore, the strategy of combining the high proton conductivity of $BaCeO_3$ based materials and good chemical stability of $BaZrO_3$ based materials has been studied [35]. $BaCe_{0.7}Zr_{0.1}Y_{0.2}O_{3-\delta}$ has proven to be a good combination [36].

1.3 Oxygen ion conducting solid oxide fuel cells

For an oxygen ion conducting SOFC, the electrolyte transfers oxygen ions from cathode to anode. Therefore, water is generated at the anode and the reactions at electrodes are expressed as:

$$Anode: H_{2\,(g)} + O^{2-} \rightleftharpoons H_2O_{\,(g)} + 2e' \quad (1.4),$$

$$Cathode: \frac{1}{2}O_{2\,(g)} + 2e' \rightleftharpoons O^{2-} \quad (1.5).$$

1.3.1 Anode

For the anodes of oxygen ion conducting SOFCs, a mixture of NiO and an oxygen ion conducting electrolyte is also used, which is similar to the anodes used for proton conducting SOFCs. It is worth noting that although the use of the mixture of NiO and electrolyte materials as anodes is popular, carbon deposition could be a drawback for NiO based anodes when natural gas (CH_4) is used as the fuel in SOFCs [21]. Therefore, Cu and Ru, which are not conducive for the formation of C-C bonds, could be used to partially substitute Ni in the anode materials [21]. However, due to the high costs, Ru is limited in use [21].

1.3.2 Cathode

As described by equation (1.5), the cathode is the place where the ORR occurs. The ORR could be separated into three individual reactions [37]:

1) Adsorption of oxygen molecules $O_{2\,(g)}$ on the surface of the cathode material:

$$\frac{1}{2}O_{2\,(g)} \rightleftharpoons \frac{1}{2}O_{2\,(ad)} \tag{1.6},$$

2) Dissociation of adsorbed oxygen molecules $O_{2\,(ad)}$ to oxygen atoms $O_{\,(ad)}$:

$$\frac{1}{2}O_{2\,(ad)} \rightleftharpoons O_{\,(ad)} \tag{1.7},$$

and 3) the reduction of oxygen atoms $O_{\,(ad)}$ to oxygen ions O^{2-}:

$$O_{\,(ad)} + 2e' \rightleftharpoons O^{2-} \tag{1.8}.$$

The last step could occur in the bulk of the cathode if MIECs are used. Both oxygen vacancies and oxygen interstitials could realise the conduction of oxygen ions. Figure **1.3.1** shows the schematic representations of the mechanism realised by these two species. The most investigated MIECs are substituted $LaCoO_3$ and $LaMnO_3$, which possess a perovskite structure [38]. By substituting the La sites with Sr, oxygen vacancies could be introduced in the systems; therefore, both $La_{1-x}Sr_xCoO_{3-\delta}$ (LSC) and $La_{1-x}Sr_xMnO_{3-\delta}$ (LSM) could be used as MIECs [38]. However, the ionic conductivity of LSM was poor at intermediate temperature range and the TEC of LSC could not match most of the oxygen ion conducting electrolytes [39]. Therefore, $La_{1-x}Sr_xCo_{1-y}Fe_yO_{3-\delta}$ (LSCF), where Fe could reduce the TEC of the cathode, was identified as a solution [39]. However, the segregation of Sr in LSCF could cause degradation of the cathode [40]. Since the segregation was mainly due to the mismatch of ionic radii between La and Sr,

this phenomenon could be supressed by substituting elements with smaller mismatch to La ion compared to Sr [38].

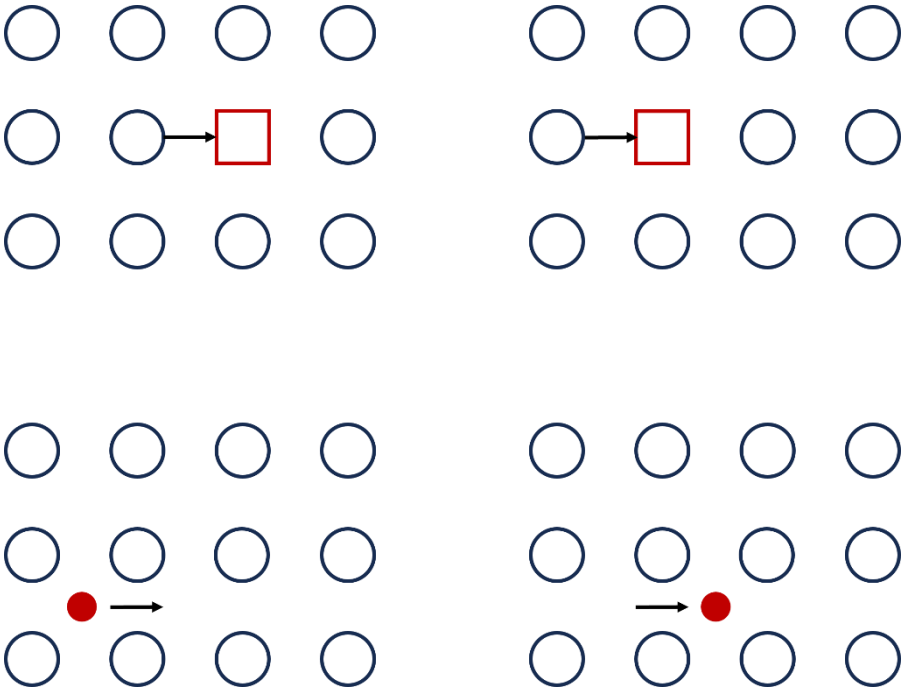


Figure 1.3.1. Schematic representations of oxygen vacancy mechanism (upper) and oxygen interstitial mechanism (lower) for oxygen ion conduction. The open circles represent the lattice oxygen ions. The squares and solid circles represent the oxygen vacancy and interstitial sites, respectively. The arrows represent the direction of the movement of the oxygen ions.

1.3.3 Electrolyte

ZrO_2 based materials are one of the commonly investigated electrolytes [41]. ZrO_2 possesses a monoclinic structure at room temperature and transitions to a tetragonal structure at 1170 °C and then a cubic structure at 2370 °C [42]. Pure ZrO_2 exhibits low ionic conductivity; therefore, substituents, such as Ca, Sc, and Y, are always used to introduce oxygen vacancies to improve the oxygen ion conductivity [41]. The substituents could also stabilise the high temperature structure. For example, with around 8 mol% or 2 mol% Y_2O_3 substituting, the structure of ZrO_2 could be stabilised to either a cubic or tetragonal structure at room temperature, respectively [43]. Sc exhibited the best electrochemical performance among the substituents, with the ionic conductivity of 11 mol% Sc_2O_3 stabilised ZrO_2 (ScSZ) peaking at 0.3 S cm^{-1} at 1000 °C due to the smaller mismatch of the ionic radii between Sc and Zr, which reduces the defect association energy [42]. However, because of the lower

abundance of Sc and lower long-term stability of ScSZ, Y_2O_3 stabilised ZrO_2 (YSZ) is still the most used ZrO_2 based electrolyte for oxygen ion conducting SOFCs with 8 mol% YSZ exhibiting an ionic conductivity of 0.1 S cm^{-1} at 1000 °C [41][44]. However, increasing Y content could decrease the conductivity due to the association of defects, which could decrease the mobility of the defects [41]. Therefore, the optimal concentration of Y is located between 6 mol% to 8 mol% [19].

CeO_2 based materials are another widely used electrolyte. Similar to Sc in ZrO_2, Sm and Gd, which possess similar ionic radii to Ce, exhibit the highest ionic conductivity [41]. The typical electrolyte of CeO_2 based materials is $Ce_{0.9}Gd_{0.1}O_{1.95}$ (CGO) [45]. Compared with YSZ, CGO exhibited one order of magnitude higher conductivity in the intermediate temperature range (around 600 °C) [46]. CGO also demonstrates good chemical stability with cathode materials, unlike ZrO_2 based materials, which could react with the cathodes such as LSC or LSM forming $La_2Zr_2O_7$ and $SrZrO_3$, which is detrimental to the cell performance due to the low conductivities of the formed products [47]. Unfortunately, Ce^{4+} in CGO is partially reduced to Ce^{3+} under reducing atmospheric conditions, for example, at the anode. This phenomenon is more pronounced with increasing the temperature [19]. The reduction of Ce^{4+} not only leads to electronic conductivity, which could cause the internal short circuit, but also leads to a crystal expansion, which could cause the mechanical failure [48].

Bi_2O_3 is a unique material, which possesses intrinsic oxygen vacancy sites without substituents [42]. Bi_2O_3 could be regarded as $BiO_{1.5}$ or $BiO_{2-\delta}$ with δ =0.5; therefore, Bi_2O_3 has 25% of the oxygen sites vacant inherently [19]. Bi_2O_3 possesses a monoclinic structure (α-Bi_2O_3) at room temperature and transitions to a cubic structure (δ-Bi_2O_3) at 727 °C [19]. The δ-Bi_2O_3 exhibits a really high oxygen ion conductivity of 2.3 S cm^{-1} at 800 °C [42]; however, the operating temperature range of δ-Bi_2O_3 is quite small, since the melting point of it is around 817 °C. Therefore, attempts of stabilising δ-Bi_2O_3 down to lower temperature have been conducted [48]. However, similar to CGO, δ-Bi_2O_3 based materials are not stable under reducing atmospheric conditions since Bi_2O_3 could be reduced to Bi metal [49].

$LaGaO_3$ based materials, which possess a perovskite structure, could also be used as electrolytes for oxygen ion conducting SOFCs. By co-substituting Sr and Mg on La and Ga sites, respectively, the ionic conductivity of $La_{0.9}Sr_{0.1}Ga_{0.8}Mg_{0.2}O_{2.85}$ (LSGM) could reach at 0.1 S cm^{-1} at 750 °C [50]. **Figure 1.3.2** shows the conductivities of YSZ ($Zr_{0.84}Y_{0.16}O_{1.92}$), CGO

($Ce_{0.9}Gd_{0.1}O_{1.95}$) and LSGM ($La_{0.8}Sr_{0.2}Ga_{0.85}Mg_{0.15}O_{2.825}$) in the temperature range from 325 °C to 800 °C. Compared with other electrolytes, LSGM exhibited one order of magnitude higher conductivity than YSZ and competitive conductivity compared to CGO. Additionally, there is no reduction of elements in LSGM with a wider range of oxygen partial pressure from 1 atm to 10^{-20} atm [51]. Based on these factors, LSGM seems to be the best candidate for the electrolyte materials for the SOFCs working under intermediate or lower temperature range. However, the drawbacks of LSGM are not negligible. First, during the synthesis, the volatilisation of Ga [44] and the formation of secondary phases like $La_4Ga_2O_9$ are main issues to obtain the single-phase materials [52]. Second, LSGM could react with Ni in the anode material, forming $LaNiO_3$ with high resistance, which hinder the oxygen ions transport [53].

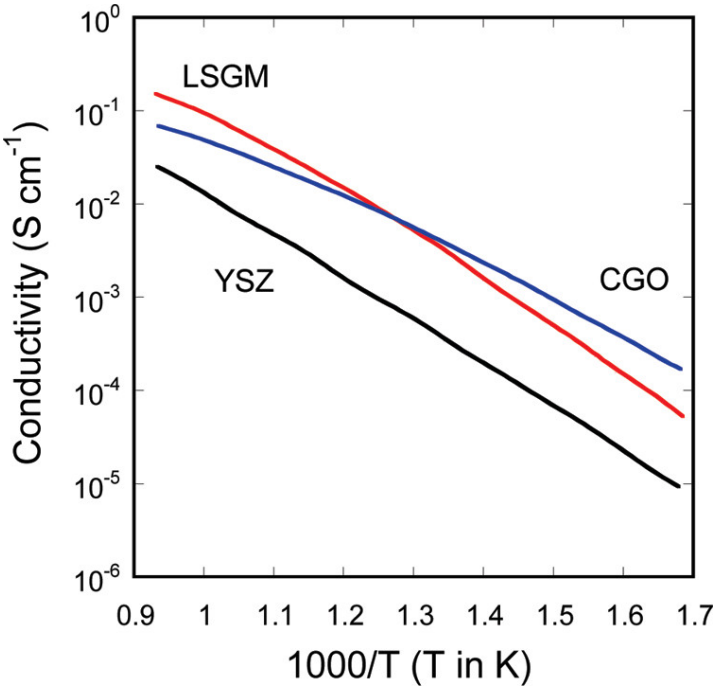


Figure 1.3.2. Conductivity data of YSZ, CGO and LSGM. Reproduced with permission [3]. Copyright (2010), American Chemical Society.

1.4 Dual-ion conducting electrolytes

There are also some electrolyte materials exhibiting dual-ion conductivity, which could bring several advantages [54]. For example, the simultaneous conduction of protons and oxygen ions could increase the total conductivity of the electrolytes; therefore, reducing the ohmic loss of the fuel cell [55]. Another advantage is related to the location where water is generated during the fuel cell operation [55]. In an oxygen ion conducting SOFC, water is

generated at the anode, which could dilute the fuel, reducing the fuel utilisation efficiency [54]. Conversely, in a proton conducting SOFC, water is generated at the cathode, avoiding the dilution of the fuel; however, to maintain high proton conductivity, the fuel still needs to be humified, which leads to requirements of a humidification system for the fuel [54]. In contrast, an electrolyte with dual-ion conductivity produces water at both electrodes, which could reduce the dilution effect and avoid the use of humidification system [54].

There are two types of dual-ion conducting electrolytes [54]. One of them is the material with a single phase, such as $BaZr_{0.1}Ce_{0.7}Y_{0.2}Yb_{0.2-x}O_{3-\delta}$ reported by Yang *et al* [56]. The material exhibited a transport of protons and oxygen ions in the temperature range of 500 – 700 °C [56]. In this material, the conduction of oxygen ions was realised by the oxygen vacancy mechanism, while the conduction of protons followed the mechanism described by equation (2.2) and is discussed in Chapter 2 [54][56]. Zhou *et al* also verified the dual-ion conductivity of this type of material as water was detected at both the anode and cathode in a fuel cell using $BaZr_{0.1}Ce_{0.7}Y_{0.2}Yb_{0.2-x}O_{3-\delta}$ as the electrolyte [57]. Another type of material of dual-ion conducting electrolyte is a composite of a proton conductor and an oxygen ion conductor [54]. Zhu *et al* reported that the fuel cell using an electrolyte made of a 25%:75% weight ration of $BaCe_{0.8}Y_{0.2}O_{3-\delta}$ and $Ce_{0.8}Sm_{0.2}O_{1.9}$ exhibited higher power density than the one with the electrolyte of either $BaCe_{0.8}Y_{0.2}O_{3-\delta}$ or $Ce_{0.8}Sm_{0.2}O_{1.9}$ solely used [58].Despite the advantages of dual-ion conducting electrolytes, there are still challenges for the development of these types of materials [54]. For example, oxygen ion conductivity is always prevalent above 800 °C; however, in this temperature range, proton conductivity is reduced due to the water loss [54]. Therefore, it is difficult to maintain significant proton and oxygen ion conductivity simultaneously [54]. In composite electrolytes of proton and oxygen ion conductors, interactions between two phases could lead to the formation of new phases, which potentially block the charge transfer at interfaces [59].

This chapter provides a general background of fuels and discusses some of the commonly used materials for different components in SOFCs. Apart from the materials mentioned above, another type of material possessing a Scheelite structure has been widely investigated [60]. $LaNbO_4$, an example of such Scheelite-type materials, serves as the parent material for this thesis and is discussed in detail in the following chapters.

Chapter 2. Literature review

In this chapter, some electrolyte materials specifically related to $LaNbO_4$ are reviewed. This review begins by introducing the structure of $LaNbO_4$, the parent material of the compositions studied in this thesis. The review then discusses the proton conduction mechanism, oxygen ion conduction mechanism and substituent strategies of $LaNbO_4$, respectively. It is noted that for the $LaNbO_4$ materials that were only substituted on La sites, they are reviewed in Section 2.4; for those substituted on Nb sites or co-substituted on both La and Nb sites, they are reviewed in Section 2.5.

2.1 The structure of $LaNbO_4$

Rare earth orthoniobates ($ReNbO_4$) are polymorphic materials [61][62], that possess a monoclinic Fergusonite structure at lower temperature and a tetragonal Scheelite structure at higher temperature with a phase transition temperature of around 500 °C [63]. **Figure 2.1.1** shows the structures of the monoclinic phase (m-phase) and the tetragonal phase (t-phase) $ReNbO_4$. In both phases, the coordination number of La is 8 [63]; however, the environments of Nb are different [63][4]. For the m-phase $ReNbO_4$, Nb has octahedral environments forming NbO_6 units with 2 long Nb-O bonds and 4 short Nb-O bonds [63]; therefore, the units are considered as a distorted octahedron [64]. As shown in **Figure 2.1.1**, these distorted octahedra array along the *c* axis by sharing edges [4]. For the t-phase $ReNbO_4$, the coordination number of Nb is 4 and the Nb sites form individual tetrahedral NbO_4 units [4][64]. During the phase transition from m-phase to t-phase, the 2 long Nb-O bonds in the m-phase will be broken [63]. This phase transition is considered as there are no changes of the components and the structure change comes from the rearrangement of atoms [65][66]. The phase transition was initially regarded as a second-order phase transition because of the continuous change of the lattice parameters [13]; however, recent studies, which examined the monoclinic angle and spontaneous strain [63], verified this transition is a first-order transition [63]. The coexistence of m-phase and t-phase and the hysteresis phenomena also evidenced this opinion [12][14]. Therefore, the phase transition in $ReNbO_4$ should be considered as a quasi-continuous first-order transition rather than a strictly second-order transition [63][12]. The phase transition temperature of $ReNbO_4$ increases with decreasing lanthanide ionic radii as smaller ionic radius cause higher lattice energy [65]. It is noticed that there is a levelling off of the transition

temperature when the lanthanide ionic radii are smaller than Gd as it is a result of the close packing [65][13]; however, from La to Lu, the total structure of $ReNbO_4$ remains the same [67].

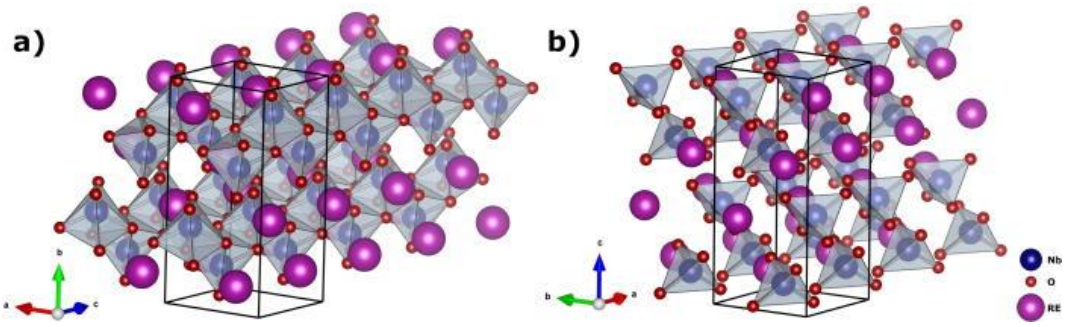


Figure 2.1.1. The structures of a) m-phase and b) t-phase $ReNbO_4$. The pink, blue and red balls represent rare earth, niobium, and oxygen atoms, respectively. Reproduced with permission [4]. Copyright (2016), American Institute of Physics.

The working temperature of SOFCs is in the range of around 500 °C - 1000 °C, which is above the transition temperature of $LaNbO_4$ [68]; therefore, most research focuses on the t-phase $LaNbO_4$ (t-$LaNbO_4$). The intrinsic disorder of $LaNbO_4$ is anti-Frenkel type [7], which generates intrinsic defects of oxygen vacancies ($V_O^{\bullet\bullet}$) and oxygen interstitials (O_i'') [7]. However, the conductivity of unsubstituted $LaNbO_4$ from the intrinsic defects is around 10^{-4} - 10^{-5} S cm^{-1} at 1000 °C [69][70], which is not enticing for SOFC devices. In order to improve the conductivity of $LaNbO_4$, substituents are always used on either La or Nb sites to introduce extrinsic defects to form ionic charge carriers [8]. For $LaNbO_4$, typically, substituents on La sites improve the proton conductivity and substituents on Nb sites improve the oxygen ion conductivity. Proton conduction and oxygen ion conduction have different mechanisms, structures, and substituent strategies, which are discussed in following sections.

2.2 Proton conduction mechanism in $LaNbO_4$

As mentioned above, the intrinsic disorder of $LaNbO_4$ is anti-Frenkel type; therefore, in Kröger-Vink notation, this process is described by equation (2.1) [7]:

$$O_O^X \rightleftharpoons V_O^{\bullet\bullet} + O_i'' \qquad (2.1).$$

The formation of oxygen vacancies in $LaNbO_4$ is always related to local condensation of Nb polyhedrons forming larger units [7][71]. The simulation work done by Mather *et al* indicated

that the formation of oxygen vacancies in t-$LaNbO_4$ was accompanied by the formation of $[Nb_2O_7]^{4-}$, which was formed by two $[NbO_4]^{3-}$ units with one oxygen shared commonly [7].

The proton conductivity is based on the protonic defects formed by the reaction between oxygen vacancies and water described by equation (2.2) [72][73]:

$$H_2O + V_O^{\bullet\bullet} + O_O^X \rightleftharpoons 2(OH)_O^{\bullet} \qquad (2.2).$$

While the protons hop among different oxygen sites, the breaking and formation of hydrogen-oxygen bonds in hydroxide ions realise the proton conductivity [74]. Because of the participation of water in this reaction, materials can be tested under both dry and humidified atmospheres to compare the difference of the conductivities, which can be used to determine whether there is proton conductivity or not.

Fjeld *et al* used density functional theory (DFT) to study the structure and mechanism of proton conduction of $LaNbO_4$ [5]. The simulation results showed that for the m-phase $LaNbO_4$ (m-$LaNbO_4$), because of the distortion of Nb, there were two different types of oxygen distinguished as O(1) and O(2); for t-$LaNbO_4$, all oxygens were isotropic [5]. **Figure 2.2.1** shows the simulated structures of m-$LaNbO_4$ and t-$LaNbO_4$. It is worth noting that in **Figure 2.1.1**, the Nb units in m-$LaNbO_4$ are considered as distorted octahedra sharing edges along the *c* axis [63][64]; however, the Nb units in m-$LaNbO_4$ simulated by Fjeld *et al* were isolated tetrahedra [5]. Although the Nb environments were slightly different from each other, the distortion of Nb coordination environments were considered in both situations [63][5]. For t-$LaNbO_4$, there were two stable proton sites labelled *a* and *b* for each oxygen site as shown in **Figure 2.2.2** a); for m-$LaNbO_4$, the stable proton sites labelled *a'* and *b'* around O(1) sites were similar to those in t-$LaNbO_4$. However, because of the existence of two different oxygens, there was one more proton site labelled *c'* around O(2) in m-$LaNbO_4$ as shown in **Figure 2.2.2** b) [5].

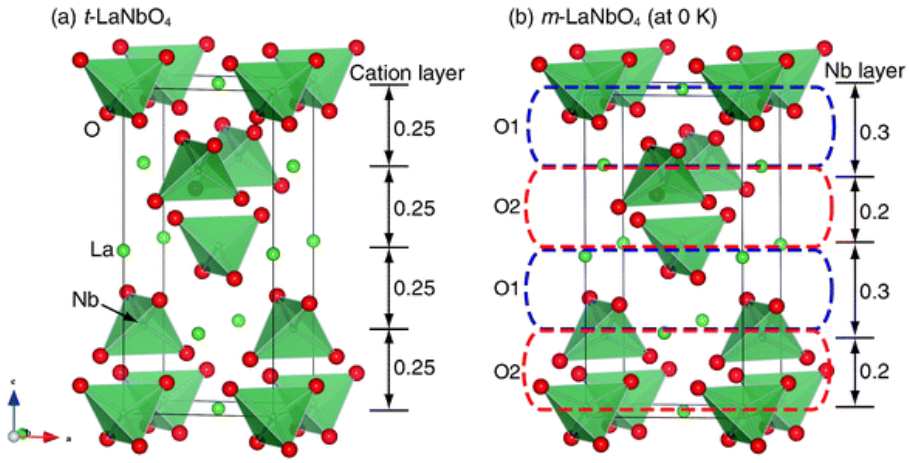


Figure 2.2.1. Structures of a) t-$LaNbO_4$ and b) m-$LaNbO_4$. The red and green balls represent O and La sites, respectively. The niobium sites are represented by the green balls in the tetrahedra. Reproduced with permission [5]. Copyright (2010), Royal Society of Chemistry.

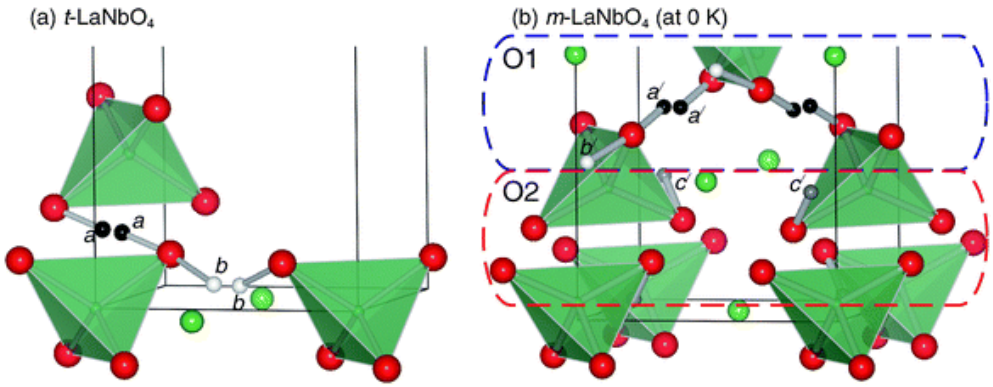


Figure 2.2.2. Stable proton sites in a) t-$LaNbO_4$ and b) m-$LaNbO_4$. Reproduced with permission [5]. Copyright (2010), Royal Society of Chemistry.

Potential proton migration paths among these sites were simulated and are shown in **Figure 2.2.3**. The results showed that the potential barriers of path 3 and 3' matched well with the calculated activation enthalpy of mobility of protons ($\Delta H_{mob,H}$) in t-$LaNbO_4$ and m-$LaNbO_4$, respectively [5]. Therefore, paths 3 and 3', which represented both the rotation and hopping of protons, were the rate-determining processes for the corresponding phases in the *ab* plane [5]. However, for the migration along the *c* axis, path 4 and paths 4' and 5' were required for t-$LaNbO_4$ and m-$LaNbO_4$, respectively [5]. The potential barriers of the migration along the *c* axis in both phases were larger than those in the *ab* plane, which exhibited the anisotropic nature of the proton conductivity in $LaNbO_4$ [5].

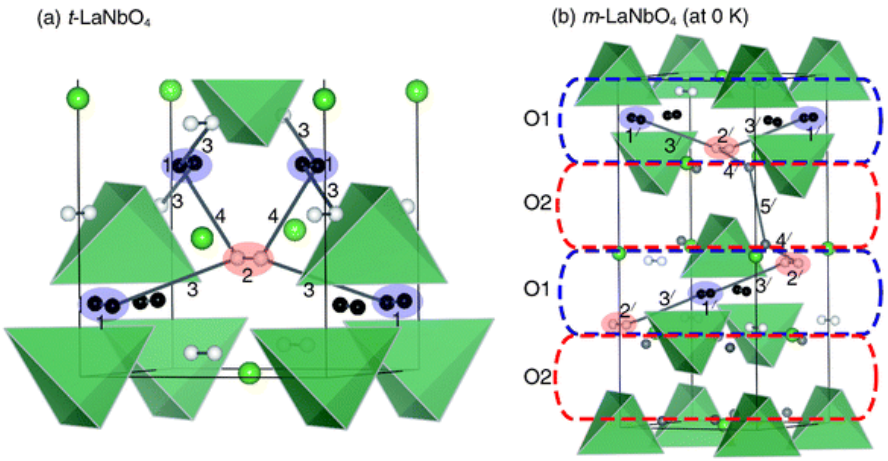


Figure 2.2.3. Potential proton migration paths in a) t-$LaNbO_4$ and b) m-$LaNbO_4$. Reproduced with permission [5]. Copyright (2010), Royal Society of Chemistry.

Huse *et al* further investigated the relationship between $\Delta H_{mob,H}$ and migration paths based on neutron diffraction (ND) data and the results showed that the distances of path 3 and 3' were determined by the separation of inter-tetrahedral oxygens and $\Delta H_{mob,H}$ was related to this separation [6]. As shown in **Figure 2.2.4**, in m-$LaNbO_4$, both $\Delta H_{mob,H}$ and O(1)-O(1) separation decreased with increasing temperature [6]. When approaching the phase transition temperature (around 500 °C), the O(1)-O(1) separation became constant as the corresponding oxygen-oxygen distance in t-$LaNbO_4$ was found to be constant and meanwhile $\Delta H_{mob,H}$ reached the lowest value [6]. As t-$LaNbO_4$ is more symmetrical than m-$LaNbO_4$, for $LaNbO_4$, $\Delta H_{mob,H}$ could increase with decreasing crystal symmetry [5][6].

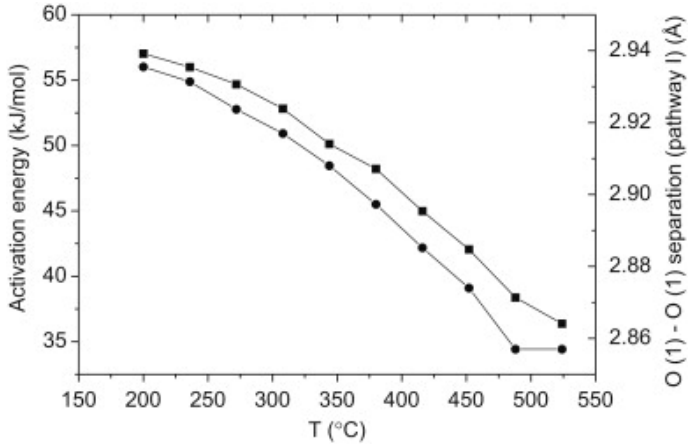


Figure 2.2.4. Temperature dependence of $\Delta H_{mob,H}$ (squares) and O(1)-O(1) separation distance of $LaNbO_4$. Reproduced with permission [6]. Copyright (2012), Elsevier.

As mentioned in Section 2.1, to improve the proton conductivity, substituents are used on La sites. Mather *et al* investigated the acceptor substituents on La sites, which introduce oxygen vacancies in the system by charge compensation to improve the proton conductivity [7]. **Figure 2.2.5** shows the incorporation energy of different substituents on La sites. Ca and Sr showed the lowest energy because of the smallest mismatch between their ionic radii and La ion radius [7]. The mismatch also led to another result: a smaller elastic strain due to a smaller mismatch could weaken the trapping effect of the substituents on the hydroxide ions [7][75]. In Section 2.4, detailed substituent strategies on La sites are discussed.

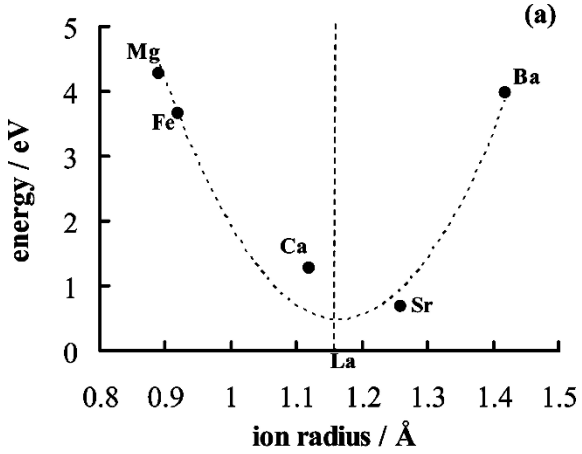


Figure 2.2.5. Relationship between incorporation energy and substituents radii for acceptor substituents on La site. Reproduced with permission [7]. Copyright (2010), American Chemical Society.

2.3 Oxygen ion conduction mechanism in $LaNbO_4$

For t-$LaNbO_4$, because of the smaller ionic radius of Nb compared with La [76], the oxygen sites are always displaced towards Nb sites leaving enough interstitial space in the lattice, which provides a possibility for oxygen ion conduction via interstitial sites [8]. Toyoura *et al* used first-principle simulation to study the potential mechanism of oxygen ion conductivity via interstitial sites in t- $LaNbO_4$ [8]. The results indicated that there were four migration paths (1-4) for interstitials between two different oxygen interstitial sites (O_{int}-1 and O_{int}-2) as shown in **Figure 2.3.1**.

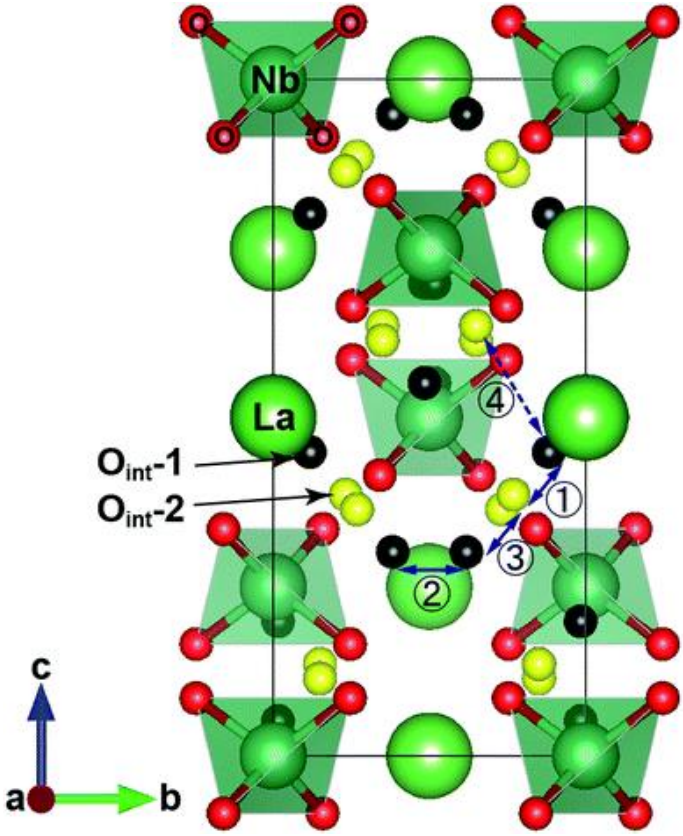


Figure 2.3.1. The connection of interstitial sites in t-$LaNbO_4$. The different migration paths are labelled by numbers and the different oxygen interstitial sites are labelled as O_{int}-1 and O_{int}-2, respectively. Reproduced with permission [8]. Copyright (2018), Royal Society of Chemistry.

The potential energy of O_{int}-2 was higher than that of O_{int}-1; therefore, O_{int}-2 was considered as a metastable site for oxygen interstitials [8]. It is worth noting that both O_{int}-1 and O_{int}-2 were located in the middle of two tetrahedral NbO_4 units forming a new unit of Nb_2O_9 [8]; therefore, for t-$LaNbO_4$ with interstitial sites, the average coordination number of Nb should be considered as 4.5, which is different from the coordination numbers of both m-$LaNbO_4$ and t-$LaNbO_4$ discussed in Section 2.1. As shown in **Figure 2.3.1**, path 1-3 only included interstitial sites; however, path 4 included a lattice oxygen site, which was described as the interstitialcy mechanism [8]. The difference of an interstitialcy mechanism from either oxygen vacancy or oxygen interstitial mechanism is that both lattice oxygens and interstitials are involved. **Figure 2.3.2** illustrates the interstitialcy mechanism.

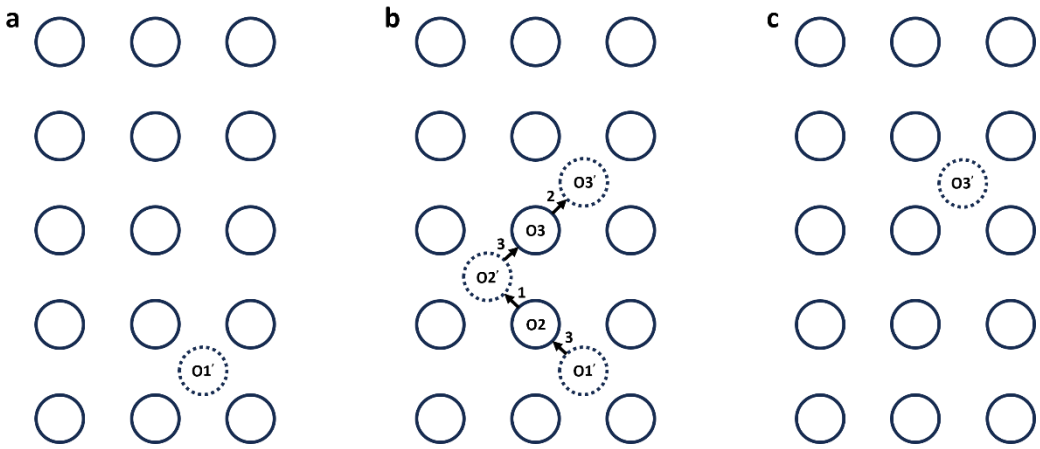


Figure 2.3.2. Schematic representations of a) the initial status of interstitialcy mechanism, b) the process of interstitialcy mechanism and c) the final status of interstitialcy mechanism. The steps are labelled as numbers. The solid and dashed circles represent the oxygen atoms at regular sites and interstitial sites, respectively.

As shown in **Figure 2.3.2** b), firstly, an oxygen atom occupying an interstitial site (O1') forces a regular oxygen atom (O2) to leave its site to an interstitial site (step 1); then, the new formed oxygen interstitial (O2') forces another regular oxygen atom (O3) to an interstitial site (step 2); finally, O1' and O2' occupy the vacancies left by O2 and O3, respectively (step 3). Therefore, if only the initial (**Figure 2.3.2** a)) and final status (**Figure 2.3.2** c)) are considered, it looks like one oxygen atom hops from one interstitial site (O1') to another interstitial site (O3'); however, the oxygens at regular lattice sites are also involved.

The simulation results showed that paths 1, 3 and 4 exhibited similar migration energies of 0.40 eV; however, the energy of path 2 was around 0.49 eV, which made this path unlikely to be involved in the longer pathways [8]. **Figure 2.3.3** a) and b) show the proposed migration pathways including paths 1, 3 and 4 in the *ab* plane and along the *c* axis, respectively. The same activation energy of the pathway in the *ab* plane as that of the pathway along the *c* axis exhibited the isotropic nature of oxygen ion conductivity via oxygen interstitials in $LaNbO_4$, which is different from the discussion of the proton conductivity in Section 2.2 [8][5].

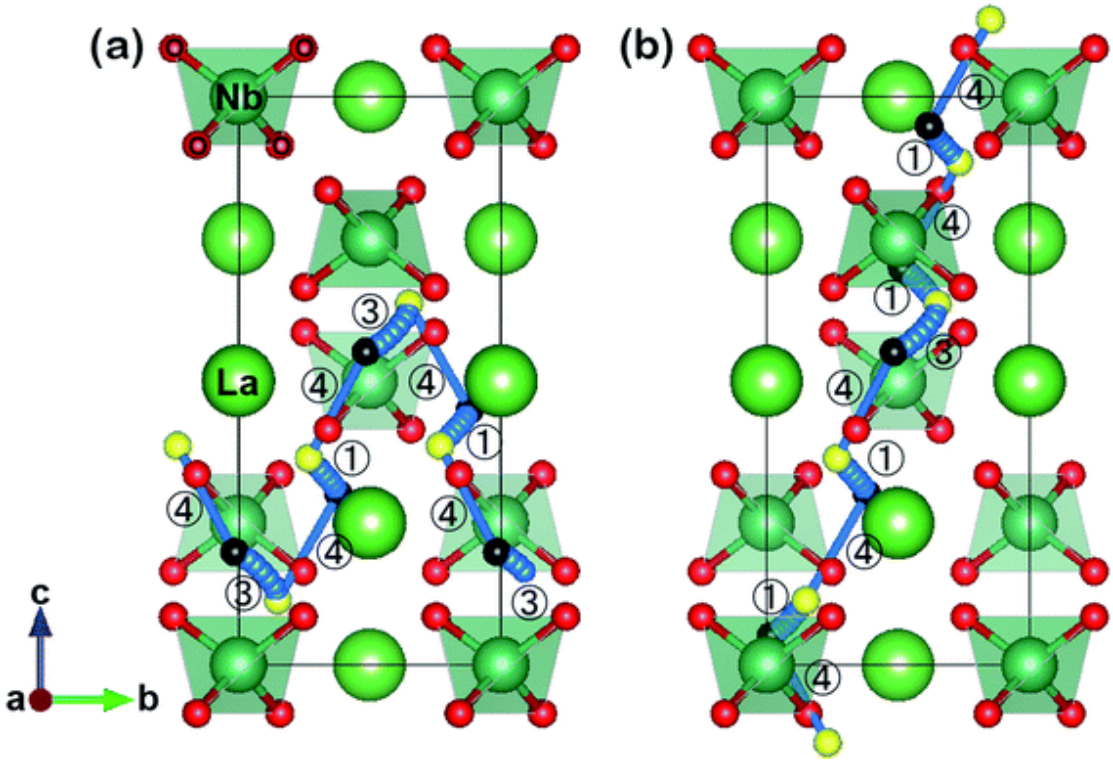


Figure 2.3.3. The migration pathways of oxygen ions conductivity via interstitials a) in the *ab* plane and b) along the *c* axis. Reproduced with permission [8]. Copyright (2018), Royal Society of Chemistry.

2.4 Substituent strategies on La site

Acceptor substituents are always used on La sites to introduce oxygen vacancies or holes depending on different conditions. Alkaline earth metals which possess a lower oxidation state compared with La are the common choices. The mechanisms in relatively reducing and oxidising atmospheres are described by equations (2.3) and (2.4), respectively, where M represents the divalent elements:

$$2MO + La_2O_3 \rightleftharpoons 2M'_{La} + V_O^{\bullet\bullet} + 5O_O^X + 2La_{La}^X \quad (2.3);$$

$$2MO + La_2O_3 + 1/2O_2 \rightleftharpoons 2M'_{La} + 2h^{\bullet} + 6O_O^X + 2La_{La}^X \quad (2.4).$$

2.4.1 Calcium

Haugsrud *et al* first synthesised Ca substituted $ReNbO_4$ (Re = La, Nd, Gd, Tb and Er) with 1 mol% of Ca on Re sites [9][77]. **Figure 2.4.1** shows the total conductivity of $La_{0.99}Ca_{0.01}NbO_4$ under different atmosphere and there were three phenomena indicated that the ionic conductivity of $La_{0.99}Ca_{0.01}NbO_4$ was protonic: first, by comparing the total

conductivities of material measured under the same atmosphere but different humidities, a significant increase could be found under humidified conditions; second, both under humidified conditions, the material exhibited an isotope effect: a higher total conductivity under H_2O than D_2O; third, in elevated temperature range, there was a decrease of total conductivity under humidified reducing atmosphere compared with it under humidified oxidising atmosphere. The third phenomenon was related to the reaction described by equation (2.4), as under high temperature and oxidising atmosphere, the acceptor substituents on La sites (Ca'_{La}) would be compensated by holes rather than oxygen vacancies and therefore, provide p-type electronic conductivity, which led to the difference [9].

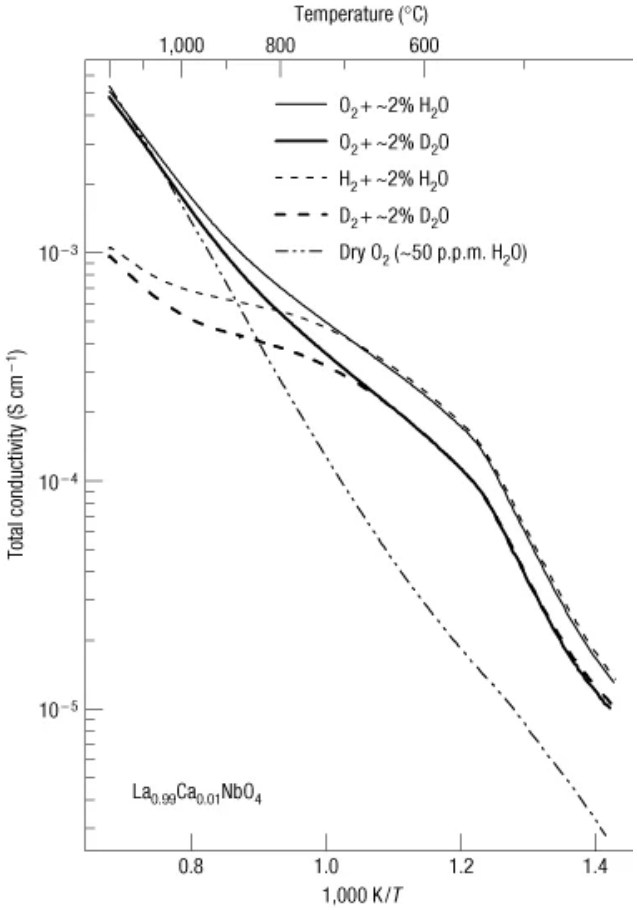


Figure 2.4.1. Total conductivities of 1 mol% Ca substituted $LaNbO_4$ under different atmospheres. Reproduced with permission [9]. Copyright (2006), Nature.

The partial protonic conductivity of Ca substituted $ReNbO_4$ was extracted by electromotive force (EMF) method and the results showed that Ca substituted $LaNbO_4$ exhibited the highest proton conductivity peaking at 10^{-3} S cm^{-1} at around 950 °C [9][77]. The reason why other lanthanides showed lower protonic conductivities could be related to their

smaller ionic radii, which led to stiffer lattices and less dynamics for proton movements [77]. The slope change observed around 500 °C in **Figure 2.4.1** coincided with the m-phase and t-phase transition of $ReNbO_4$; however, it is worth noting that from the ND data of $La_{0.99}Ca_{0.01}NbO_4$, even at 750 °C, there was still a small residual of m-phase existing in t-phase and the phase behaviour of $La_{0.99}Ca_{0.01}NbO_4$ was related to the sample preparation and thermal cycling [78], which has been discussed below.

Although more Ca substituents on La sites could introduce more charge carriers, excess Ca substituents over the solubility limit could also lead to a secondary phase [79]. Bi *et al* systematically studied $La_{1-x}Ca_xNbO_{4-\delta}$ (x = 0 - 0.025 with increment of 0.005) synthesised by a conventional solid state reaction (SSR) route [79]. The X-ray diffraction (XRD) results showed that most samples possessed a monoclinic structure at room temperature; however, small amounts of $Ca_2Nb_2O_7$ appeared in the sample with x = 0.025 [79]. Detailed scanning electron microscopy (SEM) and energy dispersive X-ray spectroscopy (EDX) results showed that $Ca_2Nb_2O_7$ was mainly located on the grain boundaries and with increasing Ca content, the amount of $Ca_2Nb_2O_7$ also increased [79]. The existence of $Ca_2Nb_2O_7$ also led to a clear increase in the grain size because of the lower melting point [79]. Therefore, theoretically, increasing Ca content, on one hand, could introduce more proton charge carriers which could decrease the bulk resistance; on the other hand, the increase of grain size could reduce the amounts of grain boundaries, which could decrease the grain boundary resistance. However, the electrochemical impedance spectroscopy (EIS) results showed that the bulk resistance almost remained constant and the grain boundary resistance increased with increasing Ca content below 600 °C [79]. The unchanged bulk resistance was related to the solubility limit of Ca and the increase of grain boundary resistance was ascribed to the high resistance of $Ca_2Nb_2O_7$ locating on the grain boundaries [79]. Combined with the results of total conductivity and activation energy measurements, the solubility of Ca on La sites should be between 0.5 mol% to 1.0 mol% [79]. This low solubility and the appearance of secondary phases could be related to the nature of a line compound of $LaNbO_4$ causing low tolerance in cation non-stoichiometry in this material, which had strong influences on the sintering behaviour and grain boundary conductivity [80].

In addition to conventional SSR method, there were also some other methods can be used to realise specific properties of Ca substituted $LaNbO_4$ [69][81][82][83][84][85]. Mokkelbost *et*

al used a spray pyrolysis (SP) method to synthesise Ca substituted $LaNbO_4$ with 2 mol% Ca on La sites with aqueous precursors [69][81]. The powders exhibited a grain size of around 1.2 µm with homogenous grain size distribution [81]. This homogenous structure could be beneficial to mechanical performance when fabricated as thin film electrolytes (around 1 µm for thickness) and the SP method led to a lower sintering temperature (around 1200 °C) [69][81] compared with SSR (around 1500 °C) [77][79] because of its higher reactive nature [81]. However, because of the increase of the grain boundaries amounts from relatively smaller grain sizes and the existence of secondary phases from excess Ca [81], the proton conductivity of 2 mol% Ca substituted $LaNbO_4$ synthesised by SP method was lower than the conductivity of 1 mol% Ca substituted $LaNbO_4$ synthesised by SSR [9][77][79].

Magrasó *et al* first applied the pulsed laser deposition (PLD) technique to fabricate Ca substituted $LaNbO_4$ thin films [82]. A thin layer with 1 µm thickness of $La_{0.995}Ca_{0.005}NbO_{4-\delta}$ was deposited on NiO-$La_{0.995}Ca_{0.005}NbO_{4-\delta}$ substrate, which exhibited a total conductivity of around 10^{-4} S cm^{-1} at 600 ˚C under humidified hydrogen [82]. Another $La_{0.995}Ca_{0.005}NbO_{4-\delta}$ epitaxial film fabricated by PLD was deposited on $NdGaO_3$ (110) single crystal by Cavallaro *et al* [83]. In this case, the film grew along the *b* axis and an 80 nm thin film of $La_{0.995}Ca_{0.005}NbO_{4-\delta}$ exhibited an m-phase to t-phase transition temperature of 250 °C and a proton conductivity of 0.13 S cm^{-1} at 650 °C under humidified hydrogen [83]. The relatively lower phase transition temperature was ascribed to the lower mismatch between the t-phase and the substrate [83]. The significantly increased proton conductivity could be related to the low density of grain boundaries [83]. Miruszewski *et al* synthesised nanocrystalline $La_{0.98}Ca_{0.02}NbO_4$ by mechanosynthesis (mechano) method [85]. The difference between mechano method and conventional SSR method was that a long time (at least 10 hours) ball milling process was included in the so-called mechano method [79][85]. The XRD results showed that this nanostructure successfully stabilised the t-phase down to room temperature; however, it also led to large amounts of high-resistive grain boundaries, which made nanocrystalline $La_{0.98}Ca_{0.02}NbO_4$ exhibit a higher activation energy compared with the materials synthesised by conventional SSR method [79][85]. Amisf *et al* applied freeze-dried precursors (FDP) route to synthesis $La_{0.99}Ca_{0.01}NbO4$ [84]. Materials prepared by this method exhibited an even lower sintering temperature (around 1150 °C) compared with the SP method mentioned above, which provides a possibility of co-sintering between electrolyte and electrode materials [84].

The lower sintering temperature could be related to the smaller particle sizes before sintering, which could increase the driving force for densification [86].

2.4.2 Other alkaline elements and divalent elements

Apart from Ca, Sr was also used as an acceptor substituent on La sites, which exhibited comparable conductivity compared with Ca substituted $LaNbO_4$ [69][77]. Several works on Sr substituted $LaNbO_4$ revealed the reason why acceptor substituted $LaNbO_4$ always exhibited a low grain boundary conductivity in terms of the grain boundary core-space charge layer model [87][88][89]. Substituents of Sr^{2+} always tended to segregate to grain boundaries to lower the electrostatic energy of the system, but still left a positively charged grain boundary core [89][90]. Because of the existence of the positively charged grain boundary core, the ionic defects possessing the same charge, in this case, oxygen vacancies, would be depleted in the space charge layer [90][91]. Therefore, the corresponding hydroxide ions would also be depleted, leading to a lower proton conductivity in the grain boundaries [88]. **Figure 2.4.2** shows a schematic representation of the grain boundary core-space charge layer model. The segregation of the substituents in Sr substituted $LaNbO_4$ also caused a smaller grain size after sintering because of the inhibition of the cation diffusion [84][92][93]. Li *et al* noticed that the segregated Sr in the grain boundaries would further diffuse to the surface of this material at around 600 °C to 800 °C, which could block the proton surface exchange process [89].

Mielewczyk-Gryn *et al* synthesised $La_{0.98}Mg_{0.02}NbO_{4-\delta}$ by molten salt (MS) method [94][95][96]. According to the simulation results of Mather *et al*, the large mismatch of ionic radii between La and Mg made Mg not a suitable substituent on La site [7]; however, the conductivity of $La_{0.98}Mg_{0.02}NbO_{4-\delta}$ peaked at 2×10^{-3} S cm^{-1} at 720 °C under humidified hydrogen, which was comparable to Ca substituted $LaNbO_4$ [96]. This relatively high conductivity was ascribed to its larger grain size (around 6.8 μm) [96] compared with Ca substituted materials (1-4 μm) [79], which decreased the grain boundary resistance [96]. Mielewczyk-Gryn *et al* also suggested that partial crystallographic orientation (along the *b* axis) realised by MS method had an influence on improving the conductivity as it may improve the inter-grain conductivity [94].

Very few attempts were conducted on other divalent elements, for instance, Ba [69] and Zn [97]. Zn substituted $LaNbO_4$ showed comparable conductivity with Ca substituted $LaNbO_4$ and a similar solubility of substituents, which was lower than 1 mol% [97]. For Ba

substituted $LaNbO_4$, a secondary phase of $BaNb_2O_6$ appeared, which exhibited an increase of grain growth; however, this increase was drastic, which left pores and cracks in the samples [69].

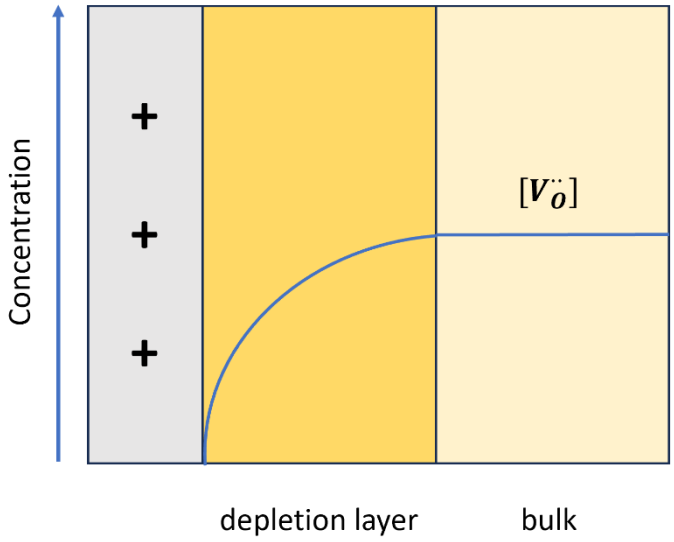


Figure 2.4.2. A schematic representation of grain boundary core-space charge layer model. The grey area represents the grain boundary core.

2.4.3 Lanthanides

Other lanthanides possess similar ionic radii to La^{3+} [76], which could also be used as substituents on La sites. The similar ionic radii could improve the substituting content compared with other substituents, which could introduce more extrinsic defects [98]; on the other hand, some lanthanides, for instance, Ce or Sm, possessing variable oxidation states, could improve the electronic conductivity especially in oxidising or reducing atmospheres, which could make these materials candidates for SOFC electrodes [99]. For instance, the mechanisms of electronic conductivity generated by holes and electrons introduced by Ce substituent are described by equations (2.5) and (2.6), respectively:

$$Ce_{La}^{\bullet} \rightleftharpoons Ce_{La}^{X} + h^{\bullet} \qquad (2.5);$$

$$Ce_{La}^{\bullet} + e' \rightleftharpoons Ce_{La}^{X} \qquad (2.6).$$

Solís *et al* substituted Pr and Ce on La sites of $La_{0.995}Ca_{0.005}NbO_{4-\delta}$, respectively [99]. The results showed that, under hydrogen atmosphere, there were no changes of total conductivities of $La_{0.995}Ca_{0.005}NbO_{4-\delta}$ and Pr substituted $La_{0.995}Ca_{0.005}NbO_{4-\delta}$ [99]. Combined

with what Dzierzgowski *et al* suggested, Pr in these materials should prefer to possess an oxidation state of Pr^{3+} [100]. Therefore, under reducing atmosphere, Pr substituted $La_{0.995}Ca_{0.005}NbO_{4-\delta}$ was a pure protonic conductor; however, under oxygen atmosphere, due to the partial oxidation of Pr^{3+} to Pr^{4+}, Pr substituted materials exhibited a combination of p-type electronic conductivity and proton conductivity, which made them a candidate for cathode materials [99]. For Ce substituted materials, under oxygen atmosphere , there was no difference of total conductivities between dry and humidified conditions as the oxidation of Ce^{3+} to Ce^{4+} could compensate the charge defects associated with Ca substituents [99][101]. Once approaching to a reducing atmosphere, the reduction of Ce^{4+} to Ce^{3+} could gradually increase the proton conductivity of these materials and they exhibited a combination of n-type electronic conductivity and proton conductivity, which made them a candidate for anode materials [99]. Cao *et al* substituted Sm on La sites of $LaNbO_4$ and claimed that the material exhibited an increase of total conductivity under humidified air atmosphere because of the existence of Sm^{2+}, which could work as an acceptor substituent like Ca [98]. However, when substituting Sm on $La_{0.99}Ca_{0.01}NbO_{4-\delta}$, the total conductivity decreased with increasing Sm content [102][103]. On one hand, the existence of oxygen vacancies from Ca substituents in the system could inhibit the generation of new oxygen vacancies from Sm substituents [102]; on the other hand, as Sm possesses smaller ionic radius than La [76], the smaller lattice volume of Sm substituted materials could cause less space for protons migration [103]. However, there was a lack of the oxidation states information of Sm substituents. Cao *et al* also synthesised Ce and Yb co-substituted $LaNbO_4$ [104]. The authors claimed that because of the partial existence of Yb^{2+}, Yb could work as an acceptor substituent; however, the oxidation states information and the corresponding conductivity results remained ambiguous [104]. Dzierzgowski *et al* substituted Tb on La site and the results showed that the conductivity was increased under humidified air atmosphere [105]. The authors claimed that the increase of the total conductivity under humidified atmosphere came from the increased protonic conductivity, and they used the mechanism described by equation (2.7) [105] to explain this phenomenon as in Tb (Tb^{3+}/Tb^{4+}) substituted $LaNbO_4$, there is no contribution from extrinsic oxygen vacancies like Ca substituted $LaNbO_4$:

$$H_2O + 2O_O^X \rightleftharpoons 2(OH)_O^{\bullet} + O_i'' \qquad (2.7);$$

However, the authors missed the most important part of this mechanism. This mechanism was first proposed by Norby *et al* [106] and explained by Islam *et al* for $Ba_2In_2O_5$ brownmillerite materials [107]. This type of material contained unoccupied interstitial sites (V_i^X) which was the premise of realising proton conductivity in this material [106][107]. The total mechanism could be described in two steps: firstly, one lattice oxygen ion jumps into an unoccupied interstitial site forming an oxygen vacancy and one oxygen interstitial at the same time; then the hydroxyl group and the proton from one water molecule associate with the newly formed oxygen vacancy and another lattice oxygen, respectively, generating two $(OH)_O^\bullet$ [107]. Therefore, the mechanism described by equation (2.7) should be corrected as equation (2.8) [106][107], where the contribution of the unoccupied interstitial sites has been included:

$$H_2O + 2O_O^X + V_i^X \rightleftharpoons 2(OH)_O^\bullet + \ O_i'' \qquad (2.8);$$

As shown in equation (2.8), more oxygen interstitials would lead to less hydroxyl groups; therefore, for a system like Tb (Tb^{3+}/Tb^{4+}) substituted $LaNbO_4$, the increased total conductivity under humidified air atmosphere could not come from this mechanism. Also, the thermogravimetric analysis (TGA) results from the work of Dzierzgowski *et al* showed there were no obvious mass changes (0.002%) found in Tb substituted $LaNbO_4$ under humidified gas [105], which was further evidence of applying the incorrect mechanism as there was no cooperation of water in these materials. Therefore, the mechanism for these materials still needs to be discussed. **Table A1** in Appendix summarises related information of La site substituted $LaNbO_4$.

2.5 Substituent strategies on Nb site

Typically, there are two main effects for Nb site substituents: on one hand, most substituents on Nb sites could have an influence on the phase transition temperature of $LaNbO_4$ [10]; on the other hand, hexavalent elements, like W or Mo, working as donor substituents could introduce oxygen interstitials or electrons depending on different conditions. The mechanisms in relatively oxidising and reducing atmospheres are described by equation (2.9) and (2.10), respectively, where M represents the hexavalent elements:

$$2MO_3 + La_2O_3 \rightleftharpoons 2M_{Nb}^\bullet + O_i'' + 8O_O^X + 2La_{La}^X \qquad (2.9);$$

$$2MO_3 + La_2O_3 \rightleftharpoons 2M_{Nb}^{\bullet} + 2e' + 8O_O^X + 2La_{La}^X + 1/2O_2 \qquad (2.10).$$

Some substituents with lower oxidation states compared with Nb could work as acceptor substituents [108] as discussed in Section 2.3, and sometimes also as a sintering aid [109]. As W and Mo substituted $LaNbO_4$ possess modulated structures [14][11] and are highly related to the work of this thesis, three categories are divided in the following discussions: elements used as acceptor substituents, elements tailoring phase transition temperature and W/Mo.

2.5.1 Elements used as acceptor substituents

Li *et al* studied Co substituted $La_{0.95}Ca_{0.05}NbO_4$ [109]. There were two effects of Co: on one hand, as a sintering aid, Co could form a liquid film around grain boundaries which reduced the friction of grain particles to lower the sintering temperature by around 200 °C [109]; on the other hand, Co was also an acceptor substituent, which could introduce more oxygen vacancies to increase the proton conductivity [109]. The total conductivity of $La_{0.95}Ca_{0.05}Nb_{0.95}Co_{0.05}O_4$ was found to be around 2.4×10^{-4} S cm^{-1} at 800 °C under humidified air [109]. However, as Co possessed mixed oxidation states of Co^{2+} and Co^{3+}, the contribution from electronic conductivity remained unknown. Li *et al* also studied Ni substituted $La_{0.95}Ca_{0.05}NbO_4$ [110]. In this work, the as-sintered $La_{0.95}Ca_{0.05}Nb_{0.95}Ni_{0.05}O_4$ was reduced under 5% H_2/Ar, which led to the exsolution of Ni metal nanoparticles on the surface [110]. The exsolved Ni nanoparticles exhibited a catalytic effect of facilitating the incorporation process of protons, which increased the conductivity through both bulk and grain boundaries [110].

Several works also investigated Sn substitution [111][112]. The results showed that $LaNb_{0.97}Sn_{0.03}O_{3.985}$ exhibited pure proton conductivity even under humidified oxidising atmospheres up to 900 °C [112] and the conductivity of $La_{0.95}Ca_{0.05}Nb_{0.95}Sn_{0.05}O_{4-\delta}$ reached 2.96×10^{-4} Scm^{-1} at 800 °C under humidified hydrogen due to the increase of the oxygen vacancies amounts from both La and Nb sites [111]. However, the solid solubility of Sn on Nb site was low, ranging from 3 mol% to 5 mol% [111][112]. Brandao *et al* systematically studied the acceptor substituents on Nb sites, including B, Al, Ga, Si, Ge, Zr Ti and P [108]. However, most of them exhibited a lower solid solubility on Nb sites and this work only focused on the electrochemical performance of $LaNb_{0.98}Ti_{0.02}O_{4-\delta}$ [108]. The total conductivity of $LaNb_{0.98}Ti_{0.02}O_{4-\delta}$ measured under humidified oxygen and humidified nitrogen mirrored each

other, suggesting lower p-type conductivity under humidified atmospheres, which was similar to what was found in other Nb site substituted materials [108][112]. Therefore, the acceptor substituents on La sites seemed to exhibit a more pronounced p-type conductivity under humidified atmospheres than acceptor substituents on Nb sites. A similar phenomenon was observed by Huse *et al* [70]. The results showed that $LaNb_{0.99}Ti_{0.01}O_4$ could still remain partly hydrated above 1000 °C under humidified atmospheres compared with $La_{0.99}Ca_{0.01}NbO_4$; however, due to a higher trapping effect, the proton conductivity of Ti substituted $LaNbO_4$ was still lower than that of Ca substituted $LaNbO_4$ with equal substituting content [70]. The appearance of a secondary phase of $LaNb_3O_9$ in $La_{0.99}Ca_{0.01}Nb_{0.99}Ti_{0.01}O_{4-\delta}$, exhibiting an n-type conductivity under reducing atmospheres, could make the Ca and Ti co-substituted $LaNbO_4$ a candidate for anode materials [70][113][114]. Ivanova *et al* further studied Ga, Ge and In substituted $LaNbO_4$ [115]. The results showed that the substituents on the Nb sites did not increase the conductivity compared to Ca substituted $LaNbO_4$ due to their higher activation energies of proton mobility [115]. Virbukas *et al* used magnetron sputtering to deposit Zr doped $LaNbO_4$ thin films [116]. The deposited materials possessed a nanocrystalline structure, and this structure stabilised t-phase down to room temperature, which fitted well with the work of Miruszewski *et al* [85][116]. However, even with t-phase stabilised at room temperature, Zr doped materials exhibited a relatively high activation energy of 1.12 eV, which made them not an ideal electrolyte [116]. Therefore, based on the above discussion, increasing the proton conductivity by substituting Nb sites with acceptor substituents was unsuccessful [115] and did not influence the phase transition temperature.

2.5.2 Elements tailoring phase transition temperature

As mentioned above, substituents on Nb site are always used to tailor the transition temperature of $LaNbO_4$. Two results could be achieved: some substituents could stabilise the m-phase up to high temperature range [117]; others could stabilise the t-phase down to lower temperature range [118][119]. Vullum *et al* first studied the structures of $LaNb_{1-x}Ta_xO_4$ [117]. In the range of $0 \leq x \leq 0.4$, the transition temperature increased with increasing Ta content on Nb sites [117]. For $LaNb_{0.6}Ta_{0.4}O_4$, the system could possess a monoclinic structure up to 800 °C [117]. The reason could be related to the difference of coordination environments between Nb and Ta [117]. As mentioned in Section 2.1, Nb sites were considered as distorted octahedra with a coordination number of 6 in m-$LaNbO_4$ and tetrahedra with a coordination number of

4 in t-$LaNbO_4$ [63]. In $LaTaO_4$, the coordination number of Ta sites was also 6, which made the coordination environments of the Nb sites in $LaNb_{0.6}Ta_{0.4}O_4$ tend towards octahedral environments; therefore, Ta substituents stabilised the m-phase to higher temperature range [117]. Ta substituents also decreased the difference of TECs between m-phase and t-phase [117]. The TECs difference of $LaNb_{0.6}Ta_{0.4}O_4$ was four times lower than that of unsubstituted $LaNbO_4$, which was an advantage for working as electrolytes [117]. Therefore, based on this advantage, several attempts of substituting Ta on Nb sites of $La_{0.99}Ca_{0.01}NbO_{4-\delta}$ and $La_{0.98}Sr_{0.02}NbO_4$ had been conducted [120][121]. The results showed that for both Ca and Sr substituted $LaNbO_4$, with further substituting 40 mol% Ta on Nb sites, the phase transition temperature was increased above 800 °C [120][121]. However, the Ta substituted materials always exhibited one order of magnitude lower conductivity compared with the materials without Ta substituents in the ideal working temperature range (around 600 °C) [120][121]. Santibanez-Mendieta *et al* also tried to synthesise $La_{0.98}Sr_{0.02}Nb_{0.6}Ta_{0.4}O_4$ via wet chemistry routes like auto-combustion and co-precipitation [122]. The conductivity of the materials synthesised via wet chemistry routes was one order of magnitude higher than the materials synthesised by SSR method because of the homogeneity of the microstructure [122]. However, because of the nature of the higher activation energy in m-phase [5], the conductivity was still lower than unsubstituted $La_{0.98}Sr_{0.02}NbO_4$ [122]. Therefore, although it could avoid the detrimental phase transition of $LaNbO_4$ by substituting Ta on Nb sites, the loss in conductivity still made the materials stabilising m-phase to high temperature not an ideal candidate for an electrolyte [118].

Therefore, the inverse solution where the t-phase was stabilised down to lower temperature range had been investigated [118][119]. The stabilisation of t-phase down to lower temperature range seemed to be related to substituents possessing smaller ionic radii compared to Nb [118]. Brandao *et al* first synthesised $La_{0.98}Sr_{0.02}Nb_{1-x}V_xO_{4-\delta}$ [118]. With 30 mol% V substituted on Nb site, the t-phase was successfully stabilised down to room temperature [118]. As the activation energy of proton conduction of t-phase was lower than that of m-phase, $La_{0.98}Sr_{0.02}Nb_{1-x}V_xO_{4-\delta}$ exhibited higher protonic conductivity than $La_{0.98}Sr_{0.02}NbO_{4-\delta}$ under humidified oxidising atmospheres below 500 °C [118]. However, under a reducing atmosphere like 10% H_2/N_2, a secondary phase of $LaVO_3$ appeared [118]. As mentioned in Section 2.4.1, the mechano method including a highly energetic ball milling process could directly stabilise the t-phase down to room temperature [85] and this effect was more obvious for V substituted

materials [119]. Brandao *et al* synthesised V substituted $La_{0.98}Sr_{0.02}NbO_{4-\delta}$ by the mechano method and this time the t-phase was stabilised down to room temperature with only 15 mol% of V on Nb sites [119]. Wachowski *et al* systematically compared the pentavalent substituents on the Nb site: Ta, V and Sb [123][124]. Although the coordination number of Sb in $LaSbO_4$ is the same as that of Nb in m-$LaNbO_4$, Sb stabilised the t-phase down to room temperature with 30 mol% Sb substituted on the Nb sites [123]. The reason why Sb exhibited a similar effect to V rather than Ta was related to the bond covalency [123] and was discussed in the following paragraph. $La_{0.98}Ca_{0.02}Nb_{0.7}Sb_{0.3}O_{4-\delta}$ exhibited a proton conductivity of around 10^{-4} Scm^{-1} at 800 °C under humidified air, which was of a similar order of magnitude of $La_{0.99}Ca_{0.01}NbO_4$ but avoided the phase transition in the working temperature range [125][126].

As mentioned above, several properties of substituents on the Nb sites, like coordination number [117] and ionic radius [118], could determine whether this substituent was an m-phase stabiliser or a t-phase stabiliser. For the perspective of coordination number, 6-fold and 4-fold coordinated substituents could stabilise m-phase and t-phase, respectively [10]; for the perspective of ionic radius, a substituent with a smaller ionic radius compared to Nb could stabilise the t-phase [118]. These could be used to explain the results of substituents like Ta, V and As [10][117][118]; however, these did not work for Sb, as Sb possessed more similar coordination number and ionic radius to Ta but stabilised the t-phase [10][123]. Therefore, electronegativity, the determining property, was proposed by Wachowski *et al* [10]. **Figure 2.5.1** shows the relative properties of substituents on Nb sites.

Wachowski *et al* suggested that compared with Nb, a higher electronegativity could stabilise the t-phase and a lower electronegativity could stabilise the m-phase, which worked well with all elements mentioned above [10]. The essence of the phase transition of $LaNbO_4$ was the realignment of $[NbO_4]^{3-}$ tetrahedra and the realignments were strongly affected by the covalency of the Nb-O bonds [10]. A more covalent Nb-O bond made the $[NbO_4]^{3-}$ more like a unit, which could weaken the interaction among the tetrahedra; therefore the realignments became easier at lower temperature, which led to a lower phase temperature [10]. A higher electronegativity substituent on Nb sites could lower the difference of electronegativities between Nb sites and oxygen sites, which made the Nb-O bond more covalent; therefore, from the mechanism discussed above, it could lower the transition temperature and vice versa [10].

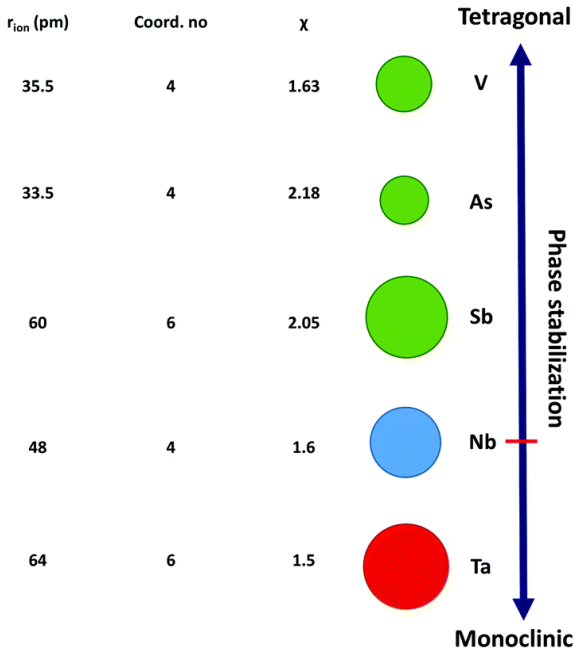


Figure 2.5.1. Ionic radius (r_{ion}), coordination number and electronegativity (χ) of Nb^{5+} and substituents (Ta^{5+}, Sb^{5+}, As^{5+} and V^{5+}) on Nb sites. Reproduced with permission [10]. Copyright (2018), Royal Society of Chemistry.

2.5.3 W and Mo

Inspired by the increase of ionic conductivity by introducing oxygen interstitials in $CeNbO_4$ system [127], Li *et al* synthesised $LaNb_{0.92}W_{0.08}O_{4.04}$ [11]. As shown in **Figure 2.5.2**, both XRD and selected area electron diffraction (SAED) patters showed satellite reflections, which clearly demonstrated the nature of possessing modulated structures [11]. As the modulated structures were highly related to the materials studied in this thesis, it is necessary to introduce the basic concepts of modulated structures before any further discussions.

For a normal crystal structure with translational symmetry, every atom should be found located at its original position (shown in **Figure 2.5.3** a)). Now considering the situation shown in **Figure 2.5.3** b), the atoms are displaced by equal amounts along ±**a** directions and the displacement could be described by a periodic wave function. This wave function is called the *modulated function* [128]. Although the atoms leave their original positions, the new structure still possesses translational symmetry, as the exact same environment of any atom can be found by moving with a distance of 2a along **a** direction. As the lattice, which exhibits the translational symmetry, is now of twice the volume of the original lattice, this new lattice is called the *superlattice* [128]. Correspondingly, this new structure is called the

commensurately modulated structure [128]. In a commensurately modulated structure, the periodicity of the modulated function is the same as the periodicity of the superlattice [128]. However, there could be a situation as shown in **Figure 2.5.3** c), where the periodicity of the modulated function cannot match any integral number of the lattice translations. In this case, the structure is called the *incommensurately modulated structure* [128].

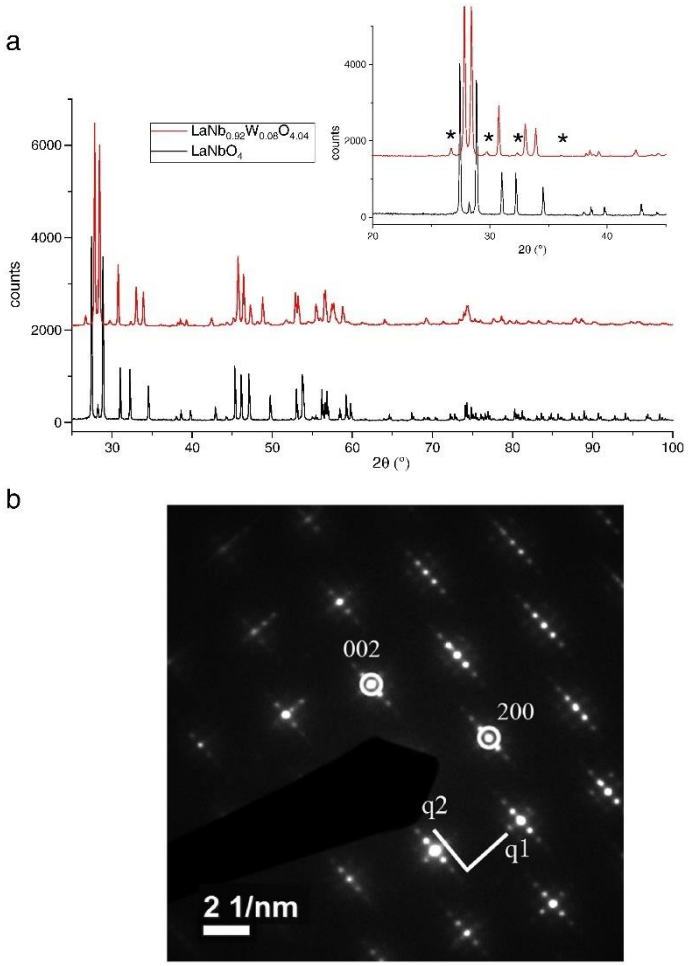


Figure 2.5.2. a) XRD patterns of $LaNb_{0.92}W_{0.08}O_{4.04}$ with satellite peaks marked with asterisk (inset), and b) ED patterns of $LaNb_{0.92}W_{0.08}O_{4.04}$ from [010] zone axis, respectively. Reproduced with permission [11]. Copyright (2013), Elsevier.

Although for an incommensurately modulated structure, the translational symmetry is broken in the original lattice, it is still preserved in the superlattice [129], which could be characterised by the satellite reflections in both XRD and ED as shown in **Figure 2.5.2**. Figure **2.5.3** d) shows the schematic diffraction patterns of the three structures discussed above. Therefore, indexing the satellite reflections from modulated structures is one of the tasks of incommensurate crystallography. The satellite reflections are indexed by modulated vectors

$\boldsymbol{q}$, which is a linear combination of reciprocal vectors $\boldsymbol{a_1^*}$, $\boldsymbol{a_2^*}$ and $\boldsymbol{a_3^*}$ [129]. The relationship between modulated vectors and reciprocal vectors is described by equation (2.11):

$$\boldsymbol{q} = \sigma_1 \boldsymbol{a_1^*} + \sigma_2 \boldsymbol{a_2^*} + \sigma_3 \boldsymbol{a_3^*} \qquad (2.11),$$

where σ_1, σ_2 and σ_3 represent the corresponding coefficients for each reciprocal vector, respectively [128]. If any of the coefficients is irrational, the structure should be incommensurately modulated [128]. If two different $\boldsymbol{q}$ vectors are needed to index the modulated structure, it is suggested that this modulated structure is a (3+2) D structure [128]. For example, as shown in **Figure 2.5.2** b), two vectors with values of $\boldsymbol{q_1} = 0.263\boldsymbol{a}^* + 0.106\boldsymbol{c}^*$ and $\boldsymbol{q_2} = 0.082\boldsymbol{a}^* + 0.2427\boldsymbol{c}^*$ were used; therefore, the structure of $LaNb_{0.92}W_{0.08}O_{4.04}$ was 2D incommensurately modulated [11].

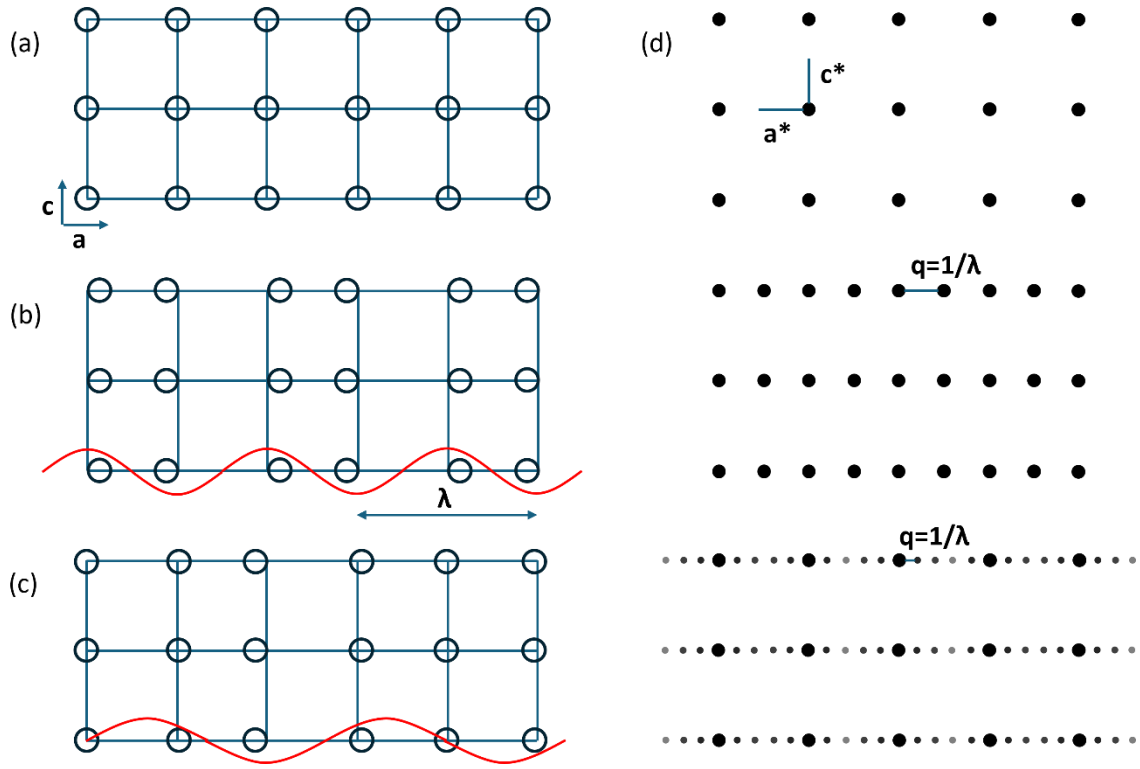


Figure 2.5.3 Schematic representations of a) a normal crystal lattice, b) a commensurately modulated lattice, c) an incommensurately modulated lattice and d) the corresponding diffraction patterns, respectively.

A detailed study of the modulated structures of $LaNb_{0.88}W_{0.12}O_{4.06}$ revealed that these modulated structures stemmed from the cation occupancy ordering in the *ac* plane and led to a distortion on Nb sites [130]. Li *et al* measured the oxygen tracer diffusivity of $LaNb_{0.88}W_{0.12}O_{4.06}$ and suggested that the interstitialcy mechanism should be the dominant

mechanism [130], which matched well with the simulation results [8][131]. Canu *et al* examined the chemical compatibility of $LaNb_{0.84}W_{0.16}O_{4.08}$ with some commercial cathode materials [132]. The results showed that $La_{0.8}Sr_{0.2}MnO_3$ was the most suitable one as after being annealed together at 1000 °C in air for 6 hours, both electrolyte and cathode materials still possessed a single phase [132]. However, a heat treatment at 1200 °C for 24 hours formed a secondary phase of $SrWO_4$ [132]. Therefore, the process of sintering a cathode layer on the W substituted $LaNbO_4$ electrolyte should be as quick as possible during the preparation of a single cell [132]. Buyanova *et al* found that the total conductivity of W substituted $LaNbO_4$ increased with increasing the W content [133] and there was no contribution from proton conductivity under air as the materials exhibited no difference in total conductivities under dry and humidified conditions [11]. The total conductivity peaked at 1.4×10^{-3} S cm^{-1} at 800 °C under air for $LaNb_{0.84}W_{0.16}O_{4.08}$ [132]. The X-ray absorption near edge structure (XANES) data showed W only possessed an oxidation state of W^{6+} under air with no existence of W^{5+} [134] and the TGA results showed there were no mass changes for W substituted materials from room temperature to 900 °C under air [135]; therefore, the series of $LaNb_{1-x}W_xO_{4+x/2}$ should be pure oxygen ion conductors under oxidising atmospheres [134][135]. However, the total conductivity of $LaNb_{0.84}W_{0.16}O_{4.08}$ increased to 2.5×10^{-3} S cm^{-1} and 6.1×10^{-3} S cm^{-1}at 800 °C under humidified and dry H_2, respectively [132]. The authors related these increased total conductivities to the n-type electronic conductivity from the reduction of W [132]; however, the W-L_3 XANES results of a work from our group (in preparation) showed that W substituents in $LaNb_{0.84}W_{0.16}O_{4.08}$ remained stable at W^{6+} after hydrogen treatment and the increased conductivity could be related to the proton conduction with a new mechanism, which was different from the one described by equation (2.2) [136]. Therefore, the stability and conductivity of W substituted $LaNbO_4$ under reducing atmospheres still needs to be studied. Another effect of W substituents was that they could stabilise the t-phase to a lower temperature [135]. As reported, the phase transition temperatures from m-phase to t-phase of $LaNb_{0.88}W_{0.12}O_{4.06}$ and $LaNb_{0.84}W_{0.16}O_{4.08}$ were around 400 °C and room temperature, respectively [135]. The transition temperatures from modulated structure to unmodulated structure were also different for these types of materials with difference content of W [135]. For example, $LaNb_{0.92}W_{0.08}O_{4.04}$ lost the modulated structures at the same time when it transitioned from a m-phase to a t-phase at around 500 °C; however, $LaNb_{0.84}W_{0.16}O_{4.08}$ could possess the modulated structures up to 800 °C [135]. For $LaNb_{0.88}W_{0.12}O_{4.06}$, it experienced three sequential

states during the transition: a modulated m-phase, a modulated t-phase, and an unmodulated t-phase [135]. Li *et al* found that the existence of the modulated structures could lead to a higher activation energy of oxygen ion conduction [11]; however, there were no more studies about this for W substituted $LaNbO_4$. Recently, a possible negative effect of the modulated structures on the electrochemical performance was proposed by Han *et al* [14][15] and is discussed in Chapter 4 and 5.

Although W substituted $LaNbO_4$ had exhibited competitive oxygen ion conductivity, based on the simulation results of Toyoura *et al*, the higher trapping effect of oxygen ions around W ions could limit the oxygen ion conductivity and Mo was suggested to be an alternative option [8]. $LaNb_{0.84}Mo_{0.16}O_{4.08}$ exhibited an oxygen ion conductivity of 7×10^{-3} S cm^{-1}at 800 °C under air, which was higher than the W substituted $LaNbO_4$ with same substitution content [12][132]. Auckett *et al* established a phase diagram of Mo substituted $LaNbO_4$ as shown in **Figure 2.5.4** [12]. It was found that the transition temperature from m-phase to t-phase decreased with increasing Mo content, which was similar to W; however, the modulated structures could not exist under higher temperature in the series of $LaNb_{1-x}Mo_xO_{4+0.5x}$ [12]. Cao *et al* claimed that $LaNb_{0.8}Mo_{0.2}O_4$ exhibited proton conductivity, although only a subtle difference of conductivity was observed under humidified and dry air atmospheres [16]. The results also showed that the total conductivity of $LaNb_{0.8}Mo_{0.2}O_4$ increased when exposed to a reducing atmosphere (5% H_2/N_2) together with a structure change from high symmetry to low symmetry [16]. The X-ray photoelectron spectroscopy (XPS) results showed the Mo in $LaNb_{0.8}Mo_{0.2}O_4$ was reduced to a lower oxidation state; therefore, the authors suggested the increased conductivity under reducing atmospheres were from the contribution of electronic conductivity [16]. As XPS measurements are inherently conducted under high vacuum conditions, and this technique is only sensitive to the surface composition, there is significant ambiguity as to the oxidation states of the bulk material. A detailed study of the oxidation states and stability of Mo in $LaNb_{0.9}Mo_{0.1}O_{4.05}$ under different atmospheres is discussed in Chapter 6. **Table A2** in Appendix summarises related information of Nb sites substituted $LaNbO_4$.

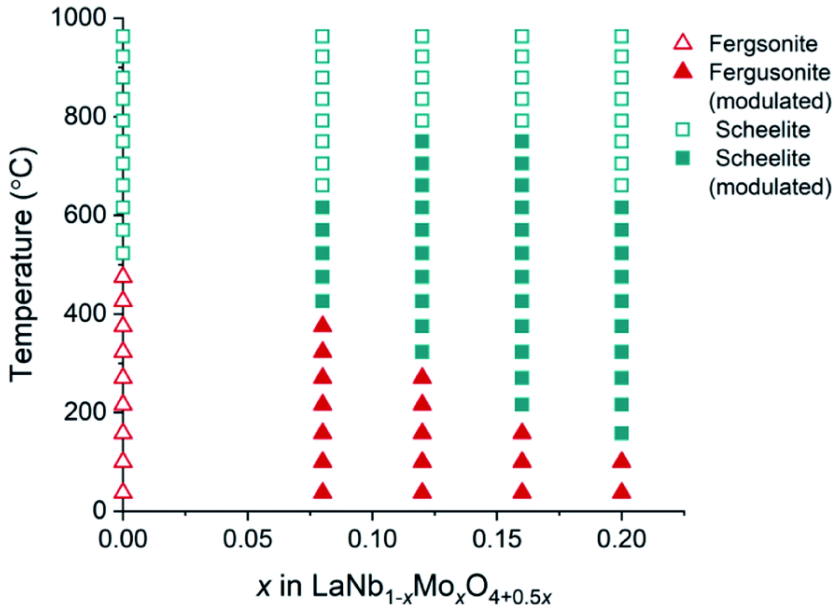


Figure 2.5.4 Phase diagram of $LaNb_{1-x}Mo_xO_{4+0.5x}$. Reproduced with permission [12]. Copyright (2021), Royal Society of Chemistry.

Chapter 3. Experimental details

In this chapter, the methods for synthesising the samples and the various techniques used for characterising the samples are discussed.

3.1 Sample preparation

All the samples investigated in this work were prepared via the conventional solid state reaction route. Powders of La_2O_3 (99.999%, Aldrich), Gd_2O_3 (99.99%, Alfa Aesar), Nb_2O_5 (99.99%, Aldrich), MoO_3 (99.5%, BDH) and WO_3 (99.8%, Alfa Aesar) were first dried for 10 hours to remove any potential adsorbed moistures and carbonates before any further heat treatments. The drying temperature for La_2O_3, Gd_2O_3, Nb_2O_5 was 1000 ˚C and for MoO_3 and WO_3, 500°C was used. Stoichiometric amounts of the as-dried powders were weighed for $La_{1-x}Gd_xNb_{0.9}Mo_{0.1}O_{4.05}$ and $LaNb_{0.8}W_xMo_{0.2-x}O_{4.1}$ series. The powders were then ground in an agate mortar by hand for at least 30 minutes. To achieve the homogeneity of the powders, acetone was added during the grinding process. After the acetone was volatilised, the mixed powders were transferred into an aluminium oxide crucible and calcined at 1000 °C in static air for 10 hours with heating and cooling rates of 5 °C per minute in a muffle furnace (BRF15/5, Elite Thermal System). Around 0.5 grams of the as-calcined powders were reground and then uniaxially pressed into pellets (Φ 13 mm) with a pressure of 3 tons for 3 minutes. The pellets were then transferred into an aluminium oxide crucible and sintered at 1400 °C in air for 10 hours with heating and cooling rates of 5 °C per minute in the same muffle furnace mentioned above. To avoid any possible volatilisation of Mo and W during the sintering process, the pellets were buried in the calcined powder with the same chemical composition.

Some of the as-sintered samples were then annealed under different atmospheres in a tube furnace (TS1 12/200/1200, Carbolite Gero). The tube furnace was connected to different gas cylinders: O_2 (99.5%, BOC), N_2 (99.998%, BOC) and 5% H_2/N_2 (5% H_2 in 95% N_2, BOC) to realise different atmospheric conditions. For the vacuum condition, the as-sintered pellets were placed in a quartz tube evacuated to a pressure of around 1.6×10^{-8} mbar. The quartz tube was then annealed in another tube furnace (CSC 12/90/600, Lenton). The heating and cooling rates were set as 5 °C per minute. The annealing temperature and dwell times are discussed in Chapter 6 in detail. Part of the as-sintered pellets and the as-annealed pellets

were then ground again into powders for further characterisation. **Figure 3.1.1** shows the flowchart for the preparation of the samples before any characterisation.

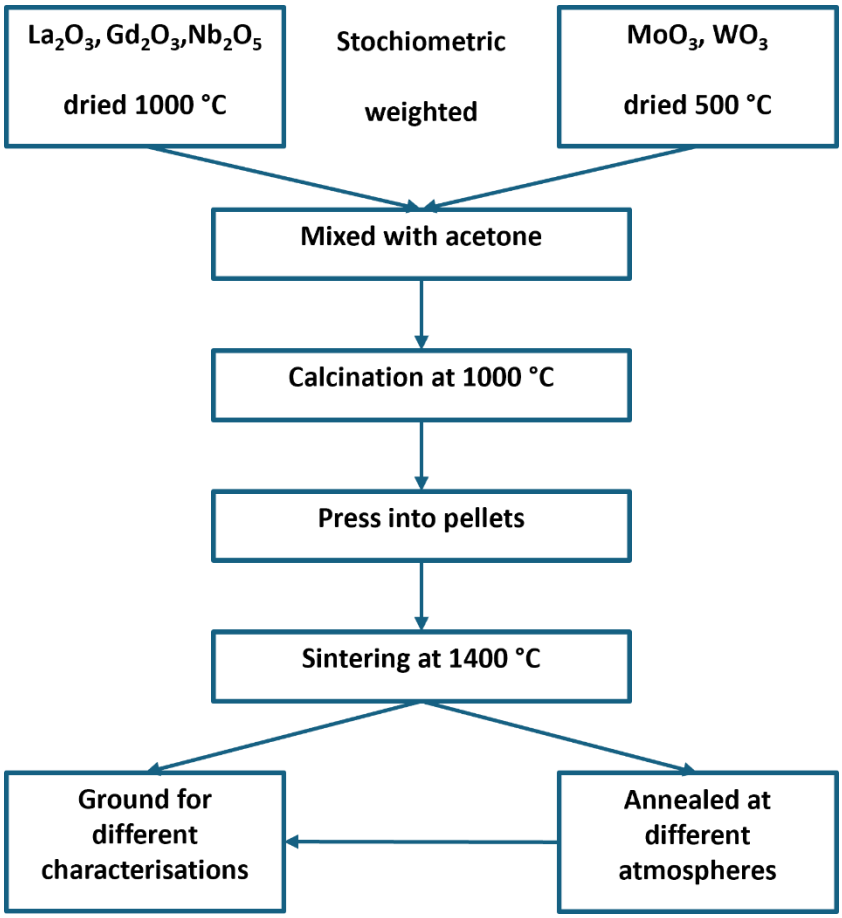


Figure 3.1.1. Flowchart of the preparation of the samples in this work.

3.2 X-Ray related techniques

Since the results of this thesis are mainly related to the X-ray related characterisations, the section of characterisation techniques used in this work is divided into two parts: X-Ray related techniques and other techniques. The interaction between X-rays and materials is a complex process and can be summarised by **Figure 3.2.1**. The intensity of the X-rays is attenuated after penetrating the materials, which is the result of absorption and scattering [137]. The X-ray related characterisation methods used in this work are X-ray diffraction (XRD), X-ray photoelectron spectroscopy (XPS) and X-ray absorption spectroscopy (XAS), which are marked in red in **Figure 3.2.1**. These three techniques are discussed in detail below.

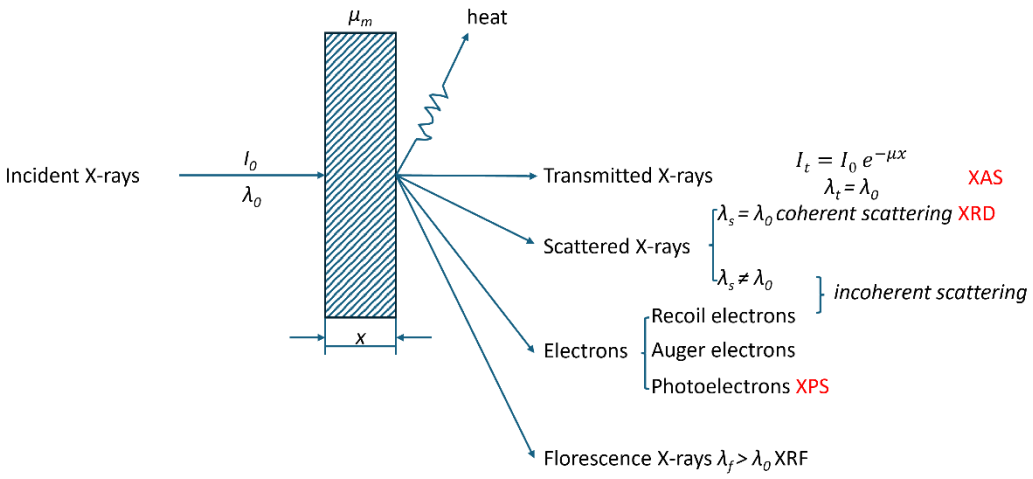


Figure 3.2.1. The interactions between X-rays and materials. ''*I*'' and ''λ'' represent the intensities and wavelengths of the X-rays. ''μ'' and ''*x*'' represent the attenuation coefficient and thickness of the materials, respectively. The subscript ''*0*'' represents incident X-rays, the others represent the corresponding X-rays. ''XRF'' represents X-ray fluorescence.

3.2.1 X-Ray diffraction

X-ray diffraction (XRD) is widely used to study crystal structures. The essence of the diffraction phenomenon of the X-rays in crystals is a result of the interference of the X-rays scattered by the electrons of the atoms. For example, when the incident waves (λ) penetrate a grating with an interval of a, at angle α_0, and are diffracted at an angle α, the path difference between the incident and scattered waves should be $a(cos\alpha - cos\alpha_0)$ (shown in **Figure 3.2.2**). For constructive interference to occur, the condition described by equation (3.1) should be obeyed:

$$a(cos\alpha - cos\alpha_0) = n\lambda \qquad (3.1),$$

where n is any integer. Since the atoms are regularly arranged in the crystals, the crystal lattice could be regarded as a three-dimensional grating for the incident X-rays. If the lengths of three axes in a lattice are a, b and c, the angles between the incident X-rays and three axes are α_0, β_0 and γ_0, and the diffraction angles are α, β, and γ, then equation (3.1) could be expanded to three dimensions, which is given by the Laue equations [138]:

$$a(cos\alpha - cos\alpha_0) = h\lambda \qquad (3.2),$$

$$b(cos\beta - cos\beta_0) = k\lambda \qquad (3.3),$$

$$c(cos\gamma - cos\gamma_0) = l\lambda \qquad (3.4),$$

where the triple set of hkl are similar to n in equation (3.1).

Consider a unit cell shown in **Figure 3.2.3**, from the Laue equations, the waves scattered by *A* ($OA = a$), *B* ($OB = b$) and *C* ($OC = c$) are h, k and l wavelengths ahead of the waves scattered by *O*. Therefore, for the waves scattered by points *P* ($OP = a/h$), *Q* ($OQ = b/k$) and *R* ($OR = c/l$), the waves are only one wavelength ahead of the waves scattered by *O*, which means the optical paths of them are equal. Based on Huygens principle [139], the optical paths of the wavelets, which combine to form the wave front of the reflected wave in a mirror reflection, must be equal; therefore, by analogy to the mirror reflection, the direction of the diffracted waves appear to be the direction of the waves reflected by the plane *PQR*.

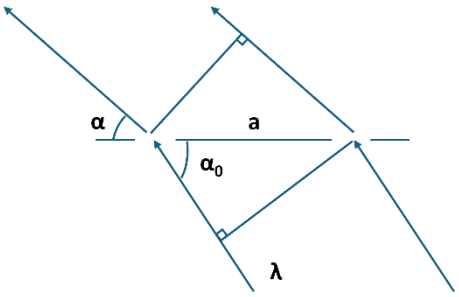


Figure 3.2.2. Schematic representation of the incident X-ray λ diffracted by the grating with the interval of a.

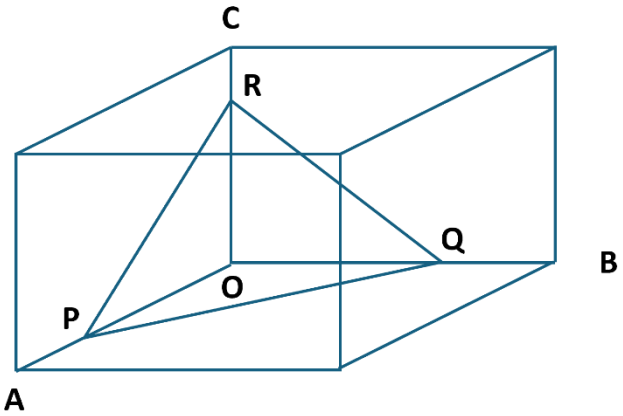


Figure 3.2.3. Schematic representation of a plane *PQR* where the direction of the diffracted waves appears to be the direction of the reflected waves.

Since in a crystal, there are also other lattice planes parallel to the lattice plane *PQR*, the path differences of the scattered waves ‘‘reflected’’ by these parallel planes should also

equal to integer multiple of wavelength to give the constructive interference, which gives Bragg's law (**Figure 3.2.4**) [140]:

$$2dsin\theta = n\lambda \quad (3.5),$$

where d is the spacing between 2 parallel lattice planes, θ is the angle between incident X-rays and lattice planes and n is any integer representing the order of the diffraction.

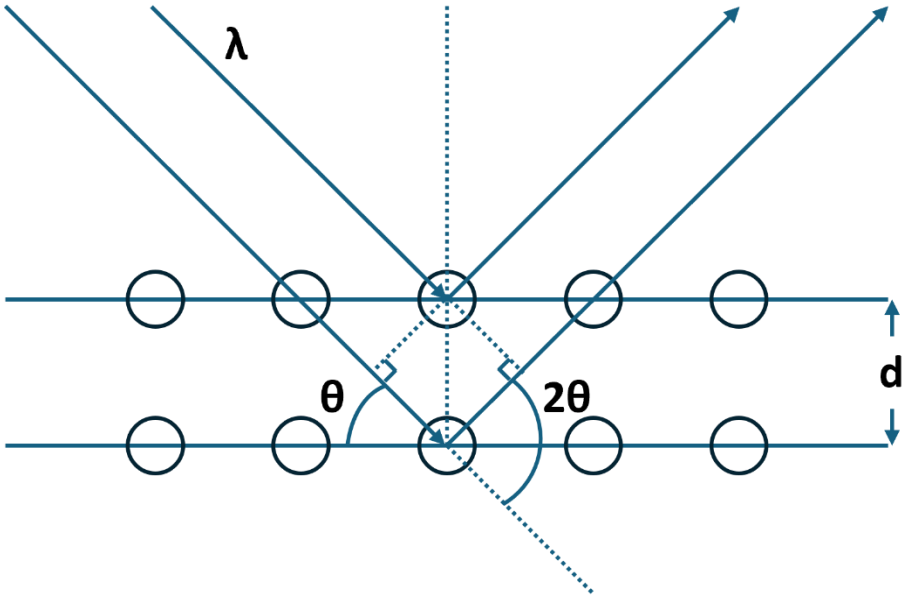


Figure 3.2.4. Schematic representation of Bragg's law.

It is worth noting that since the direction of the diffracted waves is the same as the direction of the waves reflected by the lattice planes in XRD, the analogy to the mirror reflection is used in Bragg's law to describe the XRD. However, the ''reflection'' in XRD is different from that in a mirror reflection as in the latter situation, the waves could be reflected at any angle; however, in XRD, the ''reflection'' only happens when d, θ and λ satisfy Bragg's law.

The room temperature XRD patterns in this work were collected using an X-ray diffractometer (X'Pert PRO, Malvern Panalytical) in static air. The *in-situ* high temperature XRD patterns were collected using an X-ray diffractometer (Empyrean, Malvern Panalytical) with flowing compressed air (N_2 and 21% ± 0.5% O_2, BOC) with a high temperature oven chamber (HTK 1200N, Anton Paar) connected. Cu K_α radiation (λ = 1.5406 Å) was used with a nickel filter to remove the K_β radiation. The 2θ range was set from 10° to 90° with a step size of 0.034°. For the high temperature XRD measurements, the data were collected at room

temperature and from 50 °C to 900 °C with an interval of 50 °C. Powder samples were used for the XRD measurements and were equilibrated at each temperature point for 5 minutes before the measurement.

For the *in-situ* synchrotron XRD, the data were collected on beamline B18 at Diamond Light Source [141]. Samples were mixed with BN as a dilutant and then uniaxially pressed into pellets (Φ 13 mm). To realise the high temperature environments, the diluted samples were placed into a specially designed Sankar *in-situ* furnace with water cooling system [142]. The *in-situ* XRD data were collected with a PILATUS3 X detector (300K-W, Dectris) at 17,500 eV and a Si (111) monochromator was used. For the as-sintered $LaNb_{0.9}Mo_{0.1}O_{4.05}$, data were collected at room temperature and from 200 °C to 800 °C with an interval of 50 °C during the heating process. Data were also collected at 700 °C and 250 °C during the cooling process. For the $LaNb_{0.9}Mo_{0.1}O_{4.05}$ annealed under 5% H_2/N_2 at 800 °C for 24 hours, data were collected at room temperature and from 100 °C to 800 °C with an interval of 50 °C during the heating process. Data were also collected at room temperature after the cooling process. At each temperature point, the samples were equilibrated for 10 minutes before the measurement.

3.2.2 XRD refinement

To obtain the detailed structure information, XRD refinements were conducted. Le Bail refinement is commonly used methods for the XRD refinements [143]. The Le Bail refinement focuses on refining unit cell parameters and extracting peak intensities without a model structure [144]. The structure is refined by minimising the weighted squared difference (S^2):

$$S^2 = \sum_i w_i [y_i(obs) - y_i(calc)]^2 \quad (3.6),$$

where $y_i(obs)$ and $y_i(calc)$ are the observed intensity and calculated intensity at the i^{th} observation, respectively [144]. w_i is the weight of the i^{th} observation, defined as $1/\sigma_i^2$ with σ_i representing the corresponding estimated uncertainty [145].

Although a visual inspection could be used to evaluate the quality of the refinement results [145], there are also some R factors most commonly used. The profile residual (R_p) is expressed as:

$$R_p = \sum_i [y_i(obs) - y_i(calc)] / \sum_i y_i(obs) \quad (3.7).$$

The weighted profile residual (R_{wp}) is expressed as:

$$R_{wp} = \{\sum_i w_i[y_i(obs) - y_i(calc)]^2 / \sum_i w_i[y_i(obs)]^2\}^{1/2} \quad (3.8).$$

The expected profile residual (R_{exp}) is expressed as:

$$R_{exp} = [(N - P)/\sum_i^N w_i y_i(obs)^2]^{1/2} \quad (3.9),$$

where N is the number of observations in the XRD patterns and P is the number of refined parameters. The goodness of fitting χ^2 is then defined as:

$$\chi^2 = (\frac{R_{wp}}{R_{exp}})^2 \quad (3.10).$$

It is worth noting that the value of χ^2 should not be smaller than 1 [145]. Suppose a situation where a ''true'' value for the intensity (y_T) at the i^{th} observation could be obtained. This means that if infinite measurements are conducted, the average value of $y_i(obs)$ should be $y_T \pm \sigma_i$. Therefore, for an ideal model used for refinement, the average value of $[y_i(obs) - y_i(calc)]^2$ should precisely equal to σ_i^2, which leads the numerator of R_{wp}, $\sum_i w_i[y_i(obs) - y_i(calc)]^2$, to a value of $\sum_i w_i {\sigma_i}^2$. Since w_i is defined as $1/\sigma_i^2$, the value of the numerator of R_{wp} should be equal to the numbers of the observations in the XRD patterns, which is N. Since R_{wp} and R_{exp} share the same denominator, the minimum value of χ^2 should be $[N/(N - P)]^2$. If none of the parameters are refined in one refinement ($P = 0$), this could give χ^2 a minimum value of 1, which is impossible in the realistic situations.

The XRD refinements in this work were conducted by GSAS-II software [146], where the lattice parameters were determined by the Le Bail refinement.

The theoretical densities (ρ_{theo}) of the samples were then calculated based on the results of the XRD refinements. ρ_{theo} could be calculated by equation (3.11):

$$\rho_{theo} = (N_c A)/(V_C N_A) \quad (3.11),$$

where N_c represents the number of formulae in a unit cell, which should be 4 for the samples in this work. A represents the atomic mass with a unit of g mol^{-1}. N_A is the Avogadro's number, which is 6.02 × 10^{23} mol^{-1}. V_C represents the unit cell volume with a unit of cm^3. For the monoclinic phase material, V_C could be calculated by equation (3.12):

$$V_C = abcsin\beta \quad (3.12).$$

The tetragonal phase is a simplification of monoclinic phase with $a = b$ and $\beta = 90°$. The final results should give a ρ_{theo} with a unit of g cm^{-3}.

The real densities (ρ_{exp}) of the samples were measured by Archimedes' method using a balance (CP124S, Sartorius). ρ_{exp} could be calculated by equation (3.13):

$$\rho_{exp} = 0.012 + (w_a \rho_{fl})/(0.9983G) \quad (3.13),$$

where w_a represents the mass of the sample measured in air with a unit of g. ρ_{fl} represents the density of the liquid medium used, which was water, and the value is 0.99897 g cm^{-3} at around 15.8 °C. G could be calculated by equation (3.14):

$$G = w_a - w_{fl} \quad (3.14),$$

where w_{fl} represents the mass of the sample measure in liquid medium. 0.012 is the density of air with a unit of g cm^{-3}, and 0.9983 is the correction factor for the immersion of the wires. The final results should give a ρ_{exp} with a unit of g cm^{-3}. The relative density is the ratio between ρ_{exp} and ρ_{theo}.

3.2.3 X-Ray photoelectron spectroscopy

As shown in **Figure 3.2.1**, X-ray photoelectron spectroscopy (XPS) relies on the photoelectric effect [147]. The binding energy (E_B) of each emitted electron could be determined by equation (3.15):

$$E_B = h\nu - (E_k + \Phi) \quad (3.15),$$

where $h\nu$ represents the energy of the incident X-rays, $E_k$represents the measured kinetic energy of each emitted electron, and Φ is the work function of the sample. However, in fact, something different is measured, as the work function of the spectrometer (Φ_{SP}) and the work function of the sample (Φ_{SA}) are not always the same (**Figure 3.2.5**). Therefore, the kinetic energy of the emitted electrons of the samples (E_k^{SA}) should be either increased (Φ_{SP}<Φ_{SA}) or decreased (Φ_{SP}>Φ_{SA}) to the kinetic energy of the emitted electrons of the spectrometer (E_k^{SP}). However, the samples are connected to the spectrometer, which means that the Fermi levels of them are the same and the value of Φ_{SP} is known. Therefore, the value of E_B could still be determined by equation (3.16):

$$E_B = h\nu - (E_k^{SP} + \Phi_{SP}) \quad (3.16).$$

Since the value of E_B is affected by the valence electrons and the bonding environments of the atom and only the photoelectrons from the surface of the sample could escape, XPS could be used to determine the near surface information of the samples.

XPS measurements were conducted using an X-ray photoelectron spectrometer (K-Alpha XPS, Thermo Fisher Scientific) under a high vacuum environment (< 5×10^{-7} mbar). A monochromatic aluminium K_α (1486.6 eV) X-ray source was used for recording with the spot size of 400 μm^2. To compensate the charge accumulation, a dual beam gun (Ar ions and electrons) was used during the measurements. The binding energies were calibrated with according to the C 1*s* peak position of 284.8 eV. The results were analysed using a software package (Avantage, Thermo Fisher Scientific).

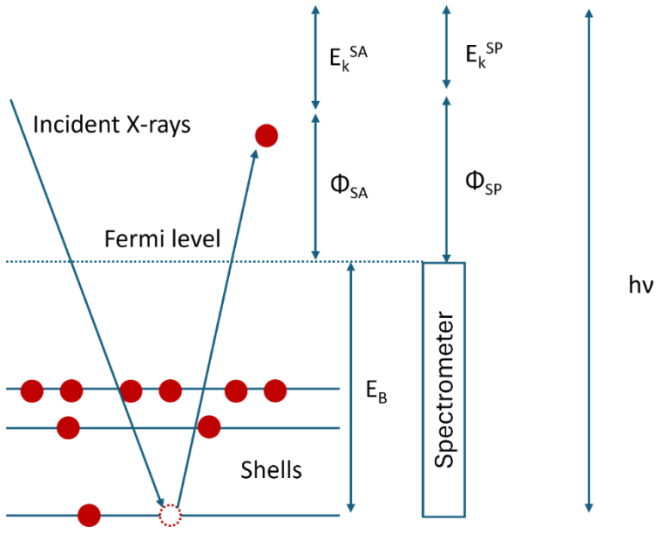


Figure 3.2.5. Schematic representations of the energy levels of the samples and the spectrometer in the XPS measurements.

3.2.4 X-Ray absorption spectroscopy

As shown in **Figure 3.2.1**, the incident X-rays could also be absorbed by the samples and the absorption of the X-rays is expressed as:

$$I_t = I_0 \exp(-\mu x) \qquad (3.17),$$

where I_0 and I_t represent the intensities of the incident and transmitted X-rays, respectively, μ is the linear absorption coefficient and x is the thickness of the sample.

The linear absorption coefficient μ is energy dependent and possesses certain discontinuities in its values. The energies, where the discontinuities appear, are called the

absorption edges. For example, if the X-rays with certain energy could eject one of the 1*s* electrons to escape into the continuum, this energy is called the K-edge of that atom. **Figure 3.2.6** a) shows the transitions of electrons from different core levels and their corresponding edges. **Figure 3.2.7** shows a schematic relationship between μ and the energy of incident X-rays in one spectrum of X-ray absorption spectroscopy (XAS). Three regions marked with different colours could be observed. The region, where μ increases dramatically, is the edge mentioned above.

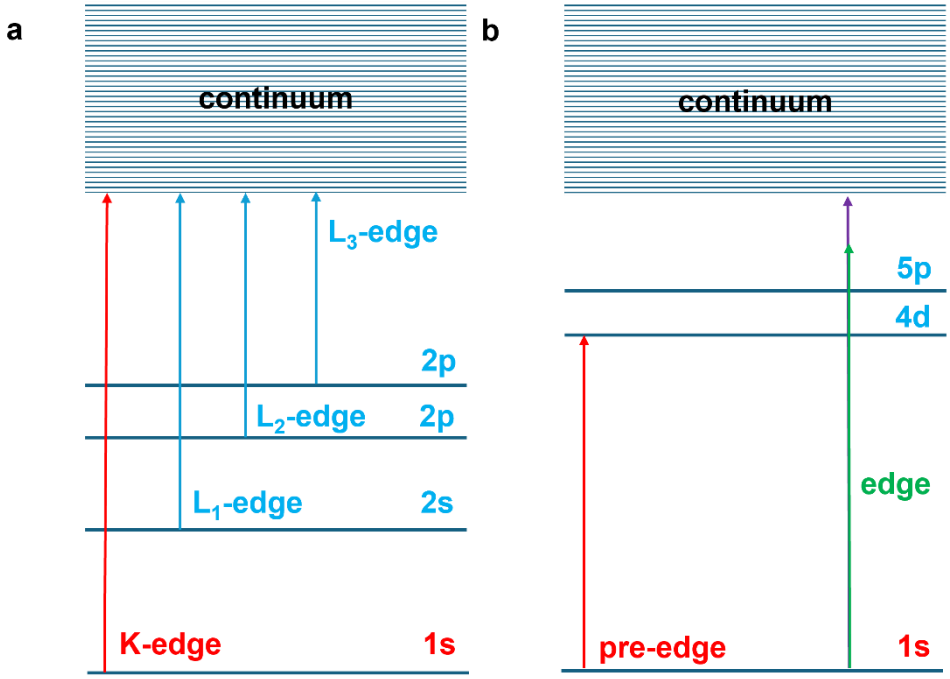


Figure 3.2.6. a) transitions of core electrons and their corresponding edges and b) energy diagram showing the origin of different regions in an XAS spectrum.

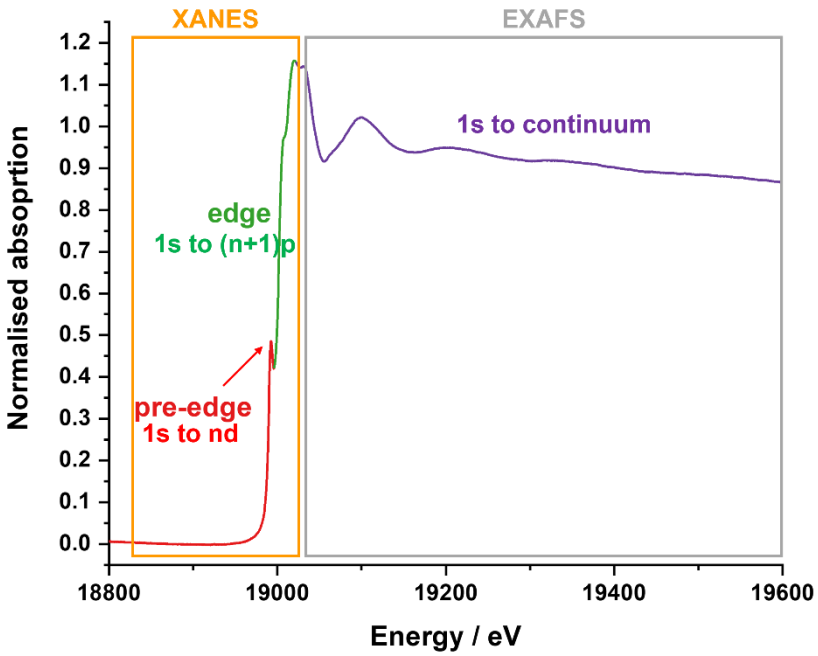


Figure 3.2.7. XAS spectrum showing regions of X-ray absorption near edge structure (XANES) and extended X-ray absorption fine structure (EXAFS). The letter ''n'' represents the principal quantum number.

However, for some elements, a small feature called the pre-edge appearing before the edge exist. This is due to the transition of the electrons from 1*s* to empty orbitals. For example, for Nb, this could arise from the 1s to 4*d* transition (**Figure 3.2.6** b) [148]. After the edge, there are always some oscillations observed in the spectrum, which originates from the ejected electrons scattered by the neighbouring atoms [148]. The regions, which include both the pre-edge and the edge, are called X-ray absorption near edge structure (XANES). This region is about 10 eV below the edge and 20 eV above the edge. The region, which includes the oscillations mentioned above, is called extended X-ray absorption fine structure (EXAFS). This region could extend to a few hundred eV beyond the edge. Since more energy is required to eject one core electron from the atom with higher effective charge, the edge position of the same elements with different oxidation states could be different [148]. Therefore, XANES could be used for the study of the oxidation states and EXAFS is used to determine the local structure [148].

The determination of the oxidation states of specific elements from XANES is quite straightforward as an increase in the oxidation state typically leads to a linear shift in the edge position of the atoms with similar ligand environments [148]. However, the analysis of EXAFS is more complicated. EXAFS is mainly about the oscillatory region after the edge, which arises from the scattering of the ejected electrons with other atoms; therefore, the concept of waves could be introduced:

$$k = \frac{1}{\hbar}\sqrt{2m_e(E - E_0)} \quad (3.18),$$

where k is the wavenumber of the scattered electrons, $\hbar$ is the reduced Planck's constant, m_e is the mass of the electron, E is the energy of the incident X-rays and E_0 is the edge position. Therefore, when the XAS measurement is conducted in the energy range, it could also be regarded as being conducted in the k space.

However, the scattering of the electrons could be modulated by a factor χ and χ could also be affected by several other factors. The expression of χ in k space is defined by equation (3.19), which is also known as the EXAFS equation:

$$\chi(k) = S_0^2 \sum_i N_i \frac{f_i(k)}{kD_i^2} e^{-\frac{2D_i}{\lambda(k)}} e^{-2k^2\sigma_i^2} \sin(2kD_i + \delta_i(k)) \quad (3.19),$$

where S_0^2 represents the amplitude reduction factor, which is an element dependent constant; i represents the different scatterings, N represents the coordination number or degeneracy for single and multiple scatterings, respectively; $f(k)$ is a term including the effects of inelastic scattering and geometrical factors, etc., D is the distance from the absorbing atom and the scattering atom, $\lambda(k)$ represents the mean free path of the electrons, σ represents the mean square radial displacement and $\delta(k)$ represents the phase shifts [149].

The oscillatory region in the XAS spectrum is defined as $\chi(E)$ and is converted to $\chi(k)$ by using equation (3.18). Since the $e^{-2k^2\sigma_i^2}$ factor in equation (3.19) always leads to small amplitude of $\chi(k)$ with increasing k, $\chi(k)$ is often multiplied by k, k^2 or k^3. Since the unit in k space is Å^{-1}, Fourier transforms are always conducted on $\chi(k)$ to get $\chi(R)$ with a unit of Å, which is referred as R space. It is worth noting that although the R space possesses a unit of Å, the Fourier transforms of $\chi(k)$ are not radial distribution functions [149].

For the *in-situ* XAS, the data were collected after the *in-situ* synchrotron XRD measurements at each temperature point. The beam energy was set between 19,840 eV and 20,800 eV and data were collected in transmission mode with a Si (111) monochromator in qexafs mode. For Nb K-edge measurements, 3 scans were conducted at each temperature point; for Mo K-edge measurements, 10 scans were conducted. Different scans were merged into one before any analysis. The results at Nb K-edge and Mo K-edge were calibrated with a Nb foil (K-edge position at 18,986 eV) and Mo foil (K-edge position at 20,000 eV), respectively. The XANES and EXAFS results were analysed with Athena and Artemis software, respectively [150]. For EXAFS, the parameters of $f(k)$, $\lambda(k)$ and $\delta(k)$ were determined by FEEF program [151] and the parameters of S_0^2, N, D, σ and the deviation of E_0 were fitted and the goodness of fitting could be evaluated by the R factor over i measured points defined by equation (3.20):

$$R = \sum_1^i (data - fit)^2 \,/\, \sum_1^i (data)^2 \qquad (3.20).$$

3.3 Other techniques

3.3.1 Thermogravimetric analysis

Thermogravimetric analysis (TGA) is a technique where the mass of a sample is determined as a function of temperature and time during a controlled temperature regime.

The mass of the sample could change during the dynamic and the isothermal temperature stage, and this mass change could be used to infer the change in oxygen stoichiometry of the sample [152]. Since the oxygen stoichiometry is related to the oxidation states of the elements in the sample, TGA could be used to study the variation of the oxidation states during oxidation and reduction processes.

The TGA results were collected by the thermogravimetric analyser (STA 449 F5, Jupiter). Powders of the samples were loaded into platinum crucibles and were heated to 900 °C with an isothermal time of 20 minutes with Al_2O_3 as reference. The heating and cooling rates were both 5 °C per minute. During TGA measurements, the gas flow rates were 50 ml per minute and 20 ml per minute for purge gas and protective gas, respectively. Compressed air (N_2 and 21% ± 0.5% O_2, BOC) and Ar (99.998%, BOC) were used as the purge gas and protective gas, respectively.

3.3.2 Scanning electron microscopy

The possible signals generated from the interaction between electrons and materials can be summarised by **Figure 3.3.1**. The signals and their corresponding characterisation methods used in this work are scanning electron microscopy (SEM), energy-dispersive X-ray analysis (EDX) and transmission electron microscopy (TEM), which are marked in red in **Figure 3.3.1.**

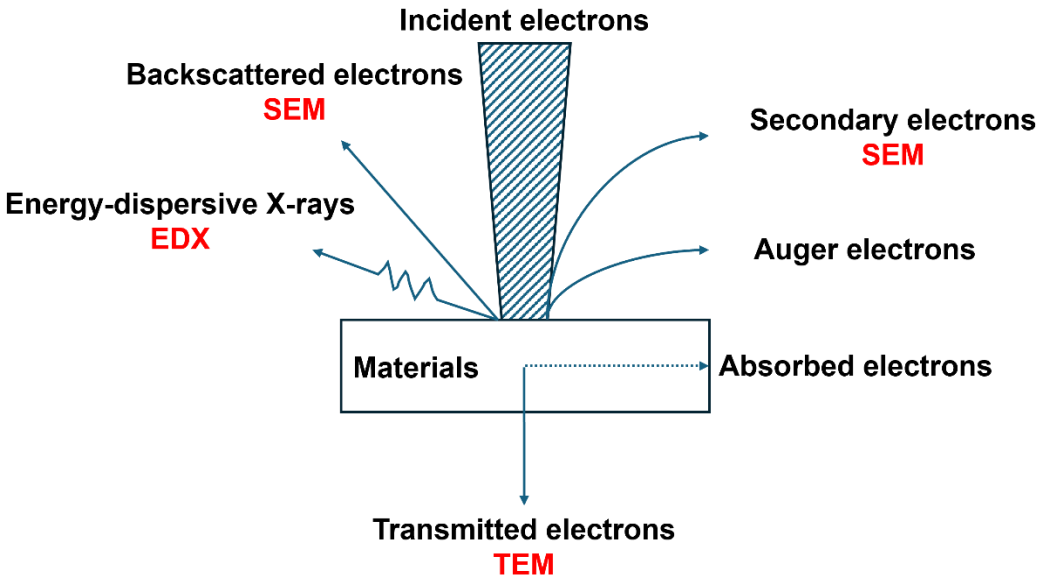


Figure 3.3.1. The signals generated from the interactions between the electrons and the materials.

Based on the Rayleigh criterion, the resolution of a microscope is proportional to the wavelength of the illuminating source [153]. Compared with the photons used in a light microscope, electrons possess much smaller wavelength. Therefore, a microscope with electrons as the illuminating source could provide higher resolution.

Scanning electron microscopy (SEM) uses a focused electron beam to scan the surface of the samples and detect different signals from the interactions between the electron beams and the samples [154]. For producing images, two signals: secondary electrons (SEs) and backscattered electrons (BSEs) are used. For the SEs, they are the electrons of the samples ejected from around 5 to 10 nm depth of the surface, which are sensitive to the roughness and porosities of the surfaces; therefore, the SEs are used to analyse the morphologies of the surfaces [154]. For the BSEs, they are the electrons elastically scattered by the atomic nucleus of the samples. The amount of the BSEs increases with increasing the atomic number of the

atoms; therefore, the BSEs could be used to not only analyse the morphologies but also yield the atomic number contrast images [154]. Typically, a scanning electron microscope is equipped with an energy-dispersive X-ray analysis (EDX) detector for chemical composition analysis. When one electron from an inner shell of the atom is ejected, another electron located at outer shells could fill the vacancy left by the ejected electron and the energies are emitted by X-rays. Since the energies between different shells are different for different elements, these X-rays are called characteristic X-rays and could be used to study the chemical information.

The SEM and BSE images of the samples were collected with a scanning electron microscope (LEO-1525, Zeiss). The EDX data were collected by the EDX detector (Ultim Max, Oxford Instruments) equipped on another scanning electron microscope (Auriga, Zeiss). To measure the particle size of the samples based on the SEM images, at least 100 particles were measured by ImageJ software [155] with the Feret diameter [156]. For some SEM images which did not include 100 particles, all particles were measured. Log-normal distribution was used to fit the distribution of the particle sizes [157]. The mean particle size and the standard error of the mean particle size are expressed as $\exp(\mu + \frac{\sigma*^2}{2})$ and $\sqrt{\frac{[\exp(\sigma*^2)-1]\exp(2\mu+\sigma*^2)}{n}}$ for the log-normal distribution; respectively. The parameters μ, $\sigma*$ and n represent the expected value, standard deviation and sample size of the log-normal distribution; respectively. For EDX, five spectra were recorded for each sample and the average values were calculated.

3.3.3 Transmission electron microscopy

Transmission electron microscopy (TEM) was used in this work to index the modulated structures by selected area electron diffraction (SAED) patterns. As mentioned in Section 2.5.3, because of the existence of the modulated structure, the translational symmetry is broken in the original lattice but preserved in the superlattice. The concept of the superlattice is an approach where the vectors $\boldsymbol{a_1^*}$, $\boldsymbol{a_2^*}$, $\boldsymbol{a_3^*}$, and $\boldsymbol{q}$ are treated as the projections of a four-dimensional space (with $\boldsymbol{a_{s1}^*}$, $\boldsymbol{a_{s2}^*}$, $\boldsymbol{a_{s3}^*}$ and $\boldsymbol{a_{s4}^*}$ as basic vectors in a reciprocal lattice) in three-dimensional space [128]. To better understand the fourth vector $\boldsymbol{a_{s4}^*}$, another coordinate axis, $\boldsymbol{b}$, is introduced with a reciprocal vector of $\boldsymbol{b}^*$, which is perpendicular to the real space. Therefore, the reciprocal lattice in *super space* could be defined by equation (3.21):

$$\begin{cases} \boldsymbol{a}_{\boldsymbol{si}}^{*} = (\boldsymbol{a}_{\boldsymbol{i}}^{*}, 0), i = 1, 2, 3 \\ \boldsymbol{a}_{\boldsymbol{s4}}^{*} = (\boldsymbol{q}, \boldsymbol{b}^{*}) \end{cases} \quad (3.21).$$

The relationship between real space and reciprocal space is given by equation (3.22):

$$\boldsymbol{a}_{\boldsymbol{si}}^{*} \cdot \boldsymbol{a}_{\boldsymbol{j}} = \delta \quad (3.22),$$

where δ = 1 for i = j and otherwise 0. Therefore, the corresponding real space could be defined by equation (3.23):

$$\begin{cases} \boldsymbol{a}_{\boldsymbol{si}} = (\boldsymbol{a}_{\boldsymbol{i}}, -\sigma_i \boldsymbol{b}), i = 1, 2, 3 \\ \boldsymbol{a}_{\boldsymbol{s4}} = (0, \boldsymbol{b}) \end{cases} \quad (3.23).$$

The super space, where the superlattice locates, at a point atom is obtained by rotating the *modulated wave* over 90° [128]. **Figure 3.3.2** shows the super space of the lattice shown in **Figure 2.5.3** c) in Chapter 2. As defined above, the coordinate axis, $\boldsymbol{b}$, is perpendicular to the real space, the string of the modulated wave precisely lies on the direction of $\boldsymbol{b}$. If the modulated waves at each point atom are rotated, the grid lines could be observed, which highlights the translational symmetry in the superlattice.

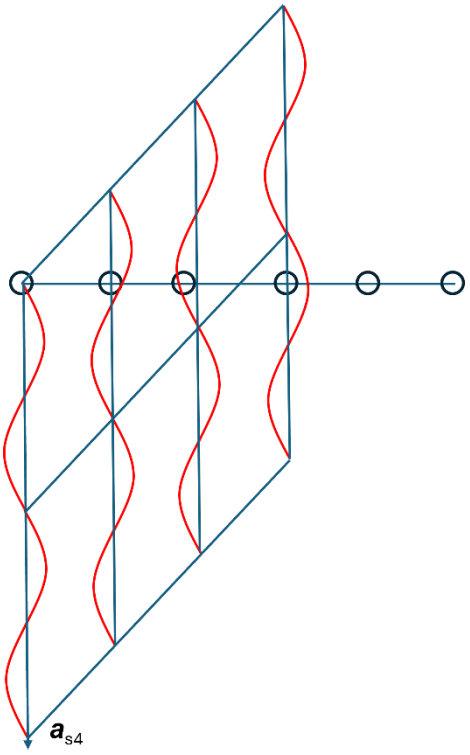


Figure 3.3.2. Schematic representation of the super space by rotating the modulation waves at each point atom. The grid lines highlight the translational symmetry in the superlattice.

In TEM, electrons are used to generate diffraction patterns based on their wave-particle duality. The wavelengths (λ) of electrons can be expressed by equation (3.24):

$$\lambda = h/\sqrt{2meV} \quad (3.24),$$

where h is the Planck's constant, m is the relativistic mass of the electron, e is the charge of an electron and V is the accelerating voltage. The wavelength of electrons accelerated at 200 kV is around 2.5 pm, which is two orders of magnitude smaller than the size of an atom. Therefore, electrons could be diffracted by the atoms in a crystal.

The SAED patterns of the modulated structures of the as-prepared sample were collected by the transmission electron microscope (JEM-2100Plus, JEOL) operated at 200 kV. Powders of the as-sintered $LaNb_{0.9}Mo_{0.1}O_{4.05}$ was first homogenously dispersed in isopropanol by an ultrasonic cleaner (USC 200 T, VWR) and then the suspension was dropped on the copper grid before measurements.

3.3.4 Electrochemical impedance spectroscopy

Electrochemical impedance spectroscopy (EIS) is used to measure the electrical properties of the electroceramics over a wide range of the frequencies (ω), where the different components of the samples could be characterised based on their relaxation times (τ). Different components of the samples are characterised by a resistance (R) and a capacitance (C), which are placed in parallel [158]. For each parallel connected ''RC'' element, the relationships among τ, R and C are expressed as:

$$\tau = RC \quad (3.25).$$

A typical impedance spectrum for electroceramics consists of three different components attributing to bulk, grain boundary and sample-electrode interface. Based on the brick layer model, an electroceramic material could be regarded as individual grains separated by grain boundaries. Therefore, as shown in **Figure 3.3.3**, the overall impedance spectrum of an electroceramic material could be simplified as three series connected RC elements. The impedance data are presented as the imaginary part of impedance (Z'') against the real part of the impedance (Z') and each RC element would give a contribution of a semicircle in an ideal situation. The values of R are determined by the intersects on the Z' axis; and the values of C are determined by applying equation (3.25) to equation (3.26):

$$\tau = 1/\omega_{max} \quad (3.26),$$

where ω_{max} represents the frequency at the maximum of each semicircle. Therefore, once the values for R and C are obtained, the distinct components could be assigned based on their characteristic capacitance values [158], which are summarised in **Table 3.1**.

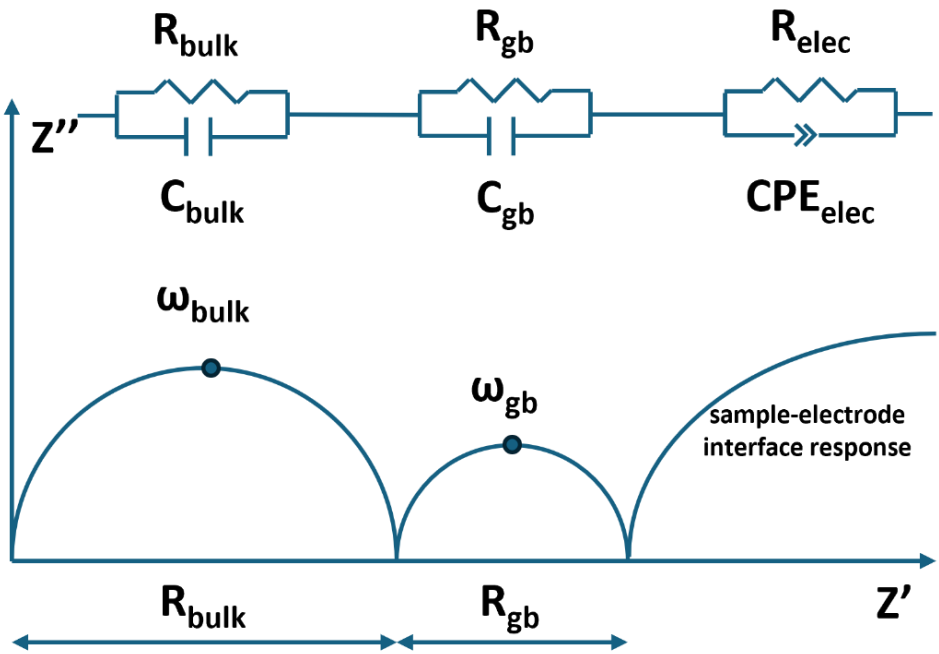


Figure 3.3.3. Schematic representation of a typical spectrum of an electroceramic material. The notation ''gb'' and ''elec'' represent the grain boundary and sample-electrode interface, respectively. The ''CPE'' represents the constant phase element.

However, an ideal C or a perfect semicircle is not often observed in reality; therefore, the constant phase element (CPE) is used instead, as shown for the response from sample-electrode interface in **Figure 3.3.3** as an example. The impedance (Z) of a CPE is defined as:

$$Z = \frac{1}{Q_0(i\omega)^n} \quad (3.27),$$

where Q_0 is a pseudo-capacitance, i is the imaginary unit. The exponent n takes a value between 0 and 1. If $n = 1$, the CPE is identical to a real capacitor; if $n = 0$, the CPE is identical to a real resistor. The real capacitance of a CPE is expressed as:

$$C = (R^{1-n}Q_0)^{1/n} \quad (3.28).$$

Table 3.1. Characteristic capacitance values and their corresponding interpretations.

Capacitance (F)	Electrochemical components
10^{-12}	Bulk
10^{-11} – 10^{-8}	Grain boundary
10^{-9} – 10^{-7}	Surface layer
10^{-7} – 10^{-5}	Sample-electrode interface

For the EIS measurements, the as-sintered pellets were painted with gold paste on both sides. The pellets were then heated to 900 °C for 1 hour under static air to remove the organic residues and achieve good connection between the gold layers and the surfaces. For the pellets studied in Chapter 6, the pellets with gold paste were dried under the corresponding atmospheres where they were annealed. The impedance data were collected over a temperature range from 500 °C to 900 °C in a tube furnace (MTF 12/38/400, Carbolite Gero) under compressed air (N_2 and 21% ± 0.5% O_2, BOC) using a frequency response analyser (1260A, AMETEK). For the EIS measurements reported in Chapter 6, the data were collected under the corresponding atmospheres where the pellets were annealed. The humified and dried conditions were realised by pumping the gas through a water bubbler (pH_2O = 0.025 atm) and a gas drying column (26800, Drierite, pH_2O = 10^{-5} atm) at room temperature, respectively. The AC potential was set at 50 mV and the frequency range was set from 1 MHz to 500 mHz. The impedance data were fitted using the ZView package (v4.0b, Scribner).

3.3.5 Ultraviolet–visible spectroscopy

The band gap energy of a semiconductor represents the minimum energy required to excite one electron from the valence band to the conduction band, which relates to the photophysical and photochemical properties of semiconductors [159]. Tauc *et al* proposed a method for approximating the band gap energy of semiconductors through analysis of the optical absorption spectra [160]. In the Tauc method, the energy-dependent absorption coefficient α could be expressed as:

$$(\alpha \cdot h\nu)^{1/\gamma} = B(h\nu - E_g) \quad (3.29),$$

where h is the Planck's constant, ν is the frequency of the photon. The factor γ equals to 1/2 or 2 for direct and indirect band gaps, respectively. B is a constant and E_g represents the band gap energy.

A diffuse reflectance spectrum could be transformed to the corresponding absorption spectrum based on Kubelka-Munk function:

$$F(R_\infty) = \frac{(1-R_\infty)^2}{2R_\infty} \quad (3.30),$$

where $R_\infty = R_{sample}/R_{standard}$. R_{sample} and $R_{standard}$ represent the reflectance of the sample and standard, respectively [161]. By using $F(R_\infty)$ as an approximation of α [159], equation (3.29) could be rewritten as:

$$(F(R_\infty) \cdot h\nu)^{1/\gamma} = B(h\nu - E_g) \quad (3.31).$$

In the Tauc plot, $(F(R_\infty) \cdot h\nu)^{1/\gamma}$ is plotted against $h\nu$. The region, where a linear increase in $(F(R_\infty) \cdot h\nu)^{1/\gamma}$ with increasing energy could be observed, is characteristic of semiconductor materials [159]. The x-axis intersection of the linear fitting of that region gives an approximate value of the band gap energy.

The absorption spectra of the pellets annealed under different atmospheres discussed in Chapter 6 were measured using a UV-Vis spectrophotometer and corresponding software (Cary 5000/Cary WinUV, Agilent) with the diffuse reflectance sphere accessory. The spectra were recorded from 200 nm to 800 nm in %R mode. The polytetrafluoroethylene disk was used to record the baseline. The step size and time per step were set to 0.1 nm and 0.1 s, respectively. The light source changeover happened at 350 nm.

3.3.6 Electron paramagnetic resonance spectroscopy

Each electron has a unique spin state, represented as +1/2 (upper state) or -1/2 (lower state), which is called the spin magnetic quantum number (m_s). In the presence of a magnetic field with strength of B, each state has a specific energy E expressed as:

$$E = m_s g_e \mu_B B \quad (3.32),$$

where g_e and μ_B are two constants representing the g-factor for the free electron and Bohr magneton, respectively. Therefore, the energy difference (ΔE) between the upper and lower states of each electron is expressed as:

$$\Delta E = g_e \mu_B B \quad (3.33).$$

According to Planck's law, this also means that for an unpaired electron, it could change the electron spin state by absorbing or emitting a photon with an energy of $h\nu$, if the resonance condition, $\Delta E = h\nu$, is obeyed. Here h is Planck's constant and ν is the frequency of the radiation. This is the basis of electron paramagnetic resonance spectroscopy (EPR). However, when electrons are at specific environments, the g-factor of them should be different from that of the free electron. Therefore, equation (3.33) should be revised as:

$$\Delta E = h\nu = (g_e + \Delta g)\mu_B B \quad (3.34),$$

where Δg represents the difference between the g-factors of the free electron and electrons at specific environments. In an EPR measurement, ν is always held constantly and B is changed to obtain the spectrum. Once the value of B matches the condition described by equation (3.34), the radiation will be absorbed and lead to a peak in the absorption spectrum. The result of EPR measurement is then present as the first derivative of the absorption spectrum. Since for Mo^{6+}, there are no electrons at the 4*d* orbital; therefore, there is no net magnetic moments to interact with the external magnetic fields. However, for Mo^{5+}, the unpaired electron at the 4*d* orbital could lead resonance peaks in the EPR spectrum. It is worth noting that EPR was only used to qualitatively determine the presence of Mo^{5+} and the quantification of g-factors is beyond the aim of this work.

The EPR data were collected by the EPR spectrometer (Magnettech ESR5000, Bruker). The measurements were conducted with X-band (around 9.8 GHz) at room temperature.

In this chapter the process of the synthesis and characterisation techniques have been discussed. The details about the data analysis have also been provided. In the following chapters, the results of this thesis obtained from the characterisation techniques mentioned above are discussed in detail.

Chapter 4. Investigation of crystal structure and electrochemical performance of Gd substituted $LaNb_{0.9}Mo_{0.1}O_{4.05}$

In this chapter, the conventional SSR method was used to synthesise single-phase $La_{1-x}Gd_xNb_{0.9}Mo_{0.1}O_{4.05}$ (where x = 0.00, 0.20, 0.40, 0.50, 0.60, 0.80 and 1.00). HT-XRD was used to examine the crystal structures of all samples. It was observed that both $LaNb_{0.9}Mo_{0.1}O_{4.05}$ and $La_{0.8}Gd_{0.2}Nb_{0.9}Mo_{0.1}O_{4.05}$ possessed modulated structures at room temperature. The modulated structure of $LaNb_{0.9}Mo_{0.1}O_{4.05}$ was indexed by SAED patterns for the first time. The electrochemical performance of all samples was assessed using EIS. $LaNb_{0.9}Mo_{0.1}O_{4.05}$ exhibited the highest total conductivity of 1.52×10^{-2} S cm^{-1} at 900 °C under dry air. However, in the intermediate temperature range, the total conductivity of $La_{0.8}Gd_{0.2}Nb_{0.9}Mo_{0.1}O_{4.05}$ surpassed that of $LaNb_{0.9}Mo_{0.1}O_{4.05}$. This difference in total conductivity could be attributed to the possibly negative effects of the modulated structures on the electrochemical performance.

4.1 Introduction

As mentioned in Section 2.5.3, both W^{6+} and Mo^{6+} substituents could introduce extrinsic oxygen interstitials and modulated structures in the system of $LaNbO_4$ [12][11]. However, the modulated structures were found to be absent in other W-substituted $ReNbO_4$ compositions [11][162][163]. Kawaguchi *et al* reported that the conductivity of $GdNbO_4$ was improved by the substitution of W and there was no modulated structures in this type of material [162]. Similar results were also found in W-substituted $PrNbO_4$ and $NdNbO_4$ by Li *et al* [11]. As Pr, Nd and Gd all possess a smaller ionic radii compared with La [76], the existence of the modulated structures could be related to the cell volumes. Li *et al* found that among $LaNb_{0.92}W_{0.08}O_{4.04}$, $PrNb_{0.92}W_{0.08}O_{4.04}$ and $NdNb_{0.92}W_{0.08}O_{4.04}$, $LaNb_{0.92}W_{0.08}O_{4.04}$ exhibited the highest activation energy of oxygen ion conduction in low temperature range, which could result from the modulated structures in this material [11]. Auckett *et al* also found that there was an activation energy decrease of $LaNb_{0.84}Mo_{0.16}O_{4.08}$ around 800 °C, and this temperature also marked the approximate temperature of the disappearance of the modulated structures of $LaNb_{0.84}Mo_{0.16}O_{4.08}$ [12]. Therefore, the modulated structures may have negative effects on

the electrochemical performance. As shown in **Figure 4.1.1**, the modulated structures introduced by Mo substituents in $LaNbO_4$ were identified by the satellite reflections in the XRD patterns [12][16]; however, the indexing of these modulated structures remained unclear as there was no study of the SAED patterns of them, and understanding their effects on the electrochemical performance was also essential.

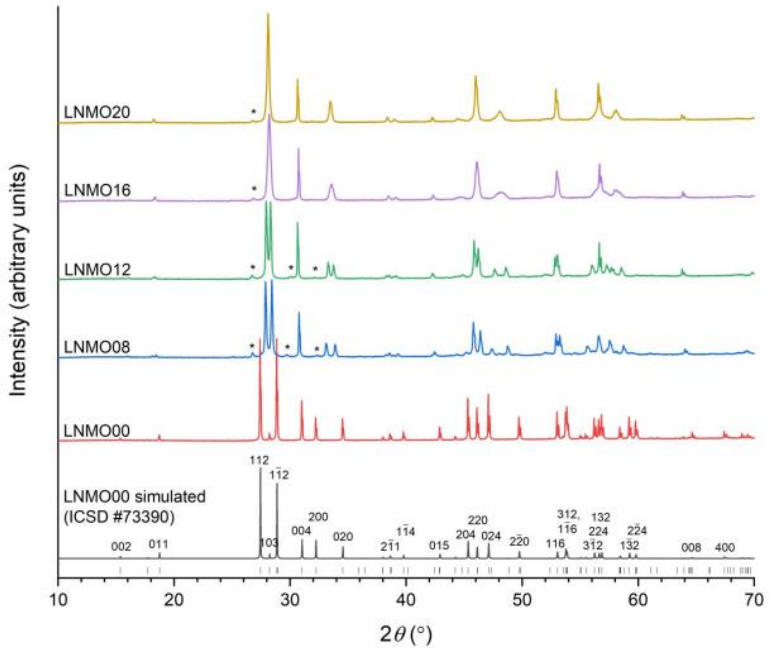


Figure 4.1.1. XRD patterns of $LaNb_{1-x}Mo_xO_{4+0.5x}$ (LNMO). The numbers denoted after LNMO are 100 times of the value of x. The satellite reflections from the modulated structures are marked by asterisks. Reproduced with permission [12]. Copyright (2021), Royal Society of Chemistry.

The aim of this chapter was to investigate the effects of the modulated structures of Mo-substituted $LaNbO_4$ by substituting dopants on the La sites. As mentioned above, the modulated structures could be eliminated by substituting lanthanides with smaller ionic radii on La sites [11]. However, lanthanides like Pr, Nd, or Sm, that possess multiple oxidation states, were not suitable for electrolyte materials due to the potential introduction of electronic conductivity. Therefore, Gd, which possesses a fixed oxidation state of Gd^{3+}, was opted to substitute on La sites to adjust the properties of $LaNb_{0.9}Mo_{0.1}O_{4.05}$. By using a substituent with a fixed oxidation state, the risk of introducing electronic conductivity could be minimised. The introduction of Gd on La sites was expected to have two potential structural effects: firstly, it may increase the transition temperature of $LaNb_{0.9}Mo_{0.1}O_{4.05}$; also, it may influence the

modulated structures, as previously reported [11]. Since the electrochemical performance is closely related to the structures of the material, Gd substitution could also influence the electrochemical performance. To investigate the effects of substituting cations on both structural and electrochemical properties, a combination of HT-XRD and EIS was used in this chapter, and samples of $La_{1-x}Gd_xNb_{0.9}Mo_{0.1}O_{4.05}$ with x = 0.00, 0.20, 0.40, 0.50, 0.60, 0.80 and 1.00, were denoted as LNM10, La8Gd2, La6Gd4, La5Gd5, La4Gd6, La2Gd8 and GNM10, respectively thereafter.

4.2 Structural and chemical study

As shown in **Figure 4.2.1**, all samples were found to be single-phase materials with monoclinic Fergusonite structures at room temperature. It is noticed that the second main peak became gradually asymmetric with increasing Gd fraction on the La sites. As shown in **Figure 4.2.1**, except for LNM10 and La8Gd2, there was always a small shoulder on the left side of the second main peaks. This was due to the different degrees of monoclinic distortion that these types of materials possessed at the different stages during the transition from m-phase to t-phase, as illustrated in **Figure 4.2.2**. As shown in **Figure 4.2.2** a), for a pure m-$LaNbO_4$, there were three peaks at around 27.4°, 28.2°, and 28.8° 2θ, which were related to lattice plane $(12\bar{1})$, (130) and (121), respectively. With increasing temperature, not only the peaks from $(12\bar{1})$ and (121) moved closer together, but also the 2θ difference between the peaks from (130) and (121) became smaller, and there could be a situation that these two peaks were not quite distinguished as shown in **Figure 4.2.2** b), where a small shoulder appeared on the left side of the peak from (121). As temperature further increased, the peak from (130) moved to the right side of the peak from (121). Since the relative intensity of the peak from (130) was much smaller than that from (121), there seemed to be only one peak at around 28.1° 2θ shown in **Figure 4.2.2** c). If the material totally transitioned from m-phase to t-phase, there would be only one peak representing the lattice plane (112) at around 27.9° 2θ, as the peaks from $(12\bar{1})$ and (121) merged into one (shown in **Figure 4.2.2** d)). Therefore, the difference of 2θ positions between the peaks from $(12\bar{1})$ and (121) could be approximately used to indicate the degree of monoclinic distortion; therefore, the symmetry level of this type of material. It was mentioned above that Mo could stabilise the t-phase down to lower temperature range [12] and the transition temperature from m-phase to

t-phase increased from La to Lu in $ReNbO_4$ [65]; therefore, with the same content of Mo substituted on Nb sites, the sample with higher La fraction on La sites should be closer to t-phase and the sample with higher Gd fraction on La sites should be closer to m-phase. Therefore, the XRD patterns of LNM10 and La8Gd2 resembled the XRD patterns of $LaNbO_4$ measured at 499 °C (**Figure 4.2.2** c)) and the others resembled the XRD patterns measured at 470 °C (**Figure 4.2.2** b)).

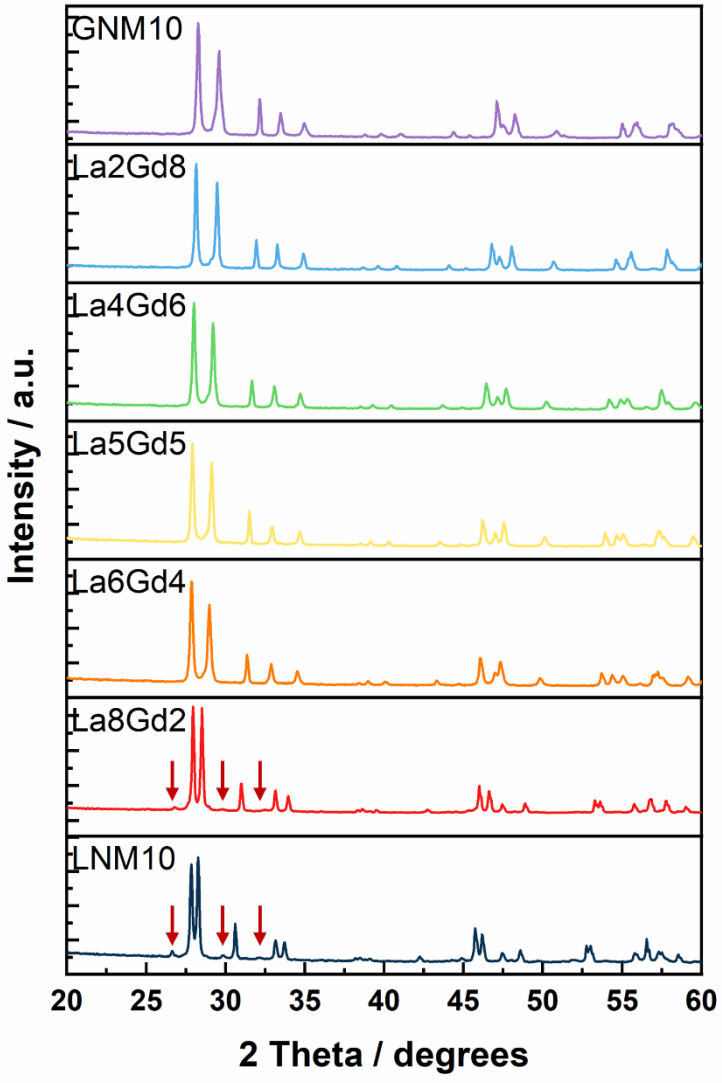


Figure 4.2.1. Room temperature XRD patterns of $La_{1-x}Gd_xNb_{0.9}Mo_{0.1}O_{4.05}$ series from 20° to 60° in 2θ. The satellite reflections of modulated structures are marked by arrows.

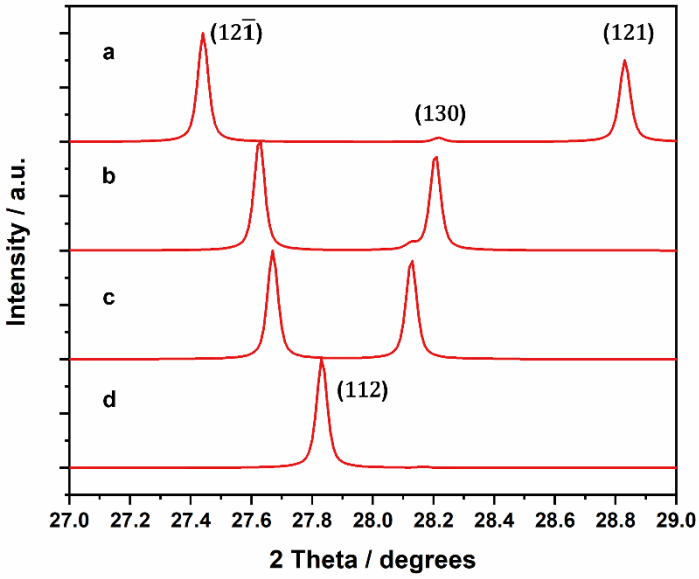


Figure 4.2.2. Simulated XRD patterns of $LaNbO_4$ at a) 20 °C, b) 470 °C, c) 499 °C and d) 716 °C, respectively. The XRD patterns were simulated with a monochromatic X Ray with a wavelength of 1.54059 Å based on the *in situ* XRD data from Sarin *et al* [13].

Le Bail refinements were conducted for all samples measured at 25 °C. **Figure 4.2.3** shows the refinement results for XRD data of La5Gd5 at 25 °C as an example. **Table A3** list the refined parameters. **Figure 4.2.4** shows the relationship between the Gd fraction on the La sites and the lattice parameters. As expected, the lattice parameters *b*, *c* and the lattice volume *V* decreased with increasing the Gd fraction on La sites, aligning with the smaller ionic radii of 8 coordinated Gd^{3+} (1.05 Å) compared to 8 coordinated La^{3+} (1.16 Å) [76]. However, the *a* lattice parameter exhibited a different behaviour, showing a slight increase when 20 mol% of Gd was substituted on La sites and peaked at a value of a = 5.4498(2) Å with 40% mol Gd substitution on La sites. Beyond this point, the *a* lattice parameter decreased with further increases in Gd fraction. Since the modulated structures were only present in LNM10 and La8Gd2 at room temperature (as shown in **Figure 4.2.1**), this unique phenomenon could be attributed to the presence of the modulated structures. Further analysis combining SAED patterns is discussed below.

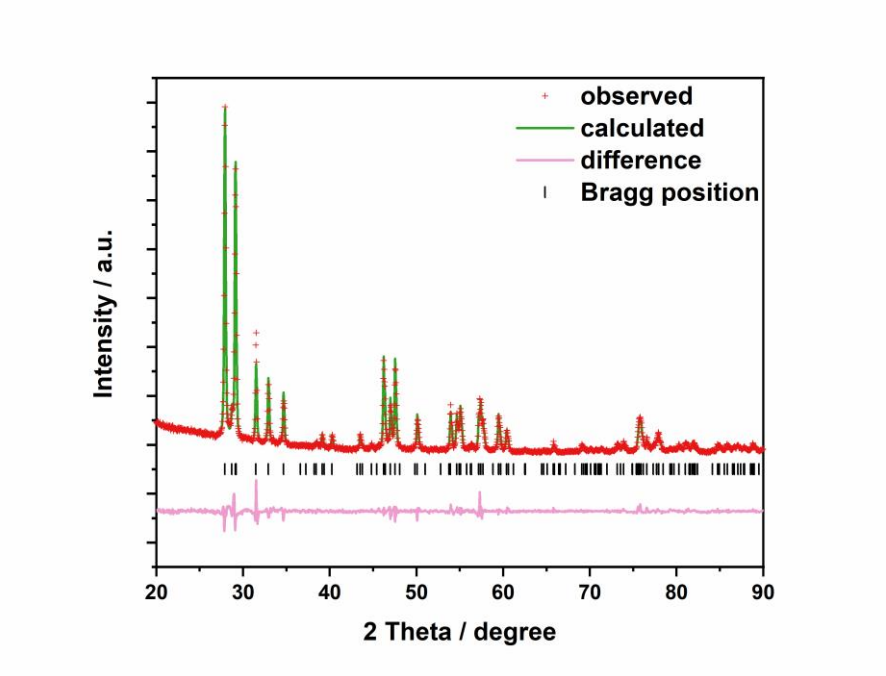


Figure 4.2.3. Le Bail refinement results for XRD data of La5Gd5 at 25 °C with R_{wp} = 3.05%, χ2 = 3.20.

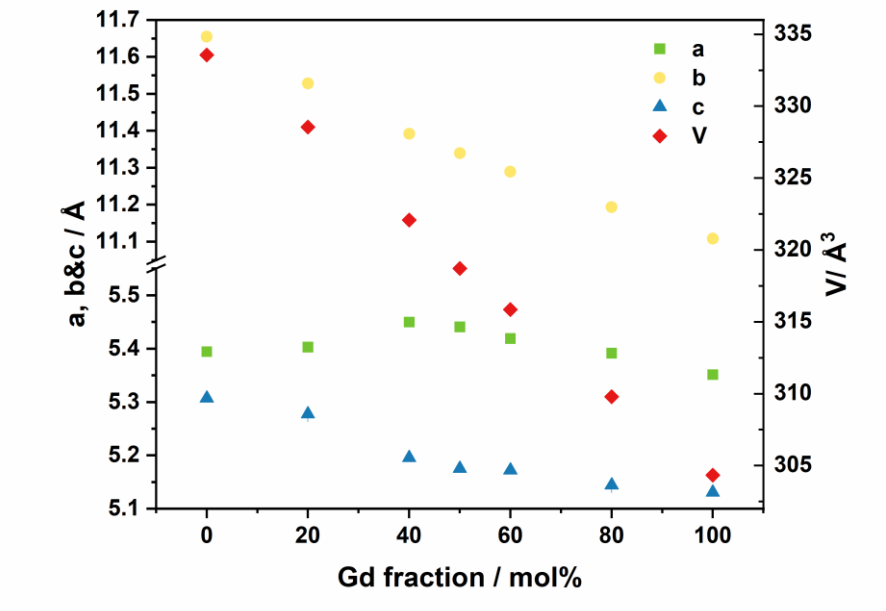


Figure 4.2.4. Lattice parameters *a*, *b*, *c*, and volume *V* of the $La_{1-x}Gd_xNb_{0.9}Mo_{0.1}O_{4.05}$ series. Error bars are smaller than symbols.

Figure 4.2.5 shows the XRD patterns of three distinct structures of LNM10 obtained at various temperatures. At room temperature, LNM10 possessed a monoclinic Fergusonite

structure, with satellite reflections from modulated structures evident in the XRD patterns, consistent with the previous findings of a similar W-substituted $LaNbO_4$ system [11]. As suggested by Li *et al*, these modulated structures arose from the modulated waves generated by the distortion of Nb sites because of the introduction of the substituents [130]. As the temperature increased to the intermediate range (around 300 °C), the XRD patterns showed a distinct transition from the lower-symmetry monoclinic Fergusonite structure to the higher-symmetry tetragonal Scheelite structure with the existence of the modulated structures, as shown in **Figure A1**. **Figure 4.2.5** shows the XRD patterns of LNM10 recorded at 500 °C as an example of modulated tetragonal Scheelite structure. When the temperature was further increased above 750 °C, the modulated structures disappeared (shown in **Figure 4.2.6**). The XRD patterns of LNM10 recorded at 900 °C was shown as an example of unmodulated tetragonal Scheelite structure in **Figure 4.2.5**.

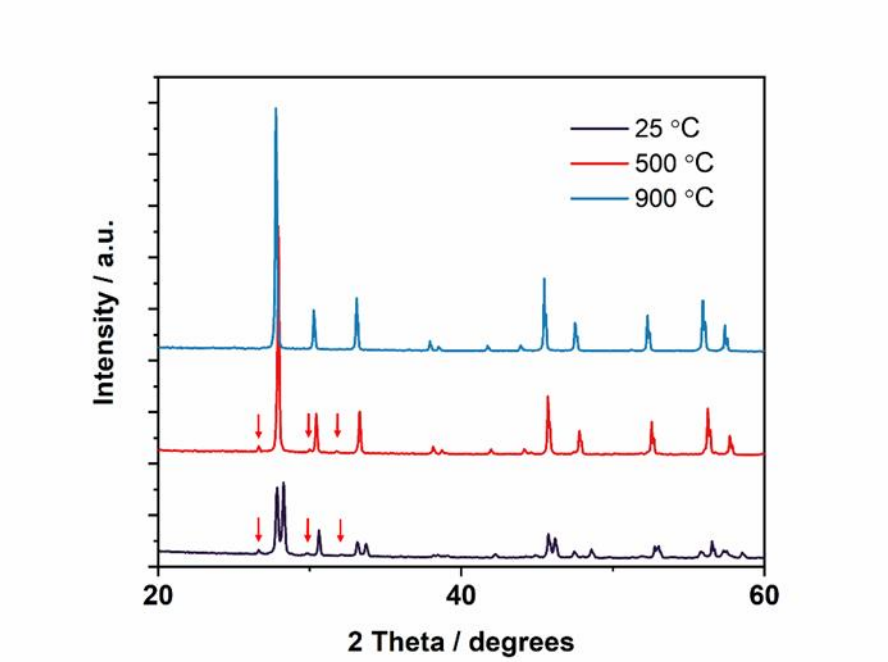


Figure 4.2.5. XRD patterns of LNM10 recorded at 25 °C, 500 °C and 900 °C, respectively. 2θ range is selected from 20° to 60°to highlight the structure change from a modulated m-phase to a modulated t-phase then to an unmodulated t-phase. The satellite reflections from the modulated structures are marked by arrows. Reproduced with permission [14]. Copyright (2023), Royal Society of Chemistry.

Figure 4.2.6 shows the XRD patterns around the temperature where the modulated structures disappeared in LNM10. This agreed well with the results of Li *et al* and Auckett *et*

al, as the modulated structures also disappeared at around 650 °C and 800°C in $LaNb_{0.88}W_{0.12}O_{4.06}$ and $LaNb_{0.88}Mo_{0.12}O_{4.06}$, respectively [12][135]. Additionally, the modulated structures were demonstrated by SAED patterns, as shown in **Figure 4.2.7** along the [010] zone axis. These SAED patterns resembled those reported for W-substituted $LaNbO_4$, featuring several satellite reflections around the main reflections [11]. As shown in **Figure 4.2.7**, there were two different modulated vectors ($\boldsymbol{q_1}$ and $\boldsymbol{q_2}$) used to index the satellite reflections; therefore, it was suggested these modulated structures were 2D incommensurate. The modulated vectors were determined to be $\boldsymbol{q_1} = 0.159\boldsymbol{a}^* + 0.418\boldsymbol{c}^*$ and $\boldsymbol{q_2} = 0.452\boldsymbol{a}^* + 0.186\boldsymbol{c}^*$, respectively. Notably, the modulated structures were observed along the [010] zone axis, indicating that the modulated waves propagated along the *ac* plane. Consequently, there were displacements of the atoms in the *ac* plane, which potentially contributed to the observed abnormal trend of the *a* lattice parameter as shown in **Figure 4.2.4**.

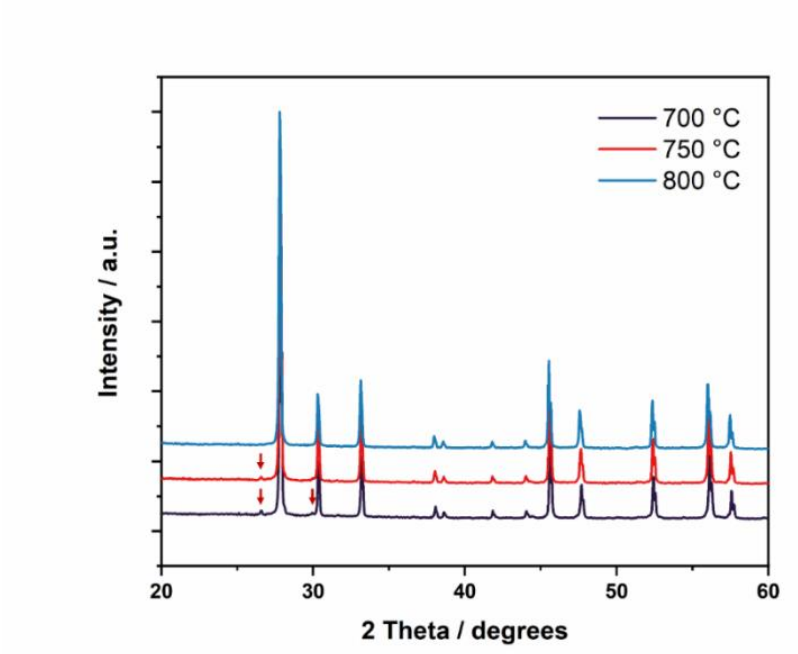


Figure 4.2.6. XRD patterns of LNM10 recorded at 700 °C, 750 °C and 800 °C, respectively. 2θ range is selected from 20° to 60°to highlight the structure change from a modulated structure to an unmodulated structure. The satellite reflections from the modulated structures are marked by arrows. Reproduced with permission [14]. Copyright (2023), Royal Society of Chemistry.

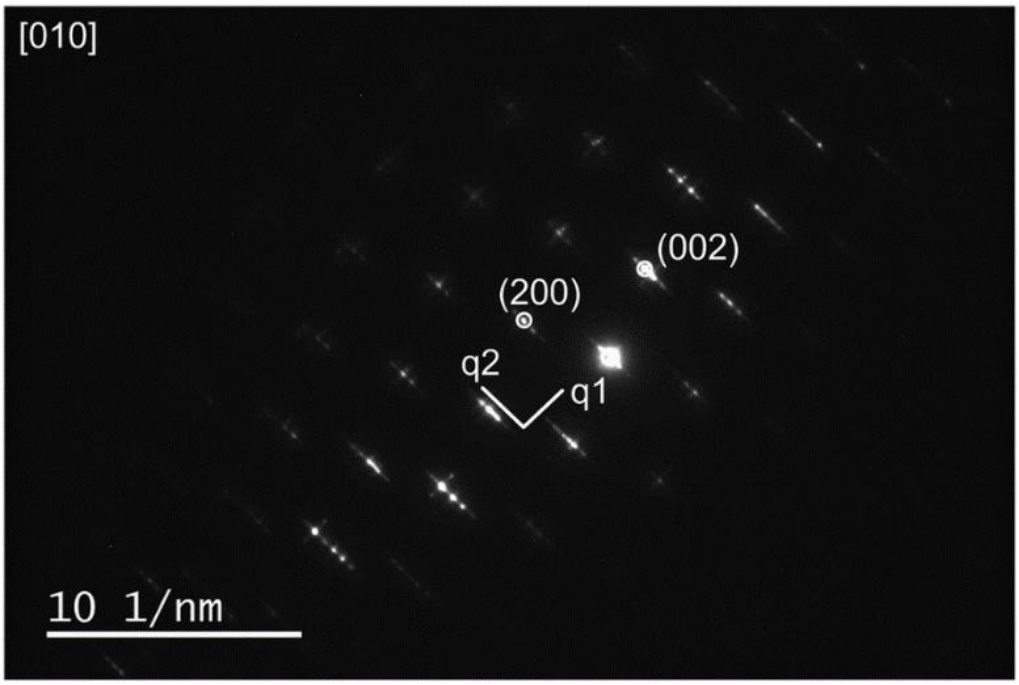


Figure 4.2.7 SAED patterns of $LaNb_{0.9}Mo_{0.1}O_{4.05}$ along [010] zone axis. Two modulated vectors denoted as $\boldsymbol{q_1}$ and $\boldsymbol{q_2}$ are used. Reproduced with permission [14]. Copyright (2023), Royal Society of Chemistry.

For the transition from m-phase to t-phase, La8Gd2 exhibited a similar phase transition behaviour to the LNM10 composition (**Figure A1** and **A2**). However, there was always a small shoulder or peak on the left side of the main peak in the t-phase in La6Gd4, La5Gd5, La4Gd6 and La2Gd8 (**Figure A3** to **A6**). This small shoulder or peak was more pronounced in GNM10 during the phase transition from m-phase to t-phase. As shown in **Figure 4.2.8**, at 500 °C, the XRD patterns of GNM10 shows there were three pairs of satellite peaks adjacent to the main peaks around 28.7°, 34.1°, and 47.4° 2θ. These satellite peaks only appeared around specific main peaks and consistently appeared in pairs before the sample transitioned to t-phase; therefore, this indicated that the material contained two structures, comprising m-phase and t-phase. However, the m-phase found in the XRD patterns at 500 °C could be different from the m-phase at room temperature, and an examination of the XRD patterns of GNM10 around 500 °C (**Figure 4.2.9**) shows that the ‘‘m-phase’’ in this sample consisted of two different m-phases.

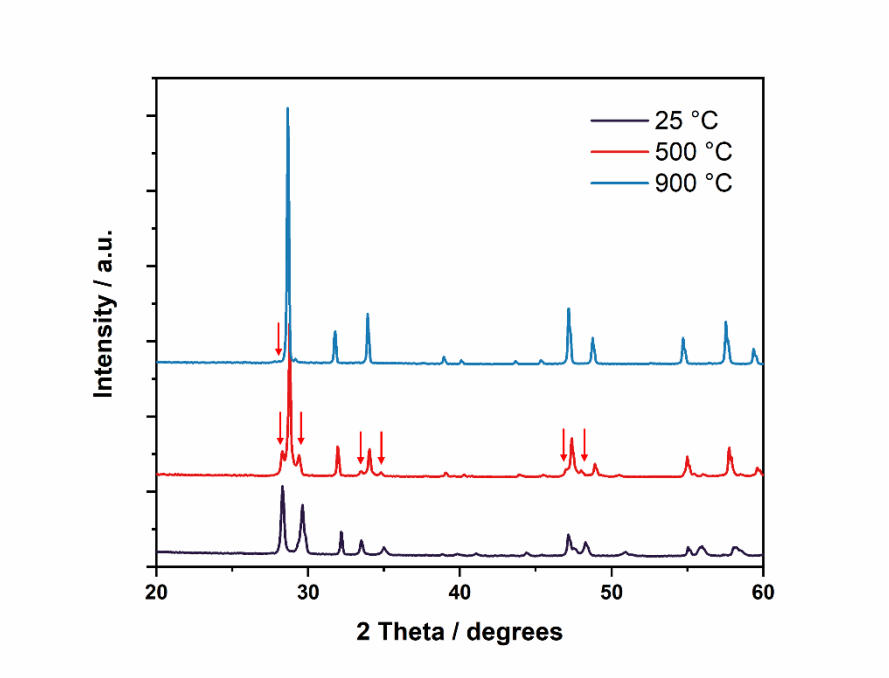


Figure 4.2.8. XRD patterns of GNM10 recorded at 25 °C, 500 °C and 900 °C, respectively. 2θ range is selected from 20° to 60°to highlight the coexistence of m-phase and t-phase during the transition. The satellite reflections from the m-phase are marked by arrows.

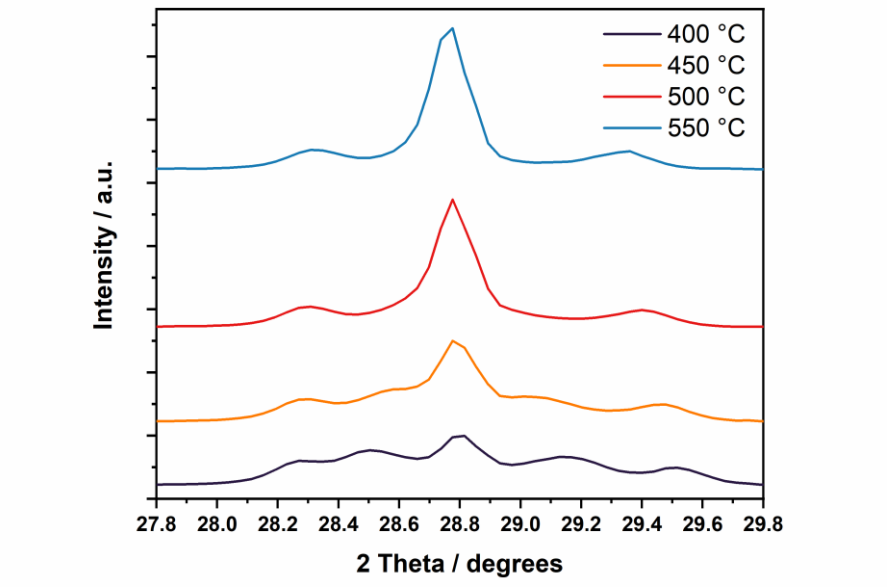


Figure 4.2.9. XRD patterns of GNM10 from 27.8° to 29.8° 2θ recorded at 400 °C, 450 °C, 500 °C and 550 °C, respectively, showing the coexistence of two m-phases.

As shown in **Figure 4.2.9**, for the XRD patterns recorded at 400 °C and 450 °C, not only one pair but two pairs of peaks were observed next to the main peak around 28.8° 2θ. The peaks, which were found around 28.5° and 29.2° 2θ, should be considered as the peaks from the original m-phase as these two peaks merged into one during the phase transition; another two peaks, found around 28.3° and 29.5° 2θ, should be from another m-phase. The coexistence of two different m-phases was not unprecedented as Arulnesan *et al* reported a similar phenomenon for $SmNbO_4$ during the phase transition [63]. The synchrotron XRD results showed that the peaks from m-phase in $SmNbO_4$ also consisted of satellite reflections due to a new m-phase [63]. Arulnesan *et al* suggested the new m-phase should be with the space group of P2/c rather than the same as the original m-phase (I2/a) [63]. The emergence of the satellite reflections from the new m-phase could be related to the smaller ionic radius of La site, as in the work of Arulnesan *et al*, this phenomenon was only observed in $SmNbO_4$ but not in $LaNbO_4$ or $PrNbO_4$ [63]. Therefore, for the compositions with larger La sites (LNM10 and La8Gd2), there was no shoulders observed during the transition, as shown in **Figure A1** and **A2**. It is worth noting that the satellite reflections from the new m-phase were preserved after the transition, even at 900 °C (**Figure 4.2.8**, **Figure A7** and **A8**).

Figure 4.2.10 shows the derived phase diagram for all investigated samples. The transition temperature from m-phase to t-phase increased with increasing Gd fraction on La sites. Notably, the modulated structures were only observed in samples with lower Gd fractions (LNM10 and La8Gd2), indicating that the modulated structures presented solely in samples with large ionic radii of La site elements. This aligned with the findings of previous research [11][162][163]. For La8Gd2, the phase transition temperature from m-phase to t-phase coincided with the phase transition temperature from modulated structure to unmodulated structure. This phenomenon was also found in $LaNb_{0.92}W_{0.08}O_{4.04}$, where $LaNb_{0.92}W_{0.08}O_{4.04}$ only possessed two structures: a modulated m-phase and an unmodulated t-phase [135].

Figures 4.2.11 and **4.2.12** shows the microstructures of the surfaces and cross-sections of as-sintered pellets. Most samples exhibited similar dense structures, while GNM10 exhibited a lower overall density. The relative density measured using the Archimedes' methods showed a value of 82% for GNM10 and around 90% for the others. The BSE images of **Figures 4.2.11** a) and **Figures 4.2.12** e) also confirmed this. As shown in **Figure 4.2.13**, LNM10 exhibited a homogenous single-phase structure; however, for GNM10, there were

two different areas observed, and the dark areas were from the pores in this sample. **Figure 4.2.14** shows the distribution of particle sizes of LNM10 and GNM10 as examples and **Figure 4.2.15** shows the relationship between the calculated mean particle size and the Gd fraction of all samples. **Table 4.1** shows the parameters of log-normal distribution mode used for calculating the particle size for all samples. A clear trend of decrease in the particle sizes was found with increasing the Gd fraction. Therefore, the Gd substituents on the La sites could not only decrease the density of the samples but also limit the growth of the particles. **Table 4.2** presents the normalised atomic ratios of cations of all samples from EDX measurements. Oxygen contents were excluded due to the potential contamination during the process of sample preparation. Results generally agreed with the theoretical stoichiometry.

Table 4.1. Log-normal distribution parameters μ (expected value) and σ* (standard deviation) used for calculating the mean particle sizes of $La_{1-x}Gd_xNb_{0.9}Mo_{0.1}O_{4.05}$ series.

	LNM10	La8Gd2	La6Gd4	La5Gd5	La4Gd6	La2Gd8	GNM10
μ	1.92	1.95	1.70	1.57	1.56	1.18	0.67
σ*	0.41	0.37	0.41	0.47	0.34	0.55	0.54

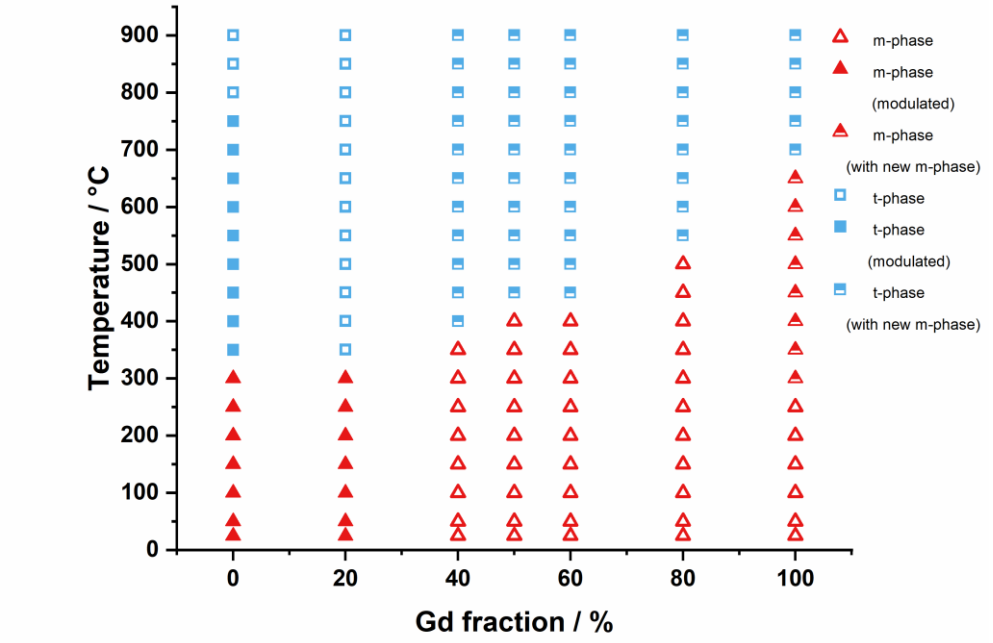


Figure 4.2.10. Phase diagram of $La_{1-x}Gd_xNb_{0.9}Mo_{0.1}O_{4.05}$ series.

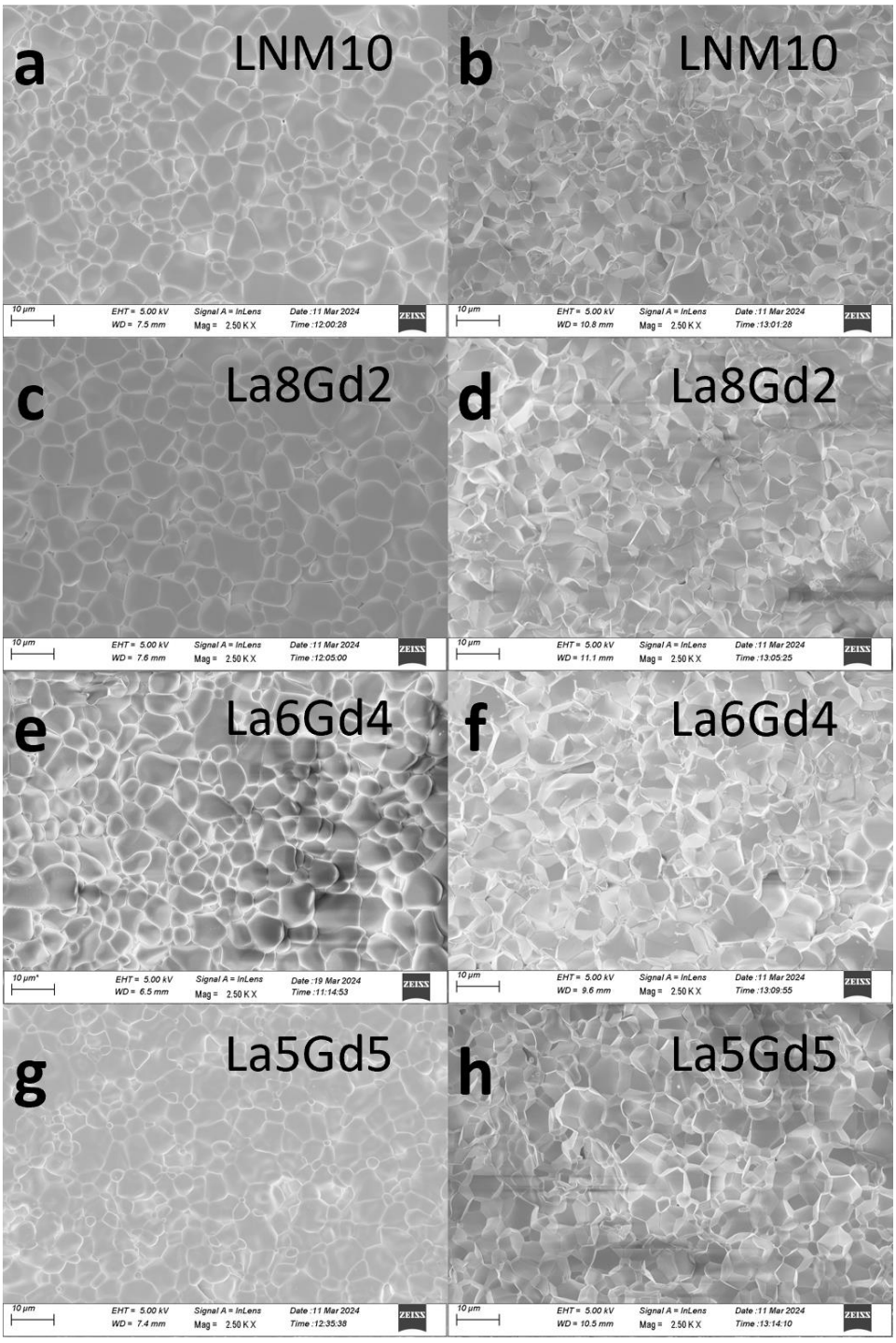


Figure 4.2.11. Microstructures of surfaces of a) LNM10, c) La8Gd2, e) La6Gd4, g) La5Gd5 and cross-sections of b) LNM10, d) La8Gd2, f) La6Gd4, h) La5Gd5. The scale bars of all figures are 10 μm.

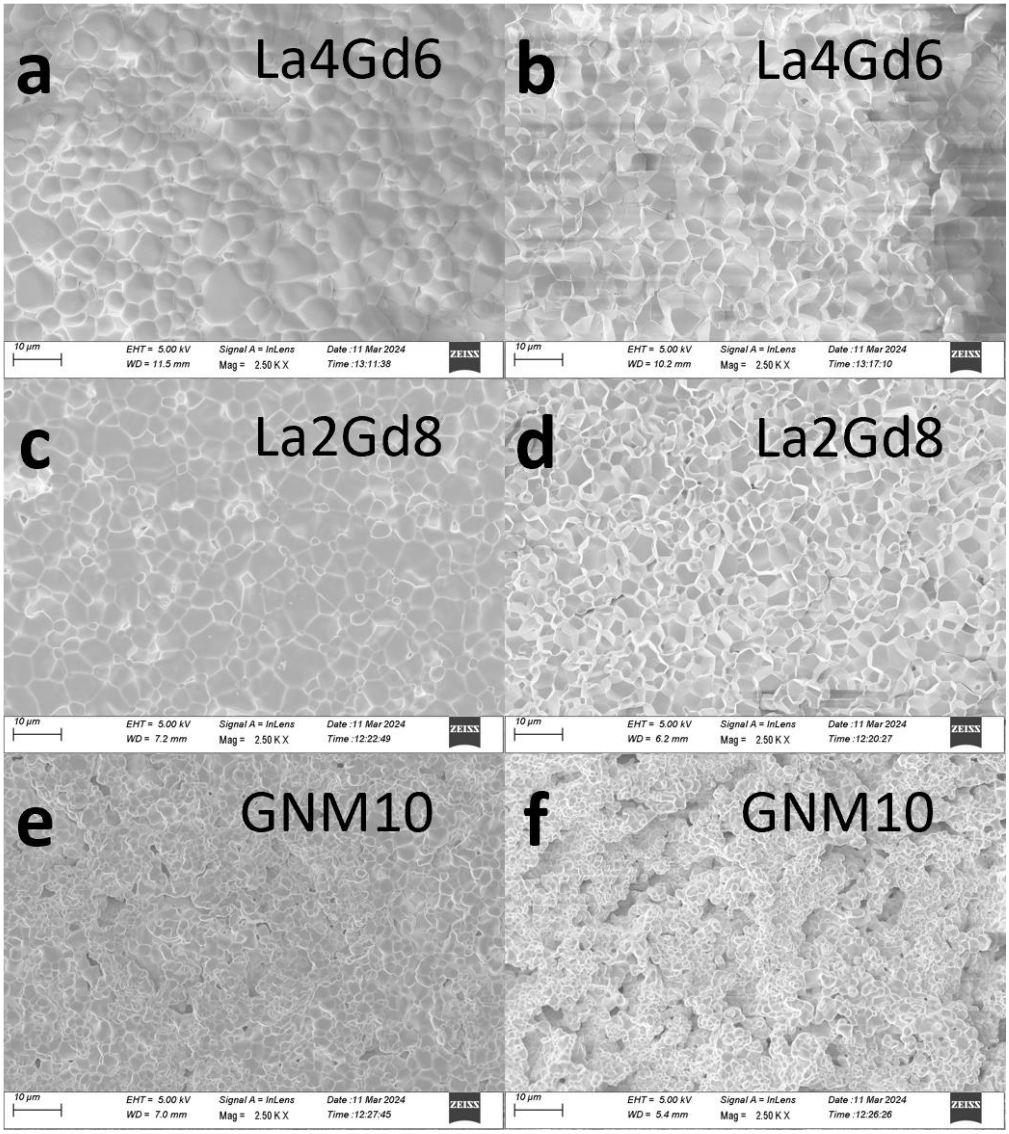


Figure 4.2.12. Microstructures of surfaces of a) La4Gd6, c) La2Gd8, e) GNM10 and cross-sections of b) La4Gd6, d) La2Gd8, f) GNM10. The scale bars of all figures are 10 µm.

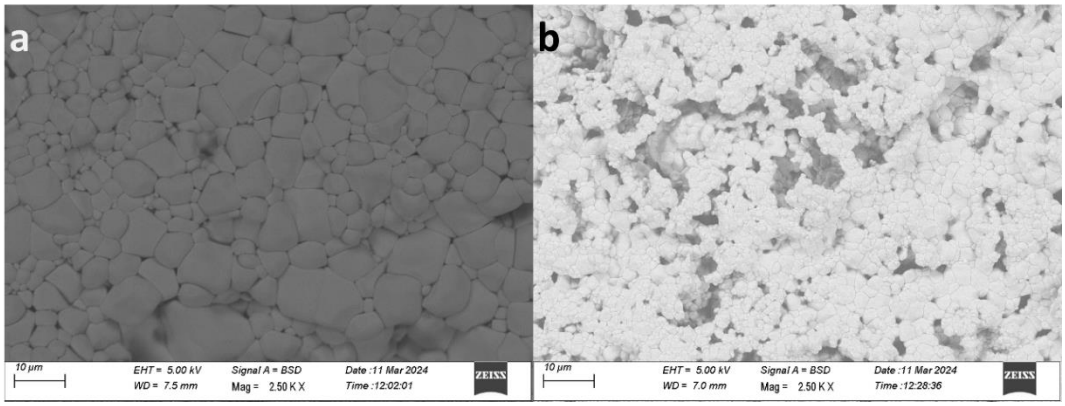


Figure 4.2.13. BSE images of the surfaces of a) LNM10 and b) GNM10.

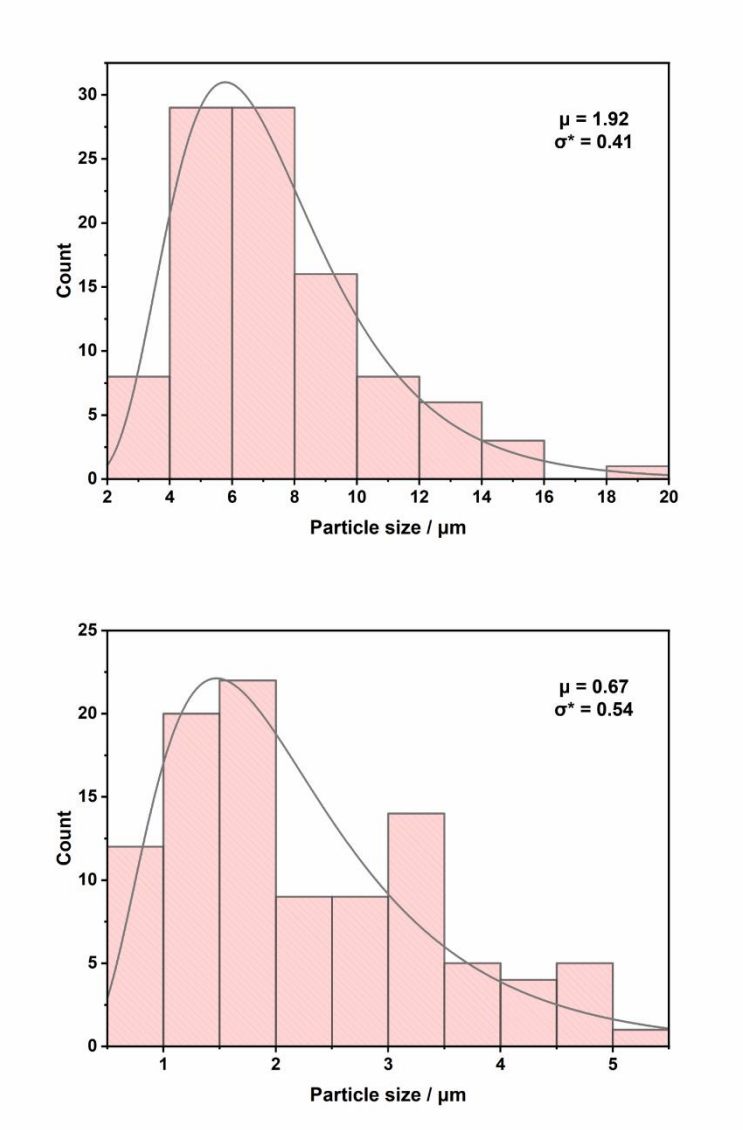


Figure 4.2.14. Particle size distribution of LNM10 (upper) and GNM10 (lower), respectively.

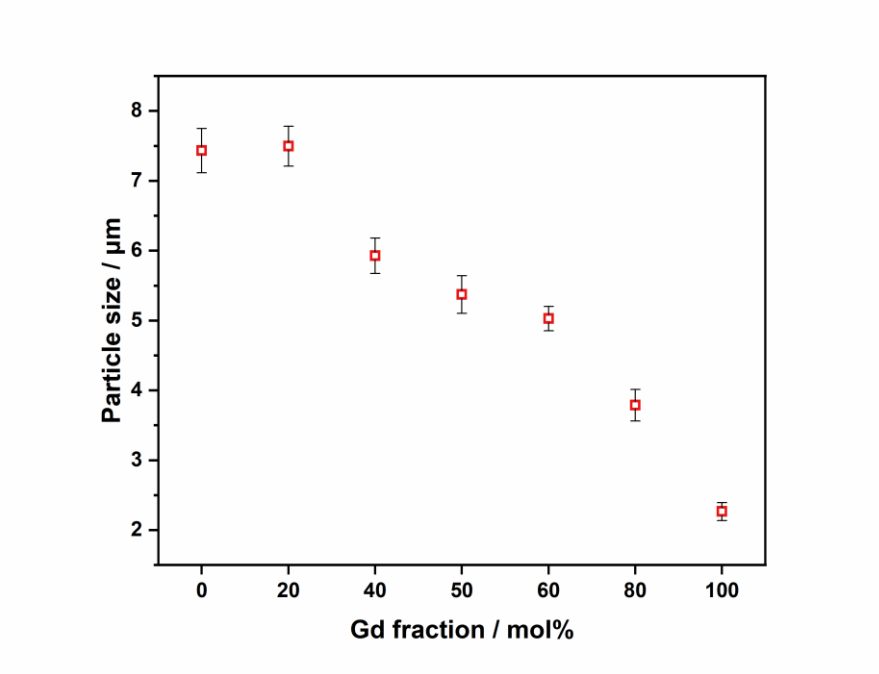


Figure 4.2.15. The calculated mean particle sizes of $La_{1-x}Gd_xNb_{0.9}Mo_{0.1}O_{4.05}$ series.

Table 4.2. Normalised atomic ratios of cations of $La_{1-x}Gd_xNb_{0.9}Mo_{0.1}O_{4.05}$ series. Reproduced with permission [14]. Copyright (2023), Royal Society of Chemistry.

	La (%)	Gd (%)	Nb (%)	Mo (%)
LNM10	50.1 ± 0.2	-	44.9 ± 0.2	5.0 ± 0.0
Theoretical	50.0	-	45.0	5.0
La8Gd2	40.3 ± 0.7	9.9 ± 0.1	44.9 ± 0.5	4.9 ± 0.2
Theoretical	40.0	10.0	45.0	5.0
La6Gd4	29.8 ± 0.6	19.6 ± 0.6	45.5 ± 0.8	5.1 ± 0.1
Theoretical	30.0	20.0	45.0	5.0
La5Gd5	24.4 ± 0.3	24.5 ± 0.4	46.0 ± 0.2	5.1 ± 0.3
Theoretical	25.0	25.0	45.0	5.0
La4Gd6	19.9 ± 0.1	30.1 ± 0.2	45.1 ± 0.1	4.9 ± 0.2
Theoretical	20.0	30.0	45.0	5.0
La2Gd8	10.3 ± 0.4	40.3 ± 0.8	44.5 ± 0.6	4.9 ± 0.1
Theoretical	10.0	40.0	45.0	5.0
GNM10	-	47.3 ± 0.7	47.4 ± 0.6	5.3 ± 0.1
Theoretical	-	50.0	45.0	5.0

4.3 Electrochemical study

Total conductivities of all samples were determined by the EIS measurements. **Figure 4.3.1** shows the Nyquist plot of LNM10 measured at 550 °C under dry air as an example. Three different components: bulk response, grain boundary response, and electrode response had been distinguished by their characteristic magnitudes of the capacitances.

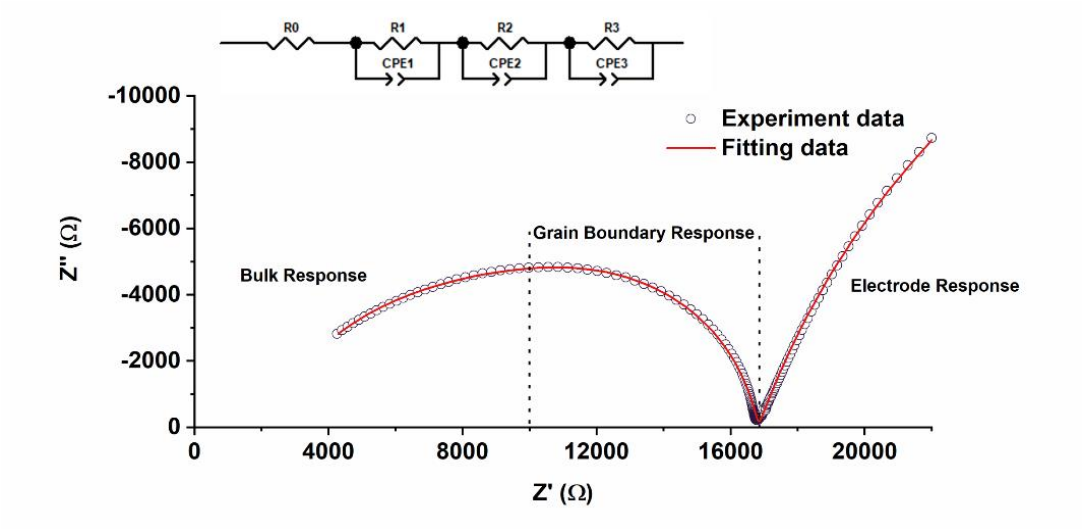


Figure 4.3.1. The Nyquist plot of LNM10 measured at 550 °C under dry air. The hollow circles show the measured value, and the red line shows the fitting results using the model in the inset. Reproduced with permission [14]. Copyright (2023), Royal Society of Chemistry.

Figure 4.3.2 shows the total conductivities of all samples measured from 500 °C to 900 °C under dry air. Substituting Mo on Nb sites noticeably improved the total conductivity of $LaNbO_4$, which was consistent with previous research [12][16]. Most samples exhibited similar conductivity levels, except for GNM10, which exhibited relatively lower conductivity, possibly due to the smaller ionic radius of Gd^{3+}. As suggested by Li *et al*, this smaller ionic radius could compress the lattice of GNM10, hindering the movement of oxide ions [11]. Another reason could be related to the microstructures. As shown in **Figure 4.2.15**, the smallest particle size of GNM10 among all samples with a porous structure could lead to a poor electrochemical performance for this sample.

Among these samples, LNM10 demonstrated the highest conductivity at 1.52×10^{-2} S cm^{-1} at 900 °C under dry air. This result aligned with studies by Cao *et al*

(2.65×10^{-2} S cm^{-1} for $LaNb_{0.8}Mo_{0.2}O_4$ at 900 °C in air) and Auckett *et al* (approximately 1.70×10^{-2} S cm^{-1} for $LaNb_{0.84}Mo_{0.16}O_{4.08}$ at 900 °C in air) [12][16]. Notably, despite containing less Mo dopant compared to previous works, the total conductivity of LNM10 was still comparable. This seemed to contradict the expectations as higher Mo content should increase the conductivity due to more oxygen interstitials introduced into the system. Similar trends were also observed in the $GdNb_{1-x}W_xO_{4+\delta}$ series, where total conductivity decreased when W content exceeded 40 mol% [162]. Possible reasons include the trapping effects of Mo substituents on the charge carriers for oxygen ion conduction. As suggested by Kawaguchi *et al*, since the hexavalent substituents on Nb sites possessed opposite charges to the oxygen interstitials, the electrostatic attractive interactions between these species could stabilised the charge carriers around the substituents and reduced their mobilities [162]. Therefore, the total conductivity tended to decrease or remain at the same magnitude when the substituents exceed their optimal level. It is worth mentioning that the ''optimal level'' discussed here was different from what was discussed for Ca substituted $LaNbO_4$ in Section 2.4.1. As mentioned above, the total conductivity of $La_{1-x}Ca_xNbO_{4-\delta}$ decreased when the Ca content exceeded 0.5 mol% [79]. This was due to the solubility limit of the Ca substituent on La sites as a secondary phase of $Ca_2Nb_2O_7$ emerged with increasing the Ca content on La sites [79]; however, for Mo-substituted $LaNbO_4$, a single-phase material could be obtained up to 20% Mo substitution [12]. Actually, from the EIS results of Auckett *et al*, there was no significant difference of total conductivities between $LaNb_{0.84}Mo_{0.16}O_{4.08}$ and $LaNb_{0.8}Mo_{0.2}O_{4.1}$ from 400 °C to 1000 °C; therefore, the optimal level of Mo substituent could be between 10 mol% and 16 mol%. LNM10 also exhibited higher conductivity compared to materials reported by Li *et al* (3.00×10^{-3} S cm^{-1} for $LaNb_{0.92}W_{0.08}O_{4.04}$ at 800 °C under air) and Canu *et al* (1.40×10^{-3} S cm^{-1} for $LaNb_{0.84}W_{0.16}O_{4.08}$ at 800 °C under air) [11][132]. This aligned well with the simulation results reported by Toyoura *et al*, suggesting Mo as the ideal dopant on Nb sites, due to its reduced trapping effects on oxygen interstitials [8].

Although LNM10 exhibited the highest conductivity in the high temperature range (800 °C - 900 °C), it did not dominate across all temperature ranges. As shown in **Figure 4.3.2**, between 500 °C and 600 °C, La8Gd2, La6Gd4, and La5Gd5 all exhibited higher conductivities. As temperature increased, LNM10 surpassed La6Gd4 and La5Gd5 but remained lower than La8Gd2 until reaching 750 °C, where their conductivities equalised. Notably, a change in the

slope of the conductivity plot for LNM10 occurred at 750 °C, which could be related to a change in activation energy (E_a) of oxygen ion conduction. However, within the temperature range of 800 °C to 900 °C, there were only 3 data points recorded for LNM10, which was insufficient to conduct the linear fitting to calculate the E_a. Consequently, another precise EIS measurement was conducted for LNM10 from 800 °C to 900 °C, with a temperature interval of 10 °C. **Figure 4.3.3** shows the Arrhenius plot of the total conductivity and calculated E_a of LNM10. Combined with **Figure 4.2.10**, the change in E_a of LNM10 from 1.53 eV to 0.64 eV could be attributed to LNM10 transitioning from a modulated t-phase to an unmodulated t-phase. The E_a of 0.64 eV could lead to a consideration of the appearance of electronic conductivity, as at elevated temperature range, the contribution of electronic conductivity cannot be neglected. However, for all the other samples, there was no significant change in the E_a in the same temperature range and as shown in **Figure 2.4.1** in Chapter 2, $La_{0.99}Ca_{0.01}NbO_4$ exhibited a mixed p-type electronic and oxygen ion conductivity at higher temperature range under dry oxidising atmosphere, but there was no slope change either. Therefore, the change of E_a in LNM10 should arise from the change of the structure of LNM10 itself. Since the same phenomenon was also observed for $LaNb_{0.84}Mo_{0.16}O_{4.08}$ and $LaNb_{0.8}Mo_{0.2}O_{4.1}$, this significant change in E_a suggested that the modulated structures could have adverse effects on the electrochemical performance of this type of material as suggested by Auckett *et al* [12].

Table 4.3 lists the activation energy (E_a) of all samples, with no significant changes observed in the Arrhenius plot of conductivities for other samples over the temperature range, as most transitioned to the t-phase below 500 °C. However, from **Figure 4.2.10**, it was suggested that the phase transition temperature of GNM10 was around 650 °C, possibly leading to a slight change in the slope of the Arrhenius plot, as previously noted [12][9][11]. The lack of change in GNM10 could be attributed to the mixed phase region of GNM10, where the transition from a mixture of m-phase and t-phase to a pure t-phase should have a smaller effect compared to a transition from a pure m-phase to a pure t-phase.

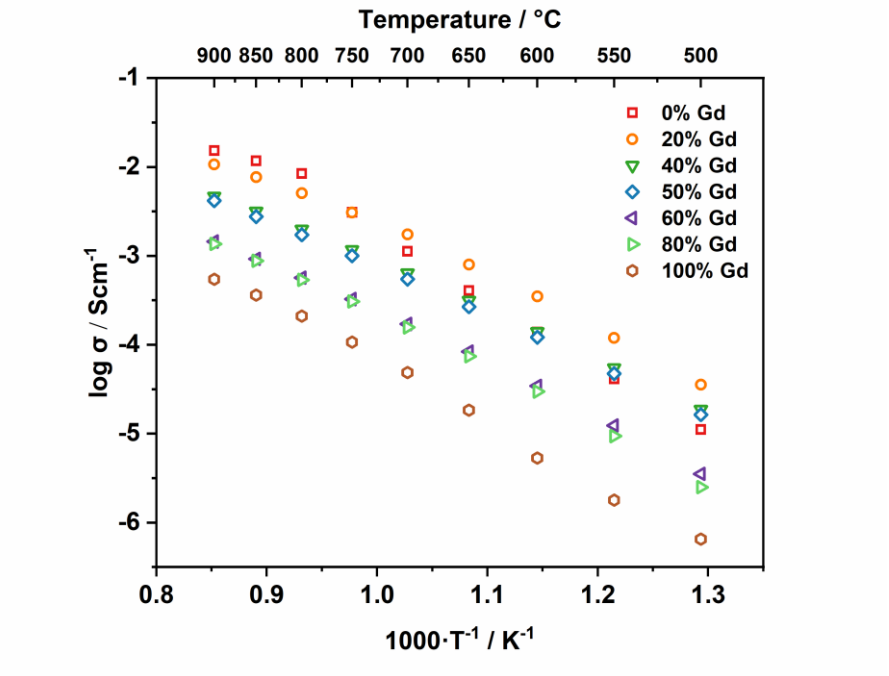


Figure 4.3.2. Total conductivity of $La_{1-x}Gd_xNb_{0.9}Mo_{0.1}O_{4.05}$ series under dry air.

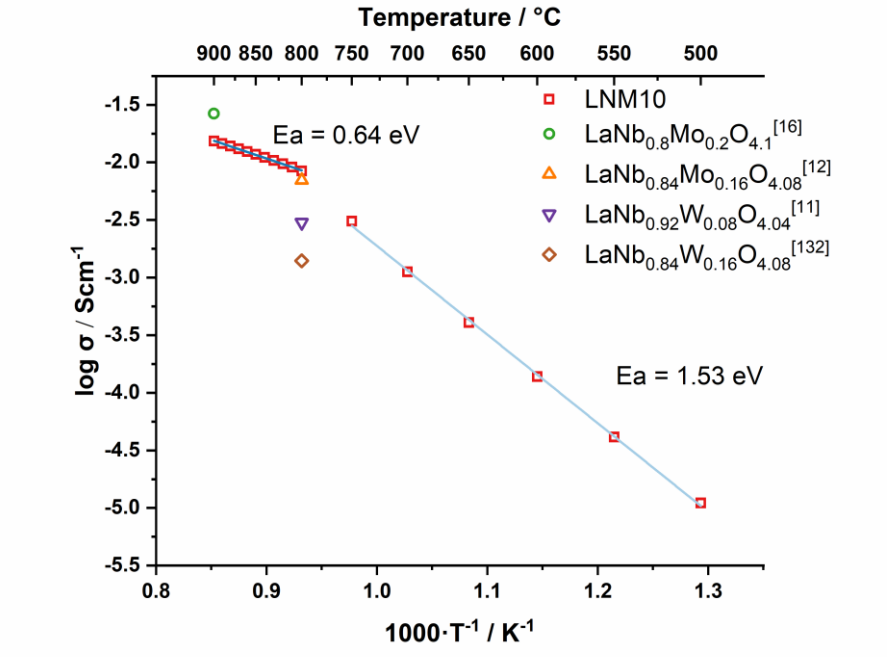


Figure 4.3.3. Arrhenius plot of the total conductivity of LNM10 showing the change of E_a. The results are also compared with other similar materials.

Table 4.3 Activation energies, E_a, of $La_{1-x}Gd_xNb_{0.9}Mo_{0.1}O_{4.05}$ series calculated from the linear regressions from the Arrhenius plot. The subscripted U and M represent the unmodulated t-phase and modulated t-phase, respectively.

	$LNM10_U$	$LNM10_M$	La8Gd2	La6Gd4	La5Gd5	La4Gd6	La2Gd8	GNM10
Ea (eV)	0.64(1)	1.53(2)	1.11(4)	1.08(2)	1.08(1)	1.16(2)	1.22(3)	1.37(3)

4.4 Conclusion

In summary, single-phase samples of $La_{1-x}Gd_xNb_{0.9}Mo_{0.1}O_{4.05}$ were successfully synthesised by SSR method. All samples exhibited a phase transition from a monoclinic Fergusonite phase at lower temperature to a tetragonal Scheelite phase at higher temperature. The transition temperature gradually increased with increasing Gd content on the La sites. However, for GNM10, two different m-phases emerged during the phase transition. The modulated structures were found to exist only for LNM10 and La8Gd2 samples. Based on the indexation from the SAED patterns, the modulated structures in LNM10 were suggested to be 2D incommensurate. However, from the EIS results, these modulated structures could have negative effects on the electrochemical performance, as the activation energy of an unmodulated LNM10 (0.64 eV) was lower than that of a modulated LNM10 (1.53 eV). On being substituted by a small fraction of Gd (20 mol%) on La site, the total conductivity of LNM10 increased between 500 °C to 700 °C; with more Gd substituted on La sites, the total conductivity decreased. Gd could also influence the microstructures of these types of materials. With substituting more Gd on La sites, the particle sizes gradually decreased, and the structure became porous for GNM10. Therefore, on one hand, the Gd could eliminate the modulated structures which could lower the activation energy for oxygen ion conductivity; on the other hand, the Gd could also impede the sintering. These results provide a Gd substituents trade-off and will be useful in the development of a new type of oxygen ion conductor in different temperature ranges.

Chapter 5. Effect of W and Mo co substitution on conductivity and structure of $LaNbO_4$

In this chapter, the conventional SSR method was used to synthesise single-phase $LaNb_{0.8}W_xMo_{0.2-x}O_{4.1}$ (where x = 0.00, 0.02, 0.04, 0.10, 0.16, 0.18 and 0.20). Among all the samples, that with x = 0.02 exhibited the highest total conductivity in the intermediate temperature range (2.37×10^{-3} S cm^{-1}at 665 °C under dry air). Analysis of XRD patterns revealed that the stabilisation of t-phase at room temperature could be achieved when x > 0.02. The phase diagram constructed from *in-situ* XRD indicated the existence of the modulated structures from room temperature to 900 °C when x ≥ 0.10. With the combination of EIS measurements and XRD refinements, the total conductivities of the samples were found to be proportional to the volume of the unit cells. It is also worth noting that the presence of modulated structures adversely affected the overall electrochemical performance of these types of materials, which confirmed the findings in Chapter 4.

5.1 Introduction

As discussed above, substituting W at levels ranging from 8 mol% to 16 mol% on Nb sites could substantially improve the total conductivity of $LaNbO_4$, which exhibited an 1.5 orders of magnitude increase [11]. Concurrently, the phase transition temperature from m-phase to t-phase experienced a notable decrease, with 16 mol% W-substituted samples possessing a t-phase at room temperature [135]. As shown in **Figure 5.1.1**, a clear change of the slope of the Arrhenius plot of $LaNbO_4$ could be observed because of the transition from m-phase to t-phase, which means the activation energy of oxygen ion conduction in t-phase was lower than that in m-phase; therefore, to maintain these types of materials in t-phase could be ideal for use as the electrolyte for SOFCs. Another substituent Mo, which was proposed because of its lower trapping effect on oxygen interstitials, exhibited higher total conductivities than W-substituted $LaNbO_4$ with similar substituting content on Nb sites [14]. However, the phase transition temperatures of Mo-substituted $LaNbO_4$ were always higher than those of W-substituted $LaNbO_4$. As shown in **Figure 2.5.4**, even with 20 mol% Mo substituted on Nb sites, the t-phase still could not be stabilised down to room temperature

[12]. Therefore, there was a trade-off between W and Mo concerning the phase transition temperature and total conductivity.

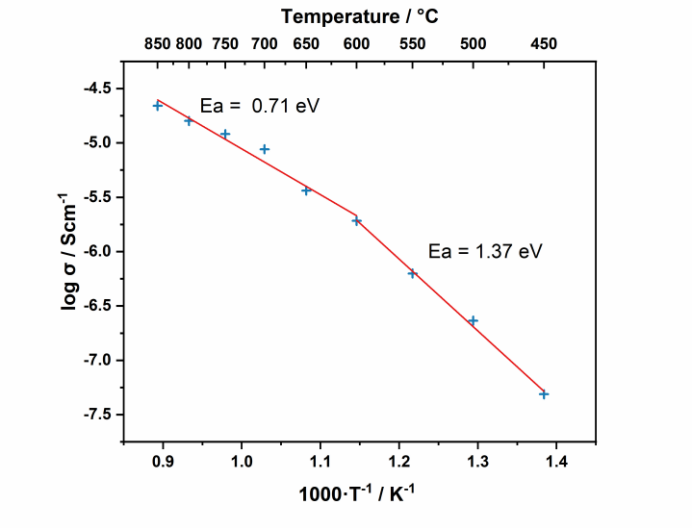


Figure 5.1.1. Arrhenius plot of the total conductivity of $LaNbO_4$. Data were extracted from the work of Li *et al* [11].

To achieve both low phase transition temperature and high conductivity, a strategy of co-substituting W and Mo has been suggested. In this chapter, the focus lies on the structural changes and correlating electrochemical performance of a series W and Mo co-substituted $LaNbO_4$. A phase diagram for co-substituted samples across temperature ranges from 25 °C to 900 °C using *in-situ* XRD was generated, with particular attention to the emergence and absence of the modulated structures. The modulated structures in some of the samples were also indexed from SAED patterns. The relationship between lattice parameters and total conductivities was discussed together with the impact of the modulated structures. Samples of $LaNb_{0.8}W_xMo_{0.2-x}O_{4.1}$ with x = 0.00, 0.02, 0.04, 0.10, 0.16, 0.18 and 0.20, were denoted as LNMo20, LNW2Mo18, LNW4Mo16, LNW10Mo10, LNW16Mo4, LNW18Mo2, and LNW20, respectively thereafter.

5.2 Structural evolution of $LaNb_{0.8}W_xMo_{0.2-x}O_{4.1}$ series

Figure 5.2.1 shows the XRD patterns of $LaNb_{0.8}W_xMo_{0.2-x}O_{4.1}$ series collected at room temperature. Except for LNMo20 and LNW2Mo18, which possessed a monoclinic Fergusonite structure, other samples exhibited a transition to tetragonal Scheelite structure at room temperature as the W content increased. This transition was evident as the merging of the

two split main peaks into a single peak (at around 28.1° 2θ), as depicted in the top right corner of **Figure 5.2.1**. Notably, the modulated structures were present in all samples at room temperature, indicated by the peak at around 26.7° 2θ. The XRD patterns suggested that the co-substitution of W and Mo could facilitate a decrease in the phase transition temperature and the appearance of the modulated structures. However, low-level of impurities were observed in samples with higher W fraction. As marked by blue dots, peaks from another phase appeared in both LNW18Mo2 and LNW20. This secondary phase could be either $La_2W_2O_9$ [164] or $La_7Nb_3W_4O_{30}$ [165]. Although it was difficult to identify the accurate stoichiometry of the secondary phase based on XRD results, the secondary phase should be a W-rich phase.

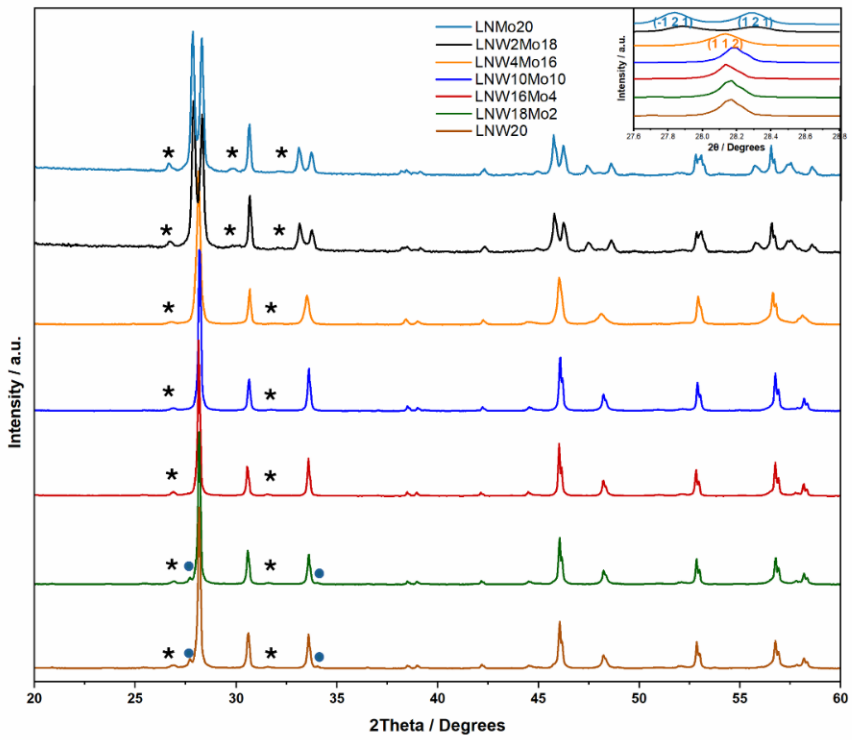


Figure 5.2.1. XRD patterns of the $LaNb_{0.8}W_xMo_{0.2-x}O_{4.1}$ series, displayed as a function of increasing fraction of W from top to bottom. Peaks corresponding to the modulated structures are marked by asterisks. Impurities in LNW20 and LNW18Mo2 are marked by blue dots. Change of main peaks are exhibited in top right corner inset. Lattice planes in monoclinic Fergusonite phase of LNMo20 are labelled in blue, while lattice planes of the tetragonal Scheelite phase of LNW4Mo16 are labelled in orange.

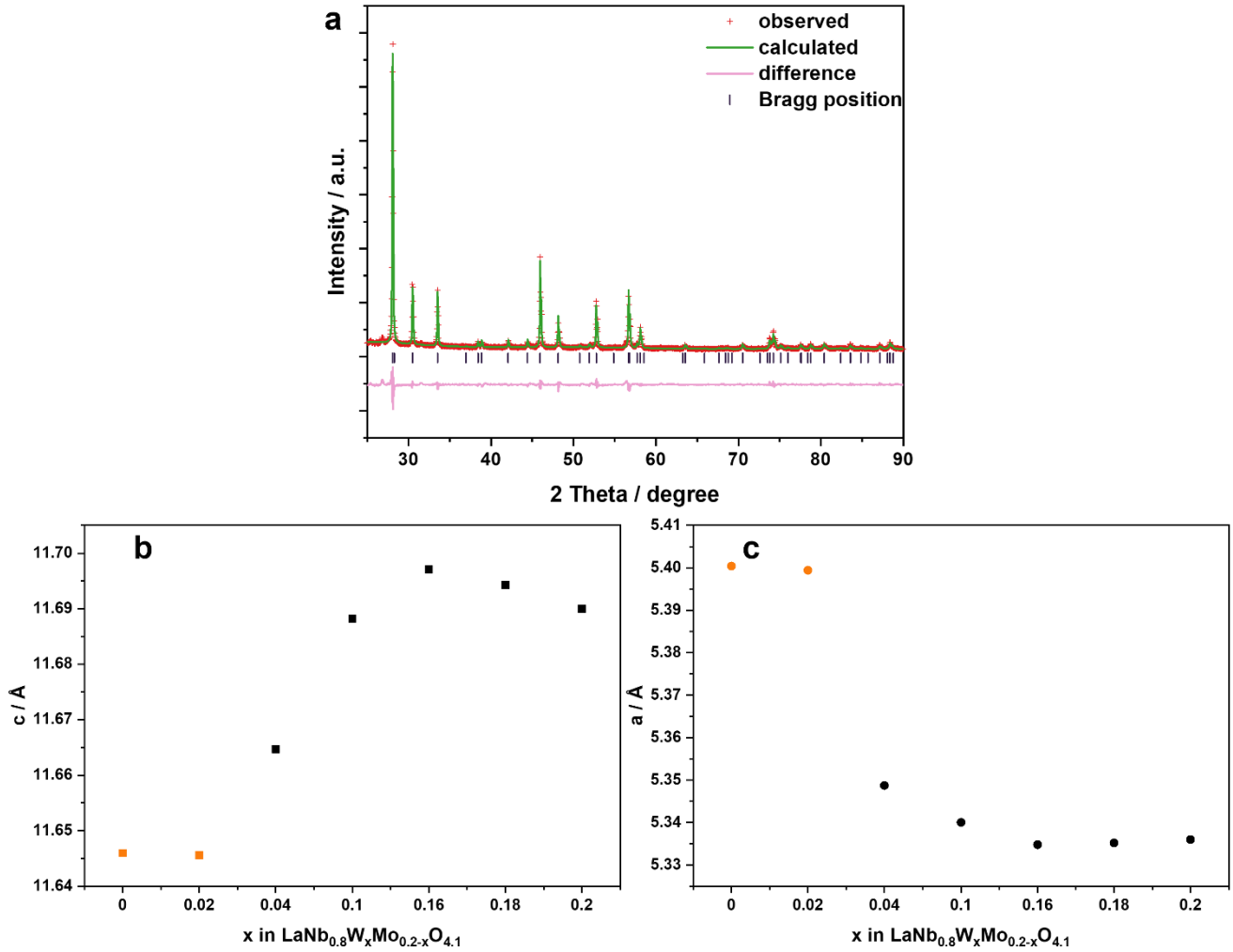


Figure 5.2.2. a) Plot of XRD refinement result of LNW16Mo4 at room temperature, R_{wp}=6.07%, χ^2 = 3.99; lattice parameters of b) *c* and c) *a* in $LaNb_{0.8}W_xMo_{0.2-x}O_{4.1}$ series at room temperature. The symbols in orange represent the m-phase. Error bars are smaller than the symbols.

The lattice parameters of the $LaNb_{0.8}W_xMo_{0.2-x}O_{4.1}$ series were investigated through Le Bail refinements of XRD data obtained at room temperature, as depicted in **Figure 5.2.2** a), using the results of LNW16Mo4 as a representative example. **Table A4** presents a summary of the refined parameters of all samples. Lattice parameters of different compositions were plotted in **Figure 5.2.2** b) and c), where the data corresponding to LNMo20 and LNW2Mo18 denote the m-phase. It is worth noting that the lattice parameters of LNMo20 and LNW2Mo18 in **Figure 5.2.2** b) was the *b* lattice parameter since both were m-phase. Except

for the monoclinic LNMo20 and LNW2Mo18 compositions, both the *a* and *c* lattice parameters remained relatively constant with minimal variation across the entire tetragonal regime, this could be related to the similar ionic radius of Mo^{6+} ions (0.41 Å in 4-coordinate) and W^{6+} ions (0.42 Å in 4-coordinate) [76]. Additionally, the lattice parameters stabilised when x > 0.16. This plateau observed above x = 0.16 could be attributed to the appearance of the W-rich impurity, as confirmed by XRD patterns. The emergence of the secondary phase suggested a solubility limit at the x = 0.16 composition.

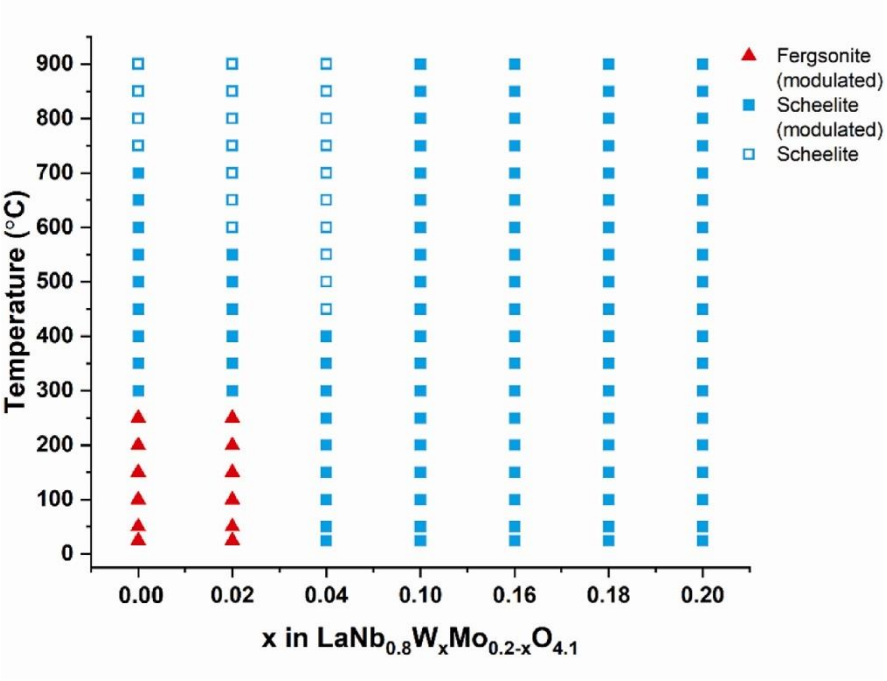


Figure 5.2.3. The phase diagram of $LaNb_{0.8}W_xMo_{0.2-x}O_{4.1}$ series from room temperature to 900 °C. Reproduced with permission [15]. Copyright (2024), Elsevier.

Figure 5.2.3 shows the phase diagram derived from *in-situ* XRD data collected from room temperature to 900 °C. A distinct reduction in the transition temperatures between m-phase and t-phase was observed with increasing W content, as the phase transition temperature decreased from around 250 °C (for LNMo20) to room temperature (for LNW4Mo16). For the disappearance temperature of the modulated structures of LNMo20, it aligned well with the work of Auckett *et al*, both were around 650 °C [12]. However, for the whole series, this temperature initially decreased with lower W fraction (x = 0.00-0.04). When x ≥ 0.10, the modulated structures existed continuously from room temperature to 900 °C. The reason why with initially increasing the W fraction the disappearance temperature of the modulated structures decreased is still unknown; however, a similar phenomenon was

observed in Mo-substituted $LaNbO_4$ [12]. The disappearance temperatures of the modulated structures did not show a proportional relationship with the Mo fraction on Nb sites, as this temperature varied in different samples [12]. Therefore, when the fraction of Mo was larger than W ($x \leq 0.10$), there could be some uncertainties about the disappearance temperatures of the modulated structures.

Figure 5.2.4 shows the SAED patterns of LNW18Mo2. The modulated structures observed along the [010] zone axis resembled those in the previous work reported for $LaNb_{0.88}W_{0.12}O_{4.06}$ and $LaNb_{0.9}Mo_{0.1}O_{4.05}$, where satellite reflections were observed in two directions and needed two different modulation vectors to index [14][11]. However, an additional modulated structure along the $[1\bar{1}1]$ zone axis, not previously documented for these types of materials, was also identified. This new modulated structure differed from that observed along the [010] zone axis, as the satellite reflections were present only in one direction. The modulated vectors were determined to be $\boldsymbol{q_1} = 0.349\boldsymbol{a}^* + 0.344\boldsymbol{c}^*$ and $\boldsymbol{q_2} = 0.175\boldsymbol{a}^* + 0.657\boldsymbol{c}^*$ along the [010] zone axis. As for the modulated structure along $[1\bar{1}1]$ zone axis, only one modulated vector $\boldsymbol{q} = 0.165\boldsymbol{a}^* + 0.329\boldsymbol{b}^* + 0.165\boldsymbol{c}^*$ was used. Consequently, the modulated structures observed along the [010] and $[1\bar{1}1]$ zone axes were categorised as (3+2) D and (3+1) D incommensurate modulated structures, respectively.

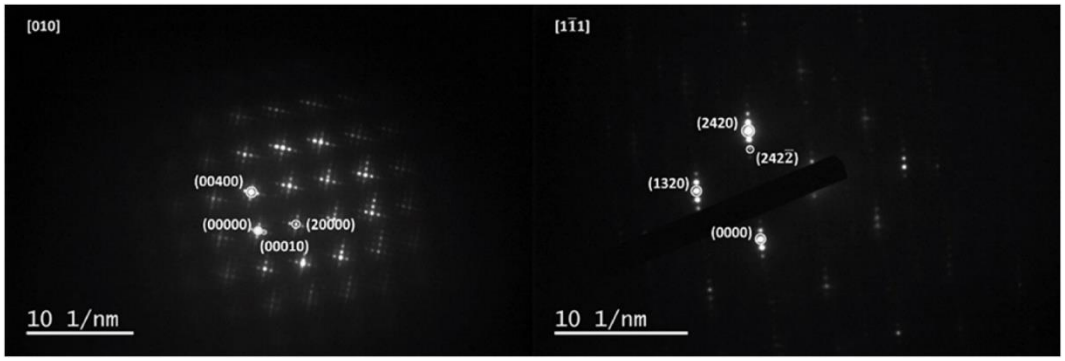


Figure 5.2.4. SAED patterns of LNW18Mo2 along zone axis [010] and $[1\bar{1}1]$ highlighting the modulated structures. Reproduced with permission [15]. Copyright (2024), Elsevier.

5.3 Microstructure of $LaNb_{0.8}W_xMo_{0.2-x}O_{4.1}$ series

The morphologies of both surfaces and cross-sections of all samples were investigated by SEM (**Figure 5.3.1** and **5.3.2**). As shown in the figures, all samples showed a dense

structure, and the relative densities measured by the Archimedes method reached around 90% after sintering.

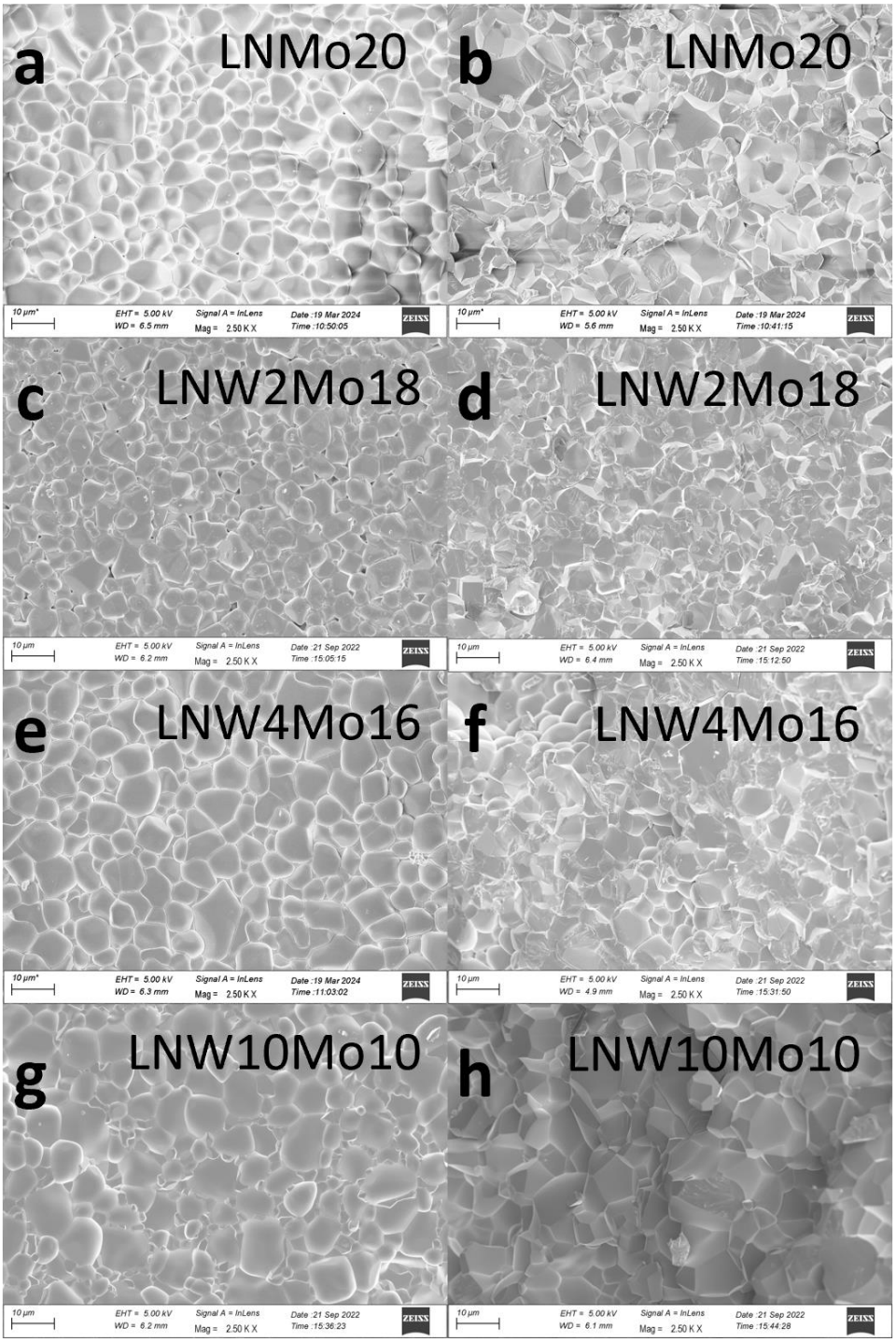


Figure 5.3.1. Microstructures of surfaces (left column) and cross-sections (right column) of a), b) LNMo20, c), d) LNW2Mo18, e), f) LNW4Mo16 and g), h) LNW10Mo10. The scale bars of all figures are 10 µm.

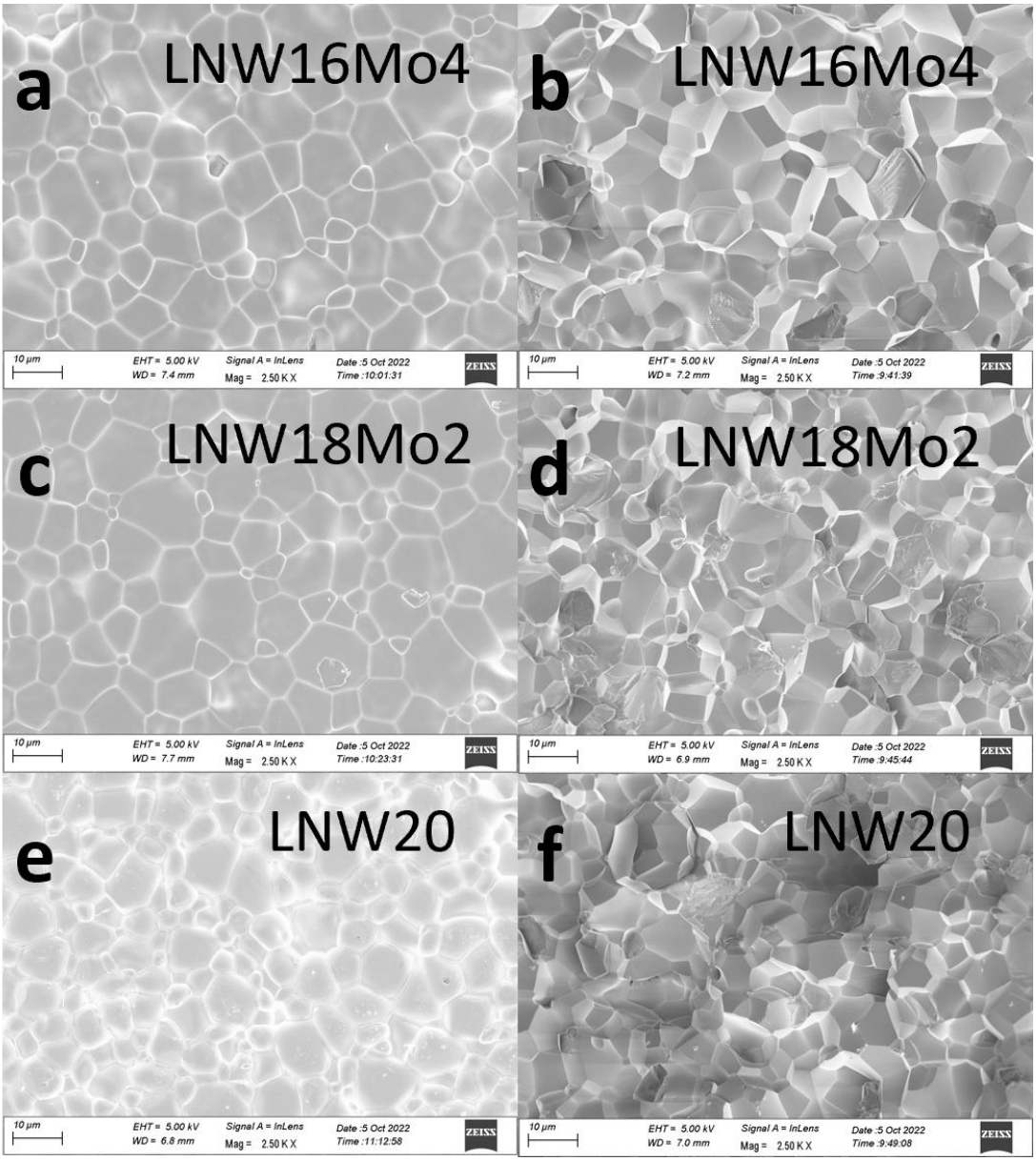


Figure 5.3.2. Microstructures of surfaces (left column) and cross-sections (right column) of a), b) LNW16Mo4, c), d) LNW18Mo2 and e), f) LNW20. The scale bars of all figures are 10 µm.

The morphologies of the samples could be divided into two different categories: lower W fraction ($x < 0.10$) and higher W fraction ($x > 0.10$). When the W fraction remained at the lower level, the observed features of the samples remained consistent and the calculated mean particle sizes were smaller than those of the samples with higher W fraction. As shown in **Figure 5.3.1** a), c), and e), the particle sizes were uniform. The cross sections of the samples with lower W fraction exhibited compact structures, where fragments of grains could be observed. For the samples with higher W fraction, as shown in **Figure 5.3.2** a), c), and e), the

calculated mean particle sizes of the samples were increased significantly. However, the particle sizes were distributed as several particles with larger diameters were found to be surrounded by smaller particles. The cross-section of these samples also exhibited a different structure of well-cut facets with sharp edges. The samples with same fraction of W and Mo exhibited a structure at ''intermediate state''. As shown in **Figure 5.3.1** g), the particles started to become non-uniform. **Figure 5.3.3** shows the distribution of particle sizes of LNMo20 and LNW20 as examples and **Figure 5.3.4** shows the calculated mean particle size of $LaNb_{0.8}W_xMo_{0.2-x}O_{4.1}$. As shown in **Figure 5.3.4**, overall, the particle sizes of the samples were also divided into two categories of samples with lower W fraction ($x < 0.10$) and samples with higher W fraction ($x > 0.10$). For all samples with lower W fraction ($x < 0.10$), the average particle sizes (6.34 ± 0.12 µm) were smaller than them of LNW16Mo4 (9.79 ± 0.46 µm) and LNW18Mo2 (9.72 ± 0.53 µm). The reason why LNW10Mo10 exhibited smaller particle size than samples with less W fraction could be related to the ''intermediate state'' mentioned above. As shown in **Table 5.1**, LNW10Mo10 exhibited the highest value of σ* among all the samples; therefore, there was a mixture of larger and smaller particles in LNW10Mo10, which could lead to a smaller calculated mean particle size.

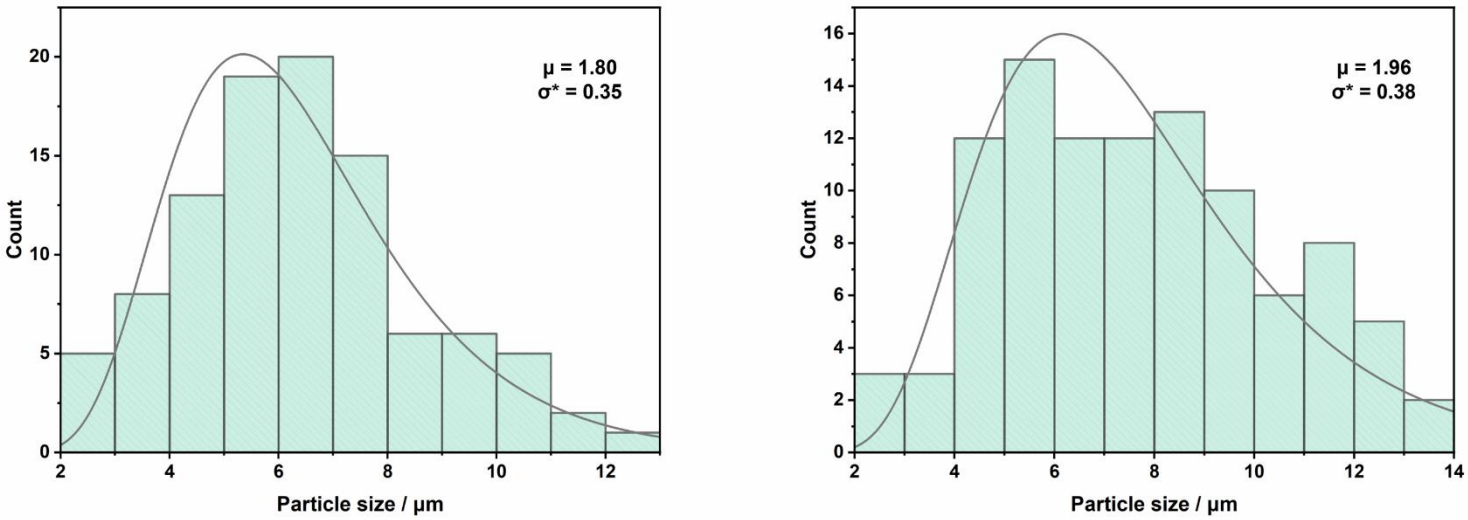


Figure 5.3.3. Particle size distribution of LNMo20 (left) and LNW20 (right), respectively.

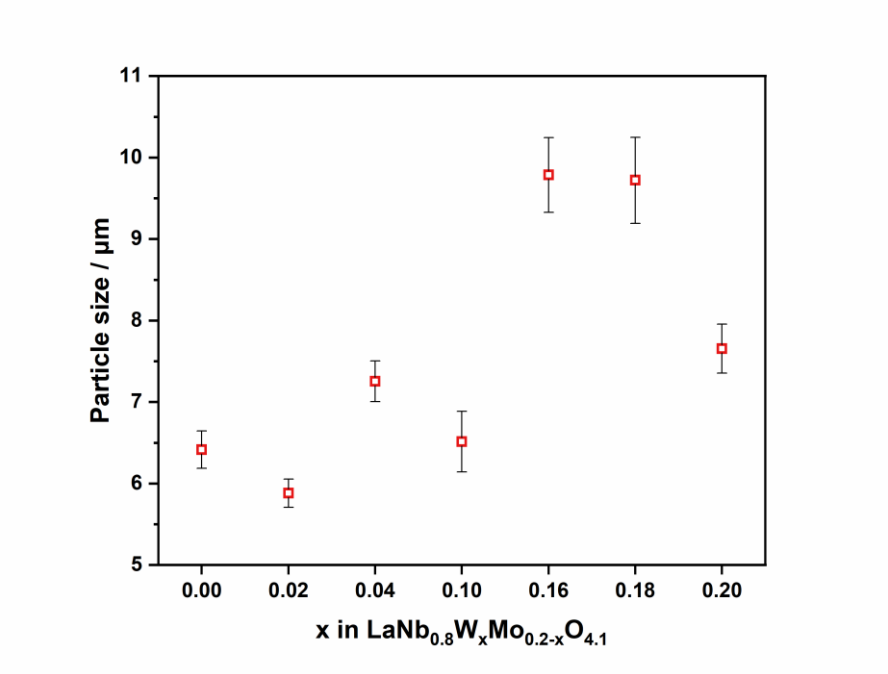


Figure 5.3.4. The calculated mean particle sizes of $LaNb_{0.8}W_xMo_{0.2-x}O_{4.1}$ series.

Table 5.1. Log-normal distribution parameters µ (expected value) and σ* (standard deviation) used for calculating the mean particle sizes of $LaNb_{0.8}W_xMo_{0.2-x}O_{4.1}$ series.

	LNMo20	LNW2Mo18	LNW4Mo16	LNW10Mo10	LNW16Mo4	LNW18Mo2	LNW20
µ	1.80	1.73	1.93	1.72	2.18	2.17	1.96
σ*	0.35	0.30	0.34	0.55	0.44	0.46	0.38

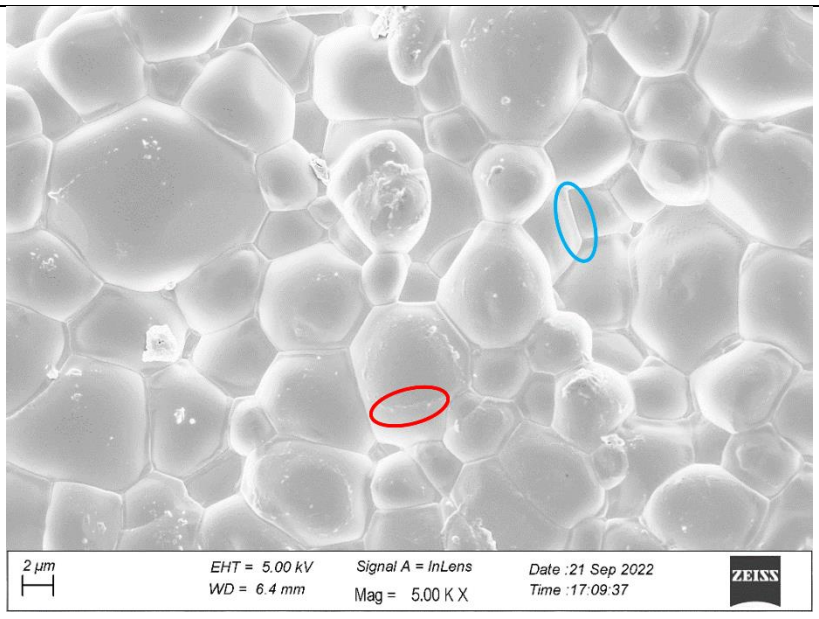


Figure 5.3.5. Higher magnification surface image of LNW20. The red and blue ellipses highlight the raised stripes on the surface and grain boundaries, respectively.

Table 5.2. Normalised atomic fractions of cations of $LaNb_{0.8}W_xMo_{0.2-x}O_{4.1}$ series. Reproduced with permission [15]. Copyright (2024), Elsevier.

	La (%)	Nb (%)	W (%)	Mo (%)
LNMo20	50.3 ± 0.4	40.2 ± 0.1	-	9.4 ± 0.1
Theoretical	50.00	40.00	-	10.00
LNW2Mo18	50.1 ± 0.7	40.6 ± 0.1	0.9 ± 0.1	8.4 ± 0.2
Theoretical	50.00	40.00	1.00	9.00
LNW4Mo16	49.3 ± 0.7	40.9 ± 0.6	1.9 ± 0.5	7.9 ± 0.2
Theoretical	50.00	40.00	2.00	8.00
LNW10Mo10	49.0 ± 0.3	41.3 ± 0.1	4.9 ± 0.2	4.8 ± 0.1
Theoretical	50.00	40.00	5.00	5.00
LNW16Mo4	50.1 ± 0.4	40.5 ± 0.2	7.5 ± 0.1	1.9 ± 0.1
Theoretical	50.00	40.00	8.00	2.00
LNW18Mo2	50.8 ± 0.7	40.3 ± 0.2	7.9 ± 0.1	0.9 ± 0.1
Theoretical	50.00	40.00	9.00	1.00
LNW20	48.8 ± 0.3	41.9 ± 0.2	9.3 ± 0.1	-
Theoretical	50.00	40.00	10.00	-

LNW16Mo4 and LNW18Mo2 exhibited similar particle sizes; however, LNW20 showed a decrease. As shown in **Figure 5.3.5**, raised stripes on the particle surfaces and grain boundaries were observed in LNW20. These stripes could arise from the appearance of the secondary phase. However, because of the detection limit, it was difficult to determine the composition based on the EDX analysis. As discussed in Section 5.2, the secondary phase could be either $La_2W_2O_9$ or $La_7Nb_3W_4O_{30}$, which are both W-rich phases. Therefore, it was assumed that the excess W cannot dissolve into the grains, forming W-rich phases in the surface and grain boundaries. As discussed in Section 2.4.2, the segregation of Sr towards grain boundaries in Sr substituted $LaNbO_4$ could cause a smaller grain size; therefore, the W-rich secondary phase assumed in this sample could also lead to a smaller particle size compared with LNW16Mo4 and LNW18Mo2. **Table 5.2** shows the normalised atomic fractions of cations of $LaNb_{0.8}W_xMo_{0.2-x}O_{4.1}$ series. Oxygen contents were excluded due to the potential contamination during the process of sample preparation. Results generally agreed with the theoretical stoichiometry.

5.4 Electrochemical properties of $LaNb_{0.8}W_xMo_{0.2-x}O_{4.1}$ series

Figure 5.4.1 shows the Arrhenius plot of the total conductivities of the $LaNb_{0.8}W_xMo_{0.2-x}O_{4.1}$ series measured under air from 500 °C to 900 °C. **Figure 5.4.2** shows one Nyquist plot of LNW20 as an example. It was observed that the total conductivities of Mo-rich samples ($x < 0.10$) were approximately one order of magnitude higher than those of W-rich samples ($x > 0.10$), with all W-rich samples exhibiting similar conductivities. This similarity in total conductivities among the W-rich samples could be attributed to the solubility limit of W mentioned in Section 5.2. The trend in conductivities suggested two possible conclusions: firstly, Mo dopants primarily influenced the electrochemical performance, as conductivity increased with increasing Mo content, with LNMo20 exhibiting the highest conductivities, except at 665 °C. Alternatively, in the phase diagram, the modulated structures disappeared in Mo-rich samples at high temperatures, existed only in the remaining compositions, suggesting a potential negative impact of the modulated structures on ionic conductivity, which has been discussed in Chapter 4. Further examination revealed the changes in the slopes of the conductivity plot at elevated temperatures in the Mo-rich samples ($x \leq 0.04$), correlating with changes in the activation energy of ion conduction, particularly evident in LNW2Mo18. The detailed analysis of LNW2Mo18 is discussed in Section 5.5.

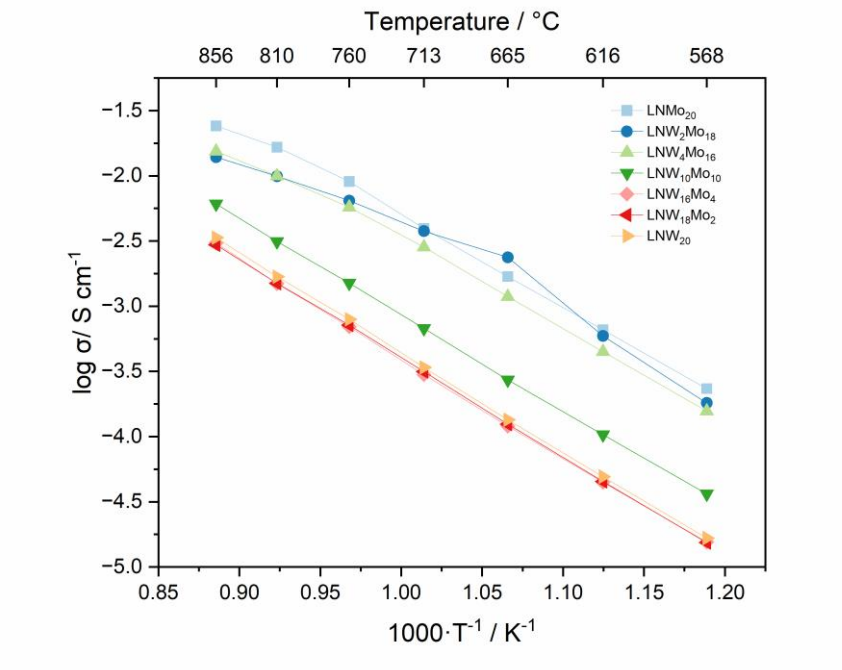


Figure 5.4.1. Total conductivities of the $LaNb_{0.8}W_xMo_{0.2-x}O_{4.1}$ series measured in the 500 °C – 900 °C temperature regime.

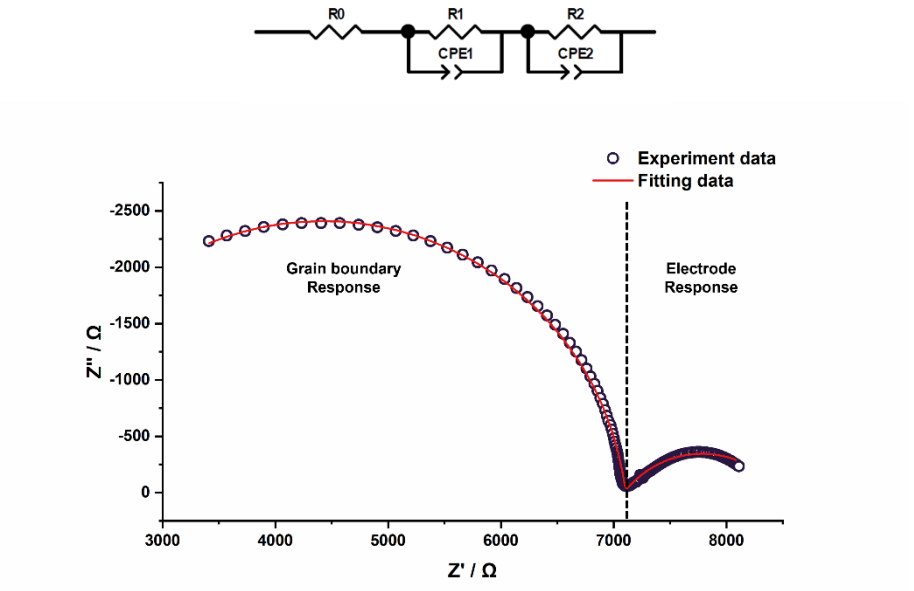


Figure 5.4.2. Impedance spectrum of LNW20 measured at 616 °C. The hollow circles represent the experimental data, and the red line represents the fitting results using the model in the inset.

Figure 5.4.3 shows the relationship between unit cell volumes and total conductivities of the $LaNb_{0.8}W_xMo_{0.2-x}O_{4.1}$ series at 856 °C, revealing a clear proportionality between volumes and conductivities. **Table A5** provides a summary of the refined parameters for all samples recorded at 850 °C from *in-situ* XRD. An unusual trend in both unit cell volumes and total conductivities was observed at 850 °C, dividing into two distinct regions. Remarkably, the volumes of Mo-rich samples ($x < 0.10$) were larger than those of W-rich samples ($x > 0.10$). A notable decline in volume occurred between x = 0.04 and x = 0.16, followed by a stabilisation thereafter. Although as discussed in Section 5.2, since the difference of ionic radius between W^{6+} (0.42 Å in 4-coordinate) and Mo^{6+} (0.41 Å in 4-coordinate) is small [76], the absolute change in volumes was negligible, this phenomenon could relate to the notion that a smaller lattice size may impede the transport of charge carriers, consequently decreasing the total conductivity. Combined with **Figure 5.2.3**, it became evident that all Mo-rich samples exhibited unmodulated structures at 850 °C, whereas all W-rich samples exhibited modulated structures. Therefore, the modulated structures, the unit cell volume and the emergence of the W-rich secondary phase all could contribute to detrimental effects on the total conductivities of these types of materials. It is worth noting that the conductivity of LNW2Mo18 was slightly lower than that of LNW4Mo16; however, at 850 °C, the

conductivities of all Mo-rich samples were in the range of 0.017(4) S cm^{-1}, which were higher than the conductivities of W-rich samples 0.003(0) S cm^{-1}. Results generally agreed with the conclusions.

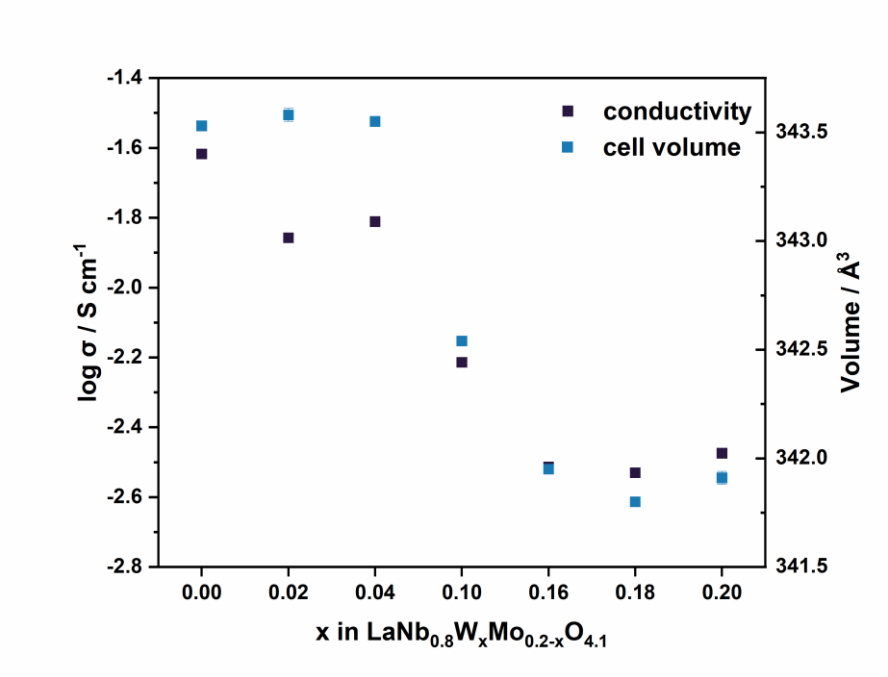


Figure 5.4.3. Unit cell volumes and total conductivities of $LaNb_{0.8}W_xMo_{0.2-x}O_{4.1}$ series at around 850 °C. Error bars are smaller than the symbols.

5.5 Detailed analysis of $LaNb_{0.8}W_{0.02}Mo_{0.18}O_{4.1}$

In this section, a comprehensive examination of LNW2Mo18 is described. **Figure 5.5.1** records the phase transition and lattice parameters of LNW2Mo18 from room temperature to 900 °C. LNW2Mo18 underwent a phase transition from m-phase to t-phase at 300°C, with the absence of the modulated structures observed at temperatures above 600°C. As the temperature increased from 25 °C to 300 °C, the *a* and *c* lattice parameters of the m-phase progressively converged to form the *a* lattice parameter of the t-phase, while *c* lattice parameter (*b* for m-phase) increased consistently throughout the whole temperature range. Within the t-phase, the *a* and *c* lattice parameters exhibited approximately linear growth with a fixed *β* angle of 90°. The unit cell volume displayed steady linear expansion in both m-phase and t-phase regions. The TECs along the *a* and *c* axis in the t-phase region were 11.4 × 10^{-6} K^{-1} and 13.3 × 10^{-6} K^{-1}, respectively, which led to an average TEC around 12.0 × 10^{-6} K^{-1}. These values were in the range of the one reported for Mo substituted $LaNbO_4$ (10.4 – 15.5 × 10^{-6} K^{-1})

[12], which suggested good thermomechanical compatibility with electrode materials like Ni-YSZ (10.3 – 14.1 × 10^{-6} K^{-1}) and LSM (11.2 × 10^{-6} K^{-1}) [12].

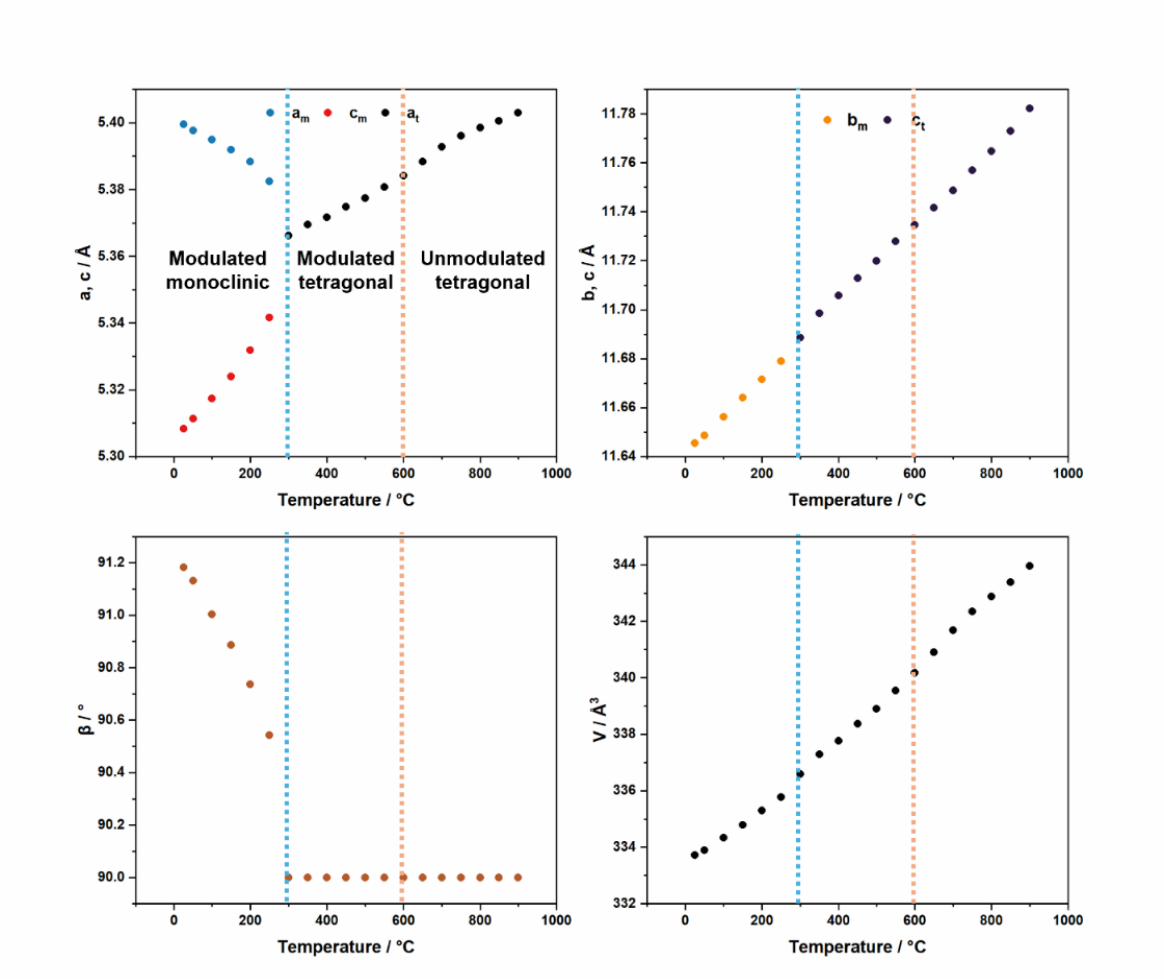


Figure 5.5.1. Lattice parameters *a*, *b*, *c*, *β* and volume of unit cell *V* of LNW2Mo18 within the temperature range from room temperature to 900 °C. 'm' and 't' symbolises m-phase and t-phase, respectively. Error bars are smaller than the symbols.

To ensure adequate data points for linear regression analysis to determine the activation energy, two additional EIS data points were measured at 475°C and 520°C for LNW2Mo18 (**Figure 5.5.2**). At 665°C, within a temperature range where the modulated structures disappeared, the activation energy decreased from E_2 of 1.80 eV to E_1 of 0.85 eV. A similar decrease of activation energy of 10 mol% Mo-substituted $LaNbO_4$ was observed in Chapter 4, where the activation energy decreased from 1.53 eV to 0.64 eV during the transition from a modulated to an unmodulated structure. The coincidence of the phase transition from modulated structure to unmodulated structure and the decrease in activation

energy of 0.90 eV suggested that modulated structures could adversely affect total conductivity. However, further investigation was still needed to conclusively ascertain this impact.

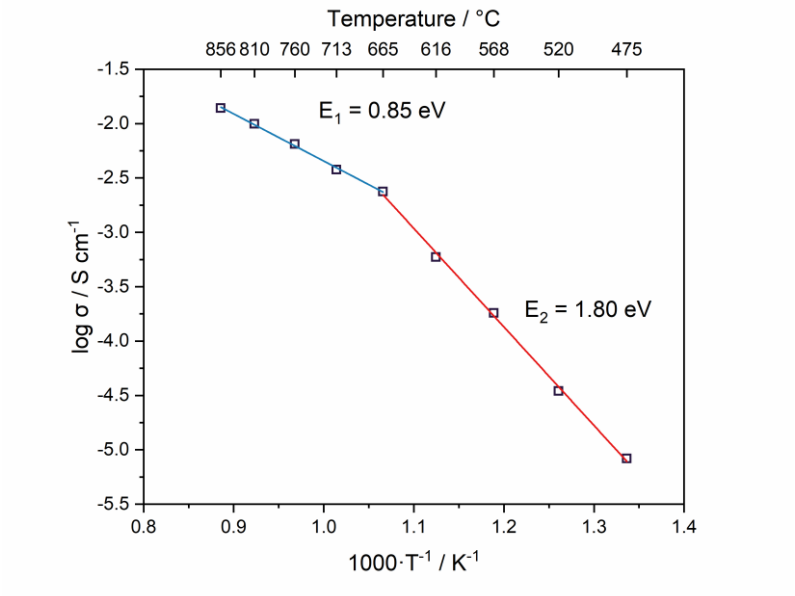


Figure 5.5.2. Arrhenius plot of the total conductivity of LNW2Mo18 with calculated activation energy.

5.6 Conclusion

In summary, the strategy of co-substituting W and Mo on Nb sites in $LaNbO_4$ could successfully reduce the phase transition temperature from m-phase to t-phase at room temperature. Most of the samples of $LaNb_{0.8}W_xMo_{0.2-x}O_{4.1}$ exhibited a single-phase structure after sintering; however, for the samples with higher W fraction (x = 0.18 and 0.20), a W-rich secondary phase appeared. As the W fraction increased, the particle sizes also increased; however, the particle sizes further slightly decreased because of the emergence of the W-rich secondary phase. The samples with higher Mo fraction exhibited higher total conductivities than the samples with higher W fraction, which verified the higher trapping effects of W than Mo. In addition, the detailed study of $LaNb_{0.8}W_{0.02}Mo_{0.18}O_{4.1}$ revealed a decrease in activation energy of oxygen ion conduction from modulated structure to unmodulated structure, which confirmed the negative effect of modulated structures on the electrochemical performance proposed in Chapter 4. Therefore, on one hand, slightly substituting Mo with W at the intermediate temperature range could eliminate the modulated structures; on the other

hand, more W could lead to higher trapping effects and secondary phase. These results provide a trade-off of the strategy of co-substituting W and Mo and will be useful in the development of a new type of oxygen ion conductor in different temperature ranges.

Chapter 6. Investigation of stability and oxidation states of Mo in $LaNb_{0.9}Mo_{0.1}O_{4.05}$ under different atmospheres

In this chapter, in order to investigate the stability and oxidation states of Mo in $LaNb_{0.9}Mo_{0.1}O_{4.05}$ under different atmospheres, several different characterisation methods were applied. The XPS results showed that there was a mixture of Mo^{6+} and other Mo species with lower oxidation states in the as-sintered sample; however, the TGA results showed there was no mass change for the as-sintered sample upon heating to 900 °C under compressed air. The XANES results also showed that the Mo in the as-sintered sample possessed an oxidation state of Mo^{6+} under static air. To further investigate the stability of Mo under different atmospheres, $LaNb_{0.9}Mo_{0.1}O_{4.05}$ was annealed under pure O_2, pure N_2, vacuum (around 1.6×10^{-8} mbar), and 5% H_2/N_2 at 800 °C for different dwell times, respectively. The XRD results showed that a secondary phase which resembled the undoped $LaNbO_4$ appeared under reducing atmospheres (vacuum and 5% H_2/N_2) and the colours of the samples also changed when annealed under different atmospheres with Tauc plots showing there was a large difference of the band gap between the as-sintered sample and the sample annealed under 5% H_2/N_2. The *in-situ* XANES results showed that the oxidation state of Mo in the sample annealed under 5% H_2/N_2 gradually changed from Mo^{5+} to Mo^{6+} from room temperature to 400 °C and stabilised at Mo^{6+} afterwards. The *in-situ* EXAFS results also showed the coordination environments of Nb sites of the sample annealed under 5% H_2/N_2 changed from an environment resembling the undoped $LaNbO_4$ back to one resembling the as-sintered $LaNb_{0.9}Mo_{0.1}O_{4.05}$. Therefore, all the changes in colour, structure and band gap could be related to the reduction of Mo^{6+} to Mo^{5+}. The EPR results also suggested the emergence of Mo^{5+} in the samples annealed under 5% H_2/N_2. The EIS results showed that after being annealed under 5% H_2/N_2 for 24 hours, $LaNb_{0.9}Mo_{0.1}O_{4.05}$ exhibited a lower activation energy than the as-sintered samples. Also, there was no difference of the total conductivities of the as-sintered sample measured under dry and humidified air; however, an increase in the total conductivity was observed under humidified 5% H_2/N_2 compared to the total conductivity measured under dry 5% H_2/N_2. These phenomena could be ascribed to the changes of the charge carriers and corresponding mechanism together with the reduction of Mo^{6+} to Mo^{5+}.

6.1 Introduction

As discussed in Chapter 4 and 5, Mo-substituted $LaNbO_4$ exhibited higher conductivity than W-substituted $LaNbO_4$ [12] and the modulated structures observed in these types of materials always led to a negative impact on the electrochemical performance [14][15]. Although Mo-substituted $LaNbO_4$ always exhibited a pure oxygen ion conduction under air [12][16], there was still a lack of study about the electrochemical performance of these type of materials under different atmospheric conditions. Cao *et al* measured the total conductivities of $LaNb_{0.8}Mo_{0.2}O_4$ under different dry and humidified atmospheres and claimed there was a contribution from proton conduction under humidified conditions [16]. However, the difference between the total conductivities under dry and humidified air was subtle and the mechanism used to explain the phenomenon was based on the proton conduction described by equation (2.2) [16]. The mechanism described by equation (2.2) was realised by oxygen vacancies, which was suitable for acceptor substituted $LaNbO_4$; therefore, it was not appropriate to use that mechanism to describe a system like Mo-substituted $LaNbO_4$, where the donor substituents were compensated by oxygen interstitials.

The authors also found after the EIS measurement under 5% H_2/N_2, the structure of $LaNb_{0.8}Mo_{0.2}O_4$ was changed to a structure resembling the undoped $LaNbO_4$ [16]. As shown in **Figure 6.1.1**, the reduced $LaNb_{0.8}Mo_{0.2}O_4$ could transition back to the structure of the as-sintered sample after being re-oxidised under air at 900 °C for 5 hours [16]. Based on the XPS results, the authors also suggested that there was a reduction of Mo in the samples from Mo^{6+} to lower oxidation states under reducing atmospheres, which could lead to a contribution of electronic conductivity; however, since the XPS measurements are inherently conducted under high vacuum conditions, and this technique is only sensitive to the surface composition, there was significant ambiguity as to the oxidation states of Mo in the bulk material of these samples [166]. Therefore, to clarify this, some other techniques which could measure the properties of the bulk material of these samples under ambient conditions should be considered.

Mo-substituted $LaNbO_4$ were proposed to work as better electrolytes than W-substituted $LaNbO_4$ because of their lower trapping effects on oxygen interstitials [8]; however, based on the possible reduction of Mo under reducing atmospheres, further investigation of the stability of Mo in these materials under different atmospheres was still

needed. In this chapter, the oxidation states of Mo at room temperature were determined by TGA, XPS, and XANES. The stability of Mo in $LaNb_{0.9}Mo_{0.1}O_{4.05}$ under other atmospheres, including O_2, N_2, vacuum and 5% H_2/N_2, was also investigated, especially focusing on the changes of the structure. The changes of Mo oxidation states and the corresponding coordination environments of Nb sites in $LaNb_{0.9}Mo_{0.1}O_{4.05}$ annealed under 5% H_2/N_2 were investigated by *in-situ* XANES and EXAFS. The relationship between the changes of structures and electrochemical performance was investigated and possible mechanisms of ion transportation of $LaNb_{0.9}Mo_{0.1}O_{4.05}$ under dry and humidified 5% H_2/N_2 were also proposed. The same notations for the samples as defined in Chapters 4 and 5 are used in this chapter. The as-sintered sample was denoted as ''Air'' and the samples annealed under pure O_2, pure N_2, vacuum (around 1.6×10^{-8} mbar) and 5% H_2/N_2 were denoted as ''O_2'', ''N_2'', ''Vacuum'' and ''H_2'', respectively from Section 6.3.

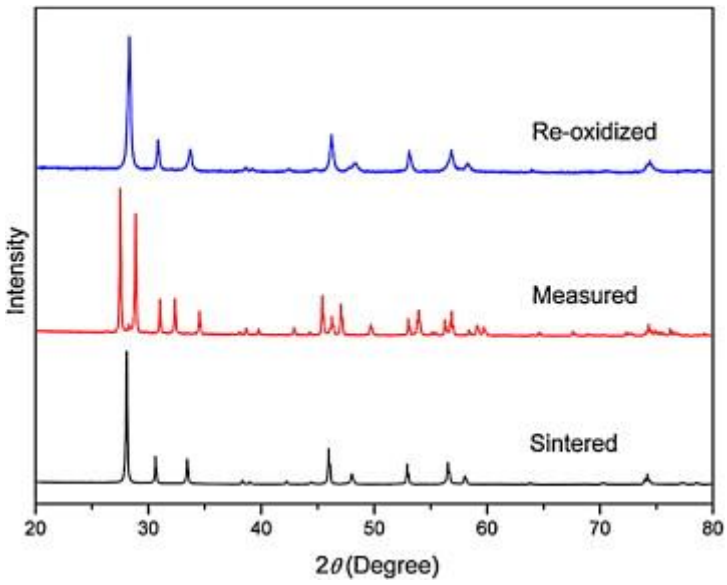


Figure 6.1.1. Room temperature XRD patterns of $LaNb_{0.8}Mo_{0.2}O_4$ after sintering, EIS measurement under 5% H_2/N_2 and reoxidisation under air at 900 °C for 5 hours. Reproduced with permission [16]. Copyright (2015), Elsevier.

6.2 Oxidation states of Mo in as-sintered LNM10

Figure 6.2.1 shows the TGA results of the as-sintered LNM10 measured from room temperature to 900 °C under compressed air. The mass change of the as-sintered LNM10 was in the range of 0.1%. It is also worth noting that this 0.1% mass change only happened at the initial stage of the heating process, and the mass stayed stable afterwards. The negligible

mass change could arise from the instrument errors, which means that there were no significant changes of oxygen stoichiometry and the Mo in the as-sintered LNM10 was stable under air, which possessed a fixed oxidation state [167].

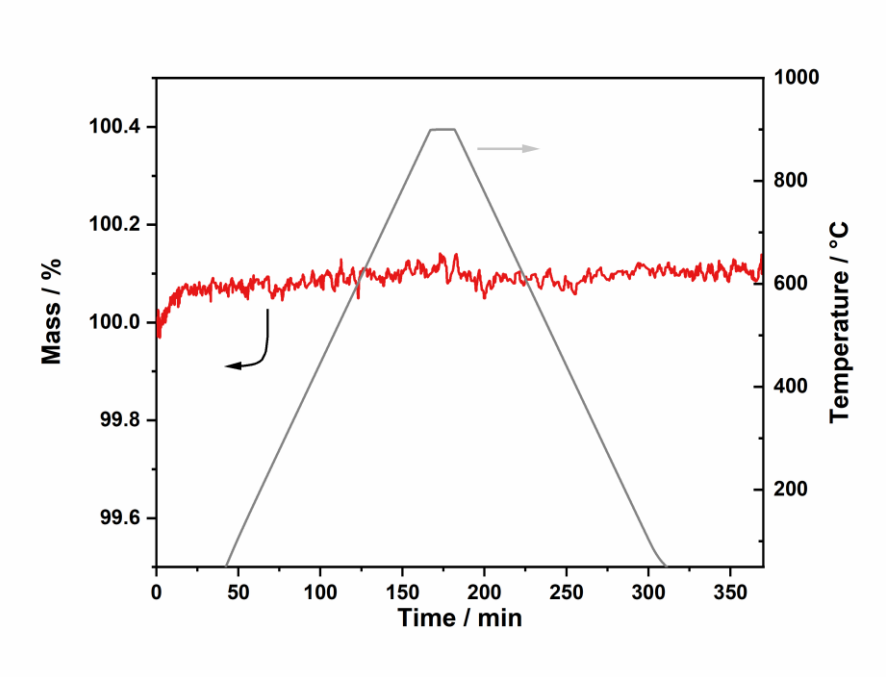


Figure 6.2.1. TGA results of the as-sintered LNM10 from room temperature to 900 °C with an isothermal heating time of 20 minutes under air.

To determine the oxidation state of Mo in the as-sintered LNM10 under air, XANES measurements were conducted for the sample at the Mo K-edge at room temperature under static air. **Figure 6.2.2** shows the normalised XANES results of the as-sintered LNM10 between 19,800 eV and 20,200 eV. Before the absorption edge (around 20,017 eV), an intense pre-edge feature at around 20,006 eV was observed. This pre-edge feature was related to the electric dipole transition from Mo 1*s* orbital to 4*d* orbital and the intensity of the pre-edge feature could be increased if the 4*d* orbital is emptier [168]. Therefore, a more pronounced pre-edge could be observed if the oxidation state of Mo is closer to Mo^{6+} [168]. However, there is not a quantitative relationship between the position or intensity of the pre-edge and the oxidation states of Mo; therefore, two other methods were used instead.

As reported by Zhou *et al*, there is a linear relationship between Mo oxidation states and their K-edge positions (E_0) [17][169]. As shown in **Figure 6.2.3**, a clear linear increase in the E_0 could be found with increasing the oxidation state of Mo from Mo foil to Mo^{6+} [17].

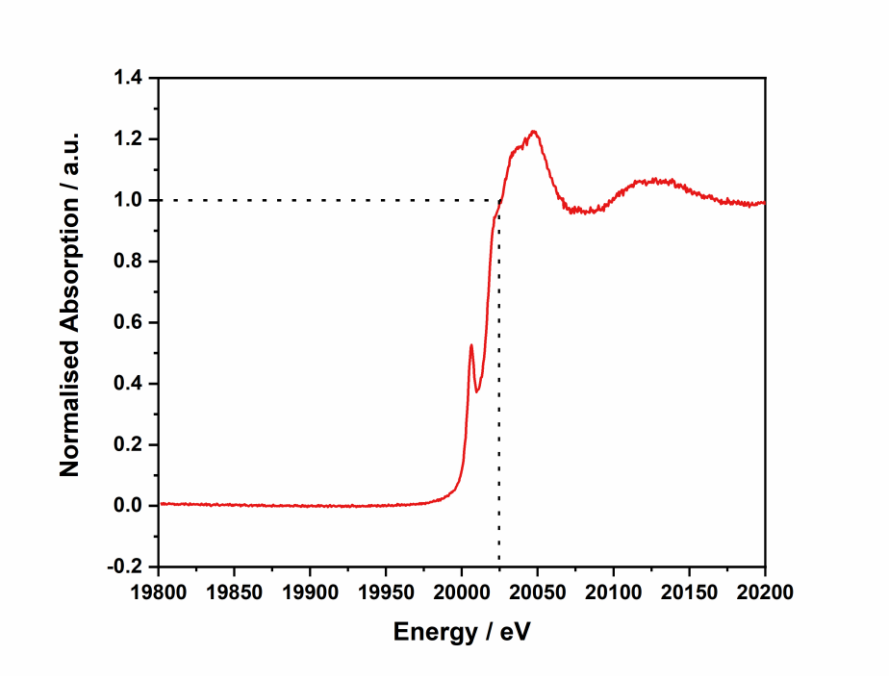


Figure 6.2.2. Normalised XANES spectrum of the as-sintered LNM10 from Mo K-edge at room temperature under static air. Data were calibrated to a Mo reference foil with a K-edge position of 20,000 eV. The dashed lines represent the energy when normalised absorption equals to 1.

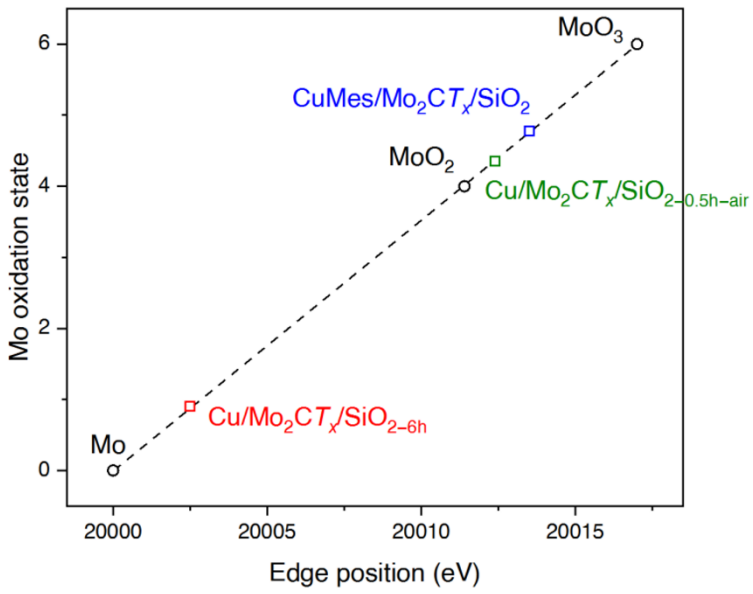


Figure 6.2.3. The relationship between Mo K-edge positions from XANES spectra of different materials and their corresponding Mo oxidation states. Reproduced with permission [17]. Copyright (2021), Nature.

From **Figure 6.2.3**, the difference (D_1) between the E_0 of a Mo foil and the E_0 of Mo with other oxidation states could be described by equation (6.1):

$$D_1 = 3x - 1 \quad (6.1),$$

where x represents the Mo oxidation state. From equation (6.1), it was suggested that if the oxidation state of Mo was Mo^{6+}, the value of D_1 should be around 17 eV. **Table 6.1** lists the E_0 values of the as-sintered LNM10 and the Mo foil used as the reference. The D_1 value of the as-sintered LNM10 was around 17 eV, which suggested that Mo in the as-sintered sample should possess an oxidation state of Mo^{6+}. It should be noted that in this method and the method discussed below, only the relative differences were calculated, which could not be influenced by whether the data were calibrated or not; therefore, all the values listed in **Table 6.1** were from the raw data before calibration.

To double check the oxidation states of Mo, another method proposed by Farges *et al*, where the energies when normalised absorption (μ) equals to 1 were compared, was used instead [168]. The dashed lines in **Figure 6.2.2** shows the example of how to determine this energy in the as-sintered LNM10. The difference (D_2) between the energy of Mo foil when normalised μ equals to 1 and the energy of Mo with other oxidation states when normalised μ equals to 1 could be described by equation (6.2):

$$D_2 = 2x - 1 \quad (6.2),$$

where x represents the Mo oxidation state and the value of D_2 should be around 11 eV if the oxidation state of Mo was Mo^{6+}. From the results listed in **Table 6.1**, the value of D_2 of the as-sintered LNM10 was around 11 eV. Combined with the E_0 value discussed above, it is suggested that the oxidation states of Mo in the as-sintered LNM10 should not be lower than Mo^{6+} under an air atmosphere. The XANES results were in good agreement with the TGA results, which confirm that the Mo^{6+} in the as-sintered LNM10 did not change on annealing under air.

Table 6.1. Values of K-edge positions, energies when normalised μ = 1 of the as-sintered LNM10 and the reference Mo foil and the differences (D_1 and D_2) among them. The values listed here are from the raw data without calibration.

Foil E_0	LNM10 E_0	D_1	Foil μ=1	LNM10 μ=1	D_2
19998.4 eV	20015.7 eV	17.3 eV	20013.6 eV	20024.7 eV	11.1 eV

However, the XPS results of the as-sintered LNM10 exhibited something different. As shown in **Figure 6.2.4**, based on the fitting results, three different Mo species with different Mo oxidation states could be observed. The peaks at around 232.6 eV, 231.4 eV and 230.0 eV could be assigned to the 3*d* 5/2 orbitals of Mo^{6+}, Mo^{5+} and Mo^{4+}, respectively [170]. The atomic ratio of these three species was around 75%:18%:7%. This result was different from what was reported by Cao *et al*, as the as-sintered $LaNb_{0.8}Mo_{0.2}O_4$ only possessed one oxidation state of Mo^{6+} while the sample after EIS measurement under 5% H_2/N_2 possessed a mixture of Mo^{6+} and lower oxidation states from their XPS results [16]. As mentioned in Section 6.1, the oxidation states of Mo could be influenced by the conditions of XPS measurements. For example, Jayaseelan *et al* reported that because of the Ar ions sputtering on the sample, the presence of Mo^{5+} was observed along with Mo^{6+}, and with increasing the sputtering time, the peak corresponding to the Mo^{5+} became more pronounced [171]. As a dual beam gun consisting of Ar ions and electrons was also used in this work to compensate the charge accumulation, the presence of various oxidation states of Mo in the as-sintered LNM10 may not arise from itself. Similar results were also reported by Uchida *et al* [172]. The authors found that the surface of $Bi_2Mo_3O_{12}$ was reduced due to the Ar ion beam and at least two oxidation states for Mo (Mo^{6+} and Mo^{5+}) were present on the reduced surface [172].

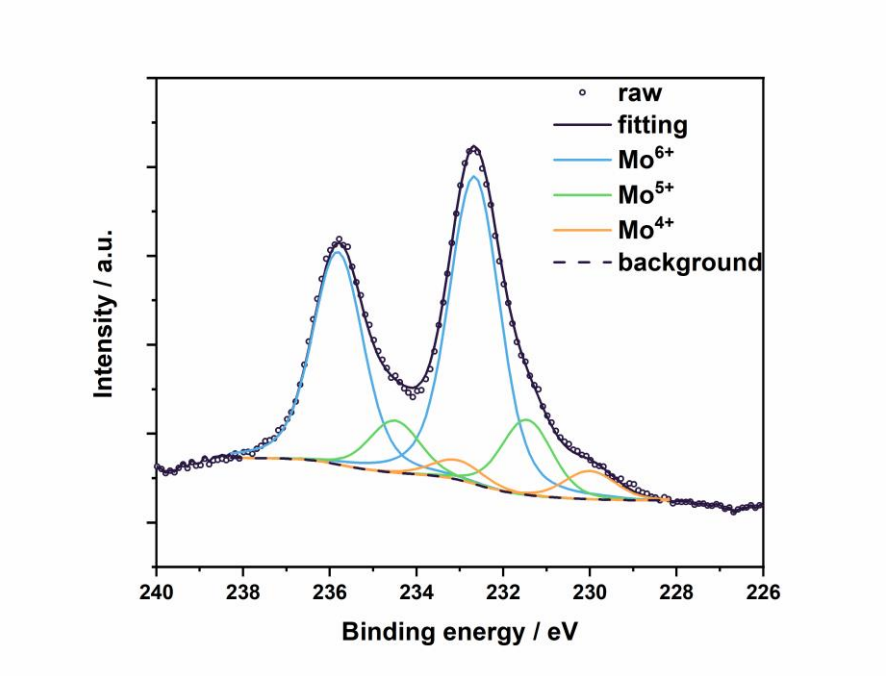


Figure 6.2.4. XPS spectra and the fitting results of Mo 3*d* orbitals of the as-sintered LNM10. The binding energy of C 1*s* peak (284.8 eV) was used for calibration.

To verify this, an iterative scan of Mo 3*d* orbitals on the precursor MoO_3 was conducted. **Figure 6.2.5** shows the XPS results of Mo 3*d* orbital in MoO_3 with different scan loops. It was clearly observed that there was a hump next to the main peak of Mo^{6+} and this hump became more pronounced when the sample was exposed under vacuum and Ar ion beam with longer time. This small hump represented the Mo species with lower oxidation states compared to Mo^{6+}; therefore, the Mo^{5+} and Mo^{4+} species observed in the as-sintered LNM10 could arise from the conditions of XPS measurement. It is also worth noting that the vacuum level of the XPS measurements in this work was around 10^{-7} mbar, where the oxygen partial pressure was in the reducing atmosphere range suggested by Johansen for W/Mo co-substituted $LaNbO_4$ [173]; therefore, except the Ar ion beam, the high vacuum condition of XPS measurement could also influence the oxidation states of Mo in LNM10.

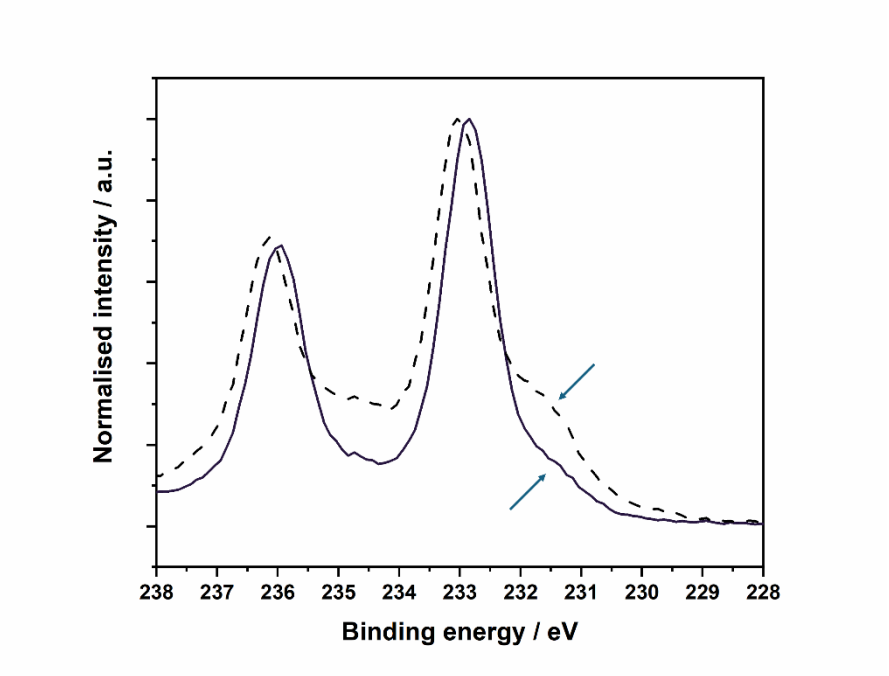


Figure 6.2.5. Iteration scan of Mo in MoO_3. The solid and dashed lines represent the 1st and 30th scan of the iteration, respectively. The humps from lower Mo oxidation states are marked by arrows. The binding energy of C 1*s* peak (284.8 eV) was used for calibration.

6.3 Study of LNM10 annealed under different atmospheres

As discussed in Section 6.2, the oxidation states of Mo in LNM10 were strongly influenced by different environments. To investigate the influence of different atmospheres for these types of materials, the as-sintered LNM10 was annealed under pure O_2, pure N_2, vacuum (around 1.6×10^{-8} mbar) and 5% H_2/N_2 at 800 °C for 2 hours, respectively. **Figure 6.3.1** shows the XRD patterns and colours of the annealed LNM10 and the as-sintered LNM10.

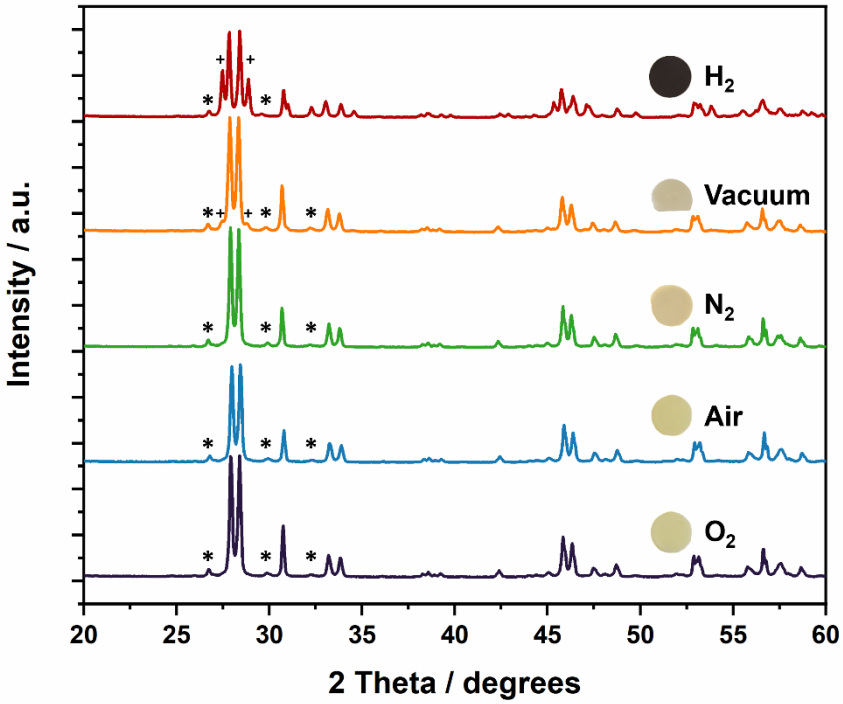


Figure 6.3.1. Room temperature XRD patterns of LNM10 after being annealed under different atmospheres at 800 °C for 2 hours. The satellite reflections of the modulated structures are marked by asterisks. The secondary phase observed after the sample being annealed under vacuum and 5% H_2/N_2 is marked by crosses.

It was clearly observed that there was a progressive darkening of the colours of the pellets from higher oxygen partial pressure (pure O_2) to lower oxygen partial pressure (5% H_2/N_2). The change of the colour of the materials containing Mo after being annealed under different atmospheres was not unprecedented. As reported by Arvizu *et al*, the as-deposited MoO_3 thin film would be bleached after being annealed under air at 300 °C for 2 hours and the colour of the as-deposited MoO_3 thin film would be darkened after being annealed under Ar at the same temperature and dwell time [174][175]. The change in the colour of MoO_3 under Ar could be ascribed to the significant narrowing of the band gap, which is also discussed for these types of materials. However, except for the changes in the colour, the as-deposited MoO_3 thin film also underwent a partial phase transition from higher symmetry orthorhombic phase to lower symmetry monoclinic phase after being annealed under Ar. Similar behaviour was also observed for the LNM10 composition in this work.

As shown in **Figure 6.3.1**, the modulated structures were found to exist under all atmospheres, although the intensity of one of features at around 32.2° 2θ was negligible under 5% H_2/N_2 atmosphere. However, the total structures changed when the atmosphere became more reducing. LNM10 possessed a single m-phase under both O_2 and N_2, which was similar to the as-sintered LNM10. However, a secondary phase emerged when the atmosphere changed to vacuum and 5% H_2/N_2. The secondary phase that emerged under reducing atmospheres matched well with the structure of the undoped $LaNbO_4$ [13], which should be considered as another m-phase with lower symmetry. Since the peaks from this secondary phase became more pronounced under 5% H_2/N_2 than under vacuum, it was suggested that a more reducing atmosphere could have a more obvious effect on the structure change of LNM10. Alternatively, under the same reducing atmosphere, a longer annealing time could have the same effect. **Figure 6.3.2** shows the XRD patterns of the as-sintered LNM10 annealed under 5% H_2/N_2 at 800 °C for different dwell time. A clear trend could be observed: the intensities of the peaks from the secondary phase gradually increased with LNM10 being annealed under 5% H_2/N_2 longer. Meanwhile, the intensities of the peaks related to the modulated structures became lower and disappeared when the dwell time was around 6 hours. When LNM10 was annealed under 5% H_2/N_2 at 800 °C with a dwell time of 8 hours, the structure totally transitioned to a structure resembling the undoped $LaNbO_4$ without the modulated structure. Similar results were reported by Cao *et al* for $LaNb_{0.8}Mo_{0.2}O_4$ as shown in **Figure 6.1.1** in Section 6.1 [16].

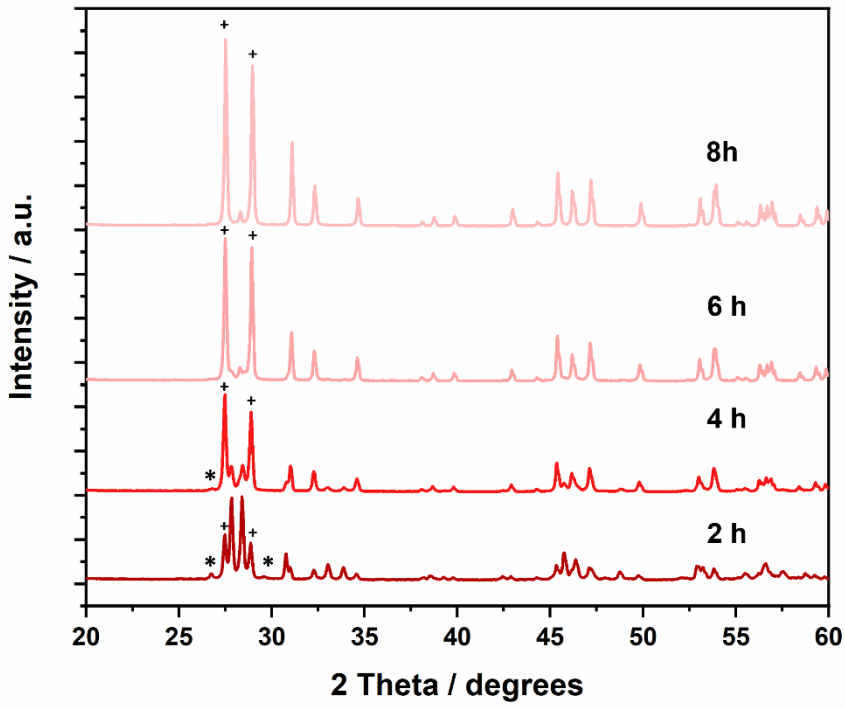


Figure 6.3.2. Room temperature XRD patterns of LNM10 after being annealed under 5% H_2/N_2 at 800 °C for different dwell times. The satellite reflections of the modulated structures are marked by asterisks. The secondary phase that emerged after the sample being annealed under 5% H_2/N_2 is marked by crosses.

However, it is worth noting that the reducing effects on the structural changes shown in **Figure 6.3.2** may only be suitable for Mo-substituted $LaNbO_4$ with 10 mol% Mo on Nb sites annealed under 5% H_2/N_2 at 800 °C with heating and cooling rates of 5 °C per minute, as there were many factors could influence the final structures. To simplify the context, a factor could lead to a structure with more secondary phase was described as exhibiting a better reducing effect in the discussion below. **Figure 6.3.3** shows the influences of the possible factors. Firstly, different Mo fractions on Nb sites could have different effects. As shown in **Figure 6.3.3** a), with the same annealing conditions, LNMo20 possessed more secondary phase than LNM10. This was unexpected since the structure change in these types of materials was always accompanied with the reduction of Mo from Mo^{6+} to Mo^{5+}, as discussed below. Theoretically, the reducing effect of the same annealing condition on a sample with more Mo fraction should be worse than in a sample with lower Mo fraction. For example, to

achieve the same reducing effect, a sample with more Mo fraction should need longer annealing time. However, the results showed LNMo20 was much easier to be reduced than LNM10; therefore, the reduction of Mo in these types of materials was not intuitive and needed to be further studied. Secondly, the effects of the reducing atmospheres were also influenced by the ‘‘hydrogen partial pressure’’. As shown in **Figure 6.3.1**, the as-sintered LNM10 annealed under vacuum and 5% H_2/N_2 exhibited different fractions of the secondary phase. The oxygen partial pressure in these two atmospheres should be almost the same; however, the hydrogen contents were different. Therefore, it was suggested that being annealed at the same temperature with the same dwell time, the sample exposed under an atmosphere with more hydrogen content should have a better reducing effect. Thirdly, as shown in **Figure 6.3.3** b), the sample annealed at different temperatures possessed different structures. The structures of the as-sintered LNM10 were almost unchanged before and after being annealed at 200 °C; therefore, there should be a trigger point of the temperature where the sample started to be reduced. Finally, only the dwell time was considered in the discussions above; however, the heating and cooling time could also have a significant influence. **Figure 6.3.3** c) shows the XRD patterns of the as-sintered LNM10 annealed under 5% H_2/N_2 at 800 °C for 8 hours with heating and cooling rates of 10 °C per minute. It was clearly observed that the one with a rate of 10 °C per minute still possessed a small residue of the original phase; however, the one with a rate of 5 °C per minute totally transitioned to the secondary phase. The heating and cooling rates determined the time of heating and cooling processes, which related to the time of the samples exposed to the reducing atmospheres; therefore, a quicker rate should exhibit worse reducing effect. As mentioned, there must be some trigger points of the temperature, hydrogen partial pressure and the time of sample exposed to the reducing atmospheres for the as-sintered LNM10 and the trigger points of the as-sintered LNM10 should be different from those of other samples with different Mo contents. However, these factors were closely related to each other. For example, if the annealing temperature was set at 900 °C, it would take longer time to reach this temperature point, which led to a longer exposure time of the samples under the reducing atmosphere.

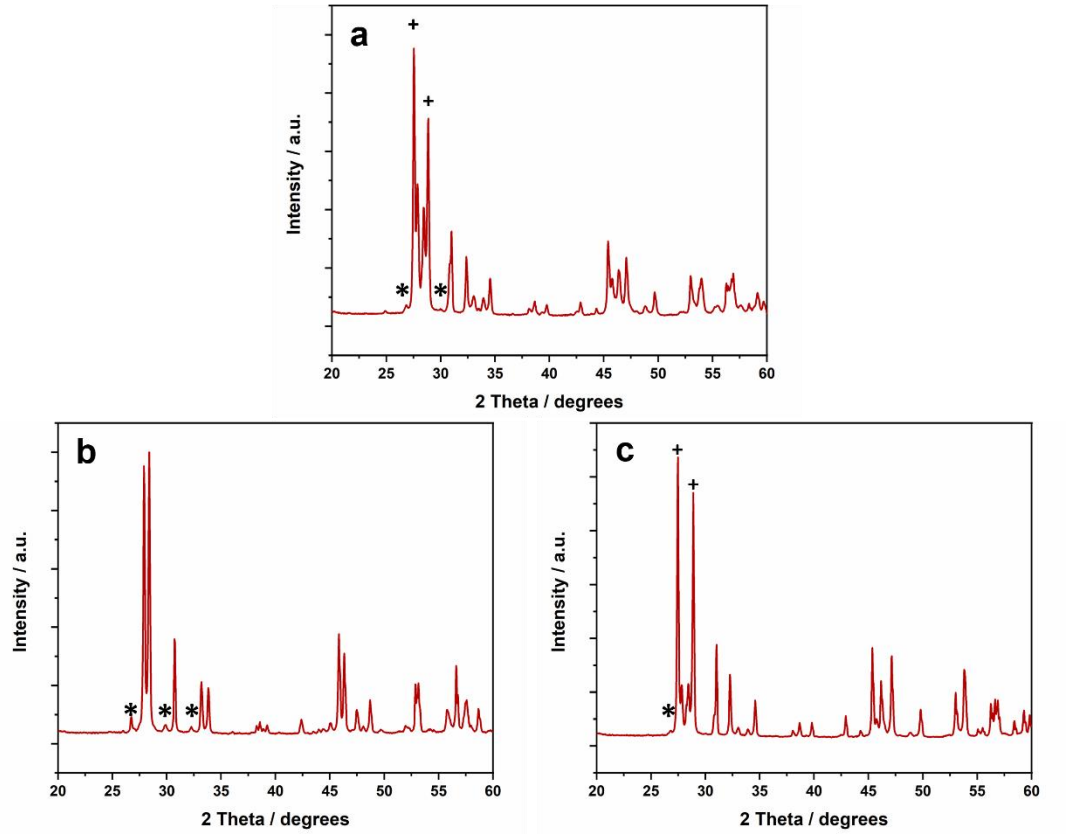


Figure 6.3.3. Room temperature XRD patterns of a) LNMo20 after being annealed under 5% H_2/N_2 at 800 °C for 2 hours, b) LNM10 after being annealed under 5% H_2/N_2 at 200 °C for 2 hours and c) LNM10 after being annealed under 5% H_2/N_2 at 800 °C for 8 hours with heating and cooling rates of 10 °C per minute. The satellite reflections of the modulated structures are marked by asterisks. The secondary phase is marked by crosses.

Since the structure of the as-sintered LNM10 annealed under 5% H_2/N_2 at 800 °C for 8 hours was close to the structure of undoped $LaNbO_4$ even without the modulated structure, it was proposed that during the exposure under the reducing atmospheres, the Mo in LNM10 was gradually reduced from Mo^{6+} to Mo^{5+}, which means the chemical formula of LNM10 would change from $LaNb_{0.9}Mo_{0.1}O_{4.05}$ to $La(Nb_{0.9}Mo_{0.1})O_4$. As discussed in Chapter 4, a smaller difference of 2θ positions between the peaks indexed as $(12\bar{1})$ and (121) in the XRD patterns indicated a relatively higher symmetry of the structure in these types of materials and vice versa; therefore, accompanied with the changes of colour and the reduction of Mo, there was also a decrease in the symmetry of LNM10 annealed under reducing atmospheres. To verify the existence of the formation of Mo^{5+}, EPR measurements were conducted on the selected samples. **Figure 6.3.4** shows the EPR results of some selected samples shown in **Figure 6.3.1**.

For the as-sintered LNM10, there was no obvious resonance peak observed in the spectra; however, for the sample annealed under 5% H_2/N_2, two peaks at around 340 mT and 380 mT were observed, which matched well with the EPR results reported by Farges *et al* for Mo^{5+} [168]. The resonance peaks were related to the unpaired 4*d* electron in Mo^{5+}, there were no peaks found in the spectrum of the as-sintered samples. Compared with the as-sintered sample, the sample annealed under N_2 exhibited a small hump at around 350 mT, which means there could be a small amount of Mo^{6+} reduced to Mo^{5+}; however, with the detection limits of XRD, there were no structural changes observed in this sample.

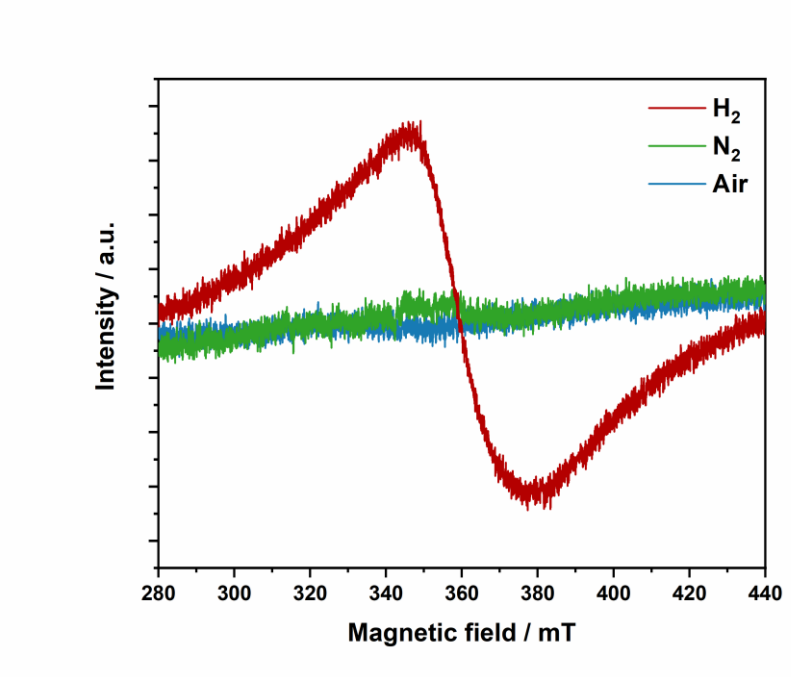


Figure 6.3.4. Room temperature EPR results of LNM10 annealed under different atmospheres at 800 °C for 2 hours.

As mentioned above, the changes of the colours of the samples could be related to the changes of the band gaps; therefore, the diffuse reflectance spectra of the samples shown in **Figure 6.3.1** were analysed. **Figure 6.3.5** shows the corresponding Tauc plots. The estimated band gaps of different samples were determined by the *x* axis intersections of the linear fits in the region showing a linear increase of light absorption in the Tauc plots [159]. Since the difference of the Tauc plots among the as-sintered sample and the samples annealed under O_2 and N_2 was negligible, only the band gap of the as-sintered sample was calculated. The results showed that the band gap energy of the sample annealed under 5% H_2/N_2 was around 1.13 eV, which was much lower than that of the as-sintered sample

(2.88 eV) and the sample annealed under vacuum (2.92 eV). A smaller band gap always leads to an absorption of a broader range of light [176]; therefore, the sample annealed under 5% H_2/N_2 was much darker than the others. The reason why the band gap energy became smaller in the sample annealed under 5% H_2/N_2 and its influences on the electrochemical performance are discussed in Section 6.5.

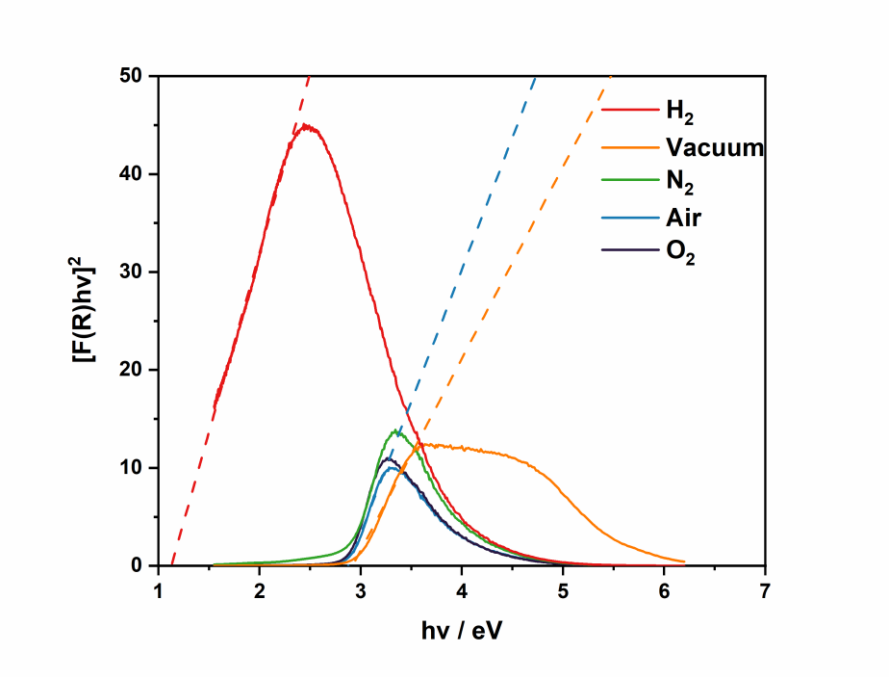


Figure 6.3.5. Tauc plots measured at room temperature of LNM10 annealed under different atmospheres at 800 °C for 2 hours. The dashed lines represent the linear fits.

Figures 6.3.6 and **6.3.7** show the microstructures of the cross-sections of the samples shown in **Figure 6.3.1**. Although the structures and the oxidation states of Mo changed in these samples, there were no obvious changes in their microstructures.

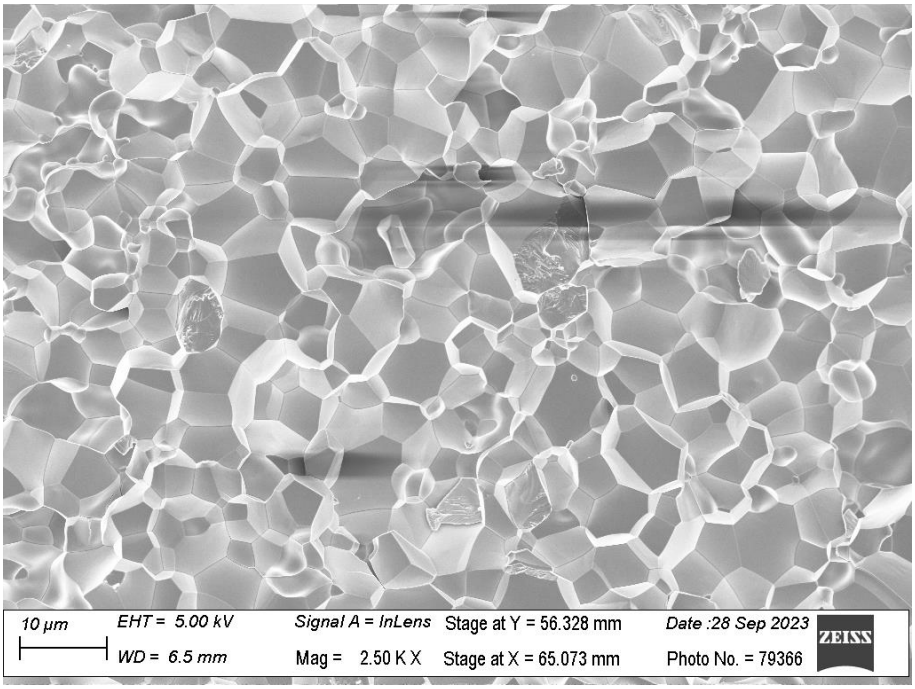


Figure 6.3.6. Microstructure of the cross-section of the as-sintered LNM10.

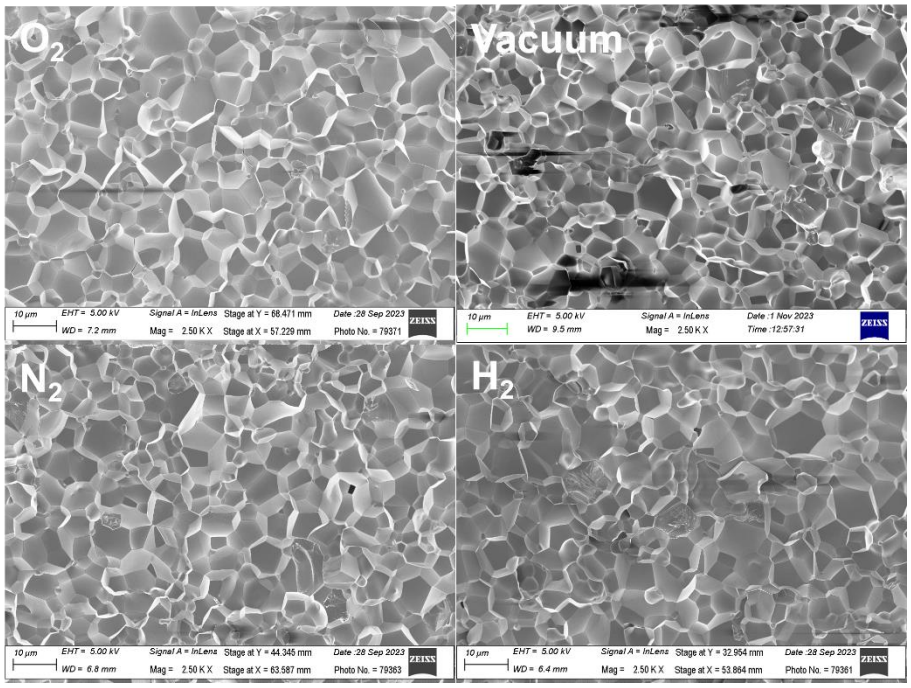


Figure 6.3.7. Microstructures of the cross-sections of LNM10 annealed under O_2, N_2, vacuum and 5% H_2/N_2 at 800 °C for 2 hours, respectively.

6.4 In-situ XAS study of LNM10 annealed under 5% H_2/N_2

To investigate the change of these types of materials during the reduction process, *in-situ* XAS measurements from room temperature to 800 °C were conducted on the

as-sintered sample and the sample annealed under 5% H_2/N_2 at 800 °C. It is worth noting that to ensure all the Mo in LNM10 was fully reduced from Mo^{6+} to Mo^{5+}, the reduced samples used for the *in-situ* XAS measurements were annealed under 5% H_2/N_2 at 800 °C for 24 hours. **Figure 6.4.1** shows the XRD patterns of the sample annealed under 5% H_2/N_2 at 800 °C for24 hours along with the XRD patterns of the annealed sample after being re-oxidised under static air at 800 °C for 4 hours. The sample annealed for 24 hours possessed the same structure as the undoped $LaNbO_4$ and when it was re-oxidised, the structure underwent a transition back to the structure of the as-sintered LNM10 with the resurgence of the modulated structures. Therefore, it indicated the reversible nature of the structural changes of these types of materials under different atmospheric conditions, which agreed well with the work reported by Cao *et al* [16].

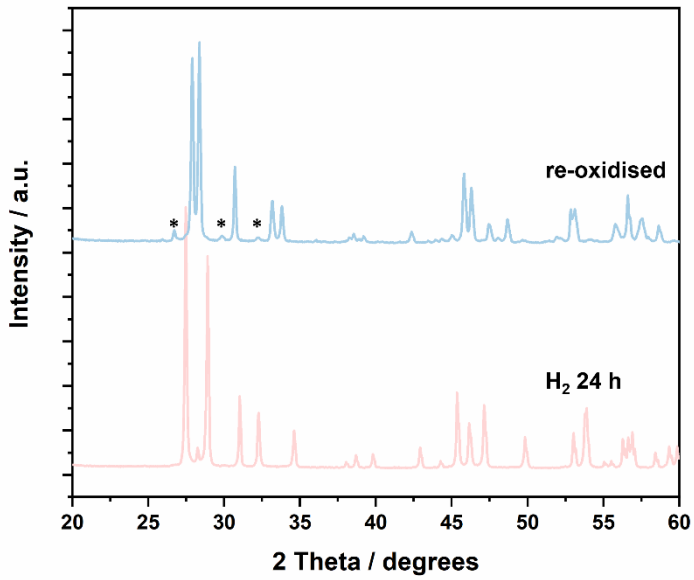


Figure 6.4.1. Room temperature XRD patterns of the as-sintered LNM10 annealed under 5% H_2/N_2 at 800 °C for 24 hours and it after being re-oxidised under static air at 800 °C for 4 hours. The satellite reflections of the modulated structures are marked by asterisks.

Figure 6.4.2 shows the XPS data obtained from the Mo 3*d* spectrum of the sample annealed for 24 hours. To be able to be compared with **Figure 6.2.4**, the fitting range here was also set from 238 eV to 228 eV. It was clearly observed there were also three peaks from three Mo species with different oxidation states. The peaks at around 232.7 eV, 231.3 eV and

229.5 eV could be assigned to the 3*d* 5/2 orbitals of Mo^{6+}, Mo^{5+} and Mo^{4+}, respectively [170]. As anticipated, the Mo in the as-sintered LNM10 should be totally reduced to Mo^{5+} after being annealed under 5% H_2/N_2 for 24 hours; however, there was still a contribution from Mo^{6+} in the XPS spectrum. The existence of Mo^{6+} from XPS results was also found in other materials which were supposed to only possess Mo with lower oxidation states [177]. As reported by Katrib *et al*, the surface of MoO_2 was partially covered by several layers of MoO_3 because of the oxidation of Mo^{4+} [177]. Therefore, even in MoO_2, the XPS results could reveal a greater contribution of Mo^{6+} (65%) in the surface of the materials [177]. Although the presence of Mo^{6+} in the surface of the sample annealed for 24 hours could lead to a deviation, the atomic ratio among Mo^{6+}, Mo^{5+} and Mo^{4+} changed from 75%:18%:7% (as sintered) to 57%:39%:4%. Such an increase in the fraction of the Mo species with lower oxidation states suggested the reduction of Mo in the samples. It is noted that there was also a small shoulder at around 228 eV, which was outside of the fitting range. This small shoulder could come from Mo species with even lower oxidation states [178].

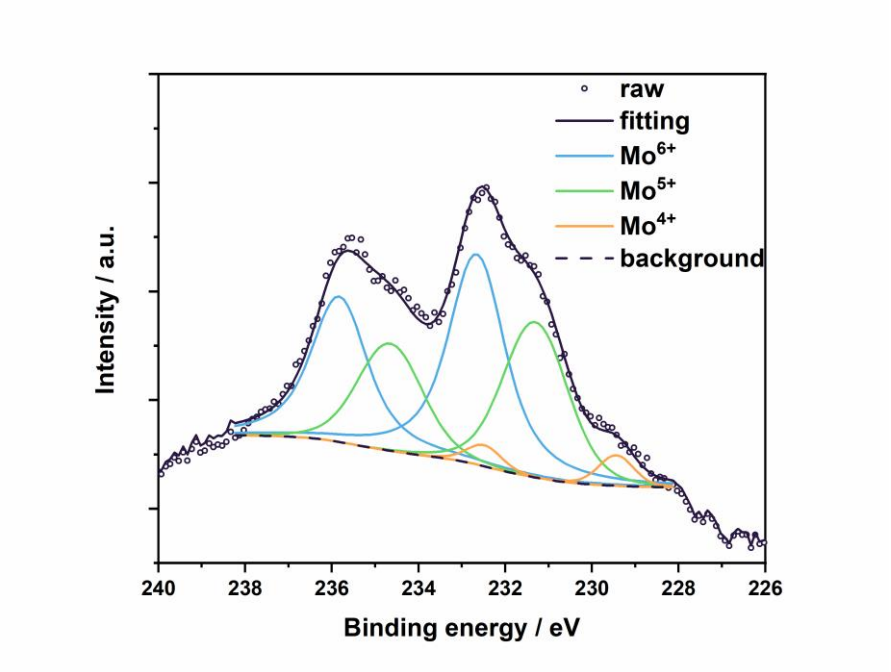


Figure 6.4.2. XPS spectra and the fitting results of Mo 3*d* orbitals of LNM10 annealed under 5% H_2/N_2 at 800 °C for 24 hours. The binding energy of C 1*s* peak (284.8 eV) was used for calibration.

Figure 6.4.3 shows the TGA results of the sample annealed for 24 hours measured from room temperature to 900 °C under compressed air. As expected, the colour of the

sample bleached back to the colour of the as-sintered LNM10. As defined by the dashed lines, there were three temperature regions of the sample during the heating process. When the temperature was lower than 100 °C, there was no obvious mass change observed (initial stage); when the temperature was above 100 °C, the mass of the annealed sample started to increase until the temperature reached around 350 °C (intermediate stage); the mass of the sample then stayed stable afterwards also in the cooling process (final stage). As mentioned in Section 6.3, if the Mo in the as-sintered LNM10 was fully reduced from Mo^{6+} to Mo^{5+}, the supposed chemical formula of LNM10 should be $La(Nb_{0.9}Mo_{0.1})O_4$. Therefore, the theoretical mass increase of the annealed sample under air should be around 0.27%. The mass change of the sample in the ''intermediate stage'' was around 0.33%, which was slightly higher (0.06%) than the theoretical value. It is noting that the sample only start to be oxidised when the temperature reaching at 100 °C under air. This suggested that there could also be a trigger point of temperature for the re-oxidation of the samples, which coincided with what was proposed for the reduction of the as-sintered LNM10. The detailed investigation of the three stages proposed for the annealed sample is discussed below with the *in-situ* XAS results.

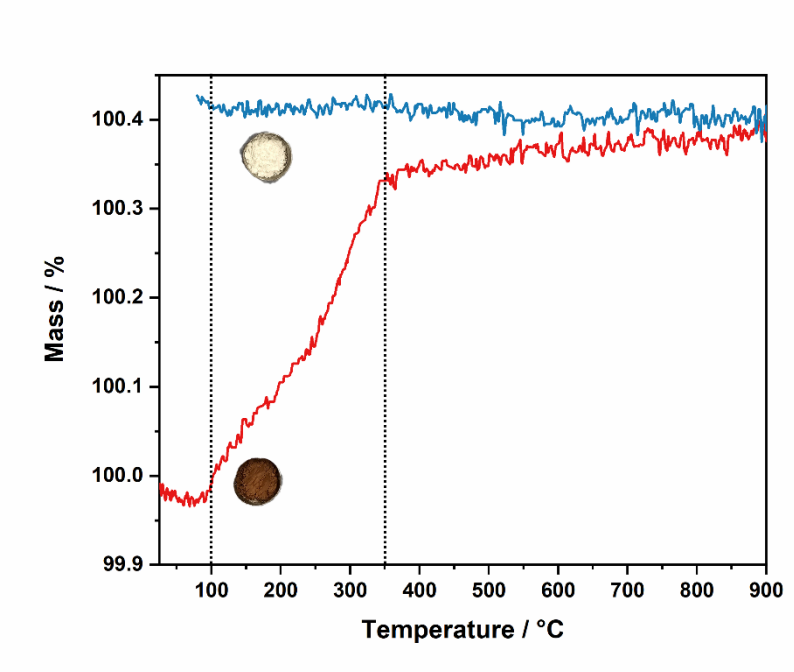


Figure 6.4.3. TGA results of LNM10 annealed under 5% H_2/N_2 at 800 °C for 24 hours measured from room temperature to 900 °C with an isothermal heating time of 20 minutes under compressed air. The dashed lines define the region where the mass changed. The red line and blue line represent the heating and cooling process, respectively.

Figure 6.4.4 shows the *in-situ* synchrotron XRD patterns of the annealed sample measured from 100 °C to 400 °C. It needs to be clarified that the peaks from BN used to dilute the sample are not marked in this work and the peaks from BN could be referred to the XRD patterns simulated in the figures. Compared with the *in-situ* synchrotron XRD patterns of the annealed sample measured at room temperature (**Figure 6.4.5**), there was no obvious change of the structure observed compared with the one measured at 100 °C except the slight peak shifts from the lattice expansion due to the heating.

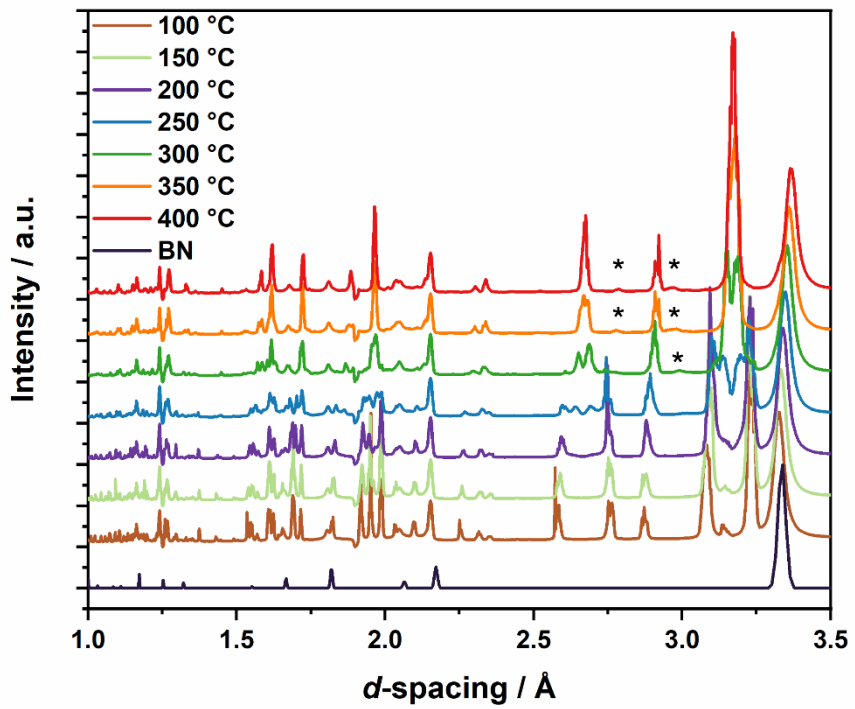


Figure 6.4.4. *In-situ* synchrotron XRD patterns of LNM10 annealed under 5% H_2/N_2 at 800 °C for 24 hours measured from 100 °C to 400 °C. The modulated structures are marked by asterisks. The simulated XRD pattern of BN was based on the data from Li *et al* [18].

During the heating process, it could be clearly observed that the structure of the annealed sample changed from a structure with lower symmetry to one with higher symmetry as the peaks at around 3.07 Å and 3.21 Å merged into one (3.17 Å). The modulated structures also emerged from around 300 °C. When the temperature reached at 400 °C, the annealed sample exhibited a similar structure to the as-sintered sample at 400 °C (**Figure 6.4.5**). The structure change of the annealed sample could readily be related to the phase transition of

these types of materials from m-phase to t-phase, which was also shown in **Figure 6.4.5** for the as-sintered sample. However, a close examination of the XRD patterns of the annealed sample measured at 250 °C revealed there was also a coexistence two m-phases.

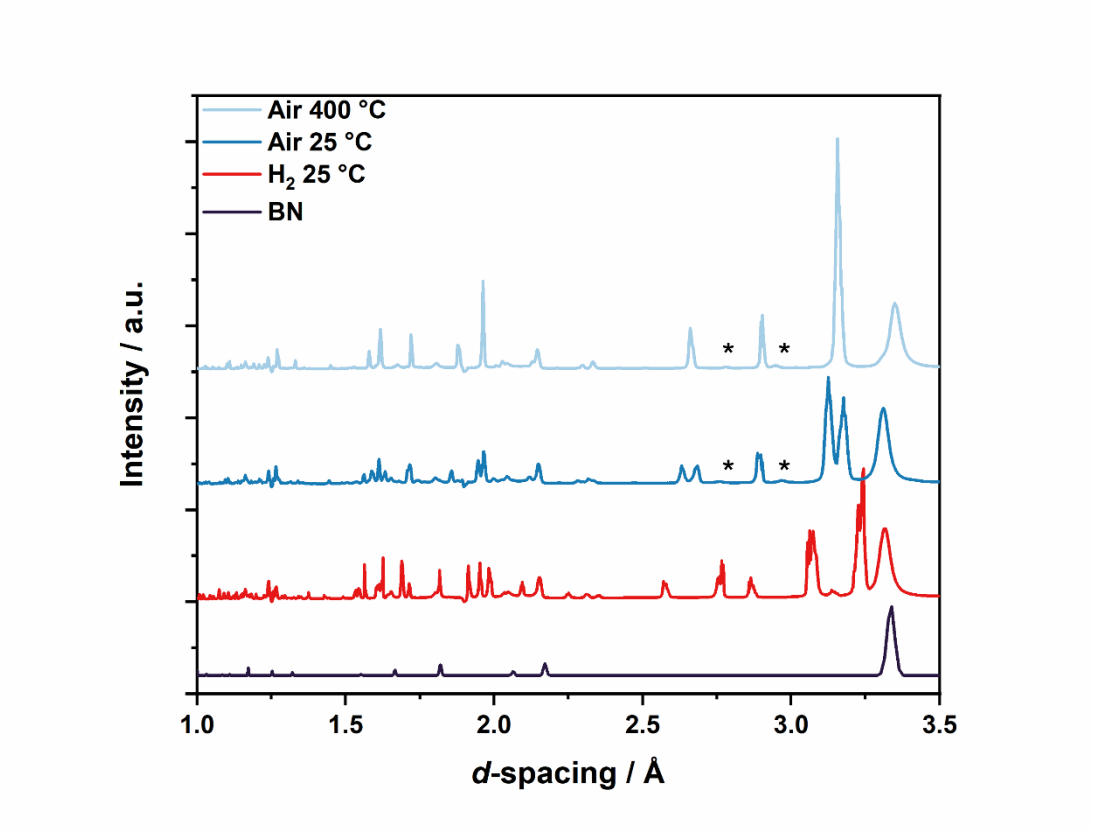


Figure 6.4.5. Synchrotron XRD patterns of the as-sintered LNM10 and LNM10 annealed under 5% H_2/N_2 at 800 °C for 24 hours measured at different temperatures. The modulated structures are marked by asterisks. The simulated XRD pattern of BN was based on the data from Li *et al* [18].

As shown in **Figure 6.4.6**, two pairs of peaks marked by crosses emerged in the annealed sample measured at 250 °C. The peaks at around 2.64 Å and 2.69 Å represented the lattice planes (002) and (200), and the peaks at around 3.13 Å and 3.19 Å represented the lattice planes (121) and $(12\bar{1})$, respectively. As discussed in Chapter 4, during the phase transition from m-phase to t-phase, the as-sintered LNM10 only exhibited a merger of these two pairs of peaks without the emergence of another set of peaks. Therefore, these two pairs of peaks should come from another m-phase. Since the difference of *d* positions between the peaks from $(12\bar{1})$ and (121) in the new emerging m-phase was smaller than the one in the original m-phase, this new emerging m-phase was related to the structure resembling the

as-sintered LNM10, which possessed a higher symmetry than the annealed sample. Therefore, except the typical phase transition from m-phase to t-phase, there was also a gradual oxidation of the Mo^{5+} back to Mo^{6+} during the heating process, which could also be confirmed by the resurgence of the modulated structures. A similar but opposite process could be found in **Figure 6.3.2**. It is also worth noting that the synchrotron XRD patterns of the annealed sample exhibited a trend where below 100 °C, there was no structure changes; however, the structure of the annealed sample started to change from 100 °C and finished around 400 °C. Therefore, three stages defined as ''initial stage'', ''intermediate stage'' and ''final stage'' were observed again, which was similar to the TGA result.

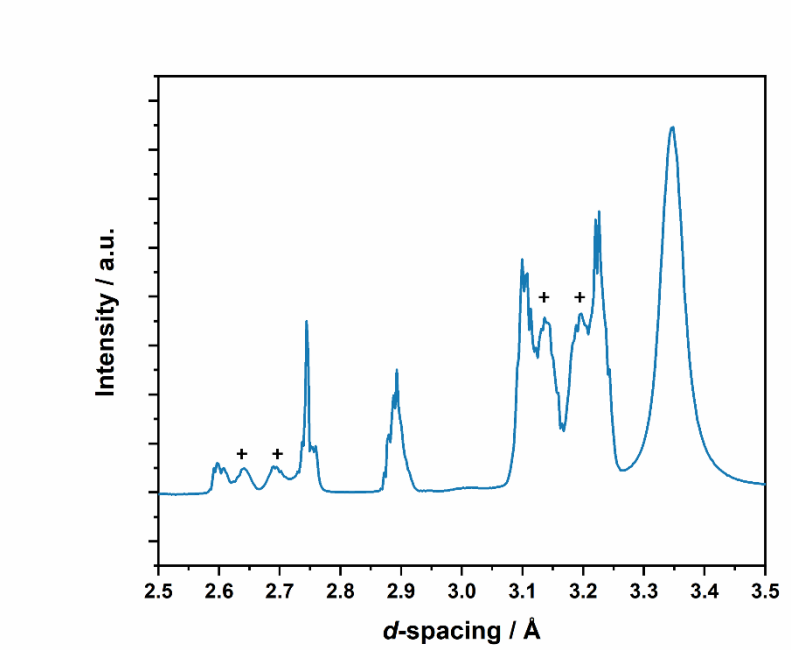


Figure 6.4.6. Zoom-in synchrotron XRD patterns of LNM10 annealed under 5% H_2/N_2 at 800 °C for 24 hours measured at 250 °C. The peaks from the m-phase with higher symmetry are marked by crosses.

Figure 6.4.7 shows the *in-situ* XANES results of the annealed sample measured from 100 °C to 400 °C. As shown in the inset, there was a clear shift in the E_0 to higher energy of the annealed sample with increasing temperature. When the temperature was above 400 °C, the values of E_0 were almost unchanged. **Figure 6.4.8** shows the values of difference (D_1) between the E_0 of the annealed sample and the E_0 of its corresponding reference Mo foil at each temperature point. The oxidation states of Mo at each temperature point were calculated using equation (6.1).

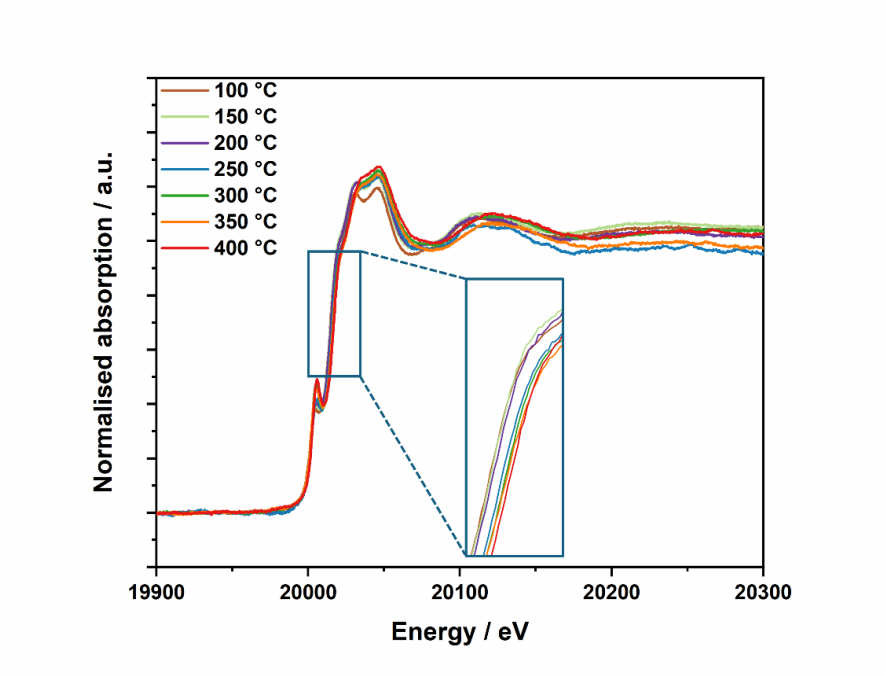


Figure 6.4.7. *In-situ* Mo K-edge XANES results of LNM10 annealed under 5%H_2/N_2 at 800 °C for 24 hours measured from 100 °C to 400 °C The inset shows the shift of E_0. Data were calibrated to a Mo reference foil with a K-edge position of 20,000 eV.

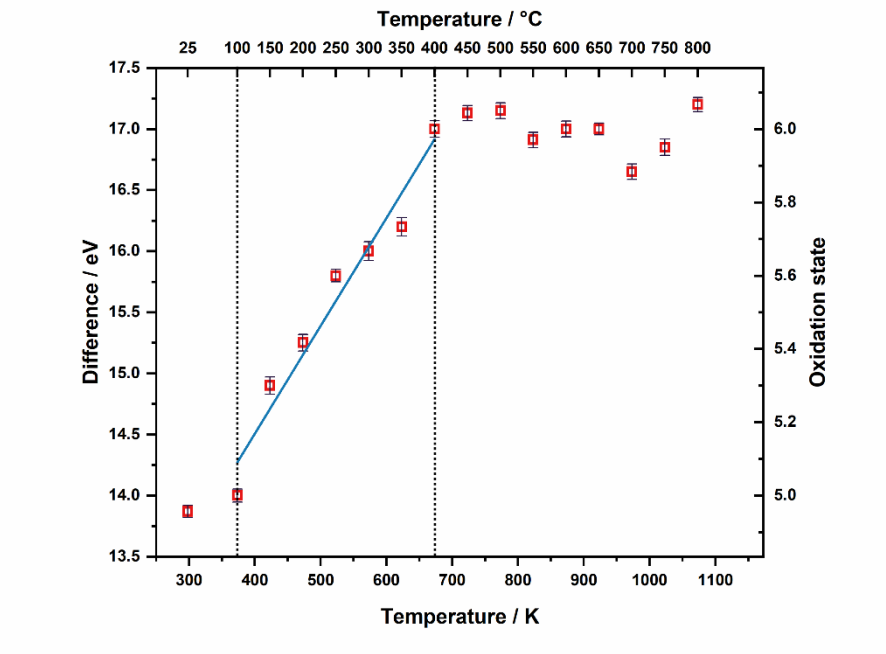


Figure 6.4.8. Values of D_1 and the calculated oxidation states of Mo in the annealed sample from room temperature to 800 °C. The blue line represents the linear fitting in the temperature range from 100 °C to 400 °C. Different stages are defined by dashed lines.

At room temperature, the calculated oxidation state of Mo in the annealed sample was Mo^{5+}. The calculated oxidation states of Mo then increased from 100 °C and became stable when the temperature reached around 400 °C. The final oxidation state of Mo was around Mo^{6+}. Three stages defined by dashed lines could be observed in **Figure 6.4.8**, which were similar to what was found in the TGA and *in-situ* synchrotron XRD results. In the ''varying stage'' (100 °C to 400 °C), a linear fitting of the oxidation state against the temperature was conducted and the relationship between them could be described by equation (6.3):

$$y = 0.00294 \times x + 3.993 \quad (6.3),$$

where y represents the oxidation state of Mo and x represents the temperature with units in K. Therefore, the oxidation state of Mo in the annealed sample increased linearly with increasing temperature and the starting temperature of re-oxidisation was around 100 °C based on the TGA, *in-situ* synchrotron XRD and XANES results. However, as shown in **Figure 6.4.9**, except the changes in the oxidation states of Mo, there was something else also varying in the annealed sample during the re-oxidation.

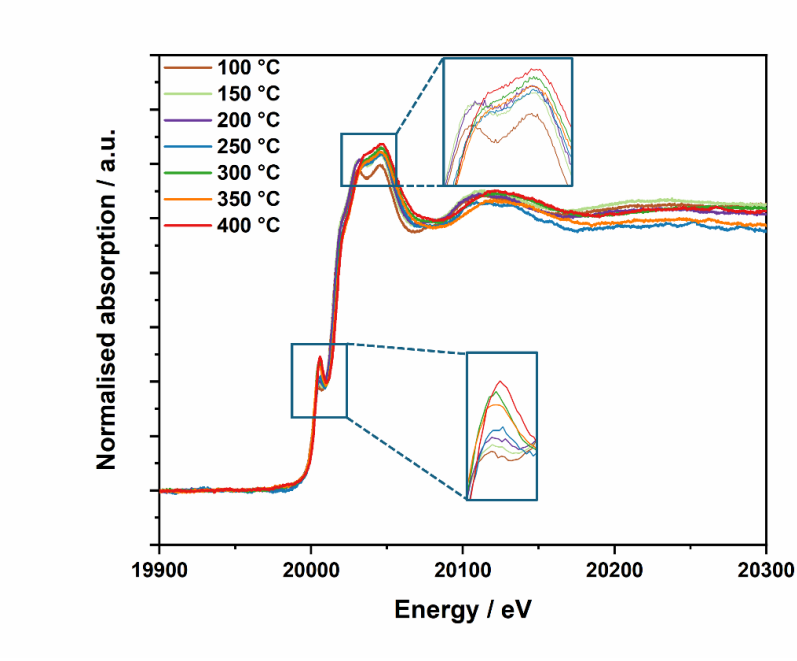


Figure 6.4.9. *In-situ* Mo K-edge XANES results of LNM10 annealed under 5% H_2/N_2 at 800 °C for 24 hours measured from 100 °C to 400 °C The insets show the changes at different energy ranges. Data were calibrated to a Mo reference foil with a K-edge position of 20,000 eV.

It was clearly observed there was an increase in the intensities of the pre-edges. As mentioned in Section 6.2, this could be related to the increase of the oxidation states of the Mo. However, this increase could also be related to the different coordination environments of the Nb sites of the annealed samples at different temperature points. As shown in **Figure 6.4.10**, the intensity of the pre-edge of the as-sintered LNM10 measured at 800 °C was slightly higher than that at room temperature, with Mo at both temperature points possessing an oxidation state of Mo^{6+}.

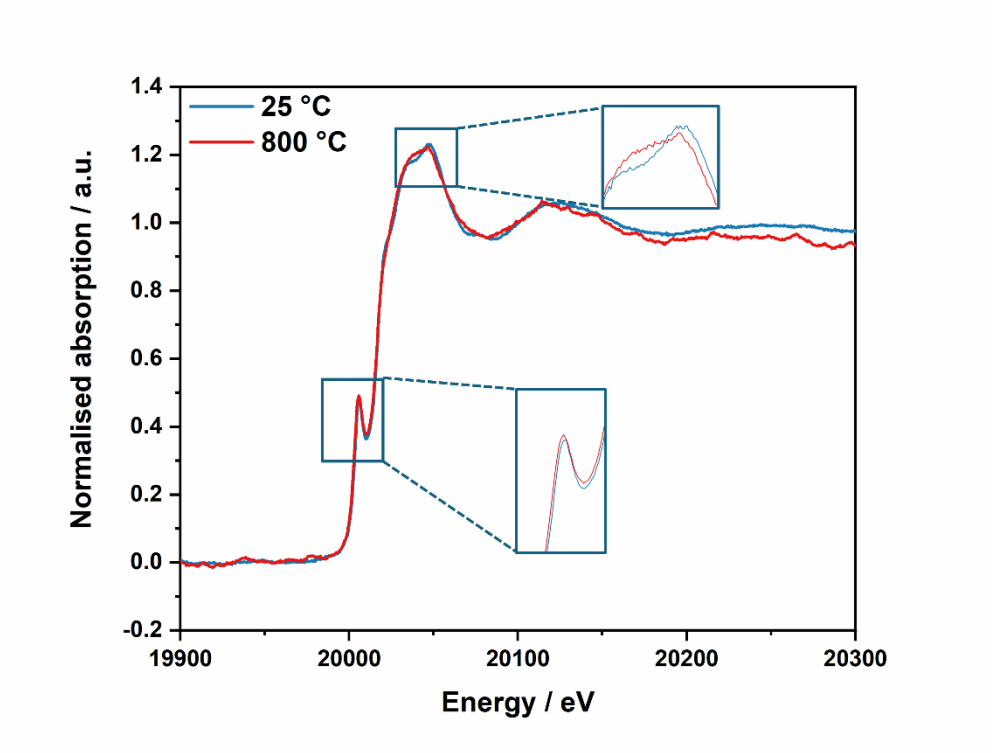


Figure 6.4.10. Mo K-edge XANES results of the as-sintered LNM10 measured at room temperature and 800 °C The insets show the changes at different energy ranges. Data were calibrated to a Mo reference foil with a K-edge position of 20,000 eV.

As suggested by Yamamoto, the intensity of the pre-edge for Mo with an octahedral environment was smaller than that with a tetrahedral environment [179]. This was due to the different covalencies of the Mo-O bonds in different coordination environments [180]. The pre-edge feature arose from the 1*s* to 4*d* transition because of the combination of 4*d*-5*p* mixing of Mo and the hybridisation of Mo 4*d* orbitals and O 2*p* orbitals [181]. Compared with the octahedral environment, the tetrahedral environment possessed lower symmetry and Mo-O bonds with higher covalency, which led to a stronger 4*d*-5*p* mixing of Mo; therefore,

more pronounced pre-edge features were observed [181]. Smith *et al* also reported the intensity of the pre-edge of $BaMoO_4$ was higher than $BaMoO_3$ because of the tetrahedral geometry [182][183]. As mentioned in Chapter 2, the coordination environments of Nb sites for m-phase $LaNbO_4$ and t-phase $LaNbO_4$ should be octahedral and tetrahedral, respectively. As shown in **Figure 6.4.4**, there was also a m-phase to t-phase transition of the annealed sample with increasing the temperature; therefore, the changes of the intensities of the pre-edges matched well with the suggested changes of the coordination environments of the Nb sites. Another change was found in the energy range from 20,030 eV to 20,050 eV with increasing temperature (upper insets of both Figure **6.4.9** and **6.4.10**). For the sample measured at lower temperatures, there were always two clearly distinguished peaks in that range, while with increasing the temperature, these two peaks merged into one broader peak. The peak at around 20,033 eV was related to the Mo 1*s* to 5*p* transition [184] and this peak was more pronounced in octahedral environments than it in tetrahedral environments [185]. Similar results were also observed in the Nb K-edge XANES spectra. As shown in Figure **6.4.11**, at room temperature, there were two distinguished peaks in the energy range from 19,000 eV to 19,050 eV; however, with increasing temperature, these two merged into one.

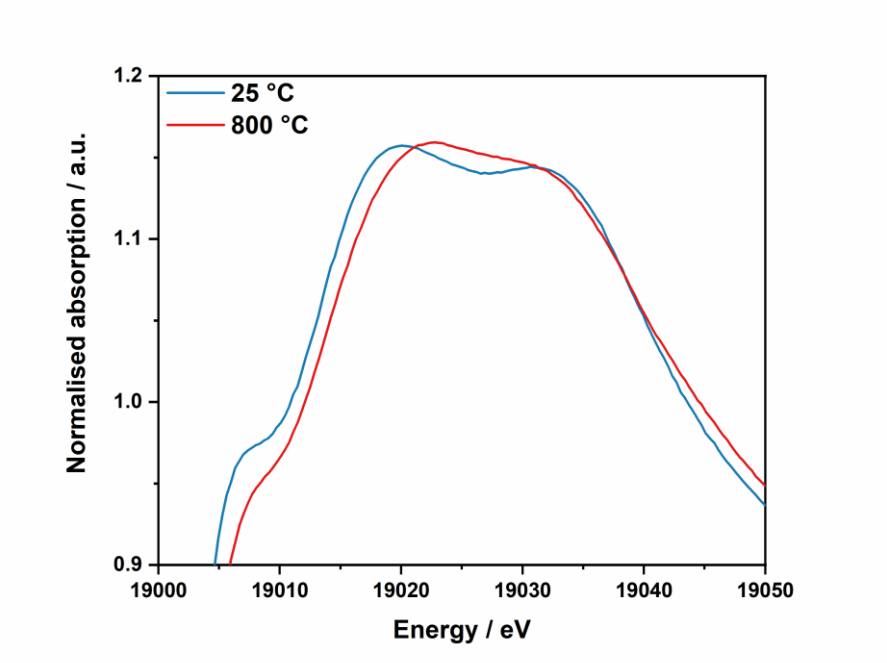


Figure 6.4.11. Nb K-edge XANES results of the as-sintered LNM10 measured at room temperature and 800 °C in the energy range from 19,000 eV to 19,050 eV. Data were calibrated to a Nb reference foil with a K-edge position of 18,986 eV.

Therefore, all the changes discussed above for the annealed sample could be related to the changes of the coordination numbers of the Nb sites. However, the Mo content in the studied sample was low as this was a dilute sample, which led to noisy EXAFS spectra; therefore, Nb *in-situ* EXAFS data were used to determine the coordination numbers of the Nb sites for the samples. **Figure 6.4.12** shows the fitting results of the EXAFS of the annealed sample measured at room temperature as an example. Since the coordination numbers of Nb sites were only related to the Nb-O bonds, the fitting range was set from 1 Å to 2 Å in *R* space. **Table 6.2** and **6.3** list the derived structural parameters for the samples at different temperature points from the EXAFS fitting results. The amplitude deduction factor S_0^2 was fit using the reference Nb foil EXAFS spectrum, and a value of 1.03 ± 0.12 was obtained. As the value of S_0^2 should be less than 1.00 [150], S_0^2 was set as 1.00 for all the fittings. The result of the undoped $LaNbO_4$ measured at room temperature in **Table 6.3** was used as a reference.

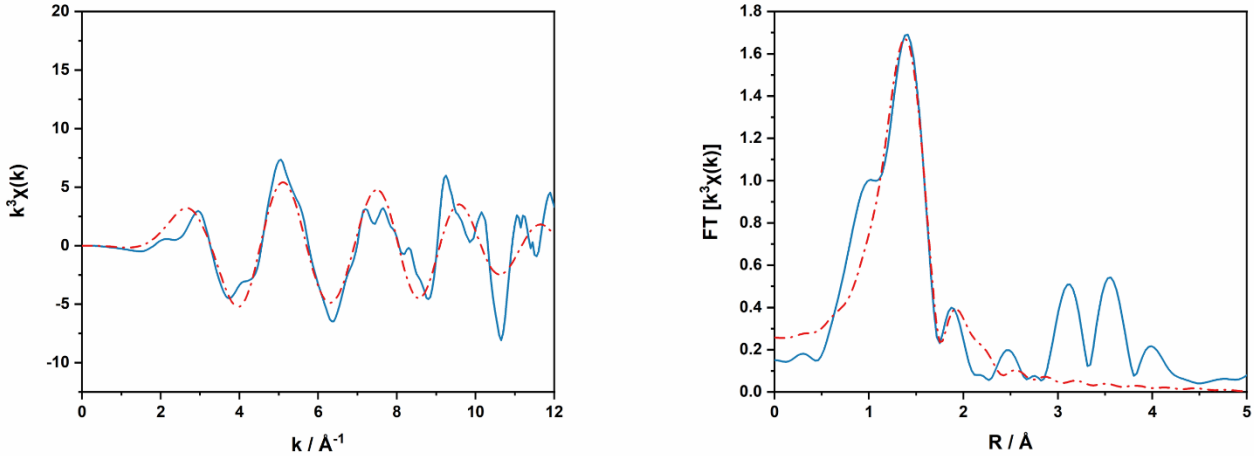


Figure 6.4.12. The fitting results of (left) $k^3\chi(k)$ and (right) Fourier transform (FT) of the $k^3\chi(k)$ of the EXAFS results of annealed sample measured at room temperature. The blue and red lines represent the raw data and fitting results, respectively.

Table 6.2. The derived structural parameters for the annealed sample at different temperature points (Temp). ''CN'' and ''d'' represent the average coordination number and bond length, respectively.

Temp (°C)	CN	d (Å)	R-factor	σ^2	ΔE_0
25	6.25 ± 0.91	1.884 ± 0.012	0.016	0.005 ± 0.001	-3.788 ± 2.041
100	6.13 ± 0.91	1.877 ± 0.013	0.017	0.005 ± 0.002	-4.637 ± 2.083
150	6.04 ± 0.78	1.871 ± 0.012	0.028	0.006 ± 0.001	-6.072 ± 1.826
200	5.96 ± 0.90	1.872 ± 0.013	0.015	0.006 ± 0.002	-5.491 ± 2.108
250	5.85 ± 0.94	1.870 ± 0.013	0.015	0.006 ± 0.002	-5.637 ± 2.241
300	5.55 ± 0.92	1.869 ± 0.013	0.016	0.005 ± 0.002	-5.877 ± 2.343
350	5.55 ± 0.95	1.867 ± 0.014	0.019	0.005 ± 0.002	-5.589 ± 2.411
400	4.52 ± 0.55	1.867 ± 0.011	0.011	0.005 ± 0.001	-7.620 ± 1.725
450	4.53 ± 0.45	1.865 ± 0.009	0.025	0.005 ± 0.001	-8.446 ± 1.375
500	4.62 ± 0.53	1.866 ± 0.010	0.009	0.005 ± 0.001	-7.835 ± 1.617
550	4.51 ± 0.51	1.865 ± 0.010	0.009	0.005 ± 0.001	-8.299 ± 1.588
600	4.59 ± 0.59	1.864 ± 0.012	0.014	0.005 ± 0.002	-8.648 ± 1.821
650	4.69 ± 0.57	1.862 ± 0.011	0.012	0.006 ± 0.001	-8.389 ± 1.703
700	4.70 ± 0.60	1.862 ± 0.011	0.012	0.006 ± 0.001	-8.368 ± 1.768
750	4.69 ± 0.67	1.862 ± 0.013	0.015	0.006 ± 0.002	-8.099 ± 1.989
800	4.66 ± 0.62	1.860 ± 0.012	0.014	0.006 ± 0.001	-8.140 ± 1.866

As shown in **Table 6.2** and **6.3**, for the annealed sample, when the temperature was at 25 °C, the average coordination number of Nb sites was close to that of the undoped $LaNbO_4$, which suggested that after being annealed for 24 hours, the structure of the LNM10 was fully reduced to an undoped $LaNbO_4$ structure because of the reduction from Mo^{6+} to Mo^{5+}. As mentioned in Chapter 2, at room temperature, the Nb in $LaNbO_4$ has octahedral environments forming NbO_6 units with 2 long Nb-O bonds and 4 short Nb-O bonds. It is worth noting that all Nb-O bonds were considered as identical here; therefore, the bond lengths reported here at room temperature (1.881 Å) were shorter than the longer bonds (1.919 Å/2.596 Å) but longer than the shorter bonds (1.810 Å) from the reported ND data [63]. Although there was a simplification for the bond lengths, the average coordination number of Nb sites at room temperature from the EXAFS results was still around 6. With increasing temperature, the average coordination number gradually changed and matched with that of

the as-sintered sample at around 350 °C. This temperature point was close to the temperature discussed in relation to the *in-situ* synchrotron XRD results where the structure of the annealed sample underwent a transition back to the structure of the as-sintered sample. The average coordination number then dramatically decreased to around 4.5 when the temperature reached 400 °C as the oxygen interstitials were located in the middle of two tetrahedral NbO_4 units forming a new unit of Nb_2O_9 [8]. This temperature point again matched well with the proposed final temperature point of the ''intermediate stage'' discussed above. When the temperature was above 400 °C, there were no more obvious changes for the average coordination number of the Nb sites for the annealed sample. For the as-sintered sample, the initial value of the average coordination number was around 5.5 because of its higher symmetry compared to the undoped $LaNbO_4$ and it did not change when the temperature was below 400 °C. The average coordination number changed at 400 °C because of the m-phase to t-phase transition, then remained around 4.5 afterwards.

Table 6.3. The derived structural parameters for the as-sintered sample at different temperature points (Temp) and them for the undoped $LaNbO_4$ at room temperature. ''CN'' and ''d'' represent the average coordination number and bond length, respectively.

Temp (°C)	CN	d (Å)	R-factor	σ^2	ΔE_0
$LaNbO_4$	6.36 ± 0.89	1.881 ± 0.012	0.013	0.007 ± 0.002	-3.537 ± 1.941
25	5.42 ± 0.81	1.874 ± 0.014	0.013	0.005 ± 0.001	-4.893 ± 2.116
200	5.34 ± 0.89	1.866 ± 0.014	0.020	0.005 ± 0.002	-5.768 ± 2.344
250	5.56 ± 0.92	1.866 ± 0.014	0.019	0.006 ± 0.002	-6.164 ± 2.325
300	5.58 ± 0.95	1.870 ± 0.013	0.018	0.006 ± 0.002	-5.508 ± 2.389
350	5.37 ± 0.82	1.868 ± 0.013	0.015	0.005 ± 0.002	-5.478 ± 2.151
400	4.54 ± 0.49	1.864 ± 0.009	0.009	0.005 ± 0.001	-7.998 ± 1.541
450	4.49 ± 0.58	1.868 ± 0.011	0.013	0.005 ± 0.002	-7.800 ± 1.823
500	4.57 ± 0.43	1.864 ± 0.008	0.020	0.005 ± 0.001	-8.525 ± 1.304
550	4.33 ± 0.53	1.866 ± 0.011	0.013	0.005 ± 0.001	-7.553 ± 1.745
600	4.43 ± 0.61	1.866 ± 0.012	0.016	0.005 ± 0.002	-7.852 ± 1.947
650	4.51 ± 0.78	1.866 ± 0.015	0.027	0.006 ± 0.001	-7.713 ± 2.412
700	4.32 ± 0.73	1.866 ± 0.015	0.026	0.005 ± 0.002	-7.544 ± 2.395
750	4.39 ± 0.82	1.864 ± 0.017	0.034	0.005 ± 0.002	-7.793 ± 2.644
800	4.39 ± 0.74	1.860 ± 0.015	0.028	0.005 ± 0.002	-8.514 ± 2.402

It is worth noting that due to the finite fitting range in *R* space, the fitting process cannot perfectly resolve fine structures [149]. The mathematical model, which is described by equation (3.19), essentially averages the possible structural configurations, introducing broader uncertainty ranges in coordination number that represents averaged structural characteristics [149]. However, the results generally agreed with the trend of the change of the coordination number of these types of materials during a phase transition from m-phase to t-phase; therefore, the reducing atmosphere could not only drive the reduction of the Mo from Mo^{6+} to Mo^{5+}, but also drive the LNM10 from a higher symmetry structure to a lower symmetry structure. Since both the oxidation states of Mo and the structure of LNM10 changed, there should also be a change of the electrochemical performance which is discussed in section 6.5.

6.5 Electrochemical study of LNM10 under different atmospheres

Figure 6.5.1 shows the total conductivities of the as-sintered sample and the annealed sample measured from 450 °C to 900 °C under corresponding atmospheres. For the as-sintered sample measured under air, the results were comparable to what was discussed in Chapter 4 and the change of the slope in the elevated temperature range (above 810 °C) could be related to the disappearance of the modulated structures. For the annealed sample measured under 5% H_2/N_2, a clear decrease in the slope could be observed compared with the slope of the as-sintered sample measured under air. The calculated activation energy measured under dry 5% H_2/N_2 (0.61 eV) in the temperature range from 472 °C to 856 °C was much lower than that measured under dry compressed air (1.53 eV) in the temperature range from 472 °C to 810 °C. As discussed in Section 6.4, the oxidation state of Mo in LNM10 under air should be Mo^{6+} and it should be fully reduced to Mo^{5+} when annealed for 24 hours. Therefore, the as-sintered sample under air should possess a pure oxide ion conductivity as reported before [12][14]. However, the change of the activation energy under reducing atmosphere should be related to the changes of the mechanism or the charge carriers.

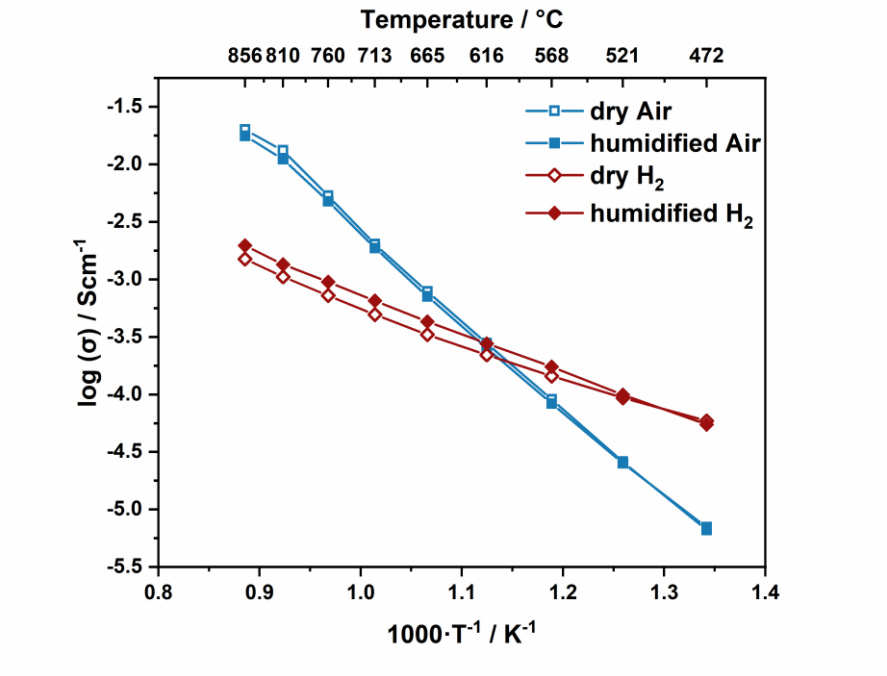


Figure 6.5.1. Total conductivities of the as-sintered LNM10 measured under compressed air and LNM10 annealed under 5% H_2/N_2 at 800 °C for 24 hours measured under 5% H_2/N_2 in the temperature range of 450 °C to 900 °C.

As discussed in Section 6.3 with the Tauc plot, the sample annealed under 5% H_2/N_2 exhibited a smaller band gap. This change in the band gap could be related to an intermediate band within the original band gap because of Mo^{5+} [186]. As reported by Ansari *et al*, GeTe substituted with Mo always exhibited a smaller band gap compared to the pure GeTe because of the presence of the intermediate band [186]. As reported by Reddy *et al*, during the reduction of MoO_3 to MoO_2, the formation of the Mo^{5+} species was observed [187]. It was suggested the presence of the Mo^{5+} could change the conductivity because of the Mo 4*d*1 electronic configuration, since the 4*d*1 state, which was close to the conduction band minimum, could provide an additional state [187]. **Figure 6.5.2** shows the schematic representations of the band gap structures of the as-sintered sample and the annealed sample. Because of the reduction of Mo^{6+} to Mo^{5+}, an intermediate band (IB) was introduced to the original band gap structure. The presence of IB caused the forbidden gap to be divided into two narrower sub gaps: upper gap and lower gap. This division could facilitate the energetic excitation of the valence electrons to the conduction band (CB), since the IB could effectively act as a ‘‘stepping stone’’ for electron transitions [186]. Since instead of directly crossing the original forbidden gap from the valence band (VB) to the CB, electrons could

utilise the lower gap to transition to the IB first, followed by a subsequent jump across the upper gap to the CB. Therefore, the decrease in the activation energy in the annealed sample measured under 5% H_2/N_2 could be related to the electronic conductivity because of the change of the band gap structure due to the presence of Mo^{5+}.

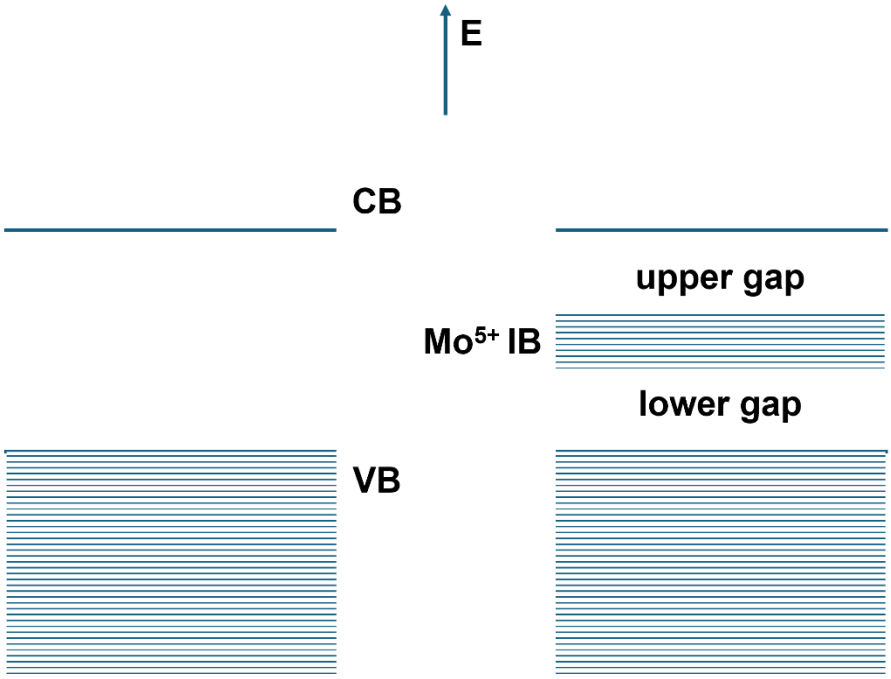


Figure 6.5.2. Energy-band scheme for (left) the as-sintered LNM10 and (right) LNM10 annealed under 5% H_2/N_2 at 800 °C for 24 hours.

There was also something different observed for the samples measured under dry and humidified conditions. For the as-sintered sample measured under dry and humidified air, there was no obvious change of the total conductivities, which again confirmed that these types of materials should exhibit a pure oxygen ion conductivity under air. However, the annealed sample exhibited something different. The total conductivity of the annealed sample measured under humidified 5% H_2/N_2 was higher than that measured under dry 5% H_2/N_2. The increase in the total conductivity under humidified conditions could readily lead to a consideration of the existence of the proton conductivity. However, since there should not be enough oxygen vacancies introduced by substituents in these types of materials, the mechanism described by equation (2.2) could not be used to explain the phenomenon observed here. As discussed in Section 2.4.3, another proton conduction mechanism described by equation (2.8) could be used to explain. Since Mo^{6+} was fully reduced to Mo^{5+} in the annealed sample, the structure of the annealed sample was closer to the undoped

$LaNbO_4$, containing unoccupied interstitial sites (V_i^X). The proton conductivity in the annealed sample could be described below. Firstly, one lattice oxygen ion jumped into an unoccupied interstitial site forming an oxygen vacancy and one oxygen interstitial at the same time:

$$O_O^X + V_i^X \rightleftharpoons V_O^{\bullet\bullet} + \ O_i'' \qquad (6.3);$$

then the water molecule was dissolved into one hydroxyl group and one proton:

$$H_2O \rightleftharpoons OH' + H^{\bullet} \qquad (6.4);$$

then the hydroxyl group and the proton associated with the newly formed oxygen vacancy and another lattice oxygen, respectively, generating two $(OH)_O^{\bullet}$:

$$OH' + V_O^{\bullet\bullet} \rightleftharpoons OH_O^{\bullet} \qquad (6.5);$$

$$H^{\bullet} + O_O^X \rightleftharpoons OH_O^{\bullet} \qquad (6.6).$$

The overall process gave a result of the mechanism described by equation (2.8).

Figure 6.5.3 shows the XPS results of O 1*s* orbitals of the as-sintered sample and the annealed sample. The shift of the binding energy of O 1*s* orbitals could be related to the change of the covalency of the Mo-O bonds as discussed in Section 6.4. It was also clearly observed that there was a hump at higher binding energy (532.1 eV) in the annealed sample, which could be attributed to the hydroxyl species [188]. The existence of the hydroxyl species meant the structure of the annealed sample could provide an environment where the protons favourably associated with the oxygen ions. Therefore, it provided a possibility to take the hydroxyl groups from the water molecules to realise the proton conductivity. However, it should be worth noting that the XPS results was collected from the sample before the EIS measurement under humidified conditions, which suggested there had already been the existence of hydroxyl species without the presence of water. This phenomenon could provide a novel mechanism for these types of materials since they could potentially incorporate the protons directly from the hydrogen molecules. As suggested by Huang *et al*, this mechanism could be described by equation (6.7) [136]:

$$H_2 + 2O_O^X \rightleftharpoons 2OH_O^{\bullet} + 2e' \qquad (6.7).$$

Therefore, for the annealed sample, it could exhibit a combination of proton conductivity and electronic conductivity even under dry 5% H_2/N_2. However, it is worth nothing that based on

the results in this chapter, there was still a lack of direct evidence of proton conductivity. The experiments such as measuring the transport number by EMF method and measuring the isotope effect by exchanging the sample under D_2 atmosphere has been discussed and planned.

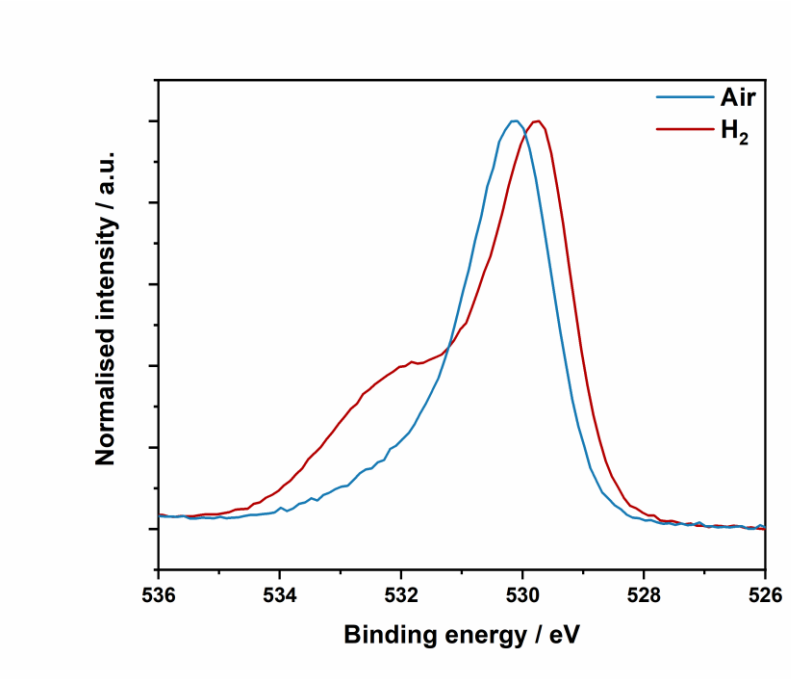


Figure 6.5.3. XPS spectra of O 1*s* orbitals of as-sintered LNM10 and LNM10 annealed under 5% H_2/N_2 at 800 °C for 24 hours. The binding energy of C 1*s* peak (284.8 eV) was used for calibration.

6.6 Conclusion

In summary, the stability and oxidation states of Mo in LNM10 under different atmospheres were investigated by different characterisation methods in this work. Under air, the oxidation states of Mo remained stable, and the oxygen stoichiometry did not change from room temperature to 900 °C. It was demonstrated that these materials could be used as a pure oxygen ion conductor in oxidising atmospheres.

However, under a more reducing atmosphere like vacuum, not only the Mo started to be reduced to lower oxidation states, but also the total structure changed. A secondary phase, which possessed the same structure as the undoped $LaNbO_4$, emerged. After being annealed under 5% H_2/N_2 for 8 hours, the structure of LNM10 fully transitioned to the structure of undoped $LaNbO_4$ with the modulated structure also being eliminated. The reduction of Mo

and the change of the total structure both suggested that the chemical formula of LNM10 was likely to be $La(Nb_{0.9}Mo_{0.1})O_4$. With the analysis of the *in-situ* XAS data, all the changes of the oxidation states of Mo and the total structure were accompanied with the changes of the coordination numbers of the Nb sites. The coordination numbers of Nb sites gradually decreased from 6 to 4.5 when the annealed sample was heated up under air. It was also observed that the starting temperature of the re-oxidation was around 100 °C and the process would finish at 400 °C.

After being annealed under 5% H_2/N_2 for 24 hours, LNM10 exhibited a lower activation energy of 0.61 eV from the EIS data measured under 5% H_2/N_2. The decrease in the activation energy could be related to the existence of the Mo^{5+}, which introduced an intermediate band between the CB and VB. The existence of the intermediate band narrowed the original band gap, which not only introduced the electronic conductivity, but also changed the colour of the sample. The annealed sample also exhibited possible proton conduction in both dry and humidified conditions under 5% H_2/N_2. This novel phenomenon could be related to the structure of the annealed sample, which was favourable for the associations of protons and lattice oxygens to form hydroxyl groups. Therefore, with the nature of a combination of protonic and electronic conductivity under reducing atmospheres, this material could be used as the anode for SOFCs. However, all these were concluded from the initial findings and assumptions. Several experiments have been discussed. For instance, to verify the existence of the intermediate band due to the formation of Mo^{5+}, the DFT simulation of the band gap structure have been planned for the annealed samples. To directly prove the proton conductivity, the isotope effect of the electrochemical performance should be preferred by exchanging the samples under D_2 or D_2O. Therefore, the proton conductivity of these types of materials still needs to be further studied.

Unfortunately, it is still unknown what is the starting point of the structure change for these types of materials under reducing atmospheres. For example, in this study, it required at least 8 hours to reduce the structure of LNM10 to a structure of undoped $LaNbO_4$ under 5% H_2/N_2 at 800 °C; however, changing the temperature or ‘‘hydrogen partial pressure’’ could accelerate the reduction process.

Chapter 7. Conclusions and future works

7.1 Conclusions

The crystal structure, electrochemical performance and the stability of Mo substituted $LaNbO_4$ based materials have been investigated in this work. Both $La_{1-x}Gd_xNb_{0.9}Mo_{0.1}O_{4.05}$ and $LaNb_{0.8}W_xMo_{0.2-x}O_{4.1}$ series were successfully synthesised by conventional solid state reaction route. For $La_{1-x}Gd_xNb_{0.9}Mo_{0.1}O_{4.05}$, the compositions with $x \leq 0.20$ were found to possess modulated structures. The modulated structure in $LaNb_{0.9}Mo_{0.1}O_{4.05}$ was observed along [010] zone axis in reciprocal space, which was indexed with two modulated vectors ($\boldsymbol{q_1} = 0.159\boldsymbol{a}^* + 0.418\boldsymbol{c}^*$ and $\boldsymbol{q_2} = 0.452\boldsymbol{a}^* + 0.186\boldsymbol{c}^*$). Therefore, the modulated structure was identified as (3+2) D incommensurately modulated. However, based on the EIS results, the modulated structures in these types of materials could have negative effects on the electrochemical performance. For $LaNb_{0.9}Mo_{0.1}O_{4.05}$, the activation energy of the unmodulated structure was around 0.9 eV lower than that of the modulated structure. Since modulated structure did not exist in $GdNb_{0.9}Mo_{0.1}O_{4.05}$, slightly substituting Gd on La site (20 mol%) could eliminate the modulated structure; therefore, increasing the total conductivity in the intermediate temperature range. However, with increasing the Gd content on La site, on one hand, the transition temperature from monoclinic phase to tetragonal phase increased; on the other hand, the particle sizes gradually decreased and the sample with pure Gd on La site exhibited a porous structure. Therefore, the results provide a trade-off with Gd substituents. Similar results and effects were also found in $LaNb_{0.8}W_xMo_{0.2-x}O_{4.1}$ series. All samples were found to possess a modulated structure at room temperature. For the samples with lower W fraction ($x < 0.10$), the modulated structure disappeared at intermediate temperature range and this temperature point decreased with increasing the W content. However, for the samples with higher W fraction ($x \geq 0.10$), the modulated structure existed from room temperature to 900 °C. The study of $LaNb_{0.8}W_{0.02}Mo_{0.18}O_{4.1}$ revealed a decrease in activation energy of around 0.9 eV from modulated structure to unmodulated structure, which confirmed the negative effect of modulated structure on electrochemical performance. Therefore, with slightly substituting W on Mo site, the total conductivity could be increased in the intermediate temperature range; however, more W fraction on Mo site (x = 0.18 and

0.20) led to higher trapping effect of oxygen interstitials and a W-rich secondary phase, which was not ideal for the electrochemical performance of these types of materials.

This work also proceeded to investigate the stability of $LaNb_{0.9}Mo_{0.1}O_{4.05}$ under different atmospheric conditions with different techniques. Based on the TGA results, Mo in as-sintered $LaNb_{0.9}Mo_{0.1}O_{4.05}$ should possess a fixed oxidation state; however, the XPS results contradicted with this. Mixed oxidation states of Mo^{6+}, Mo^{5+} and Mo^{4+} were exhibited in the as-sintered sample, which could be ascribed to the high vacuum working condition of XPS measurements. An iteration XPS scan of MoO_3 verified this, since the proportion of Mo species with lower oxidation than Mo^{6+} kept increasing with being exposed under vacuum for a longer time. To determine the oxidation state of Mo in the as-sintered sample under ambient conditions, XANES measurements were conducted. By comparing the Mo K-edge positions of the sample and the Mo foil, the oxidation state of Mo in the as-sintered sample should be Mo^{6+} under air. The oxidation states of Mo in these types of materials seemed to be highly influenced by the oxygen partial pressure of the atmosphere; therefore, the as-sintered $LaNb_{0.9}Mo_{0.1}O_{4.05}$ were annealed under different atmospheric conditions (pure O_2, pure N_2, vacuum (around 1.6×10^{-8} mbar), and 5% H_2/N_2) at 800 °C for 2 hours to study the influence of oxygen partial pressure on these types of materials. The results showed that the sample were darkened after being annealed under 5% H_2/N_2 and there was a decrease in band gap from 2.88 eV to 1.13 eV after 5% H_2/N_2 treatment based on the Tauc plots. The EPR results confirmed the existence of Mo^{5+} in the 5% H_2/N_2 annealed sample. Apart from the changes of the colour, there were also structural changes observed for these types of materials. The XRD results showed that a secondary phase resembling the undoped $LaNbO_4$ appeared under reducing atmospheres (vacuum and 5% H_2/N_2) and after being annealed under 5% H_2/N_2 at 800 °C for 8 hours, the structure of $LaNb_{0.9}Mo_{0.1}O_{4.05}$ totally transitioned to the structure of $LaNbO_4$. This suggested that there were no more oxygen hyperstoichiometry in the system and the Mo should be fully reduced to Mo^{5+} leading to an overall chemical formula of $La(Nb_{0.9}Mo_{0.1})O_4$.. To verify this, TGA and *in-situ* XAS measurements were conducted for the sample annealed under 5% H_2/N_2 at 800 °C for 24 hours. The TGA results showed that the mass of the sample remained unchanged below 100 °C and then increased until the temperature reached at around 400 °C. Beyond this temperature point, the mass kept stable. Similar results were also found in the *in-situ* XAS

measurements. The *in-situ* XANES results showed that the oxidation state of Mo in the annealed sample was Mo^{5+} at room temperature. It kept unchanged below 100 °C and gradually increased to Mo^{6+} in the temperature range from 100 °C to 400 °C. Therefore, the reoxidation of these types of materials under air started at around 100 °C finished at around 400 °C. The synchrotron XRD results showed that after fully reoxidsed, the structure of the annealed sample transitioned back to the structure of as-sintered $LaNb_{0.9}Mo_{0.1}O_{4.05}$, which suggested this process is reversible. *In situ* EXAFS results revealed that along with the change of the oxidation states of Mo from Mo^{5+} to Mo^{6+}, there was also a change of the coordination number of Nb sites from 6 to 4.5. To correlate these changes to electrochemical performance, EIS measurements were conducted for the as-sintered sample and annealed sample under air and 5% H_2/N_2, respectively. The results showed that the activation energy of the annealed sample measured under 5% H_2/N_2 was much lower than that of the as-sintered sample measured under air. This could be ascribed to the existence of Mo^{5+} as it introduced an intermediate band in the original band gap, which could increase the electronic conductivity. Additionally, there seemed to be proton conductivity in the annealed sample as an obvious contribution of hydroxyl group was showed in the O *1s* XPS spectrum, which suggested potential incorporation of protons direct from the hydrogen molecules. However, more direct evidence of proton conductivity still needs to be provided and corresponding experiments is discussed in Section 7.2.

7.2 Future works

The current work of Chapter 4 and 5 has focused on the relationship between modulated structures and the electrochemical performances of these types of materials whereas next step could shift to further understanding of the origin of the modulated structures in crystallography. Since the intensities of the satellite reflections from modulated structures from laboratory XRD were low, the XRD data in this work were refined with the basic space group rather than super space group. Therefore, to obtain more accurate modulated vectors, the synchrotron XRD data of $LaNb_{0.9}Mo_{0.1}O_{4.05}$ could be used to conduct the refinement with a super space group. Additionally, the current work has studied the electrochemical performance only based on the EIS results; however, since these types of materials are good oxygen ion conductors under air, the measurements of ^{18}O diffusivity should be more straightforward to investigate the oxygen mobility. The ^{18}O diffusivity of these

types of materials could be obtained by exchanging the samples under an $^{18}O_2$ rich environment and then conducting secondary ion mass spectrometry measurements.

For Chapter 6, the current work led to a conclusion of potential proton conductivity of 5% H_2/N_2 annealed $LaNb_{0.9}Mo_{0.1}O_{4.05}$ without direct evidence. Therefore, several works could be proposed. First, it is necessary to conduct the EMF measurements for the samples. Since most of the materials exhibit proton conductivity under humidified conditions, the EMF measurements are always conducted by building a difference of water partial pressure on two electrodes to obtain the transport number of protons. However, since $LaNb_{0.9}Mo_{0.1}O_{4.05}$ was proposed to incorporate the protons directly from the hydrogen molecules, a gradient of H_2 could be built across the 5% H_2/N_2 annealed sample to measure the transport number of protons. Another method could provide direct evidence of proton conductivity is measuring the H/D isotope effects of these types of materials. Two samples of $LaNb_{0.9}Mo_{0.1}O_{4.05}$ will be annealed and conducted EIS measurements under H_2 and D_2, respectively. Since the mobilities of H^+ and D^+ are different, there should be a difference of the conductivities of the samples measured under different atmospheres. Finally, if these types of materials are proven to exhibit proton conductivity under hydrogen without of water, these materials will be suitable for the use of anode materials for SOFCs. Single cells with appropriate electrolyte and cathode will be fabricated to test the overall electrochemical performance, for example, the power density.

References

[1] BP Energy Outlook, **2023**.

[2] A. Seong, D. Jeong, M. Kim, S. Choi, G. Kim, *J. Power Sources.* **2022**, *530*, 231241.

[3] A. J. Jacobson, *Chem. Mater.* **2010**, *22*, 660.

[4] C. Nico, M. R. N. Soares, F. M. Costa, T. Monteiro, M. P. F. Graça, *J. Appl. Phys.* **2016**, *120*, 051708.

[5] H. Fjeld, K. Toyoura, R. Haugsrud, T. Norby, *Phys. Chem. Chem. Phys.* **2010**, *12*, 10313.

[6] M. Huse, A. W. B. Skilbred, M. Karlsson, S. G. Eriksson, T. Norby, R. Haugsrud, C. S. Knee, *J. Solid State Chem.* **2012**, *187*, 27.

[7] G. C. Mather, C. A. J. Fisher, M. S. Islam, *Chem. Mater.* **2010**, *22*, 5912.

[8] K. Toyoura, Y. Sakakibara, T. Yokoi, A. Nakamura, K. Matsunaga, *J. Mater. Chem. A.* **2018**, *6*, 12004.

[9] R. Haugsrud, T. Norby, *Nat. Mater.* **2006**, *5*, 193.

[10] S. Wachowski, B. Kamecki, P. Winiarz, K. Dzierzgowski, A. Mielewczyk-Gryń, M. Gazda, *Inorg. Chem. Front.* **2018**, *5*, 2157.

[11] C. Li, R. D. Bayliss, S. J. Skinner, *Solid State Ion.* **2014**, *262*, 530.

[12] J. E. Auckett, L. Lopez-Odriozola, S. J. Clark, I. R. Evans, *J. Mater. Chem. A* **2021**, *9*, 4091.

[13] P. Sarin, R. W. Hughes, D. R. Lowry, Z. D. Apostolov, W. M. Kriven, *J. Am. Ceram. Soc.* **2014**, *97*, 3307.

[14] Y. Han, S. J. Skinner, *Mater. Adv.* **2023**, *4*, 3759.

[15] Y. Han, S. Li, S. Skinner, *J. Solid State Chem.* **2024**, *332*, 124590.

[16] Y. Cao, N. Duan, X. Wang, B. Chi, JianPu, L. Jian, *J. Eur. Ceram. Soc.* **2015**, *35*, 1979.

[17] H. Zhou, Z. Chen, A. V. López, E. D. López, E. Lam, A. Tsoukalou, E. Willinger, D. A. Kuznetsov, D. Mance, A. Kierzkowska, F. Donat, P. M. Abdala, A. Comas-Vives, C.

Copéret, A. Fedorov, C. R. Müller, *Nat. Catal.* **2021**, *4*, 860.

[18] M. R. Li, Z. Deng, S. H. Lapidus, P. W. Stephens, C. U. Segre, M. Croft, R. Paria Sena, J. Hadermann, D. Walker, M. Greenblatt, *Inorg. Chem.* **2016**, *55*, 10135.

[19] R. O'hayre, S.-W. Cha, W. Colella, F. B. Prinz, *Fuel cell fundamentals*, John Wiley & Sons, **2016**.

[20] A. B. Stambouli, E. Traversa, *Renew. Sustain. Energy Rev.* **2002**, *6*, 433.

[21] S. Dwivedi, *Int. J. Hydrogen Energy.* **2020**, *45*, 23988.

[22] B. H. Rainwater, M. Liu, M. Liu, *Int. J. Hydrogen Energy.* **2012**, *37*, 18342.

[23] A. Essoumhi, G. Taillades, M. Taillades-Jacquin, D. J. Jones, J. Rozière, *Solid State Ion.* **2008**, *179*, 2155.

[24] M. Papac, V. Stevanović, A. Zakutayev, R. O'Hayre, *Nat. Mater. 2020 203* **2020**, *20*, 301.

[25] C. Duan, J. Tong, M. Shang, S. Nikodemski, M. Sanders, S. Ricote, A. Almansoori, R. O'Hayre, *Science.* **2015**, *349*, 1321.

[26] H. Dai, E. H. Da'as, S. P. Shafi, H. Wang, L. Bi, *J. Eur. Ceram. Soc.* **2018**, *38*, 2903.

[27] H. Iwahara, H. Uchida, K. Ono, K. Ogaki, *J. Electrochem. Soc.* **1988**, *135*, 529.

[28] H. Iwahara, H. Uchida, K. Morimoto, *J. Electrochem. Soc.* **1990**, *137*, 462.

[29] B. Lin, M. Hu, J. Ma, Y. Jiang, S. Tao, G. Meng, *J. Power Sources* **2008**, *183*, 479.

[30] F. A. Kröger, H. J. Vink, *Solid State Phys. - Adv. Res. Appl.* **1956**, *3*, 307.

[31] K. Katahira, Y. Kohchi, T. Shimura, H. Iwahara, *Solid State Ion.* **2000**, *138*, 91.

[32] E. Fabbri, L. Bi, D. Pergolesi, E. Traversa, E. Fabbri, L. Bi, D. Pergolesi, E. Traversa, *Adv. Mater.* **2012**, *24*, 195.

[33] K. Xie, R. Yan, X. Xu, X. Liu, G. Meng, *J. Power Sources.* **2009**, *187*, 403.

[34] E. Fabbri, D. Pergolesi, S. Licoccia, E. Traversa, *Solid State Ion.* **2010**, *181*, 1043.

[35] E. Fabbri, A. D'Epifanio, E. Di Bartolomeo, S. Licoccia, E. Traversa, *Solid State Ion.*

2008, *179*, 558.

[36] C. Zuo, S. Zha, M. Liu, M. Hatano, M. Uchiyama, [M Liu, C. Zuo, S. Zha, M. Hatano, M. Uchiyama, *Adv. Mater.* **2006**, *18*, 3318.

[37] S. C. Singhal, K. Kendall, *High-temperature solid oxide fuel cells: fundamentals, design and applications*, Elsevier, **2003**.

[38] A. Ndubuisi, S. Abouali, K. Singh, V. Thangadurai, *J. Mater. Chem. A* **2022**, *10*, 2196.

[39] S. J. Skinner, J. A. Kilner, *Mater. Today.* **2003**, *6*, 30.

[40] W. Lee, J. W. Han, Y. Chen, Z. Cai, B. Yildiz, *J. Am. Chem. Soc.* **2013**, *135*, 7909.

[41] J. W. Fergus, *J. Power Sources.* **2006**, *162*, 30.

[42] J. B. Goodenough, *Annu. Rev. Mater. Res.* **2003**, *33*, 91.

[43] D. -J Kim, T. -Y Tien, *J. Am. Ceram. Soc.* **1991**, *74*, 3061.

[44] E. Ivers-Tiffée, A. Weber, D. Herbstritt, *J. Eur. Ceram. Soc.* **2001**, *21*, 1805.

[45] V. V. Kharton, F. M. Figueiredo, L. Navarro, E. N. Naumovich, A. V. Kovalevsky, A. A. Yaremchenko, A. P. Viskup, A. Carneiro, F. M. B. Marques, J. R. Frade, *J. Mater. Sci.* **2001**, *36*, 1105.

[46] D. J. Seo, K. O. Ryu, S. Bin Park, K. Y. Kim, R. H. Song, *Mater. Res. Bull.* **2006**, *41*, 359.

[47] J. Fleig, *Annu. Rev. Mater. Res.* **2003**, *33*, 361.

[48] V. V. Kharton, F. M. B. Marques, A. Atkinson, *Solid State Ion.* **2004**, *174*, 135.

[49] T. Takahashi, T. Esaka, H. Iwahara, *J. Appl. Electrochem.* **1977**, *7*, 299.

[50] K. Huang, M. Feng, J. B. Goodenough, *J. Am. Ceram. Soc.* **1996**, *79*, 1100.

[51] T. Ishihara, J. A. Kilner, M. Honda, N. Sakai, H. Yokokawa, Y. Takita, *Solid State Ion.* **1998**, *113–115*, 593.

[52] B. C. H. Steele, A. Heinzel, *Nat.* **2001**, *414*, 345.

[53] A. V. Joshi, J. J. Steppan, D. M. Taylor, S. Elangovan, *J. Electroceramics.* **2004**, *13*, 619.

[54] J. Cao, C. Su, Y. Ji, G. Yang, Z. Shao, *J. Energy Chem.* **2021**, *57*, 406.

[55] Y. Sakuda, T. Murakami, M. Avdeev, K. Fujii, Y. Yasui, J. R. Hester, M. Hagihala, Y. Ikeda, Y. Nambu, M. Yashima, *Chem. Mater.* **2023**, *35*, 9774.

[56] M. Liu, L. Yang, S. Wang, K. Blinn, M. Liu, Z. Liu, Z. Cheng, *Science.* **2009**, *326*, 126.

[57] C. Zhou, J. Sunarso, Y. Song, J. Dai, J. Zhang, B. Gu, W. Zhou, Z. Shao, *J. Mater. Chem. A.* **2019**, *7*, 13265.

[58] B. Zhu, X. Liu, T. Schober, *Electrochem. commun.* **2004**, *6*, 378.

[59] S. Wang, J. Shen, Z. Zhu, Z. Wang, Y. Cao, X. Guan, Y. Wang, Z. Wei, M. Chen, *J. Power Sources.* **2018**, *387*, 24.

[60] T. Esaka, *Solid State Ion.* **2000**, *136–137*, 1.

[61] L. Jian, C. M. Wayman, *J. Am. Ceram. Soc.* **1997**, *80*, 803.

[62] S. Tsunekawa, H. Takei, M. Ishigame, *Mater. Res. Bull.* **1977**, *12*, 1087.

[63] S. W. Arulnesan, P. Kayser, J. A. Kimpton, B. J. Kennedy, *J. Solid State Chem.* **2019**, *277*, 229.

[64] C. Nico, T. Monteiro, M. P. F. Graça, *Prog. Mater. Sci.* **2016**, *80*, 1.

[65] V. S. Stubican, *J. Am. Ceram. Soc.* **1964**, *47*, 55.

[66] P. M. Kelly, C. J. Wauchope, *Mater. Lett.* **1996**, *27*, 7.

[67] J. Li, C. M. Huang, X. Genbao, C. M. Wayman, *Mater. Lett.* **1994**, *21*, 105.

[68] S. J. Skinner, *Adv. Mater. Interfaces.* **2019**, *6*, 1900580.

[69] T. Mokkelbost, I. Kaus, R. Haugsrud, T. Norby, T. Grande, M.-A. Einarsrud, *J. Am. Ceram. Soc.* **2008**, *91*, 879.

[70] M. Huse, T. Norby, R. Haugsrud, *Int. J. Hydrogen Energy.* **2012**, *37*, 8004.

[71] A. Kuwabara, R. Haugsrud, S. Stølen, T. Norby, *Phys. Chem. Chem. Phys.* **2009**, *11*, 5550.

[72] E. Fabbri, D. Pergolesi, E. Traversa, *Chem. Soc. Rev.* **2010**, *39*, 4355.

[73] A. Magrasó, M.-L. Fontaine, Y. Larring, R. Bredesen, G. E. Syvertsen, H. L. Lein, T.

Grande, M. Huse, R. Strandbakke, R. Haugsrud, T. Norby, *Fuel Cells.* **2011**, *11*, 17.

[74] Q. Liu, L. Xu, J. Meng, J. Meng, X. Liu, H. Zhang, *J. Phys. Chem. C* **2020**, *124*, 21232.

[75] G. C. Mather, M. S. Islam, *Chem. Mater.* **2005**, *17*, 1736.

[76] R. D. Shannon, *Acta Crystallogr. Sect. A.* **1976**, *32*, 751.

[77] R. Haugsrud, T. Norby, *Solid State Ion.* **2006**, *177*, 1129.

[78] L. Malavasi, C. Ritter, G. Chiodelli, *J. Alloys Compd.* **2009**, *475*, L42.

[79] Z. Bi, J. Peña-Martínez, J. H. Kim, C. A. Bridges, A. Huq, J. P. Hodges, M. P. Paranthaman, *Int. J. Hydrogen Energy* **2012**, *37*, 12751.

[80] G. E. Syvertsen, A. Magrasó, R. Haugsrud, M. A. Einarsrud, T. Grande, *Int. J. Hydrogen Energy* **2012**, *37*, 12751.

[81] T. Mokkelbost, Ø. Andersen, R. A. Strøm, K. Wiik, T. Grande, M.-A. Einarsrud, *J. Am. Ceram. Soc.* **2007**, *37*, 8017.

[82] A. Magrasó, H. Xuriguera, M. Varela, M. F. Sunding, R. Strandbakke, R. Haugsrud, T. Norby, *J. Am. Ceram. Soc.* **2010**, *93*, 1874.

[83] A. Cavallaro, C. Solís, P. R. Garcia, B. Ballesteros, J. M. Serra, J. L. Santiso, *Solid State Ion.* **2012**, *216*, 25.

[84] M. Amsif, D. Marrero-López, J. C. Ruiz-Morales, S. Savvin, P. Núñez, *J. Eur. Ceram. Soc.* **2012**, *32*, 1235.

[85] T. Miruszewski, P. Winiarz, K. Dzierzgowski, K. Wiciak, K. Zagórski, A. Morawski, A. Mielewczyk-Gryń, S. Wachowski, J. Strychalska-Nowak, M. Sawczak, M. Gazda, *J. Solid State Chem.* **2019**, *270*, 601.

[86] D. Nguyen, Y. H. Kim, J. S. Lee, J. G. Fisher, *Mater. Chem. Phys.* **2017**, *202*, 320.

[87] D. Poulidi, G. C. Mather, C. N. Tabacaru, A. Thursfield, I. S. Metcalfe, *Catal. Today.* **2009**, *146*, 279.

[88] H. Fjeld, D. M. Kepaptsoglou, R. Haugsrud, T. Norby, *Solid State Ion.* **2010**, *181*, 104.

[89] C. Li, S. S. Pramana, N. Ni, J. Kilner, S. J. Skinner, *ACS Appl. Mater. Interfaces.* **2017**, *9*,

29633.

[90] S. -L Hwang, I. -W Chen, *J. Am. Ceram. Soc.* **1990**, *73*, 3269.

[91] X. GUO, R. WASER, *Prog. Mater. Sci.* **2006**, *51*, 151.

[92] T. Mokkelbost, H. L. Lein, P. E. Vullum, R. Holmestad, T. Grande, M. A. Einarsrud, *Ceram. Int.* **2009**, *35*, 2877.

[93] A. Mielewczyk-Gryn, K. Gdula, T. Lendze, B. Kusz, M. Gazda, *Cryst. Res. Technol.* **2010**, *45*, 1225.

[94] A. Mielewczyk-Gryń, K. Gdula, S. Molin, P. Jasinski, B. Kusz, M. Gazda, *J. Non-Cryst. Solids*. **2010**, *356*, 1976.

[95] A. Mielewczyk-Gryn, K. Gdula-Kasica, B. Kusz, M. Gazda, *Ceram. Int.* **2013**, *39*, 4239.

[96] A. Mielewczyk-Gryn, S. Wachowski, K. Zagórski, P. Jasiński, M. Gazda, *Ceram. Int.* **2015**, *41*, 7847.

[97] Y. Cao, Y. Tan, D. Yan, B. Chi, J. Pu, L. Jian, *Solid State Ion.* **2015**, *278*, 152.

[98] Y. Cao, N. Duan, D. Yan, B. Chi, J. Pu, L. Jian, *Int. J. Hydrogen Energy.* **2016**, *41*, 20633.

[99] C. Solís, J. M. Serra, *Solid State Ion.* **2011**, *190*, 38.

[100] K. Dzierzgowski, S. Wachowski, W. Gojtowska, I. Lewandowska, P. Jasiński, M. Gazda, A. Mielewczyk-Gryń, *Ceram. Int.* **2018**, *44*, 8210.

[101] R. J. Packer, P. A. Stuart, S. J. Skinner, *J. Solid State Chem.* **2008**, *181*, 1445.

[102] Y. Cao, N. Duan, D. Yan, *J. Solid State Chem.* **2016**, *237*, 248.

[103] L. Hakimova, A. Kasyanova, A. Farlenkov, J. Lyagaeva, D. Medvedev, A. Demin, P. Tsiakaras, *Ceram. Int.* **2019**, *45*, 209.

[104] Y. Cao, B. Chi, J. Pu, L. Jian, *J. Eur. Ceram. Soc.* **2014**, *34*, 1981.

[105] K. Dzierzgowski, S. Wachowski, M. Gazda, A. Mielewczyk-Gryń, *Crystals.* **2019**, *9*, 91.

[106] T. Norby, Y. Larring, *Curr. Opin. Solid State Mater. Sci.* **1997**, *2*, 593.

[107] M. S. Islam, R. A. Davies, C. A. J. Fisher, A. V. Chadwick, *Solid State Ion.* **2001**, *145*, 333.

[108] A. D. Brandão, J. Gracio, G. C. Mather, V. V. Kharton, D. P. Fagg, *J. Solid State Chem.* **2011**, *184*, 863.

[109] M. Li, R. Wu, L. Zhu, J. Cheng, T. Hong, C. Xu, *Ceram. Int.* **2019**, *45*, 573.

[110] M. Li, T. Hong, J. Cheng, Z. Chen, C. Xu, *Mater. Chem. Phys.* **2018**, *208*, 226.

[111] X. Chi, Z. Wen, J. Zhang, Y. Liu, *Solid State Ion.* **2014**, *268*, 326.

[112] Y. Lv, S. Geng, T. Wei, J. Liu, X. Xu, H. Yi, J. Xu, *Phys. status solidi.* **2020**, *257*, 2000110.

[113] J. Palisaitis, M. E. Ivanova, W. A. Meulenberg, O. Guillon, J. Mayer, *J. Eur. Ceram. Soc.* **2015**, *35*, 1517.

[114] M. E. Ivanova, W. A. Meulenberg, J. Palisaitis, D. Sebold, C. Solís, M. Ziegner, J. M. Serra, J. Mayer, M. Hänsel, O. Guillon, *J. Eur. Ceram. Soc.* **2015**, *35*, 1239.

[115] M. Ivanova, S. Ricote, W. A. Meulenberg, R. Haugsrud, M. Ziegner, In *Solid State Ion*. **2012**, *213*, 45.

[116] D. Virbukas, K. Bočkutė, G. Laukaitis, *Medziagotyra.* **2015**, *21*, 439.

[117] F. Vullum, F. Nitsche, S. M. Selbach, T. Grande, *J. Solid State Chem.* **2008**, *181*, 2580.

[118] A. D. Brandão, I. Antunes, J. R. Frade, J. Torre, V. V. Kharton, D. P. Fagg, *Chem. Mater.* **2010**, *22*, 6673.

[119] A. D. Brando, I. Antunes, J. R. Frade, J. Torre, S. M. Mikhalev, D. P. Fagg, *Int. J. Hydrogen Energy*. **2012**, *37*, 7252.

[120] Z. Bi, C. A. Bridges, J. H. Kim, A. Huq, M. P. Paranthaman, *J. Power Sources.* **2011**, *196*, 7395.

[121] A. B. Santibáñez-Mendieta, E. Fabbri, S. Licoccia, E. Traversa, *Solid State Ion.* **2012**, *216*, 6.

[122] A. B. Santibáñez-Mendieta, E. Fabbri, S. Licoccia, E. Traversa, *J. Electrochem. Soc.* **2011**, *158*, B1485.

[123] S. Wachowski, A. Mielewczyk-Gryn, M. Gazda, *J. Solid State Chem.* **2014**, *219*, 201.

[124] A. Mielewczyk-Gryn, S. Wachowski, K. I. Lilova, X. Guo, M. Gazda, A. Navrotsky,

Ceram. Int. **2015**, *41*, 2128.

[125] S. Wachowski, A. Mielewczyk-Gryń, K. Zagórski, C. Li, P. Jasiński, S. J. Skinner, R. Haugsrud, M. Gazda, *J. Mater. Chem. A.* **2016**, *4*, 11696.

[126] A. Mielewczyk-Gryń, S. Wachowski, A. Witkowska, K. Dzierzgowski, W. Skubida, K. Świerczek, A. Regoutz, D. J. Payne, S. Hull, H. Zhang, I. Abrahams, M. Gazda, *J. Am. Ceram. Soc.* **2020**, *103*, 6575.

[127] R. J. Packer, E. V. Tsipis, C. N. Munnings, V. V. Kharton, S. J. Skinner, J. R. Frade, *Solid State Ion.* **2006**, *177*, 2059.

[128] S. van Smaalen, *Incommensurate Crystallography*, Oxford University Press, **2007**.

[129] C. Li, Structural, surface and electrochemical studies of LaNbO4 based ionic conductors, Imperial College London, **2017**.

[130] C. Li, S. S. Pramana, S. J. Skinner, *Dalt. Trans.* **2019**, *48*, 1633.

[131] C. Ferrara, A. Mancini, C. Ritter, L. Malavasi, C. Tealdi, *J. Mater. Chem. A.* **2015**, *3*, 22258.

[132] G. Canu, V. Buscaglia, C. Ferrara, P. Mustarelli, S. Gonçalves Patrício, A. I. Batista Rondão, C. Tealdi, F. M. B. Marques, *J. Alloys Compd.* **2017**, *697*, 392.

[133] E. S. Buyanova, Z. A. Mikhailovskaya, Y. V. Emel'yanova, A. A. Levina, M. V. Morozova, S. A. Petrova, N. V. Tarakina, *Russ. J. Inorg. Chem.* **2017**, *62*, 211.

[134] G. Canu, F. Giannici, A. Chiara, G. Confalonieri, A. Longo, M. T. Buscaglia, M. Dapiaggi, V. Buscaglia, A. Martorana, *J. Alloys Compd.* **2021**, *857*, 157532.

[135] C. Li, S. S. Pramana, R. D. Bayliss, C. P. Grey, F. Blanc, S. J. Skinner, *Chem. Mater.* **2020**, *32*, 2292.

[136] K. Huang, Y. Han, S. J. Skinner, *Manuscript in Preparation*, **2024**.

[137] M. Bech, O. Bunk, T. Donath, R. Feidenhans'l, C. David, F. Pfeiffer, *Phys. Med. Biol.* **2010**, *55*, 5529.

[138] R. E. Dinnebier, S. J. L. Billinge, *The Bragg equation from the Laue equation*, Vol. H,

International Union of Crystallography, **2019**.

[139] B. B. Baker, E. T. Copson, *The mathematical theory of Huygens' principle*, Vol. 329, American Mathematical Soc., **2003**.

[140] W. L. Bragg, *Nature.* **1912**, *90*, 410.

[141] K. Chan, M. Eikerling -, R. Kerr, H. Kirk, J. Di Francesco, al -, H. Shen, H. Maekawa, L. Wang, A. J. Dent, G. Cibin, S. Ramos, A. D. Smith, S. M. Scott, L. Varandas, M. R. Pearson, N. A. Krumpa, C. P. Jones, P. E. Robbins, *J. Phys. Conf. Ser.* **2009**, *190*, 012039.

[142] T. Daley, E. Raj, S. Ramos, G. Cibin, A. Dent, T. I. Hyde, G. Sankar, *J. Phys. Conf. Ser.* **2013**, *430*, 012080.

[143] H. M. Rietveld, *Aust. J. Phys.* **1988**, *41*, 113.

[144] H. Rietveld, *J. Appl. Crystallogr.* **1969**, *2*, 65.

[145] B. H. Toby, *Powder Diffr.* **2006**, *21*, 67.

[146] B. H. Toby, R. B. Von Dreele, *Appl. Crystallogr.* **2013**, *46*, 544.

[147] G. Greczynski, L. Hultman, *J. Appl. Phys.* **2022**, *132*, 11101.

[148] J. Kowalska, S. DeBeer, *Biochim. Biophys. Acta - Mol. Cell Res.* **2015**, *1853*, 1406.

[149] S. Calvin, *XAFS for Everyone*, CRC press, **2013**.

[150] B. Ravel, M. Newville, *J. Synchrotron Radiat.* **2005**, *12*, 537.

[151] M. Newville, *J. Synchrotron Radiat.* **2001**, *8*, 322.

[152] N. Saadatkhah, A. Carillo Garcia, S. Ackermann, P. Leclerc, M. Latifi, S. Samih, G. S. Patience, J. Chaouki, *Can. J. Chem. Eng.* **2020**, *98*, 34.

[153] R. J. D. Tilley, *Colour and the optical properties of materials*, John Wiley & Sons, **2020**.

[154] J. I. Goldstein, D. E. Newbury, J. R. Michael, N. W. M. Ritchie, J. H. J. Scott, D. C. Joy, *Scanning electron microscopy and X-ray microanalysis*, springer, **2017**.

[155] C. T. Rueden, J. Schindelin, M. C. Hiner, B. E. DeZonia, A. E. Walter, E. T. Arena, K. W.

Eliceiri, *BMC Bioinformatics.* **2017**, *18*, 1.

[156] W. H. Walton, *Nat.* **1948**, *162*, 329.

[157] G. S. Rohrer, *Annu. Rev. Mater. Res.* **2005**, *35*, 99.

[158] J. T. S. Irvine, D. C. Sinclair, A. R. West, *Adv. Mater.* **1990**, *2*, 132.

[159] P. Makuła, M. Pacia, W. Macyk, *J. Phys. Chem. Lett.* **2018**, *9*, 6814.

[160] J. Tauc, R. Grigorovici, A. Vancu, *Phys. status solidi.* **1966**, *15*, 627.

[161] P. Kubelka, F. Munk, *Z. Tech. Phys.* **1931**, *12*, 193.

[162] R. Kawaguchi, R. Akizawa, Y. J. Shan, K. Tezuka, T. Katsumata, *Solid State Ion.* **2020**, *355*, 115415.

[163] Y. J. Shan, R. Kawaguchi, R. Akizawa, K. Tezuka, *Ionics (Kiel).* **2023**, *29*, 2697.

[164] M. Yoshimura, A. Rouanet, *Mater. Res. Bull.* **1976**, *11*, 151.

[165] F. Goutenoire, S. Kodjikian, E. Suard, *J. Solid State Chem.* **2005**, *178*, 2811.

[166] M. Cabello, F. Nacimiento, R. Alcántara, P. Lavela, C. Pérez Vicente, J. L. Tirado, *Chem. Mater.* **2018**, *30*, 5853.

[167] Y. Yamazaki, F. Blanc, Y. Okuyama, L. Buannic, J. C. Lucio-Vega, C. P. Grey, S. M. Haile, *Nat. Mater. 2013 127* **2013**, *12*, 647.

[168] F. Farges, R. Siewert, G. E. Brown, A. Guesdon, G. Morin, *Can. Mineral.* **2006**, *44*, 731.

[169] H. Zhou, Z. Chen, E. Kountoupi, A. Tsoukalou, P. M. Abdala, P. Florian, A. Fedorov, C. R. Müller, *Nat. Commun. 2021 121* **2021**, *12*, 1.

[170] G. Seifert, J. Finster, H. Müller, *Chem. Phys. Lett.* **1980**, *75*, 373.

[171] V. Jayaseelan, R. K. Kalaiezhily, N. B. Shinde, K. Kamala Bharathi, M. Navaneethan, S. K. Eswaran, *J. Mater. Sci. Mater. Electron.* **2022**, *33*, 8741.

[172] K. Uchida, A. Ayame, *Surf. Sci.* **1996**, *357–358*, 170.

[173] H. W. Johansen, Defects and transport in donor doped LaNbO4, University of Oslo, **2020**.

[174] M. A. Arvizu, M. Morales-Luna, M. Pérez-González, E. Campos-Gonzalez, O. Zelaya-Angel, S. A. Tomás, *Int. J. Thermophys.* **2017**, *38*, 1.

[175] M. Morales-Luna, S. A. Tomás, M. A. Arvizu, M. Pérez-González, E. Campos-Gonzalez, *J. Alloys Compd.* **2017**, *722*, 938.

[176] G. Liu, C. Zhen, Y. Kang, L. Wang, H. M. Cheng, *Chem. Soc. Rev.* **2018**, *47*, 6410.

[177] A. Katrib, J. W. Sobczak, M. Krawczyk, L. Zommer, A. Benadda, A. Jablonski, G. Maire, *Surf. Interface Anal.* **2002**, *34*, 225.

[178] J. G. Choi, L. T. Thompson, *Appl. Surf. Sci.* **1996**, *93*, 143.

[179] T. Yamamoto, *X-Ray Spectrom.* **2008**, *37*, 572.

[180] S. D. B. George, P. Brant, E. I. Solomon, *J. Am. Chem. Soc.* **2005**, *127*, 667.

[181] F. Rocca, A. Kuzmin, P. Mustarelli, C. Tomasi, A. Magistris, *Solid State Ion.* **1999**, *121*, 189.

[182] A. L. Smith, M. Rutten, L. Herrmann, E. Epifano, R. J. M. Konings, E. Colineau, J.-C. Griveau, C. Guéneau, N. Dupin, *J. Eur. Ceram. Soc.* **2021**, *41*, 3664.

[183] F. A. Lima, R. Bjornsson, T. Weyhermüller, P. Chandrasekaran, P. Glatzel, F. Neese, S. DeBeer, *Phys. Chem. Chem. Phys.* **2013**, *15*, 20911.

[184] A. Gaur, M. Stehle, K. V. Raun, J. Thrane, A. D. Jensen, J. D. Grunwaldt, M. Høj, *Phys. Chem. Chem. Phys.* **2020**, *22*, 11713.

[185] A. M. Beale, S. D. M. Jacques, E. Sacaliuc-Parvalescu, M. G. O'Brien, P. Barnes, B. M. Weckhuysen, *Appl. Catal. A Gen.* **2009**, *363*, 143.

[186] S. M. Ansari, I. Taha, X. Han, D. H. Anjum, B. Mohammad, N. Amrane, M. Benkraouda, H. M. Aldosari, *J. Mater. Res. Technol.* **2023**, *24*, 2538.

[187] K. P. Reddy, N. B. Mhamane, M. K. Ghosalya, C. S. Gopinath, *J. Phys. Chem. C.* **2018**, *122*, 23034.

[188] E. Mcca, J. P. Wightman, *Surf. Interface Anal.* **1998**, *26*, 549.

[189] R. J. Cava, R. S. Roth, T. Negas, H. S. Parker, D. B. Minor, *J. Solid State Chem.* **1981**, *40*,

318.

Appendix

A1 Related information of La site substituted $LaNbO_4$

Table A1. Related information of La site substituted materials synthesised via different methods. Substitutes before and after the slash are both substituted on La sites. For activation energy, all values shown here are for t- phase.

Substituent elements	Synthesis method	Amount (mol%)	Conductivity type	Conductivity (S cm^{-1})	Temperature (°C)	Atmosphere (humidified)	E_a (eV)	Ref
Mg	MS	2.0	Total	2.00×10^{-3}	720	H_2	0.53	[96]
Ca	SP	2.0	Proton	8.00×10^{-4}	900	H_2	N/A	[81]
Ca	SSR	1.0	Proton	$\sim 10^{-3}$	800	H_2	N/A	[9]
Ca	SSR	0.5	Total	3.89×10^{-4}	850	Air	0.55	[79]
Ca	SSR	1.0	Total	$\sim 3.00 \times 10^{-4}$	850	Air	0.54	[79]
Ca	SSR	1.5	Total	$\sim 3.00 \times 10^{-4}$	850	Air	0.58	[79]
Ca	SSR	2.0	Total	2.25×10^{-4}	850	Air	0.60	[79]
Ca	PLD	0.5	Total	$\sim 10^{-4}$	600	5% H_2/Ar	N/A	[82]
Ca	PLD	0.5	Total	~20	800	O_2	0.6	[83]
Ca	mechano	2.0	Total	4.00×10^{-5}	600	Air	0.73	[85]
Ca	FDP	1.0	Total	8.00×10^{-4}	950	O_2	N/A	[84]
Zn	SSR	0.5	Total	9.80×10^{-4}	900	Air	0.43	[97]

Table A1 continues on the following page.

Table A1 (continued)

Zn	SSR	1.0	Total	9.80 × 10-4	900	Air	0.47	[97]
Zn	SSR	1.5	Total	~4.00 × 10-4	900	Air	0.50	[97]
Zn	SSR	3.0	Total	~2.50 × 10-4	900	Air	0.55	[97]
Sr	SP	2.0	Total	~5.00 × 10-4	900	H2	N/A	[81]
Sr	SSR	1.0	Total	2.70 × 10-4	500	H2	N/A	[87]
Sr	SSR	1.0	Total	5.00 × 10-5	500	O2	N/A	[87]
Ba	SP	2.0	Total	~4.00 × 10-4	900	H2	N/A	[81]
Ce/Ca	SSR	10/0.5	Total	~2.00 × 10-4	780	H2	N/A	[99]
Ce/Yb	SSR	10/10	Total	4.70 × 10-4	900	Air	N/A	[104]
Ce/Yb	SSR	10/5.0	Total	~3.50 × 10-4	900	Air	N/A	[104]
Ce/Yb	SSR	5.0/5.0	Total	~2.70 × 10-4	900	Air	N/A	[104]
Ce/Yb	SSR	5.0/10	Total	~5.0 × 10-5	900	Air	N/A	[104]
Pr	SSR	10	Total	8.40×10^{-5}	700	Air	0.55	[100]
Pr/Ca	SSR	10/0.5	Total	$\sim 10^{-4}$	727	O_2	N/A	[99]
Pr/Ca	SSR	10/2.0	Total	2.40×10^{-4}	700	Air	0.53	[100]
Pr/Ca	SSR	8.0/2.0	Total	2.30×10^{-4}	700	Air	0.53	[100]
Nd/Ca	SSR	49.5/1.0	Total	$\sim 7.90 \times 10^{-4}$	900	Air	N/A	[103]
Sm	SSR	10	Total	1.76×10^{-4}	800	Air	0.81	[98]

Table A1 continues on the following page.

Table A1 (continued)

Sm/Ca	SSR	20/1.0	Total	~4.00× 10^{-4}	700	Air	0.56	[102]
Sm/Ca	SSR	40/1.0	Total	~4.00 × 10^{-4}	700	Air	0.56	[102]
Sm/Ca	SSR	60/1.0	Total	~3.30 × 10^{-4}	700	Air	0.63	[102]
Sm/Ca	SSR	80/1.0	Total	~2.50 × 10^{-4}	700	Air	0.64	[102]
Sm/Ca	SSR	49.5/1.0	Total	~6.30 × 10^{-4}	900	Air	N/A	[103]
Gd	SSR	10	Total	~2.00 × 10^{-5}	800	Air	0.67	[98]
Yb	SSR	10	Total	~10^{-5}	800	Air	0.73	[98]
Tb	SSR	5.0	Total	3.68 × 10^{-5}	700	Air	0.56	[105]
Tb	SSR	10	Total	9.51 × 10^{-5}	700	Air	0.55	[105]
Tb	SSR	15	Total	1.13 × 10^{-4}	700	Air	0.53	[105]
Tb	SSR	20	Total	3.95 × 10^{-5}	700	Air	0.59	[105]
Tb	SSR	30	Total	3.11 × 10^{-5}	700	Air	0.69	[105]
Th	SSR	7.0	Total	2.60 × 10^{-2}	1000	N/A	1.40	[189]
Th	SSR	10	Total	2.20 × 10^{-2}	1000	N/A	1.40	[189]
Th	SSR	20	Total	6.80 × 10^{-3}	1000	N/A	1.50	[189]

A2 Related information of Nb site substituted $LaNbO_4$

Table A2. Related information of Nb site substituted materials synthesised via different methods. Substitutes which could stabilise m-phase or t-phase are marked in red or blue, respectively. Substitutes before and after the slash are substituted on La sites or Nb sites, respectively. For activation energy, values for m-phase are marked with (m).

Substituent elements	Synthesis method	Amount (mol%)	Conductivity type	Conductivity (S cm^{-1})	Temperature (°C)	Atmosphere (humidified)	E_a (eV)	Ref
Mg/Al	SSR	1.0/1.0	Proton	~10^{-5}	900	Air	N/A	[114]
Ca/Al	SSR	1.0/1.0	Proton	~10^{-4}	900	Air	N/A	[114]
Sr/Al	SSR	1.0/1.0	Total	6.00×10^{-4}	900	Air	N/A	[114]
Ba/Al	SSR	1.0/1.0	Total	~10^{-4}	900	Air	N/A	[114]
Ti	SSR	1.0	Total	~10^{-4}	900	O_2	0.81	[70]
Ti	SSR	2.0	Total	~10^{-4}	900	O_2	N/A	[108]
Ti	SSR	3.0	Total	~10^{-4}	900	O_2	N/A	[108]
Mg/Ti	SSR	1.0/1.0	Total	~3.00×10^{-5}	900	Air	N/A	[114]
Ca/Ti	SSR	1.0/1.0	Total	3.00×10^{-4}	900	O_2	N/A	[70]
Ca/Ti	SSR	1.0/1.0	Total	~10^{-4}	900	Ar	N/A	[114]
Sr/Ti	SSR	1.0/1.0	Total	~3.00×10^{-4}	900	Air	N/A	[114]
Ba/Ti	SSR	1.0/1.0	Total	~10^{-4}	900	Air	N/A	[114]
Sr/V	SSR	2.0/30	Total	~10^{-4}	900	O_2	N/A	[118]

Table A2 continues on the following page.

Table A2 (continued)

Sr/V	SSR	2.0/15	Total	~10^{-5}	600	O_2	N/A	[119]
Ca/Co	SSR	5.0/1.0	Total	6.31×10^{-5}	800	Air	N/A	[109]
Ca/Co	SSR	5.0/2.0	Total	1.05×10^{-4}	800	Air	N/A	[109]
Ca/Co	SSR	5.0/3.0	Total	1.51×10^{-4}	800	Air	N/A	[109]
Ca/Co	SSR	5.0/5.0	Total	2.40×10^{-4}	800	Air	N/A	[109]
Ca/Ni	SSR	5.0/1.0	Total	2.03×10^{-4}	800	5% H_2/Ar	0.62	[110]
Ca/Ni	SSR	5.0/3.0	Total	2.67×10^{-4}	800	5% H_2/Ar	0.51	[110]
Ca/Ni	SSR	5.0/5.0	Total	3.53×10^{-4}	800	5% H_2/Ar	0.45	[110]
Ca/Ni	SSR	5.0/10	Total	3.25×10^{-4}	800	5% H_2/Ar	0.50	[110]
Ca/Ni	SSR	5.0/20	Total	2.85×10^{-4}	800	5% H_2/Ar	0.57	[110]
Ca/Ni	SSR	5.0/30	Total	2.32×10^{-4}	800	5% H_2/Ar	0.61	[110]
Ga	SSR	1.0	Total	~10^{-4}	900	9% H_2/ N_2	N/A	[115]
Ca/Ga	SSR	1.0/1.0	Total	~4.00×10^{-4}	900	9% H_2/ N_2	N/A	[115]
Ba/Ga	SSR	1.0/1.0	Total	~2.00×10^{-4}	900	9% H_2/ N_2	N/A	[115]
Ge	SSR	1.0	Total	~10^{-4}	900	9% H_2/ N_2	N/A	[115]
Ca/Ge	SSR	1.0/1.0	Total	~2.00×10^{-4}	900	9% H_2/ N_2	N/A	[115]
Ba/Ge	SSR	1.0/1.0	Total	~8.00×10^{-5}	900	9% H_2/ N_2	N/A	[115]
Mo	SSR	20	Total	8.11×10^{-2}	900	5% H_2/ N_2	0.34	[16]

Table A2 continues on the following page.

Table A2 (continued)

Mo	SSR	20	Total	2.65×10^{-2}	900	Air	1.25	[16]
Mo	SSR	16	Total	7.00×10^{-3}	800	Dry air	1.46	[12]
Mo	SSR	20	Total	7.00×10^{-3}	800	Dry air	1.42	[12]
Mo	SSR	10	Total	1.52×10^{-2}	900	Dry air	1.53	[14]
Mo	SSR	20	Total	2.39×10^{-2}	856	Dry air	N/A	[15]
Gd/Mo	SSR	2.0/8.0	Total	1.07×10^{-2}	900	Dry air	1.11	[14]
Gd/Mo	SSR	4.0/6.0	Total	4.68×10^{-3}	900	Dry air	1.08	[14]
Gd/Mo	SSR	5.0/5.0	Total	4.26×10^{-2}	900	Dry air	1.08	[14]
Gd/Mo	SSR	6.0/4.0	Total	1.48×10^{-3}	900	Dry air	1.16	[14]
Gd/Mo	SSR	8.0/2.0	Total	1.38×10^{-3}	900	Dry air	1.22	[14]
In	SSR	1.0	Total	$\sim 10^{-4}$	900	9% H_2/ N_2	N/A	[115]
Ca/In	SSR	1.0/1.0	Total	$\sim 3.00 \times 10^{-4}$	900	9% H_2/ N_2	N/A	[115]
Ba/In	SSR	1.0/1.0	Total	$\sim 3.00 \times 10^{-4}$	900	9% H_2/ N_2	N/A	[115]
Sn	SSR	1.0	Total	$\sim 5.00 \times 10^{-4}$	900	5% H_2/Ar	N/A	[112]
Sn	SSR	3.0	Total	6.00×10^{-4}	900	5% H_2/Ar	N/A	[112]
Ca/Sn	SSR	5.0/5.0	Total	2.96×10^{-4}	800	H_2	0.47	[111]
Sb	SSR	10	Total	$\sim 5.00 \times 10^{-5}$	900	Air	0.67	[125]
Sb	SSR	30	Total	$\sim 10^{-4}$	900	Air	0.54	[125]

Table A2 continues on the following page.

Table A2 (continued)

Ca/Sb	SSR	2.0/10	Total	~6.00×10^{-4}	900	Air	0.76	[125]
Ca/Sb	SSR	2.0/30	Total	~4.00×10^{-4}	900	Air	0.83	[125]
Ca/Ta	SSR	1.0/10	Total	~3.00×10^{-4}	900	Air	0.52	[120]
Ca/Ta	SSR	1.0/20	Total	~3.00×10^{-4}	900	Air	0.53	[120]
Ca/Ta	SSR	1.0/30	Total	~3.00×10^{-4}	900	Air	0.58	[120]
Ca/Ta	SSR	1.0/40	Total	~2.00×10^{-4}	900	Air	1.08(m)	[120]
Sr/Ta	CP	2.0/40	Total	1.90×10^{-4}	800	Ar	1.05(m)	[122]
Sr/Ta	AC	2.0/40	Total	1.80×10^{-4}	800	Ar	1.14(m)	[122]
Sr/Ta	SSR	2.0/10	Total	~5.00×10^{-4}	800	Ar	0.64	[121]
Sr/Ta	SSR	2.0/20	Total	~3.00×10^{-4}	800	Ar	0.76	[121]
Sr/Ta	SSR	2.0/40	Total	~8.00×10^{-5}	800	Ar	1.07(m)	[121]
W	SSR	8.0	Total	3.00×10^{-3}	800	Dry air	0.93	[11]
W	SSR	2.0	Total	2.30×10^{-6}	800	N/A	N/A	[133]
W	SSR	4.0	Total	1.20×10^{-5}	800	N/A	N/A	[133]
W	SSR	6.0	Total	3.60×10^{-5}	800	N/A	N/A	[133]
W	SSR	8.0	Total	4.60×10^{-5}	800	N/A	N/A	[133]
W	SSR	10	Total	2.00×10^{-4}	800	N/A	N/A	[133]
W	SSR	16	Total	6.10×10^{-3}	800	Dry H_2	N/A	[132]

Table A2 continues on the following page.

Table A2 (continued)

W	SSR	20	Total	3.38×10^{-3}	856	Dry air	N/A	[15]
W/Mo	SSR	2/18	Total	2.37×10^{-3}	665	Dry air	0.85	[15]
W/Mo	SSR	4/16	Total	1.55×10^{-2}	856	Dry air	N/A	[15]
W/Mo	SSR	10/10	Total	6.16×10^{-3}	856	Dry air	N/A	[15]
W/Mo	SSR	16/4	Total	3.09×10^{-3}	856	Dry air	N/A	[15]
W/Mo	SSR	18/2	Total	2.95×10^{-3}	856	Dry air	N/A	[15]

A3 Refined structural parameters of $La_{1-x}Gd_xNb_{0.9}Mo_{0.1}O_{4.05}$ series at 25 °C

Table A3. Refined structural parameters of $La_{1-x}Gd_xNb_{0.9}Mo_{0.1}O_{4.05}$ series from Le Bail refinements against XRD data collected at 25 °C.

	LNM10	La8Gd2	La6Gd4	La5Gd5	La4Gd6	La2Gd8	GNM10
Space group	I2/a	I2/a	I2/a	I2/a	I2/a	I2/a	I2/a
a (Å)	5.3943(2)	5.4027(2)	5.4498(2)	5.4407(3)	5.4190(3)	5.3915(2)	5.3512(5)
b (Å)	11.6545(3)	11.5280(5)	11.3919(5)	11.3392(5)	11.2890(4)	11.1934(4)	11.1078(8)
c (Å)	5.3071(2)	5.2772(2)	5.1957(3)	5.1755(3)	5.1720(3)	5.1440(2)	5.1305(5)
β (°)	91.235(2)	91.605(2)	93.173(2)	93.429(2)	93.406(2)	93.715(2)	93.658(4)
V ($Å^3$)	333.57(1)	328.55(3)	322.07(3)	318.72(3)	315.85(3)	309.79(2)	304.33(6)
R_{wp} (%)	3.92	4.15	2.78	3.05	2.84	2.78	3.43
χ^2	1.81	4.47	2.92	3.20	3.29	3.41	4.61

A4 Transition behaviour of $La_{1-x}Gd_xNb_{0.9}Mo_{0.1}O_{4.05}$ series from m-phase to t-phase

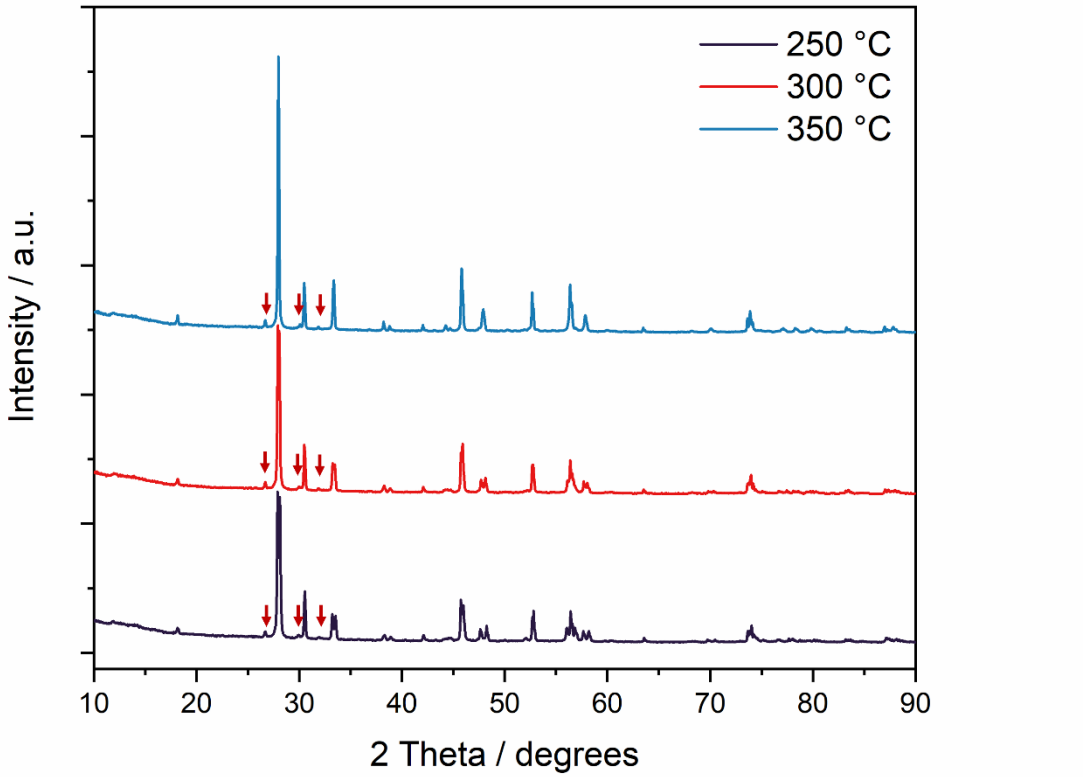


Figure A1. XRD patterns of LNM10 recorded at 250 °C, 300 °C and 350 °C, respectively. The satellite reflections of the modulated structure are marked by arrows. Reproduced with permission [14]. Copyright (2023), Royal Society of Chemistry.

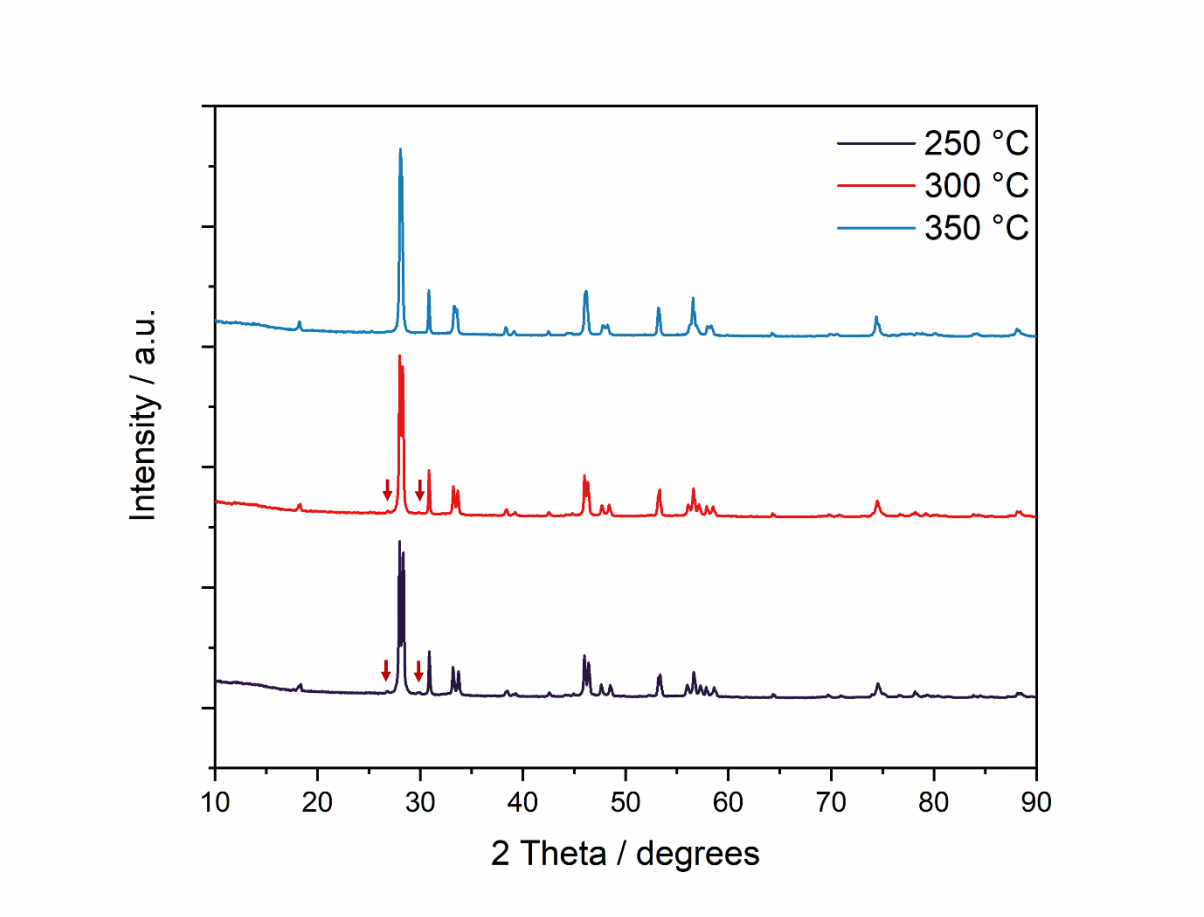


Figure A2. XRD patterns of La8Gd2 recorded at 250 °C, 300 °C and 350 °C, respectively. The satellite reflections of the modulated structure are marked by arrows. Reproduced with permission [14]. Copyright (2023), Royal Society of Chemistry.

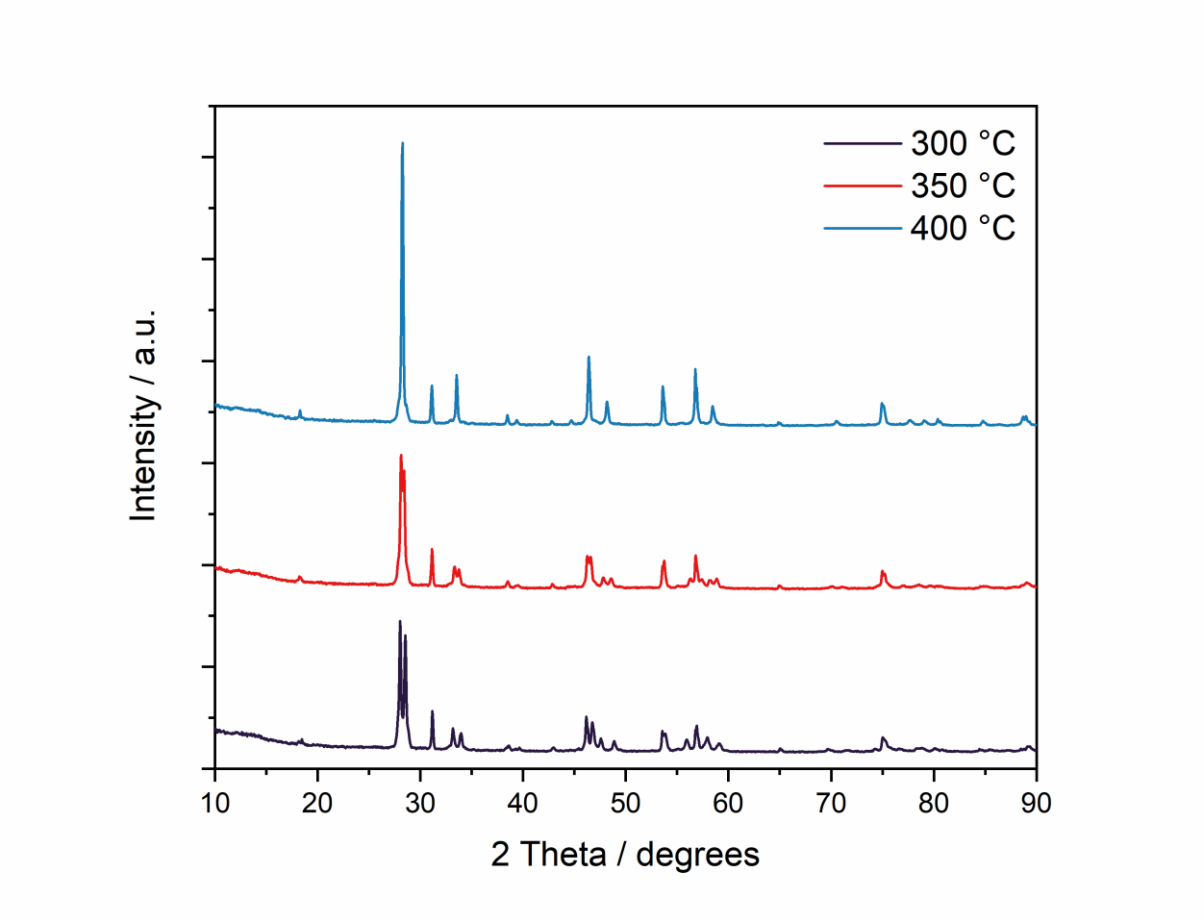


Figure A3. XRD patterns of La6Gd4 recorded at 300 °C, 350 °C and 400 °C, respectively. Reproduced with permission [14]. Copyright (2023), Royal Society of Chemistry.

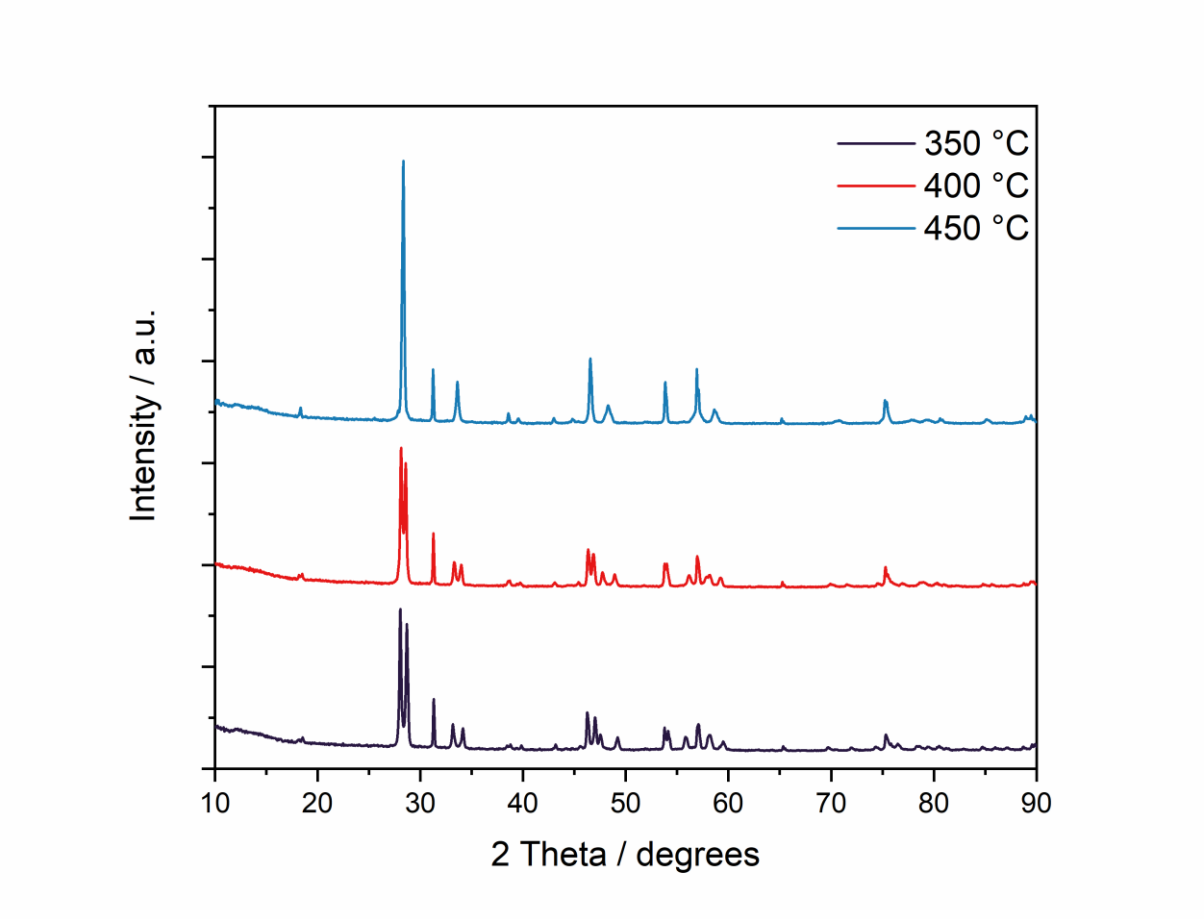


Figure A4. XRD patterns of La5Gd5 recorded at 350 °C, 400 °C and 450 °C, respectively. Reproduced with permission [14]. Copyright (2023), Royal Society of Chemistry.

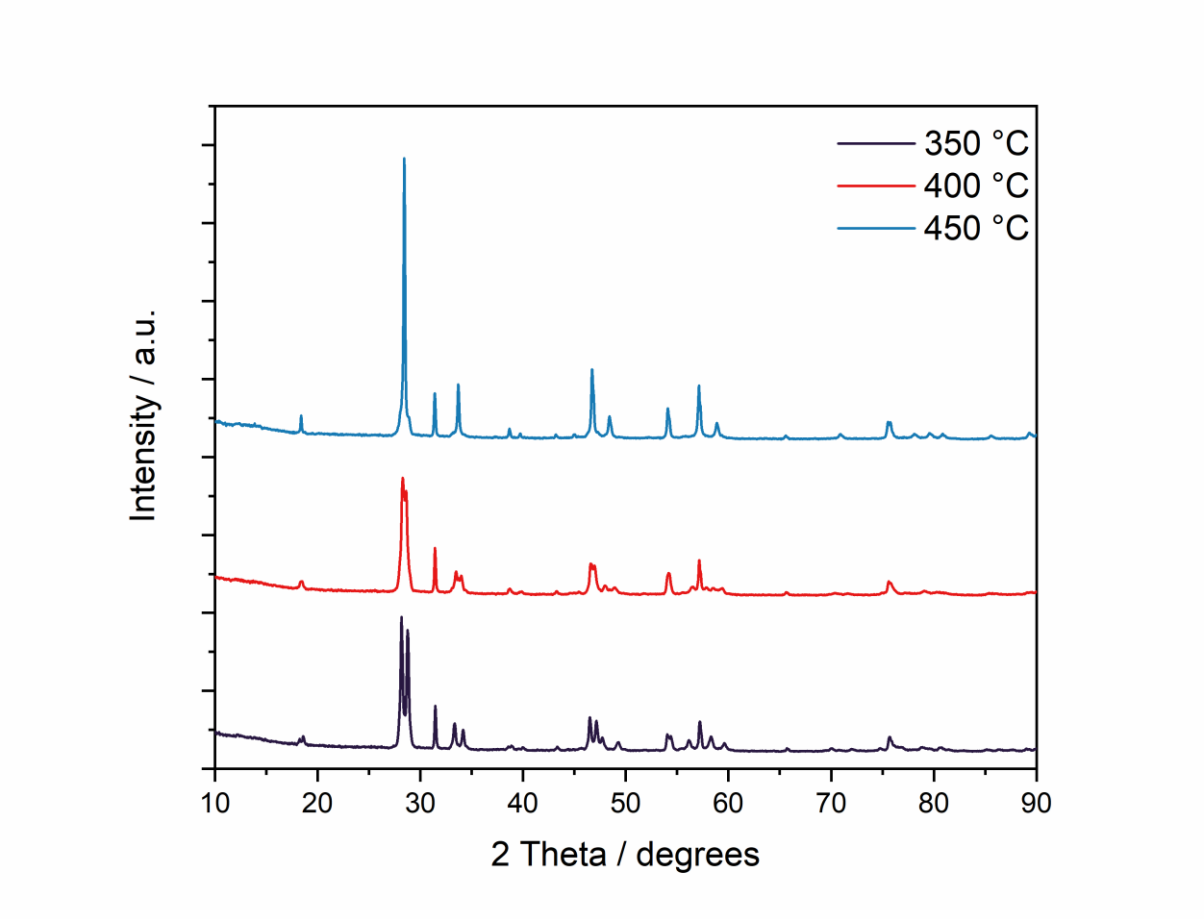


Figure A5. XRD patterns of La4Gd6 recorded at 350 °C, 400 °C and 450 °C, respectively. Reproduced with permission [14]. Copyright (2023), Royal Society of Chemistry.

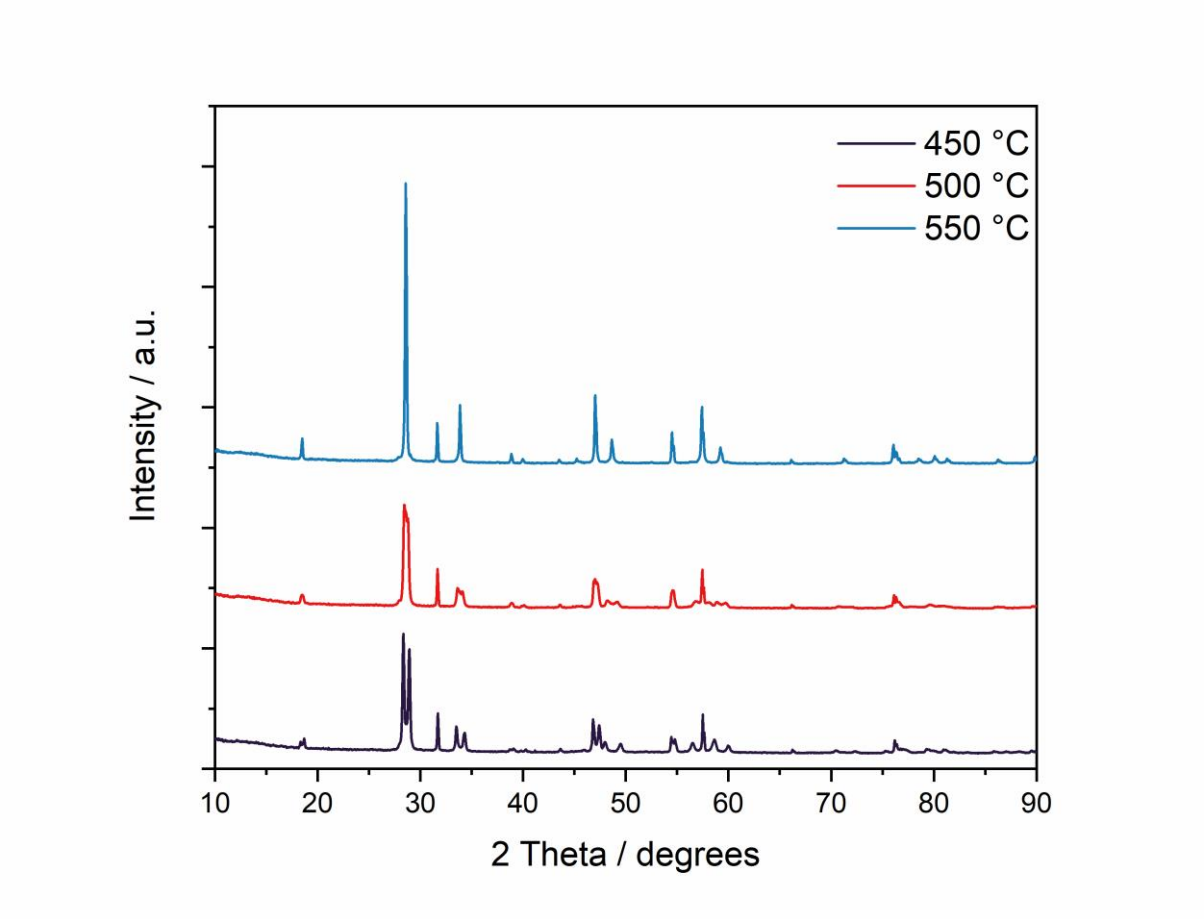


Figure A6. XRD patterns of La2Gd8 recorded at 450 °C, 500 °C and 550 °C, respectively. Reproduced with permission [14]. Copyright (2023), Royal Society of Chemistry.

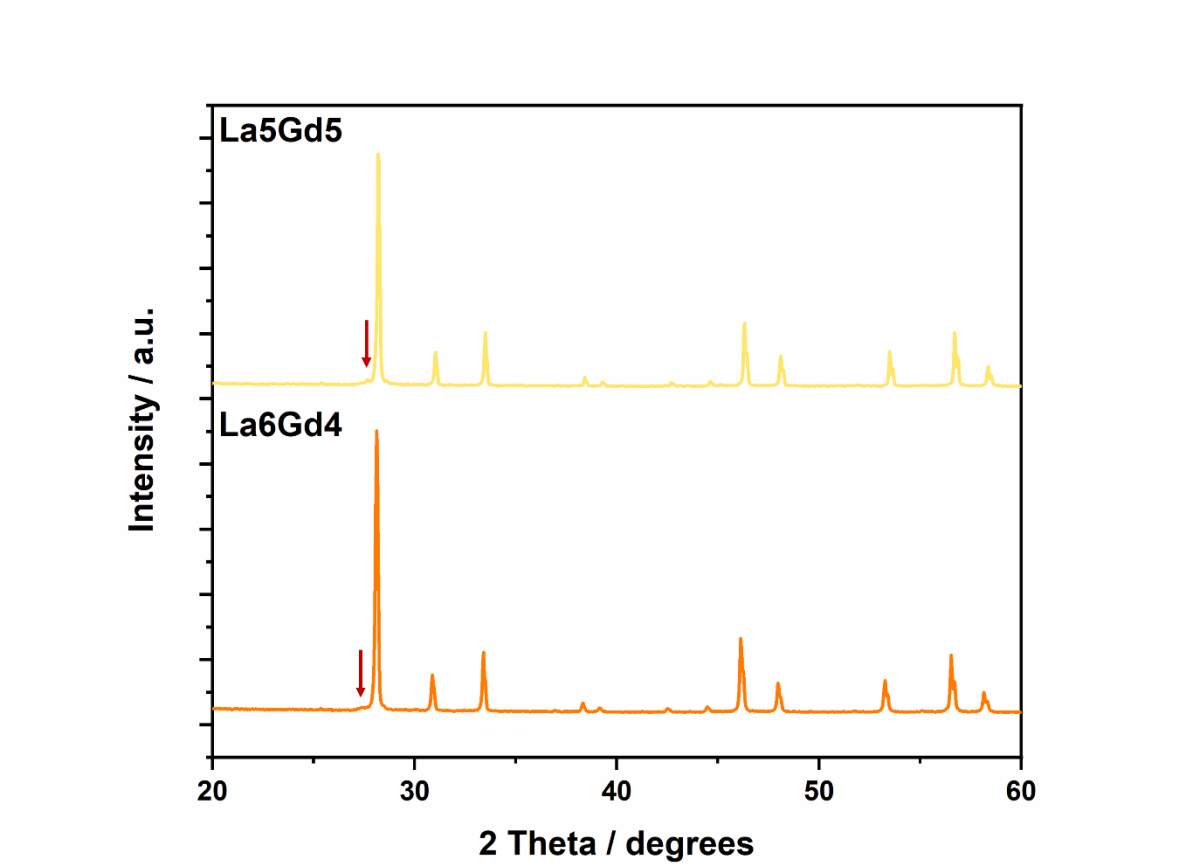


Figure A7. XRD patterns of La6Gd4 and La5Gd5 recorded at 900 °C, respectively. 2θ range is selected from 20° to 60°to highlight the existence of m-phase. The peak from the new m-phase is marked by arrows.

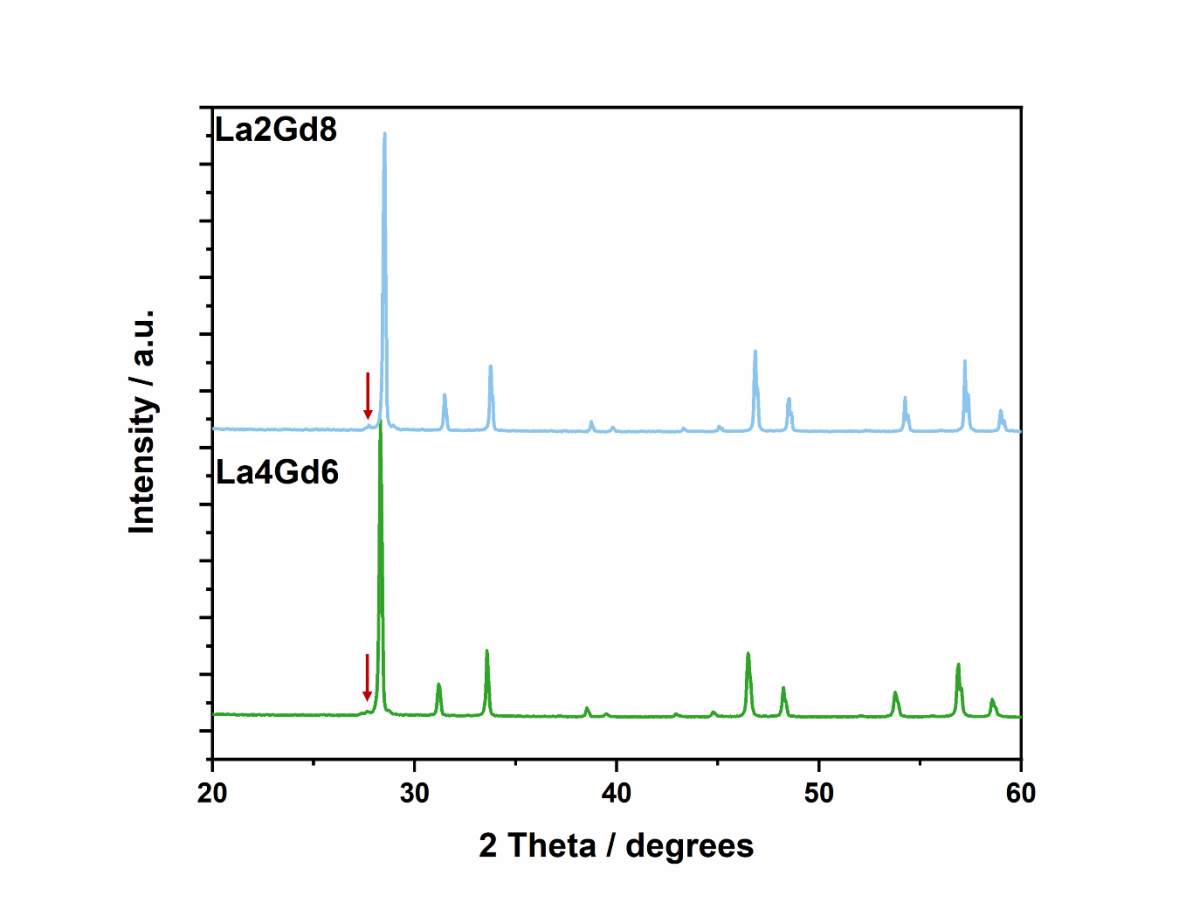


Figure A8. XRD patterns of La4Gd6 and La2Gd8 recorded at 900 °C, respectively. 2θ range is selected from 20° to 60°to highlight the existence of m-phase. The peak from the new m-phase is marked by arrows.

A5 Refined structural parameters of $LaNb_{0.8}W_xMo_{0.2-x}O_{4.1}$ series at 25 °C

Table A4. Refined structural parameters of $LaNb_{0.8}W_xMo_{0.2-x}O_{4.1}$ series from Le Bail refinements against XRD data collected at 25 °C.

	LNMo20	LNW2Mo18	LNW4Mo16	LNW10Mo10	LNW16Mo4	LNW18Mo2	LNW20
Space group	I2/a	I2/a	$I4_1/a$	$I4_1/a$	$I4_1/a$	$I4_1/a$	$I4_1/a$
a (Å)	5.4004(2)	5.3994(3)	5.3487(4)	5.3400(2)	5.3348(2)	5.3352(2)	5.3360(3)
b (Å)	11.6460(4)	11.6456(6)	-	-	-	-	-
c (Å)	5.3067(2)	5.3080(3)	11.6647(7)	11.6882(3)	11.6971(2)	11.6946(3)	11.6900(4)
β (°)	91.271(3)	91.178(4)	-	-	-	-	-
V ($Å^3$)	333.68(1)	333.69(2)	333.72(5)	333.30(2)	332.90(2)	332.88(2)	332.85(3)
R_{wp} (%)	4.64	5.81	7.05	6.72	6.07	6.18	7.99
χ^2	4.91	4.16	4.97	3.23	3.99	3.89	5.37

A6 Refined structural parameters of $LaNb_{0.8}W_xMo_{0.2-x}O_{4.1}$ series at 850 °C

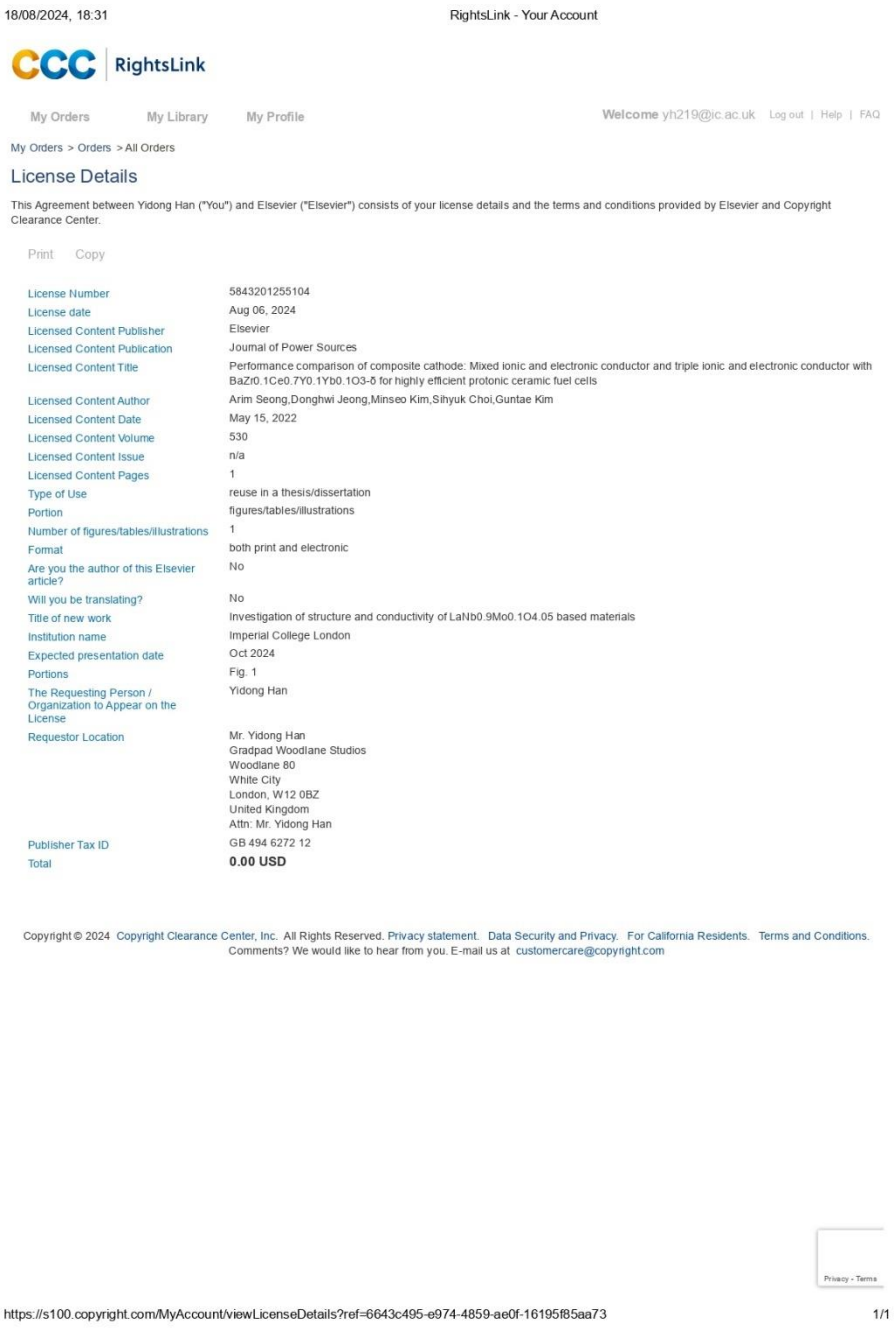
Table A5. Refined structural parameters of $LaNb_{0.8}W_xMo_{0.2-x}O_{4.1}$ series from Le Bail refinements against XRD data collected at 850 °C.

	LNMo20	LNW2Mo18	LNW4Mo16	LNW10Mo10	LNW16Mo4	LNW18Mo2	LNW20
Space group	$I4_1/a$	$I4_1/a$	$I4_1/a$	$I4_1/a$	$I4_1/a$	$I4_1/a$	$I4_1/a$
a (Å)	5.4028(1)	5.4020(2)	5.3984(2)	5.3865(2)	5.3788(2)	5.3787(2)	5.3809(3)
c (Å)	11.7685(2)	11.7741(4)	11.7887(2)	11.8061(2)	11.8191(3)	11.8143(3)	11.8086(4)
V ($Å^3$)	343.53(2)	343.58(3)	343.55(2)	342.54(2)	341.95(2)	341.80(2)	341.91(3)
R_{wp} (%)	5.25	8.13	6.28	6.02	7.45	7.61	8.464
χ^2	5.40	5.99	4.63	4.12	5.03	4.97	5.84

A7 Permission documents

The permission documents of the figures in which are copyrighted works from other journal papers are all listed below.

Figure 1.2.1. Schematic representations of active sites of TIEC (left) and mixture of MIEC and proton conducting materials (right). ‘‘PCO’’ represents the proton conducting oxides. Reproduced with permission [2]. Copyright (2022), Elsevier.



18/08/2024, 18:31 RightsLink - Your Account

CCC RightsLink

My Orders My Library My Profile Welcome yh219@ic.ac.uk Log out | Help | FAQ

My Orders > Orders > All Orders

License Details

This Agreement between Yidong Han ("You") and Elsevier ("Elsevier") consists of your license details and the terms and conditions provided by Elsevier and Copyright Clearance Center.

Print Copy

License Number	5843201255104
License date	Aug 06, 2024
Licensed Content Publisher	Elsevier
Licensed Content Publication	Journal of Power Sources
Licensed Content Title	Performance comparison of composite cathode: Mixed ionic and electronic conductor and triple ionic and electronic conductor with BaZr0.1Ce0.7Y0.1Yb0.1O3-δ for highly efficient protonic ceramic fuel cells
Licensed Content Author	Arim Seong,Donghwi Jeong,Minseo Kim,Sihyuk Choi,Guntae Kim
Licensed Content Date	May 15, 2022
Licensed Content Volume	530
Licensed Content Issue	n/a
Licensed Content Pages	1
Type of Use	reuse in a thesis/dissertation
Portion	figures/tables/illustrations
Number of figures/tables/illustrations	1
Format	both print and electronic
Are you the author of this Elsevier article?	No
Will you be translating?	No
Title of new work	Investigation of structure and conductivity of LaNb0.9Mo0.1O4.05 based materials
Institution name	Imperial College London
Expected presentation date	Oct 2024
Portions	Fig. 1
The Requesting Person / Organization to Appear on the License	Yidong Han
Requestor Location	Mr. Yidong Han Gradpad Woodlane Studios Woodlane 80 White City London, W12 0BZ United Kingdom Attn: Mr. Yidong Han
Publisher Tax ID	GB 494 6272 12
Total	**0.00 USD**

Copyright © 2024 Copyright Clearance Center, Inc. All Rights Reserved. Privacy statement. Data Security and Privacy. For California Residents. Terms and Conditions.
Comments? We would like to hear from you. E-mail us at customercare@copyright.com

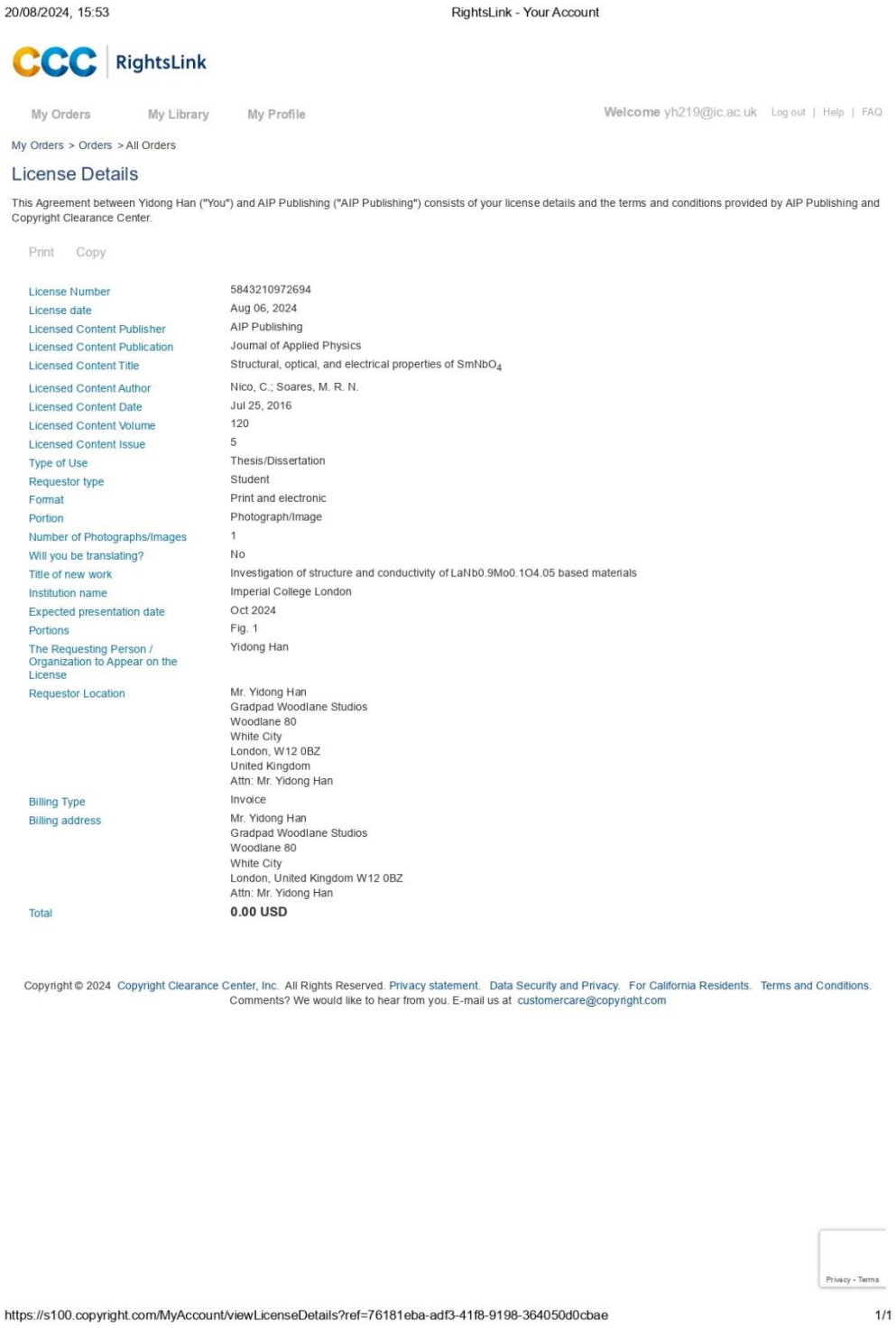
Privacy - Terms

https://s100.copyright.com/MyAccount/viewLicenseDetails?ref=6643c495-e974-4859-ae0f-16195f85aa73 1/1

Figure 1.3.2. Conductivity data of YSZ, CGO and LSGM. Reproduced with permission [3]. Copyright (2010), American Chemical Society.



Figure 2.1.1. The structures of a) m-phase and b) t-phase $ReNbO_4$. The pink, blue and red balls represent rare earth, niobium, and oxygen atoms, respectively. Reproduced with permission [4]. Copyright (2016), American Institute of Physics.



20/08/2024, 15:53 RightsLink - Your Account

RightsLink

My Orders My Library My Profile Welcome yh219@ic.ac.uk Log out | Help | FAQ

My Orders > Orders > All Orders

License Details

This Agreement between Yidong Han ("You") and AIP Publishing ("AIP Publishing") consists of your license details and the terms and conditions provided by AIP Publishing and Copyright Clearance Center.

Print Copy

License Number	5843210972694
License date	Aug 06, 2024
Licensed Content Publisher	AIP Publishing
Licensed Content Publication	Journal of Applied Physics
Licensed Content Title	Structural, optical, and electrical properties of $SmNbO_4$
Licensed Content Author	Nico, C.; Soares, M. R. N.
Licensed Content Date	Jul 25, 2016
Licensed Content Volume	120
Licensed Content Issue	5
Type of Use	Thesis/Dissertation
Requestor type	Student
Format	Print and electronic
Portion	Photograph/Image
Number of Photographs/Images	1
Will you be translating?	No
Title of new work	Investigation of structure and conductivity of LaNb0.9Mo0.1O4.05 based materials
Institution name	Imperial College London
Expected presentation date	Oct 2024
Portions	Fig. 1
The Requesting Person / Organization to Appear on the License	Yidong Han
Requestor Location	Mr. Yidong Han Gradpad Woodlane Studios Woodlane 80 White City London, W12 0BZ United Kingdom Attn: Mr. Yidong Han
Billing Type	Invoice
Billing address	Mr. Yidong Han Gradpad Woodlane Studios Woodlane 80 White City London, United Kingdom W12 0BZ Attn: Mr. Yidong Han
Total	**0.00 USD**

Copyright © 2024 Copyright Clearance Center, Inc. All Rights Reserved. Privacy statement. Data Security and Privacy. For California Residents. Terms and Conditions.
Comments? We would like to hear from you. E-mail us at customercare@copyright.com

Privacy - Terms

https://s100.copyright.com/MyAccount/viewLicenseDetails?ref=76181eba-adf3-41f8-9198-364050d0cbae 1/1

Figure 2.2.1. Structures of a) t-$LaNbO_4$ and b) m-$LaNbO_4$. The red and green balls represent O and La sites, respectively. The niobium sites are represented by the green balls in the tetrahedra. Reproduced with permission [5]. Copyright (2010), Royal Society of Chemistry.

Figure 2.2.2. Stable proton sites in a) t-$LaNbO_4$ and b) m-$LaNbO_4$. Reproduced with permission [5]. Copyright (2010), Royal Society of Chemistry.

Figure 2.2.3. Potential proton migration paths in a) t-$LaNbO_4$ and b) m-$LaNbO_4$. Reproduced with permission [5]. Copyright (2010), Royal Society of Chemistry.

20/08/2024, 16:08 marketplace.copyright.com/rs-ui-web/mp/license/3fffd22f-63a1-49e5-ad31-65588af93c1a/a9b4fb76-86a5-45d4-87a8-12e9fa4...

CCC Marketplace

This is a License Agreement between Yidong Han ("User") and Copyright Clearance Center, Inc. ("CCC") on behalf of the Rightsholder identified in the order details below. The license consists of the order details, the Marketplace Permissions General Terms and Conditions below, and any Rightsholder Terms and Conditions which are included below.

All payments must be made in full to CCC in accordance with the Marketplace Permissions General Terms and Conditions below.

Order Date	20-Aug-2024
Order License ID	1517563-1
ISSN	1463-9084
Type of Use	Republish in a thesis/dissertation
Publisher	ROYAL SOCIETY OF CHEMISTRY
Portion	Chart/graph/table/figure

LICENSED CONTENT

Publication Title	Physical chemistry chemical physics
Article Title	Proton mobility through a second order phase transition: theoretical and experimental study of LaNbO4.
Author / Editor	Royal Society of Chemistry (Great Britain)
Date	01/01/1999
Language	English
Country	United Kingdom of Great Britain and Northern Ireland
Rightsholder	Royal Society of Chemistry
Publication Type	e-Journal
Start Page	10313
Issue	35
Volume	12
URL	http://firstsearch.oclc.org/journal=1463-9076;screen=info;ECOIP

REQUEST DETAILS

Portion Type	Chart/graph/table/figure
Number of Charts / Graphs / Tables / Figures Requested	3
Format (select all that apply)	Print, Electronic
Who Will Republish the Content?	Author of requested content
Duration of Use	Current edition and up to 5 years
Lifetime Unit Quantity	Up to 499
Rights Requested	Main product
Distribution	U.K. and Commonwealth (excluding Canada)
Translation	Original language of publication
Copies for the Disabled?	No
Minor Editing Privileges?	No
Incidental Promotional Use?	No
Currency	GBP

NEW WORK DETAILS

Title	Investigation of structure and conductivity of LaNb0.9Mo0.1O4.05 based materials
Instructor Name	Stephen Skinner
Institution Name	Imperial College London
Expected Presentation Date	2024-10-05

ADDITIONAL DETAILS

Order Reference Number	N/A
The Requesting Person / Organization to Appear on the License	Yidong Han

REQUESTED CONTENT DETAILS

Title, Description or Numeric Reference of the Portion(s)	Fig. 1, Fig. 2, Fig. 3
Editor of Portion(s)	Fjeld, Harald; Toyoura, Kazuaki; Haugsrud, Reidar; Norby, Truls
Volume / Edition	12
Page or Page Range of Portion	10313
Title of the Article / Chapter the Portion Is From	Proton mobility through a second order phase transition: theoretical and experimental study of LaNbO4.
Author of Portion(s)	Fjeld, Harald; Toyoura, Kazuaki; Haugsrud, Reidar; Norby, Truls
Issue, if Republishing an Article From a Serial	35
Publication Date of Portion	2010-09-21

https://marketplace.copyright.com/rs-ui-web/mp/license/3fffd22f-63a1-49e5-ad31-65588af93c1a/a9b4fb76-86a5-45d4-87a8-12e9fa4cc5bf 1/1

Figure 2.2.4. Temperature dependence of $\Delta H_{mob,H}$ (squares) and O(1)-O(1) separation distance of $LaNbO_4$. Reproduced with permission [6]. Copyright (2012), Elsevier.

20/08/2024, 16:14 RightsLink - Your Account

RightsLink

My Orders My Library My Profile Welcome yh219@ic.ac.uk Log out | Help | FAQ

My Orders > Orders > All Orders

License Details

This Agreement between Yidong Han ("You") and Elsevier ("Elsevier") consists of your license details and the terms and conditions provided by Elsevier and Copyright Clearance Center.

Print Copy

License Number	5853120693200
License date	Aug 20, 2024
Licensed Content Publisher	Elsevier
Licensed Content Publication	Journal of Solid State Chemistry
Licensed Content Title	Neutron diffraction study of the monoclinic to tetragonal structural transition in LaNbO4 and its relation to proton mobility
Licensed Content Author	M. Huse,A.W.B. Skilbred,M. Karlsson,S.G. Eriksson,T. Norby,R. Haugsrud,C.S. Knee
Licensed Content Date	Mar 1, 2012
Licensed Content Volume	187
Licensed Content Issue	n/a
Licensed Content Pages	8
Type of Use	reuse in a thesis/dissertation
Portion	figures/tables/illustrations
Number of figures/tables/illustrations	1
Format	both print and electronic
Are you the author of this Elsevier article?	No
Will you be translating?	No
Title of new work	Investigation of structure and conductivity of LaNb0.9Mo0.1O4.05 based materials
Institution name	Imperial College London
Expected presentation date	Oct 2024
Portions	Fig. 10
The Requesting Person / Organization to Appear on the License	Yidong Han
Requestor Location	Mr. Yidong Han Gradpad Woodlane Studios Woodlane 80 White City London, W12 0BZ United Kingdom Attn: Mr. Yidong Han
Publisher Tax ID	GB 494 6272 12
Total	**0.00 USD**

Copyright © 2024 Copyright Clearance Center, Inc. All Rights Reserved. Privacy statement. Data Security and Privacy. For California Residents. Terms and Conditions.
Comments? We would like to hear from you. E-mail us at customercare@copyright.com

Privacy - Terms

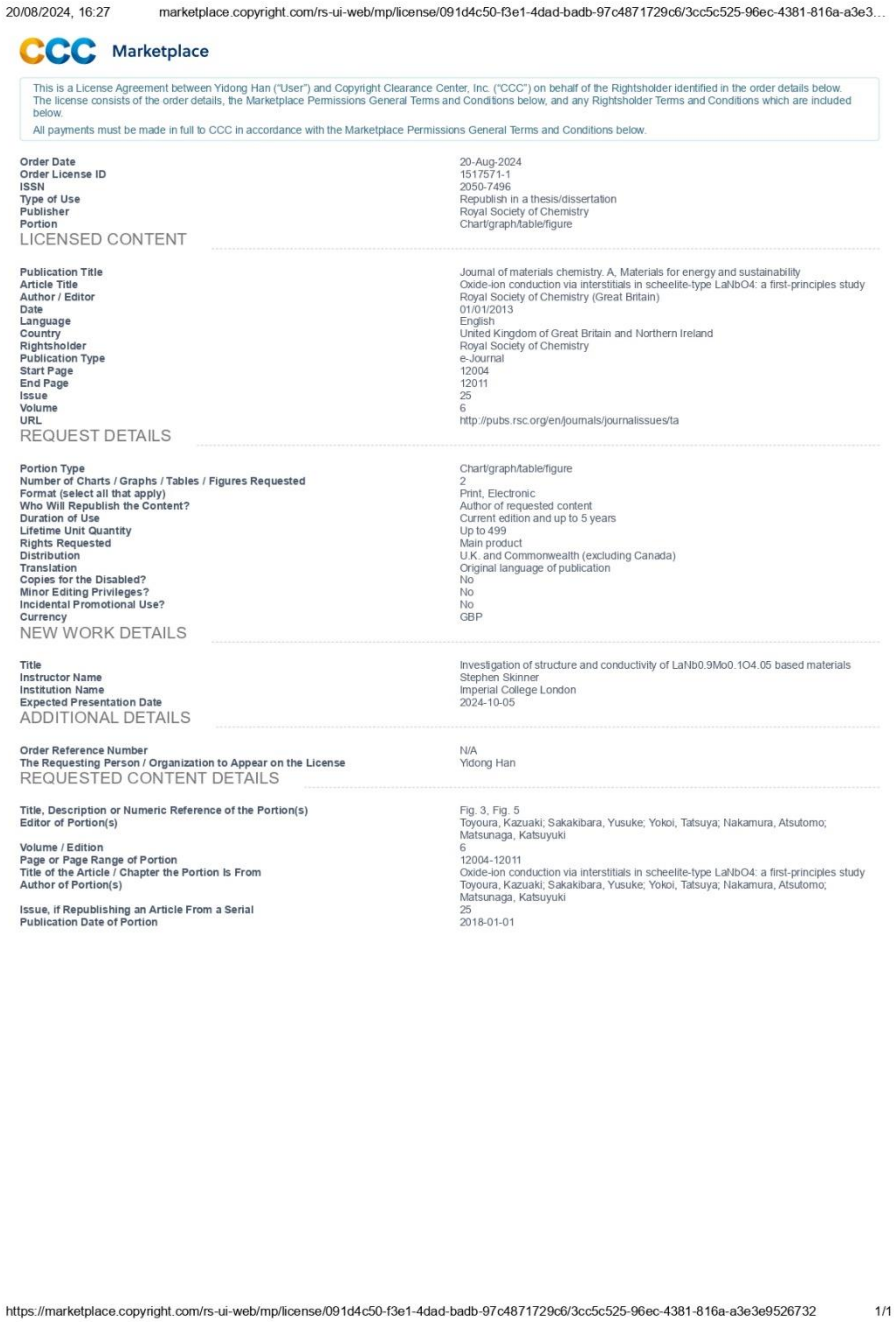
https://s100.copyright.com/MyAccount/viewLicenseDetails?ref=06a63435-9563-45a5-8805-c92915c3d4d2 1/1

Figure 2.2.5. Relationship between incorporation energy and substituents radii for acceptor substituents on La site. Reproduced with permission [7]. Copyright (2010), American Chemistry Society.



Figure 2.3.1. The connection of interstitial sites in t-$LaNbO_4$. The different migration paths are labelled by numbers and the different oxygen interstitial sites are labelled as O_{int}-1 and O_{int}-2, respectively. Reproduced with permission [8]. Copyright (2018), Royal Society of Chemistry.

Figure 2.3.3. The migration pathways of oxygen ions conductivity via interstitials a) in the *ab* plane and b) along the *c* axis. Reproduced with permission [8]. Copyright (2018), Royal Society of Chemistry.



20/08/2024, 16:27 marketplace.copyright.com/rs-ui-web/mp/license/091d4c50-f3e1-4dad-badb-97c4871729c6/3cc5c525-96ec-4381-816a-a3e3...

CCC Marketplace

This is a License Agreement between Yidong Han ("User") and Copyright Clearance Center, Inc. ("CCC") on behalf of the Rightsholder identified in the order details below. The license consists of the order details, the Marketplace Permissions General Terms and Conditions below, and any Rightsholder Terms and Conditions which are included below.

All payments must be made in full to CCC in accordance with the Marketplace Permissions General Terms and Conditions below.

Order Date	20-Aug-2024
Order License ID	1517571-1
ISSN	2050-7496
Type of Use	Republish in a thesis/dissertation
Publisher	Royal Society of Chemistry
Portion	Chart/graph/table/figure

LICENSED CONTENT

Publication Title	Journal of materials chemistry. A, Materials for energy and sustainability
Article Title	Oxide-ion conduction via interstitials in scheelite-type LaNbO4: a first-principles study
Author / Editor	Royal Society of Chemistry (Great Britain)
Date	01/01/2013
Language	English
Country	United Kingdom of Great Britain and Northern Ireland
Rightsholder	Royal Society of Chemistry
Publication Type	e-Journal
Start Page	12004
End Page	12011
Issue	25
Volume	6
URL	http://pubs.rsc.org/en/journals/journalissues/ta

REQUEST DETAILS

Portion Type	Chart/graph/table/figure
Number of Charts / Graphs / Tables / Figures Requested	2
Format (select all that apply)	Print, Electronic
Who Will Republish the Content?	Author of requested content
Duration of Use	Current edition and up to 5 years
Lifetime Unit Quantity	Up to 499
Rights Requested	Main product
Distribution	U.K. and Commonwealth (excluding Canada)
Translation	Original language of publication
Copies for the Disabled?	No
Minor Editing Privileges?	No
Incidental Promotional Use?	No
Currency	GBP

NEW WORK DETAILS

Title	Investigation of structure and conductivity of LaNb0.9Mo0.1O4.05 based materials
Instructor Name	Stephen Skinner
Institution Name	Imperial College London
Expected Presentation Date	2024-10-05

ADDITIONAL DETAILS

Order Reference Number	N/A
The Requesting Person / Organization to Appear on the License	Yidong Han

REQUESTED CONTENT DETAILS

Title, Description or Numeric Reference of the Portion(s)	Fig. 3, Fig. 5
Editor of Portion(s)	Toyoura, Kazuaki; Sakakibara, Yusuke; Yokoi, Tatsuya; Nakamura, Atsutomo; Matsunaga, Katsuyuki
Volume / Edition	6
Page or Page Range of Portion	12004-12011
Title of the Article / Chapter the Portion Is From	Oxide-ion conduction via interstitials in scheelite-type LaNbO4: a first-principles study
Author of Portion(s)	Toyoura, Kazuaki; Sakakibara, Yusuke; Yokoi, Tatsuya; Nakamura, Atsutomo; Matsunaga, Katsuyuki
Issue, if Republishing an Article From a Serial	25
Publication Date of Portion	2018-01-01

https://marketplace.copyright.com/rs-ui-web/mp/license/091d4c50-f3e1-4dad-badb-97c4871729c6/3cc5c525-96ec-4381-816a-a3e3e9526732 1/1

Figure 2.4.1. Total conductivities of 1 mol% Ca substituted $LaNbO_4$ under different atmospheres. Reproduced with permission [9]. Copyright (2006), Nature.

20/08/2024, 16:32 RightsLink - Your Account

RightsLink

My Orders My Library My Profile Welcome yh219@ic.ac.uk Log out | Help | FAQ

My Orders > Orders > All Orders

License Details

This Agreement between Yidong Han ("You") and Springer Nature ("Springer Nature") consists of your license details and the terms and conditions provided by Springer Nature and Copyright Clearance Center.

Print Copy

License Number	5853130238708
License date	Aug 20, 2024
Licensed Content Publisher	Springer Nature
Licensed Content Publication	Nature Materials
Licensed Content Title	Proton conduction in rare-earth ortho-niobates and ortho-tantalates
Licensed Content Author	Reidar Haugsrud et al
Licensed Content Date	Feb 19, 2006
Type of Use	Thesis/Dissertation
Requestor type	academic/university or research institute
Format	print and electronic
Portion	figures/tables/illustrations
Number of figures/tables/illustrations	1
Would you like a high resolution image with your order?	no
Will you be translating?	no
Circulation/distribution	1 - 29
Author of this Springer Nature content	no
Title of new work	Investigation of structure and conductivity of LaNb0.9Mo0.1O4.05 based materials
Institution name	Imperial College London
Expected presentation date	Oct 2024
Portions	Figure 1
The Requesting Person / Organization to Appear on the License	Yidong Han
Requestor Location	Mr. Yidong Han Gradpad Woodlane Studios Woodlane 80 White City London, W12 0BZ United Kingdom Attn: Mr. Yidong Han
Billing Type	Invoice
Billing address	Mr. Yidong Han Gradpad Woodlane Studios Woodlane 80 White City London, United Kingdom W12 0BZ Attn: Mr. Yidong Han
Total	**0.00 USD**

Copyright © 2024 Copyright Clearance Center, Inc. All Rights Reserved. Privacy statement. Data Security and Privacy. For California Residents. Terms and Conditions.
Comments? We would like to hear from you. E-mail us at customercare@copyright.com

Privacy - Terms

https://s100.copyright.com/MyAccount/viewLicenseDetails?ref=1006b1db-fbaf-4ff7-b438-7f643e854d0c 1/1

Figure 2.5.1. Ionic radius (r_{ion}), coordination number and electronegativity (χ) of Nb and substituents on Nb sites. Reproduced with permission [10]. Copyright (2018), Royal Society of Chemistry.



20/08/2024, 20:18 marketplace.copyright.com/rs-ui-web/mp/license/39a60302-02c7-4132-b396-8d82d332485a/5b40ddcc-9749-4725-a19e-7b7c...

CCC Marketplace

This is a License Agreement between Yidong Han ("User") and Copyright Clearance Center, Inc. ("CCC") on behalf of the Rightsholder identified in the order details below. The license consists of the order details, the Marketplace Permissions General Terms and Conditions below, and any Rightsholder Terms and Conditions which are included below.

All payments must be made in full to CCC in accordance with the Marketplace Permissions General Terms and Conditions below.

Order Date	13-Aug-2024
Order License ID	1515327-1
ISSN	2052-1553
Type of Use	Republish in a thesis/dissertation
Publisher	Royal Society of Chemistry
Portion	Image/photo/illustration

LICENSED CONTENT

Publication Title	Inorganic Chemistry Frontiers
Article Title	Tailoring structural properties of lanthanum orthoniobates through an isovalent substitution on the Nb-site
Author / Editor	Royal Society of Chemistry (Great Britain),, Zhongguo hua xue hui (Beijing, China),, Beijing da xue,
Date	01/01/2014
Language	English
Country	United Kingdom of Great Britain and Northern Ireland
Rightsholder	Royal Society of Chemistry
Publication Type	e-Journal
Start Page	2157
End Page	2166
Issue	9
Volume	5

REQUEST DETAILS

Portion Type	Image/photo/illustration
Number of Images / Photos / Illustrations	1
Format (select all that apply)	Print, Electronic
Who Will Republish the Content?	Author of requested content
Duration of Use	Current edition and up to 5 years
Lifetime Unit Quantity	Up to 499
Rights Requested	Main product
Distribution	U.K. and Commonwealth (excluding Canada)
Translation	Original language of publication
Copies for the Disabled?	No
Minor Editing Privileges?	No
Incidental Promotional Use?	No
Currency	GBP

NEW WORK DETAILS

Title	Investigation of structure and conductivity of La0.9Mo0.1O4.05 based materials
Instructor Name	Yidong Han
Institution Name	Imperial College London
Expected Presentation Date	2024-10-05

ADDITIONAL DETAILS

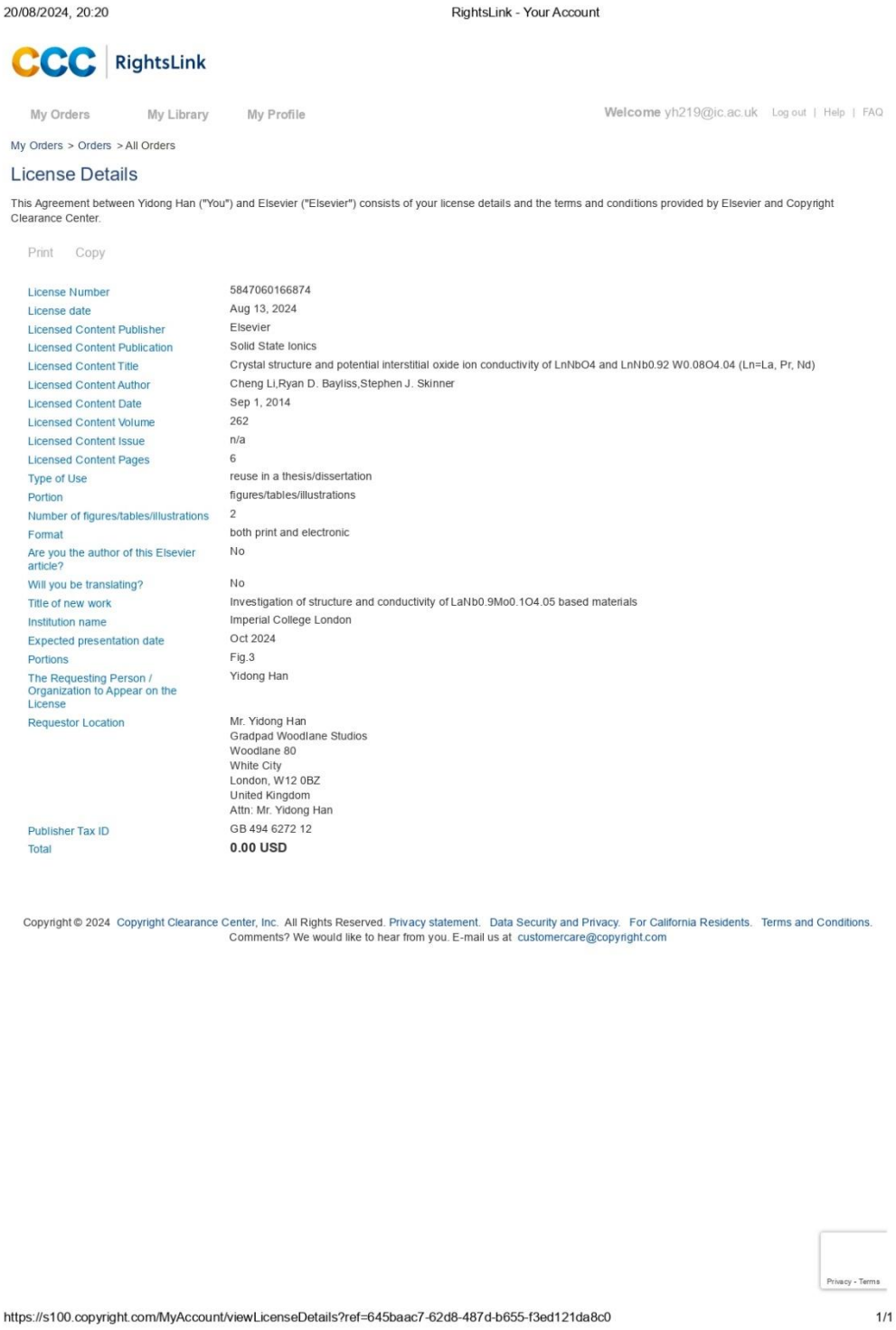
Order Reference Number	N/A
The Requesting Person / Organization to Appear on the License	Yidong Han

REQUESTED CONTENT DETAILS

Title, Description or Numeric Reference of the Portion(s)	Fig. 6
Editor of Portion(s)	Dzierzgowski, Kacper; Gazda, Maria; Kamecki, Bartosz; Mielewczyk-Gryń, Aleksandra; Wachowski, Sebastian; Winiarz, Piotr
Volume / Edition	5
Page or Page Range of Portion	2157-2166
Title of the Article / Chapter the Portion Is From	Tailoring structural properties of lanthanum orthoniobates through an isovalent substitution on the Nb-site
Author of Portion(s)	Dzierzgowski, Kacper; Gazda, Maria; Kamecki, Bartosz; Mielewczyk-Gryń, Aleksandra; Wachowski, Sebastian; Winiarz, Piotr
Issue, if Republishing an Article From a Serial	9
Publication Date of Portion	2018-01-01

https://marketplace.copyright.com/rs-ui-web/mp/license/39a60302-02c7-4132-b396-8d82d332485a/5b40ddcc-9749-4725-a19e-7b7c1e063e19 1/1

Figure 2.5.2. a) XRD patterns of $LaNb_{0.92}W_{0.08}O_{4.04}$ with satellite peaks marked with asterisk (inset), and b) ED patterns of $LaNb_{0.92}W_{0.08}O_{4.04}$ from [010] zone axis, respectively. Reproduced with permission [11]. Copyright (2013), Elsevier.



20/08/2024, 20:20 RightsLink - Your Account

CCC RightsLink

My Orders My Library My Profile Welcome yh219@ic.ac.uk Log out | Help | FAQ

My Orders > Orders > All Orders

License Details

This Agreement between Yidong Han ("You") and Elsevier ("Elsevier") consists of your license details and the terms and conditions provided by Elsevier and Copyright Clearance Center.

Print Copy

License Number	5847060166874
License date	Aug 13, 2024
Licensed Content Publisher	Elsevier
Licensed Content Publication	Solid State Ionics
Licensed Content Title	Crystal structure and potential interstitial oxide ion conductivity of LnNbO4 and LnNb0.92 W0.08O4.04 (Ln=La, Pr, Nd)
Licensed Content Author	Cheng Li,Ryan D. Bayliss,Stephen J. Skinner
Licensed Content Date	Sep 1, 2014
Licensed Content Volume	262
Licensed Content Issue	n/a
Licensed Content Pages	6
Type of Use	reuse in a thesis/dissertation
Portion	figures/tables/illustrations
Number of figures/tables/illustrations	2
Format	both print and electronic
Are you the author of this Elsevier article?	No
Will you be translating?	No
Title of new work	Investigation of structure and conductivity of LaNb0.9Mo0.1O4.05 based materials
Institution name	Imperial College London
Expected presentation date	Oct 2024
Portions	Fig.3
The Requesting Person / Organization to Appear on the License	Yidong Han
Requestor Location	Mr. Yidong Han Gradpad Woodlane Studios Woodlane 80 White City London, W12 0BZ United Kingdom Attn: Mr. Yidong Han
Publisher Tax ID	GB 494 6272 12
Total	**0.00 USD**

Copyright © 2024 Copyright Clearance Center, Inc. All Rights Reserved. Privacy statement. Data Security and Privacy. For California Residents. Terms and Conditions.
Comments? We would like to hear from you. E-mail us at customercare@copyright.com

Privacy - Terms

https://s100.copyright.com/MyAccount/viewLicenseDetails?ref=645baac7-62d8-487d-b655-f3ed121da8c0 1/1

Figure 2.5.4 Phase diagram of $LaNb_{1-x}Mo_xO_{4+0.5x}$. Reproduced with permission [12]. Copyright (2021), Royal Society of Chemistry.

20/08/2024, 20:22 marketplace.copyright.com/rs-ui-web/mp/license/c42a27d5-598a-44f5-b26a-d49edd9a04c1/3021ab14-ad03-4206-9feb-da53…

CCC Marketplace

This is a License Agreement between Yidong Han ("User") and Copyright Clearance Center, Inc. ("CCC") on behalf of the Rightsholder identified in the order details below. The license consists of the order details, the Marketplace Permissions General Terms and Conditions below, and any Rightsholder Terms and Conditions which are included below.

All payments must be made in full to CCC in accordance with the Marketplace Permissions General Terms and Conditions below.

Order Date	13-Aug-2024
Order License ID	1515331-1
ISSN	2050-7496
Type of Use	Republish in a thesis/dissertation
Publisher	Royal Society of Chemistry
Portion	Image/photo/illustration

LICENSED CONTENT

Publication Title	Journal of materials chemistry. A, Materials for energy and sustainability
Article Title	Exploring the nature of the fergusonite–scheelite phase transition and ionic conductivity enhancement by Mo6+ doping in LaNbO4
Author / Editor	Royal Society of Chemistry (Great Britain)
Date	01/01/2013
Language	English
Country	United Kingdom of Great Britain and Northern Ireland
Rightsholder	Royal Society of Chemistry
Publication Type	e-Journal
Start Page	4091
End Page	4102
Issue	7
Volume	9
URL	http://pubs.rsc.org/en/journals/journalissues/ta

REQUEST DETAILS

Portion Type	Image/photo/illustration
Number of Images / Photos / Illustrations	1
Format (select all that apply)	Print, Electronic
Who Will Republish the Content?	Author of requested content
Duration of Use	Current edition and up to 5 years
Lifetime Unit Quantity	Up to 499
Rights Requested	Main product
Distribution	U.K. and Commonwealth (excluding Canada)
Translation	Original language of publication
Copies for the Disabled?	No
Minor Editing Privileges?	No
Incidental Promotional Use?	No
Currency	GBP

NEW WORK DETAILS

Title	Investigation of structure and conductivity of LaNb0.9Mo0.1O4.05 based materials
Instructor Name	Yidong Han
Institution Name	Imperial College London
Expected Presentation Date	2024-10-05

ADDITIONAL DETAILS

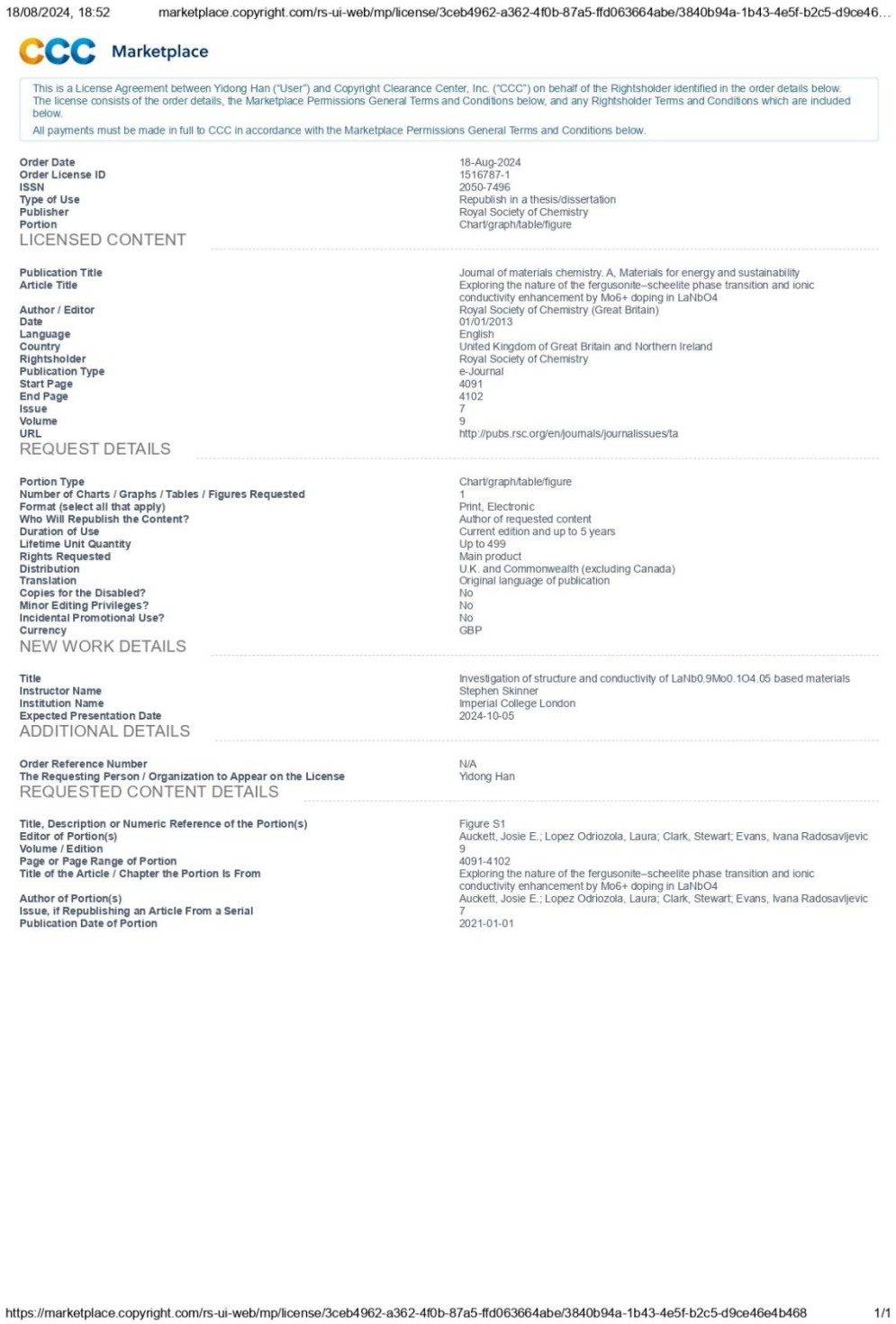
Order Reference Number	N/A
The Requesting Person / Organization to Appear on the License	Yidong Han

REQUESTED CONTENT DETAILS

Title, Description or Numeric Reference of the Portion(s)	Fig. 3
Editor of Portion(s)	Auckett, Josie E.; Lopez Odriozola, Laura; Clark, Stewart; Evans, Ivana Radosavljevic
Volume / Edition	9
Page or Page Range of Portion	4091-4102
Title of the Article / Chapter the Portion Is From	Exploring the nature of the fergusonite–scheelite phase transition and ionic conductivity enhancement by Mo6+ doping in LaNbO4
Author of Portion(s)	Auckett, Josie E.; Lopez Odriozola, Laura; Clark, Stewart; Evans, Ivana Radosavljevic
Issue, if Republishing an Article From a Serial	7
Publication Date of Portion	2021-01-01

https://marketplace.copyright.com/rs-ui-web/mp/license/c42a27d5-598a-44f5-b26a-d49edd9a04c1/3021ab14-ad03-4206-9feb-da533c890cd8 1/1

Figure 4.1.1. XRD patterns of $LaNb_{1-x}Mo_xO_{4+0.5x}$ (LNMO). The numbers denoted after LNMO are 100 times of the value of x. The satellite reflections from the modulated structures are marked by asterisks. Reproduced with permission [12]. Copyright (2021), Royal Society of Chemistry.



18/08/2024, 18:52 marketplace.copyright.com/rs-ui-web/mp/license/3ceb4962-a362-4f0b-87a5-ffd063664abe/3840b94a-1b43-4e5f-b2c5-d9ce46…

CCC Marketplace

This is a License Agreement between Yidong Han ("User") and Copyright Clearance Center, Inc. ("CCC") on behalf of the Rightsholder identified in the order details below. The license consists of the order details, the Marketplace Permissions General Terms and Conditions below, and any Rightsholder Terms and Conditions which are included below.

All payments must be made in full to CCC in accordance with the Marketplace Permissions General Terms and Conditions below.

Order Date	18-Aug-2024
Order License ID	1516787-1
ISSN	2050-7496
Type of Use	Republish in a thesis/dissertation
Publisher	Royal Society of Chemistry
Portion	Chart/graph/table/figure

LICENSED CONTENT

Publication Title	Journal of materials chemistry. A, Materials for energy and sustainability
Article Title	Exploring the nature of the fergusonite–scheelite phase transition and ionic conductivity enhancement by Mo6+ doping in LaNbO4
Author / Editor	Royal Society of Chemistry (Great Britain)
Date	01/01/2013
Language	English
Country	United Kingdom of Great Britain and Northern Ireland
Rightsholder	Royal Society of Chemistry
Publication Type	e-Journal
Start Page	4091
End Page	4102
Issue	7
Volume	9
URL	http://pubs.rsc.org/en/journals/journalissues/ta

REQUEST DETAILS

Portion Type	Chart/graph/table/figure
Number of Charts / Graphs / Tables / Figures Requested	1
Format (select all that apply)	Print, Electronic
Who Will Republish the Content?	Author of requested content
Duration of Use	Current edition and up to 5 years
Lifetime Unit Quantity	Up to 499
Rights Requested	Main product
Distribution	U.K. and Commonwealth (excluding Canada)
Translation	Original language of publication
Copies for the Disabled?	No
Minor Editing Privileges?	No
Incidental Promotional Use?	No
Currency	GBP

NEW WORK DETAILS

Title	Investigation of structure and conductivity of LaNb0.9Mo0.1O4.05 based materials
Instructor Name	Stephen Skinner
Institution Name	Imperial College London
Expected Presentation Date	2024-10-05

ADDITIONAL DETAILS

Order Reference Number	N/A
The Requesting Person / Organization to Appear on the License	Yidong Han

REQUESTED CONTENT DETAILS

Title, Description or Numeric Reference of the Portion(s)	Figure S1
Editor of Portion(s)	Auckett, Josie E.; Lopez Odriozola, Laura; Clark, Stewart; Evans, Ivana Radosavljevic
Volume / Edition	9
Page or Page Range of Portion	4091-4102
Title of the Article / Chapter the Portion Is From	Exploring the nature of the fergusonite–scheelite phase transition and ionic conductivity enhancement by Mo6+ doping in LaNbO4
Author of Portion(s)	Auckett, Josie E.; Lopez Odriozola, Laura; Clark, Stewart; Evans, Ivana Radosavljevic
Issue, if Republishing an Article From a Serial	7
Publication Date of Portion	2021-01-01

https://marketplace.copyright.com/rs-ui-web/mp/license/3ceb4962-a362-4f0b-87a5-ffd063664abe/3840b94a-1b43-4e5f-b2c5-d9ce46e4b468 1/1

Figure 4.2.5. XRD patterns of LNM10 recorded at 25 °C, 500 °C and 900 °C, respectively. The satellite reflections from the modulated structures are marked by arrows. Reproduced with permission [14]. Copyright (2023), Royal Society of Chemistry.

Figure 4.2.6. XRD patterns of LNM10 recorded at 700 °C, 750 °C and 800 °C, respectively. The satellite reflections from the modulated structures are marked by arrows. Reproduced with permission [14]. Copyright (2023), Royal Society of Chemistry.

Figure 4.2.7 SAED patterns of $LaNb_{0.9}Mo_{0.1}O_{4.05}$ along [010] zone axis. Two modulated vectors denoted as $\boldsymbol{q_1}$ and $\boldsymbol{q_2}$ are used. Reproduced with permission [14]. Copyright (2023), Royal Society of Chemistry.

Table 4.2. Normalised atomic ratios of cations of $La_{1-x}Gd_xNb_{0.9}Mo_{0.1}O_{4.05}$ series. Reproduced with permission [14]. Copyright (2023), Royal Society of Chemistry.

Figure 4.3.1. The Nyquist plot of LNM10 measured at 550 °C under air. The hollow circles show the measured value, and the red line shows the fitting results using the model in the inset. Reproduced with permission [14]. Copyright (2023), Royal Society of Chemistry.

Figure A1. XRD patterns of LNM10 recorded at 250 °C, 300 °C and 350 °C, respectively. The satellite reflections of the modulated structure are marked by arrows. Reproduced with permission [14]. Copyright (2023), Royal Society of Chemistry.

Figure A2. XRD patterns of La8Gd2 recorded at 250 °C, 300 °C and 350 °C, respectively. The satellite reflections of the modulated structure are marked by arrows. Reproduced with permission [14]. Copyright (2023), Royal Society of Chemistry.

Figure A3. XRD patterns of La6Gd4 recorded at 300 °C, 350 °C and 400 °C, respectively. Reproduced with permission [14]. Copyright (2023), Royal Society of Chemistry.

Figure A4. XRD patterns of La5Gd5 recorded at 350 °C, 400 °C and 450 °C, respectively. Reproduced with permission [14]. Copyright (2023), Royal Society of Chemistry.

Figure A5. XRD patterns of La4Gd6 recorded at 350 °C, 400 °C and 450 °C, respectively. Reproduced with permission [14]. Copyright (2023), Royal Society of Chemistry.

Figure A6. XRD patterns of La2Gd8 recorded at 450 °C, 500 °C and 550 °C, respectively. Reproduced with permission [14]. Copyright (2023), Royal Society of Chemistry.

Based on the journal author rights of Royal Society of Chemistry, the author of this article does not need to request permission to reproduce of figures and tables. The correct acknowledgement has been given.

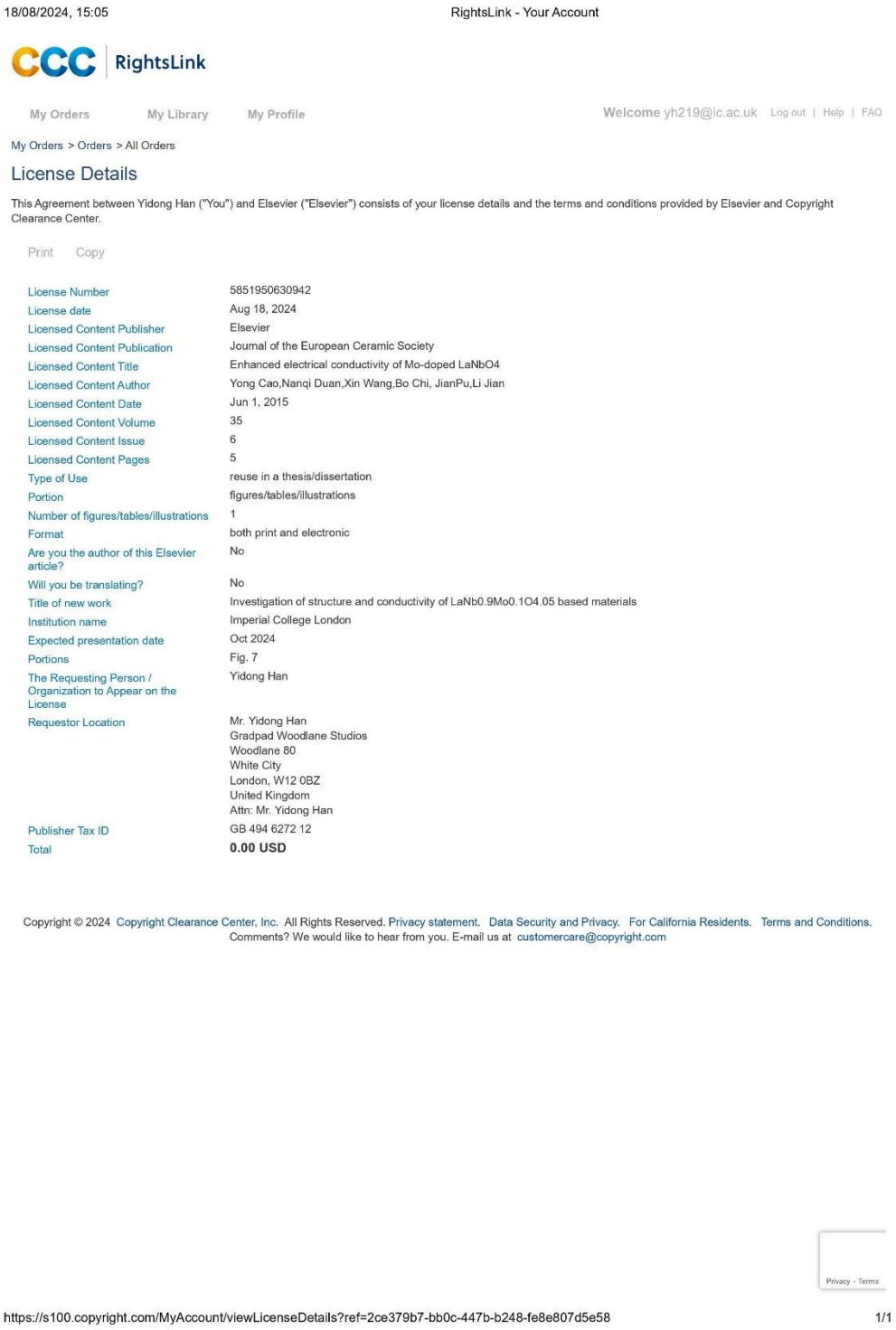
Figure 5.2.3. The phase diagram of $LaNb_{0.8}W_xMo_{0.2-x}O_{4.1}$ series from room temperature to 900 °C. Reproduced with permission [15]. Copyright (2024), Elsevier.

Figure 5.2.4. SAED patterns of LNW18Mo2 along zone axis [010] and $[1\bar{1}1]$ highlighting the modulated structures. Reproduced with permission [15]. Copyright (2024), Elsevier.

Table 5.2. Normalised atomic fractions of cations of $LaNb_{0.8}W_xMo_{0.2-x}O_{4.1}$ series. Reproduced with permission [15]. Copyright (2024), Elsevier.

Based on the journal author rights of Elsevier, the author of this article retains the right to include the figures and tables in a thesis or dissertation, provided it is not published commercially. Permission is not required. The journal has been referenced as the original source.

Figure 6.1.1. Room temperature XRD patterns of $LaNb_{0.8}Mo_{0.2}O_4$ after sintering, EIS measurement under 5% H_2/N_2 and reoxidisation under air at 900 °C for 5 hours. Reproduced with permission [16]. Copyright (2015), Elsevier.



18/08/2024, 15:05 RightsLink - Your Account

RightsLink

My Orders My Library My Profile Welcome yh219@ic.ac.uk Log out | Help | FAQ

My Orders > Orders > All Orders

License Details

This Agreement between Yidong Han ("You") and Elsevier ("Elsevier") consists of your license details and the terms and conditions provided by Elsevier and Copyright Clearance Center.

Print Copy

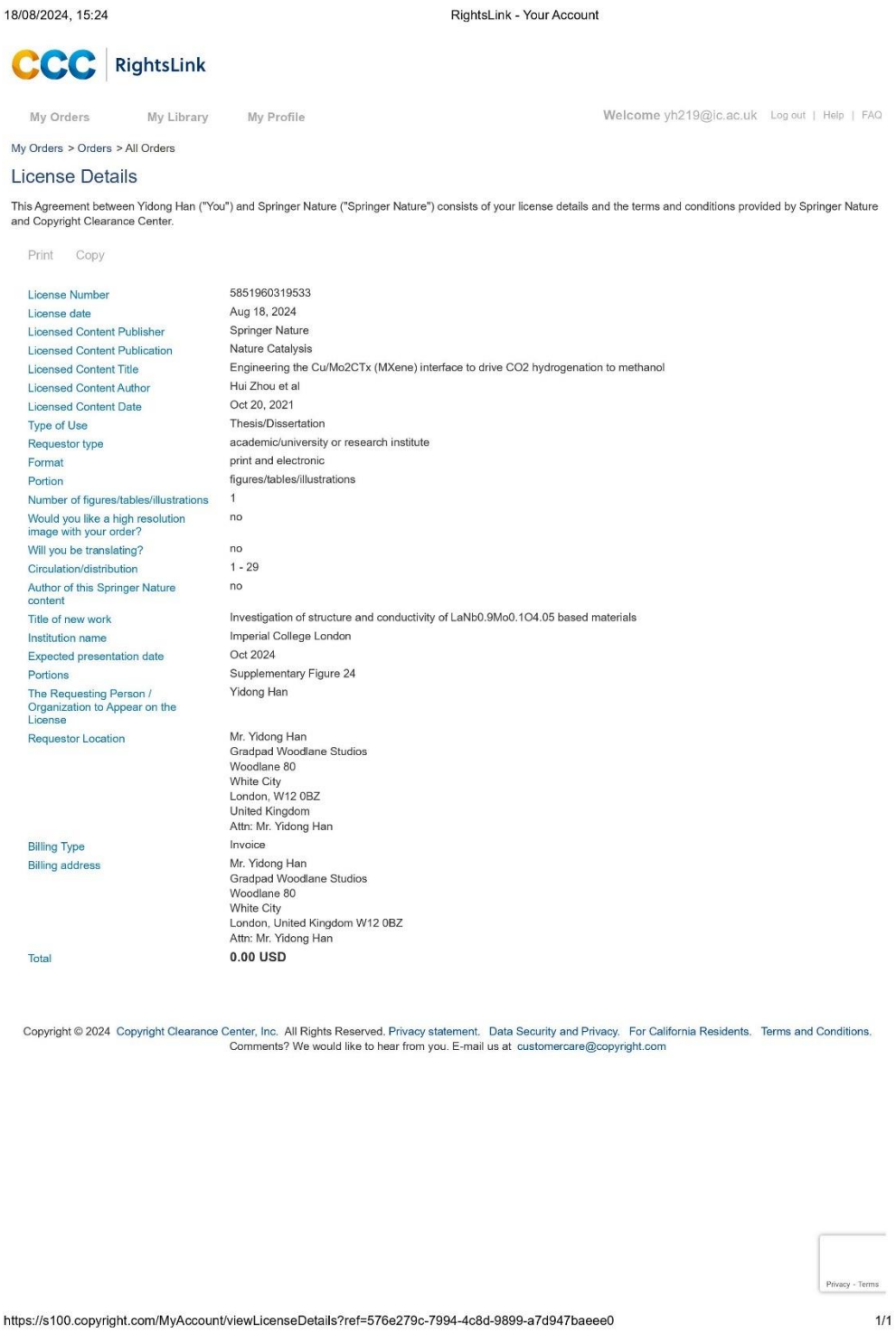
License Number	5851950630942
License date	Aug 18, 2024
Licensed Content Publisher	Elsevier
Licensed Content Publication	Journal of the European Ceramic Society
Licensed Content Title	Enhanced electrical conductivity of Mo-doped LaNbO4
Licensed Content Author	Yong Cao,Nanqi Duan,Xin Wang,Bo Chi, JianPu,Li Jian
Licensed Content Date	Jun 1, 2015
Licensed Content Volume	35
Licensed Content Issue	6
Licensed Content Pages	5
Type of Use	reuse in a thesis/dissertation
Portion	figures/tables/illustrations
Number of figures/tables/illustrations	1
Format	both print and electronic
Are you the author of this Elsevier article?	No
Will you be translating?	No
Title of new work	Investigation of structure and conductivity of LaNb0.9Mo0.1O4.05 based materials
Institution name	Imperial College London
Expected presentation date	Oct 2024
Portions	Fig. 7
The Requesting Person / Organization to Appear on the License	Yidong Han
Requestor Location	Mr. Yidong Han Gradpad Woodlane Studios Woodlane 80 White City London, W12 0BZ United Kingdom Attn: Mr. Yidong Han
Publisher Tax ID	GB 494 6272 12
Total	**0.00 USD**

Copyright © 2024 Copyright Clearance Center, Inc. All Rights Reserved. Privacy statement. Data Security and Privacy. For California Residents. Terms and Conditions.
Comments? We would like to hear from you. E-mail us at customercare@copyright.com

Privacy - Terms

https://s100.copyright.com/MyAccount/viewLicenseDetails?ref=2ce379b7-bb0c-447b-b248-fe8e807d5e58 1/1

Figure 6.2.3. The relationship between Mo K-edge positions from XANES spectra of different materials and their corresponding Mo oxidation states. Reproduced with permission [17]. Copyright (2021), Nature.



18/08/2024, 15:24 RightsLink - Your Account

RightsLink

My Orders My Library My Profile Welcome yh219@ic.ac.uk Log out | Help | FAQ

My Orders > Orders > All Orders

License Details

This Agreement between Yidong Han ("You") and Springer Nature ("Springer Nature") consists of your license details and the terms and conditions provided by Springer Nature and Copyright Clearance Center.

Print Copy

License Number	5851960319533
License date	Aug 18, 2024
Licensed Content Publisher	Springer Nature
Licensed Content Publication	Nature Catalysis
Licensed Content Title	Engineering the Cu/Mo2CTx (MXene) interface to drive CO2 hydrogenation to methanol
Licensed Content Author	Hui Zhou et al
Licensed Content Date	Oct 20, 2021
Type of Use	Thesis/Dissertation
Requestor type	academic/university or research institute
Format	print and electronic
Portion	figures/tables/illustrations
Number of figures/tables/illustrations	1
Would you like a high resolution image with your order?	no
Will you be translating?	no
Circulation/distribution	1 - 29
Author of this Springer Nature content	no
Title of new work	Investigation of structure and conductivity of LaNb0.9Mo0.1O4.05 based materials
Institution name	Imperial College London
Expected presentation date	Oct 2024
Portions	Supplementary Figure 24
The Requesting Person / Organization to Appear on the License	Yidong Han
Requestor Location	Mr. Yidong Han Gradpad Woodlane Studios Woodlane 80 White City London, W12 0BZ United Kingdom Attn: Mr. Yidong Han
Billing Type	Invoice
Billing address	Mr. Yidong Han Gradpad Woodlane Studios Woodlane 80 White City London, United Kingdom W12 0BZ Attn: Mr. Yidong Han
Total	**0.00 USD**

Copyright © 2024 Copyright Clearance Center, Inc. All Rights Reserved. Privacy statement. Data Security and Privacy. For California Residents. Terms and Conditions.
Comments? We would like to hear from you. E-mail us at customercare@copyright.com

Privacy - Terms

https://s100.copyright.com/MyAccount/viewLicenseDetails?ref=576e279c-7994-4c8d-9899-a7d947baeee0 1/1